LASER BASED STUDIES OF TRANSIENT SPECIES

IN A DISCHARGE FLOW APPARATUS

by

SCOTT SINGLETON

Ph.D
University of Edinburgh
September 1990

To my parents, who always believed

Shall I refuse my dinner because I do not fully understand the process of digestion? BUTSIR!...

This thesis is submitted in part fulfilment of the requirements for the degree of Doctor of Philosophy in the University of Edinburgh. Unless otherwise stated the work described is original and has not been previously submitted in whole or in part for any degree at this or any other University.

Scott Singleton

University of Edinburgh
September 1990

ACKNOWLEDGEMENTS

I would initially like to express my appreciation of my two supervisors, Dr J.P.T. Wilkinson (initially) and Prof R.J. Donovan (latterly, especially under the difficult circumstances of inheriting responsibility for myself following Dr Wilkinson's departure). Both are however, deserving of substantial gratitude for the provision of research facilities and constant encouragement throughout this work.

Grateful acknowledgement is made to the Science and Engineering Research Council for the provision of a Research grant.

An integral part of the success of any research effort is provided by the local support staff. In this respect, I am proud to thank several technical and support staff within the department, who have contributed in various ways to this work, in particular I would like to thank Derek, John, John, Evan and Stewart.

Similarly, I must thank Mrs Patricia Carter for her outstanding dedication to the cause of typing this thesis.

During this work I was lucky enough to obtain, from various sources, additional software. These provisions have significantly improved both the rapidity with which the work was completed, and also the quality of its conclusions. Therefore, I should specifically like to thank Prof R.N. Zare, Dr K.P. Lawley and Mr A.M. James for supplying me with working or easily modifiable versions of code which I subsequently implemented.

My warmest appreciation is also given to Dr K.G. McKendrick for his initial suggestion and subsequent substantial support and guidance on the investigation into the collision dynamics of the SiCl radical. Also, I must thank Dr J. Jeffries for kindly furnishing, in advance of publication, results of direct relevance to those carried out here on the SiCl radical.

I would also specifically like to thank Dr M.A. Brown for several interesting and informative discussions concerning multiphoton processes.

A concurrent and equally enjoyable challenge during the course of my Ph.D was to play in the department squash team. I should like to thank all my team mates, but in particular Ewan and Alistair for their tremendous camaraderie.

To those who have carried out 'long distance' favours for me, especially Mandy and Gordon, I am very grateful.

Finally I am happy to thank all my friends, colleagues and associated other drinking amigos (beastie boys), both past and present, within my research group and also the department in general, for making some of my best memories.

ABSTRACT

This thesis is concerned with spectroscopic and dynamical studies of transient species in a flow reactor.

For the SiCl radical various studies using Laser Induced Fluorescence were performed. The excitation spectra detailed the band positions of the lower lying vibrational levels of the $B^2\Sigma^+$ and $B'^2\Delta$ states, with the bands appearing to be unperturbed but suffering from spectral congestion. Dispersed fluorescence studies of these bands enabled measurement of the vibrational transition probabilities between the ground and excited states. By comparing these probabilities with calculated values, estimates of the transition dipole moment functions for the B-X and B′-X transitions were made: with the conclusion that the B-X moment was nearly constant with internuclear separation, while the B′-X moment was a strongly decreasing function with increasing internuclear separation. A simple, yet consistent, molecular orbital argument was presented as an explanation of the form of the transition moment functions. Because of the longer radiative lifetime of the B′ state (~ 1.0 μs compared to ~ 10 ns for the B state) collision induced energy transfer of the B′ state was readily observed experimentally. Total quenching cross sections for removal of $v' = 0$ and 1 of the B′-state are reported for a variety of nonpolar molecular colliders, with the magnitude of the cross sections appearing to be correlated with long range attractive forces between the collision pair. Partial cross sections for transfer from initially populated B′ state to the B state are also reported, in this case, the cross sections may be influenced by specific resonant energy transfer processes. However, for transfer to $v' = 2$ of the B state (for which no resonant processes were obvious) the magnitude of the partial cross sections again appeared to be correlated with long range attractive forces.

Resonance Enhanced Multiphoton Ionisation studies were performed on the HI molecule, formed as a result of the reaction: $H+I_2 \longrightarrow HI+I$. Spectroscopic observations on this molecule are reported at selected positions between 67500 and 73500 cm^{-1}. Wherever possible effective molecular constants were calculated from the observed spectra. While various transitions were evident from ground state hot bands, observation of nascent rotational or vibrational product state distributions, of the reaction, were not made in these relatively slow flow conditions. The complementary nature of the single photon (vuv) and two photon absorption techniques was highlighted by the apparent inversion of intensities with which bands were observed by the two techniques. Bands previously unobserved in the single photon absorption work are reported. The bands are assigned as transitions to the $i^3\Delta(2)$ and $d^3\Pi_0(0^+_-)$ states.

Additional observations of several atomic species following various multiphoton ionisation processes were made during the course of this work. Results are reported, in the appendices, for: H,C,Cl,Br,I,P and S atoms.

CONTENTS

CHAPTER 1
INTRODUCTION

This thesis is concerned with investigations into the production and characterisation of simple transient reactive atomic and molecular gaseous species. Chapter 1 is devoted to laying the foundations for the remainder of the thesis. Following a brief description which aims to highlight the importance of these species, the remainder of the chapter is devoted to a discussion of the unifying principles of the work presented. These principles are the generation of transient fragments in a discharge flow apparatus and the laser based detection techniques. The laser techniques are Resonance Enhanced Multiphoton Ionisation (REMPI) and Laser Induced Fluorescence (LIF). Where appropriate however, more detailed discussions of individual aspects of the techniques and methods used are given in the main body of the text.

Chapter 2 describes the experimental apparatus and methodologies required by the various investigations. Chapter 3 details investigations into the spectroscopy and collision dynamics of the chlorosilylidyne (SiCl) radical by LIF. In Chapter 4 a study of the spectroscopy of some of the excited states of the Hydrogen Iodide (HI) molecule using REMPI is presented, the molecule being generated via the reaction $H + I_2 \longrightarrow HI + I$.

1.1 Importance of Transient Gaseous Species

The study of chemistry is concerned with understanding the structure and properties of substances and the reactions that transform one set of substances to another.

In the gas phase 'reactions' are often found to occur in complicated schemes that are in fact composed of one or more series of elementary reactions or processes. Furthermore, the important species in these processes are often not the feedstock molecules themselves but are in

fact highly reactive and often structurally simple species such as atoms, small free radicals, electronically excited molecules or molecular ions. It is not surprising, therefore, that elucidation of these elementary processes has long been a prime motivation in chemical research, both theoretically and experimentally. While it would present a formidable task to list all the individually important reactions in which these species participate, it is possible to highlight the areas of most importance:

1) Atmospheric chemistry [1] [2]
2) Combustion chemistry [3] [4]
3) Electronics Industry [5]
4) Laser technology [6]
5) Interstellar media [7]

As a brief illustrative example, consider probably the most important area both environmentally and economically, and one that has stimulated curiosity since the dawn of natural philosophy [8], that is atmospheric chemistry. The atmosphere is an extremely complicated system, being best considered as a time dependent multi-layered photochemical process driven by the sun. While the upper layers of the atmosphere (heterosphere > 90 km) are governed by ion molecule interactions, the lower layers (homosphere < 90 km) can be described by several series of complex interacting reaction schemes between atomic and radical species containing mostly carbon, hydrogen, nitrogen, (chlorine and sulphur) and oxygen atoms. These reactions are strongly influenced by photochemical, dynamical, catalytic and sink molecule effects.

One of the most important areas of concern has been the pollution and interfering effects that anthropogenic chemicals have had on the atmosphere. These effects include photochemical smog [9] and stratospheric ozone destruction [10]. Hence, the ability to predict the global impact of such effects is of prime importance.

The fundamental importance of these simple systems has led to increases in demand for both the quantity and quality of experimental and theoretical data. This challenge has been met:

1) Experimentally

   i) Studies of complex reactions in both a diagnostic and an absolute concentration measurement sense.
   ii) Measurement of bulk (fully averaged) reaction rates.
   iii) Measurement of energy transfer probabilities.
   iv) Studies under microscopic conditions of near fully state specified reactive collisions.

2) Theoretically
   i) Electronic structure calculations.
   ii) Potential energy hypersurface and dynamical calculations.
   iii) Reaction rate theory.

1.2 Transient Fragment Generation

Investigations into the behaviour of transient species almost invariably begins by the dissociation of a suitable stable precursor species (normally closed shell). However, typical closed shell molecules need, on average, to absorb several electron volts (eV) of energy before bond rupture or fragmentation occurs. Methods of achieving bond cleavage include thermal, discharge and photolytic sources. The choice of source is however crucially dependent on the tolerance of the system under study to secondary species and the apparatus available.

All of the above methods can be coupled to a flow reactor which, due to the additional consequences of inherent simplicity and versatility has become the most successful method for investigations involving reactive gaseous species.

The foundations of the discharge flow method were laid approximately seventy years ago by work carried out separately by Wood [11] and Bonhoeffer [12], who discovered that large quantities of atoms produced in an electric discharge could be pumped considerable distances down a tube. The first kinetic measurements were subsequently made by Smallwood [13]. However, the technique and methodology as it is known today, relies heavily on the work of Kaufman [14].

There are three broad regimes of study for which flow rections have been utilised, these are: bulk kinetic measurements near 300 K; measurements of reaction rates of refractory species in high temperature fast flow reactions (HTFFR) [15] and measurements of rotational and vibrational relaxation [16] [17] and quenching of electronically excited species [18]. In all cases the tube serves the same 'cleaning' purpose of separating the generation and probing zones. While there are gross similarities between the three methods, the requirements of the individual study shapes the overall reactor design. For example, HTFFR requires high flows, very high temperatures and normally operates at elevated pressures. For relaxation or quenching studies again fast flows are needed but lower pressures reduce quenching. A typical minimum radiative lifetime of > 0.5 ms is required.

The experimental nature of the studies carried out in this thesis all fall into the general regime characterised by bulk measurements near 300 K. A somewhat generalised set of conditions can be outlined for which the important parameters of pressure drop and radial and axial diffusion are characterised, see Chapter 2, and for which normal operation of the flow tube is well described [19].

1) Pressure range: 1-10 Torr, being restricted by the gas dynamical effects of flow regimes and diffusive mixing.

2) Temperature range: 200-600 K, being limited by enhanced wall sticking probability at low temperatures and precursor and apparatus stability at high temperature.

3) Detector: any sensitive detector is suitable.

4) Reactant: the most versatile method of looking at reactive species.

5) Heterogeneous reaction: important for kinetic measurements and for studies of excited species due to high deactivation efficiency.

6) Rate constant range: for bimolecular reactions between 10^{-10} - 10^{-16} cm^3 $molecule^{-1}$ s^{-1}.

1.3 Detection Methods

The success of the discharge flow technique has to a considerable extent been dependent on the success with which various detectors have been coupled to it. An optimal choice of detector is however dependent on the study being carried out; for example, studies on relaxation processes have traditionally relied upon chemiluminescence measurements [16] [17], while quenching studies have utilised both absorption and fluoresence techniques [18]. Measurements of reaction rate have been reported with a very diverse range of methods, that cover most forms of spectroscopy.

With the availability of laser technology (optically induced) detection methods, specifically those based on ionisation and fluorescence, become very attractive for monitoring transient species. This arises from four major advantages:

1) Non-invasive, implying minimal disturbance of the gaseous system under study.

2) Spatially resolved, the signal arising only from the interaction of the interrogating laser beam and sample.

3) Selectivity, a combination of narrow linewidth and broad tunability, deep into the ultra-violet (uv) for pulsed systems implies that species can normally be unambiguously detected. In the case of fluorescence studies choice of excitation and detection wavelengths is possible and in certain circumstances the (time) rate of decay of the fluorescence can be used to distinguish between differing LIF signals.

4) Sensitivity, for pulsed systems the signal magnitude is in phase with the laser, being superimposed on a non-synchronous background. Hence, electronic discrimination and signal averaging can be usefully applied.

1.3.1 Multiphoton Processes

Multiphoton processes were first predicted in 1931 by Goppert-Mayer [20]. However, due to their inherently small cross sections they were not observed until 1953 [21]. Observation of multiphoton events using visible light were reported soon after the development of the laser [22]. However, with the subsequent development of tunable dye laser technology advances followed rapidly, with the first observations, by these processes, of a simple gaseous species, NO, being presented in 1974 by Bray et.al. [23]. The first reports of multiphoton ionisation were made independently in 1975 by Johnson and co-workers [24] and by Dalby and co-workers [25].

Multiphoton ionisation spectroscopy is thought to occur via an initial simultaneous absorption of an integer number of photons that takes the species of interest from the ground state (normally) to a real excited

intermediate state. Ionisation occurs via the subsequent absorption of additional photons until the molecule has an energy greater than its ionisation threshold. Hence, if a molecule requires the simultaneous absorption of n photons to reach the excited state and a further simultaneous absorption of m photons to reach the ionisation continuum the process is said to be an [n + m] Resonance Enhanced Multiphoton Ionisation process. Each photon absorbed up to the real excited state may be considered to transfer the species into a subsequent virtual excited state with an energy corresponding to that of the photon plus that which it has gained from previous events. The virtual excited state is a non-stationary state which, in general, is considered a superposition of an infinite number of eigenstates (stationary states) of the species. The virtual state has a lifetime associated with the passage of the photon past the species ($\sim 10^{-15}$ seconds). Hence, the multiphoton process will be completed only if the required numbers of photons arrive within the virtual state lifetime (fly-by time). It is obvious, therefore, that the probability of having n photons 'present' within this lifetime decreases rapidly as n increases. Stepping through a real state on the way to the ionisation continuum as opposed to simple multiphoton absorption to the continuum normally yields a considerably larger (resonantly enhanced) signal. The greater signal associated with resonance enhanced experiments is due to the greater lifetime ($\geq$ 1 ns) and hence greater absorption cross section of the real intermediate state.

The observed spectrum in a REMPI experiment is normally thought to map the population in the ground-state. This argument is based on the assumption that the probability of ionisation from the intermediate state is essentially independent of wavelength.

The use of multiphoton techniques has spread into several important areas associated with gas kinetics, these include spectroscopy [20], photochemistry [27] and reaction dynamics. There are several reasons for the popularity of such techniques, the first of which follow from the points outlined in Section 1.3, i.e. the high sensitivity

associated with laser techniques. Although typical multiphoton absorption cross sections are low e.g. 10^{-51} cm^4s (two photon) and 10^{-82} cm^6s^2 (three photon) [28], modern pulsed laser systems are sufficiently powerful ($\sim 10^5$ W in 10ns) that with appropriate focussing a significant population in the excited state can be achieved. The other advantages follow from the intrinsic nature of multiphoton events:

1) Absorption of light is governed by a combination of selection rules and relatedly the magnitude of the dipole matrix elements for the combining states. The selection rules for multiphoton absorption differ from the single photon situation. In fact they often permit absorption to states fully forbidden and hence normally unobservable in a single photon process.

2) The use of polarisation measurements make it possible to identify state symmetries by simple empirical means [28].

3) Simple species often have their first excited states lying in the uv or vacuum uv (vuv, $\leq$ 180 nm). Studies using two or more photons of visible or uv radiation are much easier to perform than using single photon vuv radiation.

It is generally agreed that ionisation offers a greater sensitivity to detection than fluorescence for most multiphoton processes. This is due to:

1) The potential for 100% collection efficiency of the charged species generated by the laser pulse and additionally in a mass selected way.

2) There is normally a high probability of subsequent ionisation of the intermediate state. This is due to the larger ionisation cross section and the intense laser field required to initially overcome the small absorption cross section associated with the initial multiphoton process.

3) Less background noise effects, such as scattered light and dark current in the photosensitive device.

4) Competing rapid non-radiative loss processes such as predissociation, can prevent the occurrence of fluorescence from some states. While ionisation methods will also be affected by such processes, their inherently shorter timescale means that ionisation will often still be detectable even in the presence of a rapid non-radiative mechanism.

The concept of a REMPI experiment is very simple. It consists of focussing the tunable laser beam into the gas sample and collecting, amplifying and recording the current pulse associated with the ionic species generated as a function of excitation wavelength.

However, considerable caution should be exercised before any interpretation of results as being due to REMPI is made. Problems may arise because the small cross sections associated with multiphoton events and the concomitant intense light fields necessary to detect an appreciable signal may cause several other non-linear optical or dynamical processes to occur simultaneously. A non-linear optical process is one where the (index variation of) signal intensity behaves non-linearly as the incident power increases. These processes include: third harmonic generation (THG), photodissociation, Raman phenomena and saturation effects including Rabi cycling. Hence, a complete description of the above processes together with ionisation and fluorescence presents a very difficult task [29].

The most general treatment of any multiphoton ionisation (MPI) process follows from considering the equations of motion of the density matrix of the system and is appropriate if there is coherence between the laser field and the gaseous system [29].

Such a description is not necessary within the bounds of the present work, instead a population rate equation (PRE) analysis provides an adequate description of the dynamics of the situation. The rate equation approach may be applied with confidence if the following conditions are satisfied [31].

1) The laser bandwidth is much larger than the natural linewidth of the resonant transition.

2) The Rabi cycling frequency is significantly slower than the rate of ionisation.

3) The Rabi cycling frequency of the transition is long compared to the coherence time of the laser light field.

Point 2 is equivalent to saying that any coherence will be eroded if the ionisation rate is sufficiently fast (very intense fields). However, the stochastic nature of the light field associated with a multi-mode dye laser ($\sim$ 1 cm^{-1} bandwidth and 33 ps coherence time) is sufficiently great that coherence effects are normally negligible.

The population rate analysis as presented by Zakheim and Johnson [32] describes the ionisation of a molecule initially in the ground state X, through an intermediate state R, to the ionisation continuum C in an [n + m] process, Figure 1.1. The differential equations governing the populations in each level are given by:

$$\dot{X} = -\alpha X + \phi R \qquad (1)$$

$$\dot{R} = \alpha X - AR \qquad (2)$$

$$\dot{C} = \beta R \qquad (3)$$

where $\phi = \alpha + k_o$ and $A = \alpha + k_o + k_p + \beta$.

FIGURE 1.1: The rate processes in a three level PRE model. The individual rate constants are the n photon stimulated absorption (emission) constant $\alpha(= \sigma_I I^n)$, the m photon ionisation constant $\beta\ (= \sigma_{II} I^m)$, the one photon spontaneous emission constant k_o, and the spontaneous irreversible decay constant k_p of the resonant intermediate state.

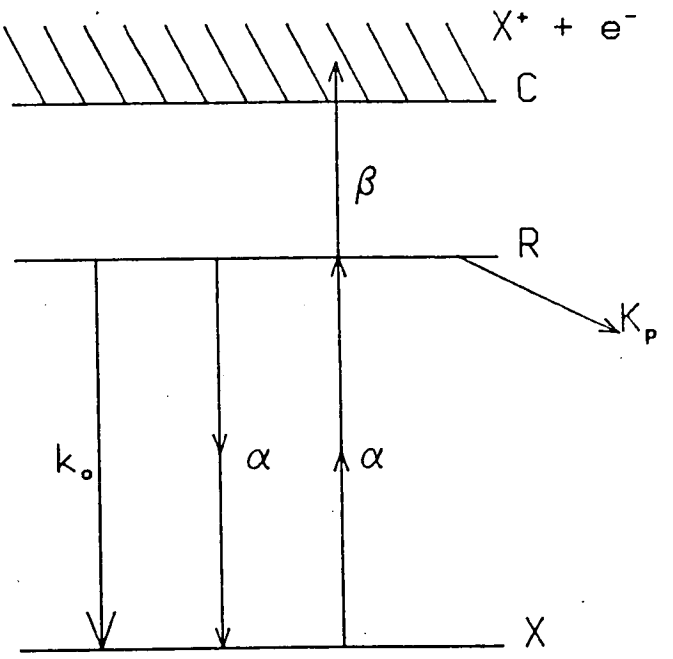

The solution to these equations yields the ion concentration C, and assumes that the initial ground state population is X_o and the laser pulse is square and of duration t_L.

$$C = \frac{\beta X_o}{\beta + k_p} \left[1 + \frac{L}{K-L} e^{-Kt_L} - \frac{K}{K-L} e^{-Lt_L} \right] \qquad (4)$$

where

$$\left\{ \begin{matrix} K \\ L \end{matrix} \right\} = \left(\frac{A + \alpha}{2} \right) \left\{ \begin{matrix} + \\ - \end{matrix} \right\} \frac{[(A + \alpha)^2 - 4\alpha (\beta + k_p)]^{1/2}}{2} \qquad (5)$$

α is defined as $\sigma_I I^n$ and β is defined as $\sigma_{II} I^m$. The exponentials exhibit limiting case behaviour: at low intensity the probability of ionisation is proportional to I^{n+m}, while at moderate intensity (typical laser pulse and focussing conditions) and since $\beta >> \alpha$, the ionisation step will become saturated. In this case the overall probability is proportional to I^n.

Measurements of the slope of a plot of ln C versus ln I are most often interpreted in terms of the non-linear order of the rate determining process. In the limit of high intensity full saturation of all absorption processes would be expected and a graph of ln C versus ln I would be expected to yield a zero gradient. In fact, for a typical experimental situation consisting of a spherical lens with conical focussing geometry an I^o dependence of the signal at saturation is not attained. The intensity dependence for such a situation scales as $I^{3/2}$, the effect is purely geometric in nature, being independent of the order of multiphoton process [33] [34], and dependent only on the nature of the focussing system and is called geometric saturation. Further increasing the laser intensity simply causes an increase in the interaction zone over which ionisation is produced.

A PRE description of REMPI processes is equally valid for either atomic or molecular species. However, molecular species are capable of exhibiting additional physical phenomena not available to atomic species, most notably internal radiationless transitions and dissociation. The effect of any additional competing loss mechanism will normally manifest itself in changes in the intensities and widths of spectral lines. The additional loss mechanism implies an overall reduction in the excited state lifetime and, therefore, the line width of the transition is concomitantly broadened. Such an effect is known as lifetime broadening and if severe enough will prevent a line appearing in the spectrum.

Although non-radiative mechanisms form the most important reason for 'lack of appearance' of spectral lines [35], other effects that arise from the intense fields associated with focussed laser beams can become evident.

Power broadening can affect both LIF and REMPI spectra, although the effect is two-fold for a REMPI process. When the laser intensity becomes too high, in the initial excitation step, stimulated emission begins to be observed. The appearance of stimulated emission is normally called saturation, and is evidenced by a weaker than n intensity dependence for an n photon transition. At complete saturation the ground and excited state populations are in a ratio of their degeneracies, with species being incoherently pumped between the upper and lower levels. If the stimulated emission pumping rate is comparable to the rate of spontaneous emission then the lifetime of the state is reduced and line broadening occurs. This kind of power broadening is manifest in LIF experiments. An additional aspect of power broadening occurs in a REMPI experiment and arises because the ionisation process is normally much more likely than the initial multiphoton excitation. Therefore, if the interaction time of the excited species with the laser field (ionisation process) is

significantly less than the natural lifetime of the state, such that the lifetime of the state is reduced, power broadening will again occur [36]. If the intensity is high enough this effect would seriously affect the appearance of the spectrum, both in terms of experimental resolution and line intensity.

An important non-linear optical effect for gaseous species is THG. In atomic systems the conditions under which THG is observed are well documented and understood [37] [38] [39] [40] [41], where it is evident that it is crucially dependent on the pressure and laser intensity. THG has also been reported in molecular systems [42] where 'quenching' of expected REMPI features was observed. The disappearance of expected REMPI features is explained as an interference between two different, but coherent, pathways to a state in an optically thick sample.

A typical line on a spectrum will normally be found to have a so-called Voigt profile. The Voigt profile is a convolution of Gaussian and Lorentzian functions and is given by:

$$I(\omega'_o - \omega, {}^{\Gamma}/_{\Delta}) = \int_o^{\infty} G(\omega'_o - \omega, \Delta)\, L(\omega - \omega'_o, \Gamma)\, d\omega'_o \quad [43] \qquad (6)$$

where ω'_o is the resonance frequency
ω is the frequency distribution about ω'_o
Γ and Δ are the full width half heights of the distributions.

The Lorentzian distribution is a convolution of natural and collisional linewidths while the Gaussian distribution reflects the Doppler broadening. For a typical species with mass 100 amu; 10 ns radiative lifetime; radiating at 500 nm; with an optical collision cross section of 5×10^{-15} cm^2; pressure of 10 Torr; temperature 300 K, the contributions to the linewidth are:

Natural linewidth (Lorentzian)	0.53×10^{-3} cm^{-1}
Collision linewidth (Lorentzian)	0.30×10^{-3} cm^{-1}
Doppler linewidth (Gaussian)	24.8×10^{-3} cm^{-1}

The above values should be compared to a typical dye laser resolution of ~ 0.5 cm^{-1}. Hence, under circumstances with minimal external broadening effects the observed linewidth and shape will be governed by the experimental apparatus.

There is however an important phenomenon which can lead to the observation of assymetric lineshapes: this is the quadratic a.c. Stark effect. The effect is so-called because the energy level shift (Stark shift) depends quadratically on the electric field strength. The effect has been shown in the low pressure REMPI spectrum of NO [44,45] and is well-known in atomic systems [46,47]. The a.c. Stark shift depends purely on intensity and hence arises from both temporal and spatial effects within the laser pulse. However, a normal experimental configuration (conically focussed beam) is such that spatial effects dominate. Consider two identical species at positions A and B within the focussed beam where the intensity $I_A > I_B$. The quadratic a.c. Stark shift predicts that the shift in the resonance frequency ν_r is proportional to the radiation intensity. Hence, the line shift at A will be greater than that at B. This process results in a broadening of the transition. An asymmetric line profile follows from the fact that there will be more absorbing species in the lower intensity regions. The resonance frequencies are normally observed to shift to the blue [44], this is consistent with the excited state being more

polarisable than the ground state. The effect is observed to be a complicated function of pressure, laser intensity and bandwidth and has been observed to be quenched at sufficiently high pressure [45]. These observations have been described in terms of a quantum interference effect [45]. That is, at low pressure it is permissible to think of individual molecules in the light field, but at high pressures it is necessary to think of a laser ensemble system, with coupling of the gaseous species occuring via the intense electric field. In the presence of an a.c. Stark effect, the effective order of the non-linear dependence on intensity for a multiphoton process may differ considerably from that predicted from a PRE analysis [48].

1.3.2 Laser Induced Fluorescence

LIF has become a workhorse technique in the study of gas kinetics and has been successfully applied to such diverse areas as: spectroscopy, state to state reaction dynamics [49], quantitative species concentration measurements including collision dynamics data [50] and the measurements of angular momentum distributions [51].

LIF has been successfully applied with both linear [52] and non-linear excitation processes [23] in both atomic and molecular systems. The description given here is of more relevance to the linear regime, being in accord with the experimental procedure of the study on the SiCl radial. However, the arguments presented can normally be extended to non-linear excitation without loss of generality.

The successful application of LIF to the areas outlined above has relied on two factors, these are: the inherent operational advantages briefly discussed in section 1.3 and the successful theoretical interpretation of the basis of LIF and hence the results it engenders.

The basic experimental configuration employed for most LIF experiments is quite simple. The laser beam is directed through the gas sample, which is contained in a suitable vessel. The fluorescence emitted at right angles to the direction of beam propagation is collected by appropriate optics, passed through a 'filter' and onto a photoelectric detector. The 'filter' in the experiment is either fixed, as with a colour glass or interference filter, or may be scanned as for a monochromator.

There are two modes of spectroscopic data acquisition available with a LIF experiment, these are the so-called excitation and fluorescence scans.

In an excitation scan the 'filter' is chosen such that fluorescence from all pumped levels can be detected with equal efficiency. Hence, as the laser frequency is scanned through an absorption region, each time it matches that of an absorption line, fluorescence results. An excitation scan therefore, closely mimics a conventional absorption scan, the main difference is however that the fluorescence overlays a near zero background and hence absorptions down to $\sim 10^{-6}$ can be seen, while absorption spectra can normally only be recorded down to absorbances of $\sim 10^{-2}$ [50]. Excitation scans, therefore, provide information on ground state population distributions, state symmetries and spectroscopic constants, although as discussed previously this information is affected by any loss processes in the upper state.

In a fluorescence scan the laser will typically be 'parked' on a single rovibronic level and the 'filter' (monochromator) scanned such that the fluorescence emitted by the pumped level can be investigated sequentially. For an isolated molecule the emitted fluorescence will be that emitted only by the pumped level. However, as a result of any collisional process other levels may be populated by collisional energy transfer and they may also emit.

When the rate of pumping is low the intensity I, of LIF emission is normally assumed to be given by:

$$I = k'n\, B_{12}\, \rho\Delta t_L \qquad (7)$$

k' is a proportionality constant accounting for the sensitivity of the detection system and incorporates various angular and geometric factors (see following notes).

n is the population density in the lower state.

B_{12} is the Einstein coefficient for absorption

ρ is the radiation density at the absorption frequency.

Δt_L represents a square wave excitation laser pulse of duration Δt_L.

Equation (7) is however only valid if the following three conditions are satisfied [51].

1) The polarisation of the laser and detected fluorescence are unchanged during the experiment.

2) The distributions of all molecules in all states probed by the laser are characterised by the same values of the angular momentum moment distributions (isotropic sample) specifically $A_o^{(2)}$ and $A_o^{(4)}$. These moment distributions reflect the effective populations in the m sublevels for a particular J. Where the total m distribution can be characterised by various combinations of angular momentum distribution functions, for example a quadrupolar distribution is given the symbol $A_o^{(2)}$, while a hexadecapole distribution is given by $A_o^{(4)}$.

3) The fraction of collected fluorescence due to Q branch and P or R branch transitions are the same for all states studied.

For a beam of linearly polarised light incident on an isotropic distribution of ground state molecules (all m sublevels within a given J level being equally populated) absorption can occur on either a Q or a P, R branch. The intermediate state formed will be effectively aligned through the preferential excitation of those molecules having larger projections of their transition dipole moments on the electric field vector of the linearly polarized laser beam. The initial absorption step therefore defines an axis of symmetry for the system. Subsequent emission occurs and since in the classical limit Q and P, R branch transitions have transition dipole moments that lie respectively parallel and perpendicular to the total angular momentum vector J, it can be seen that the various combinations of P, Q and R branches for excitation and emission, may produce differences in the observed intensity predicted by the simple model in equation (7). The alignment effect is important since it will affect interpretation of, for example, the temperature of a system. It should be noted that other angular momentum moments can be determined in this and other multiphoton experiments [53].

The most dramatic factor influencing the appearance of LIF spectra results however from saturation effects, see power broadening discussion earlier. If present, saturation affects the interpretation of results that are based on the assumption that the observed intensity relates only to a combination of linestrength and population factors. The effect is most pronounced in comparisons of states which have significantly different transition strengths since the state with the greater transition strength will saturate at much lower powers [54]. However, there are conditions when saturation is useful. This occurs when increasing the laser power will increase the experimental signal to noise (s/n) ratio and is most appropriate if the states under

study have similar transition strengths. At complete saturation it becomes possible, in principle, to obtain population information without knowledge of transition strengths [51]. Experimental difficulties are quite manifest in this regime however, and arise due to the Gaussian intensity profile and inhomogeneities in the beam. Saturation also significantly diminishes the amount of information obtainable from alignment measurements [55].

REFERENCES

1. R.P. Wayne in 'Chemistry of Atmospheres' (Clarendon Press, Oxford 1985).
2. B.J. Findlayson-Pitts and J.N. Pitts Jr. in 'Atmospheric Chemistry' (Wiley, New York 1986).
3. G.J. Minkoff and C.F.H. Tipper in 'Chemistry of Combustion Reactions' (Butterworths, London 1962).
4. C.F. Cullis, Chem. Britain, 3 370 (1967).
5. R.F. Karlicek, V.M. Donnelly and W.D. Johnson in 'Laser Diagnostics and Photochemical Processing for Semiconductor Devices', Materials Research Society Proceedings 17 151 (1983).
6. M.C. Lin, M.E. Umstead and N. Djeu, Ann. Rev. Phys. Chem. 34 557 (1983).
7. S.S. Prased and W.T. Huntress, Ap. J. Suppl., 43 1 (1980).
8. Aristotle, Meteorologia.
9. F. Kaufman, Science 230 313 (1985).
10. G. Brasseur and S. Solomon in 'Aeronomy of the Middle Atmosphere: Chemistry and Physics in the Stratosphere and Mesosphere' (D. Reidel, Dordrecht 1984).
11. R.W. Wood, Proc. Roy. Soc. A. 102 1 (1922).
12. K.F. Bonhoeffer, Z. Phys. Chem., 113 199, 492 (1922).
13. H.M. Smallwood, J. Am. Chem. Soc., 51 1985 (1929).
14 F. Kaufman in 'Progess in Reaction Kinetics', 1 11 (1961).
15. A. Fontijn and W. Felder in 'Reactive Intermediates in the Gas Phase: Generation and Monitoring' ed. D.W. Setser (Academic Press, New York 1979).
16. J.C. Polanyi and K.B. Woodall, J. Chem. Phys., 56 1563 (1972).
17. J.P. Sung and D.W. Setser, Chem. Phys. Lett., 48 413 (1977).
18. J.H. Kolts and D.W. Setser in 'Reactive Intermediates in the Gas Phase: Generation and Monitoring' ed. D.W. Setser (Academic Press, New York 1979).
19. C.J. Howard, J. Chem. Phys., 83 3 (1979).
20. M. Goppert-Mayer, Ann. Phys., 9 273 (1931).
21. J. Brussel, B. Cagnac and A. Kastler, C.R. Acad. Sci. [Paris] 237 984 (1953).

REFERENCES (Cont/d.)

22. W. Kaiser and C.G.B. Garret, Phys. Rev. Lett., 7 229 (1961).
23. R.G. Bray, R.M. Hochstrasser and J.E. Wessel, Chem. Phys. Lett., 27 167 (1974).
24. P.M. Johnson, M.R. Berman and D. Zakheim, J. Chem. Phys., 62 2500 (1975).
25. G. Petty, C. Tai and F.W. Dalby, Phys. Rev. Lett., 34, 207 (1975).
26. M.N.R. Ashfold, Mol. Phys., 58 1 (1986).
27. R.J. Donovan in 'Gas Kinetics and Energy Transfer', Specialist Periodical Reports 4 117 ed. R.G. Ashmore and R.J. Donovan.
28. W.M. McClain and R.A. Harris in 'Excited States', Vol.3 ed. E.C. Lim (Academic Press, London 1977).
29. P. Lambropoulos, Adv. At. Mol. Phys., 12 87 (1976).
30. P. Agostini, A.T. Georges, S.E. Wheatley, P. Lambropoulos and M.D. Levinson, J. Phys. B., 11 1733 (1978).
31. D.C. Jacobs and R.N. Zare, J. Chem. Phys., 85 5457 (1986).
32. D.S. Zakheim and P.M. Johnson, Chem. Phys., 40 263 (1980).
33. P.M. Johnson and C.E. Otis, Ann. Rev. Phys. Chem., 32 139 (1981).
34. M.R. Cervenan and N.R. Isenor, Opt. Comm., 13 175 (1975).
35. M.N.R. Ashfold, J.M. Bayley and R.N. Dixon, Can. J. Phys., 62 1806 (1984).
36. W. Demtroder in 'Laser Spectroscopy - Basic Concepts and Instrumentation', (Springer-Verlag, 1982).
37. R.N. Compton, J.C. Miller, A.E. Carter and P. Krüct, Chem. Phys. Lett., 45 114 (1980).
38. J.H. Glownia and R.K. Sander, Phys. Rev. Lett., 49, 21 (1982).
39. D.J. Jackson and J.J. Wayne, Phys. Rev. Lett., 49 543 (1982).
40. D.J. Jackson, J.J. Wayne and P.H. Kes, Phys. Rev. Lett., A28 781 (1983).
41. J.J. Wayne, Phys. Rev. Lett., 52 751 (1984).
42. L. Li, M. Wu and P.M. Johnson, J. Chem. Phys., 86 1131 (1987).

REFERENCES (Cont/d.)

43. A. Corney in 'Atomic and Laser Spectroscopy' (Clarendon Press, Oxford 1986).
44. L. Li, B.X. Yang and P.M. Johnson, J. Opt. Soc. Am. B., 2, 748 (1985).
45. L. Li, R.N. Porter and P.M. Johnson, Phys. Rev. Lett., 53 1336 (1984).
46. J. Morellec, D. Normand and G. Petite, Phys. Rev., A14 300 (1976).
47. J. Morellec, D. Normand, G. Mainfray and C. Marcus, Phys. Rev. Lett., 44 1394 (1980).
48. C.E. Otis and P.M. Johnson, Chem. Phys. Lett., 83 73 (1981).
49. R. Zhang, D.J. Rakestraw, K.G. McKendrick and R.N. Zare, J. Chem. Phys., 89 6283 (1988).
50. D.R. Crosly, J. Chem. Ed., 59 446 (1982).
51. R. Altkorn and R.N. Zare, Ann. Rev. Phys. Chem., 35 265 (1984).
52. J.P. Booth, S.L. Bragg and G. Hancock, Chem. Phys. Lett., 113, 509 (1985).
53. A.C. Kummel, G.O. Sitz and R.N. Zare, J. Chem. Phys., 85 6874 (1986).
54. J. Allison, M.A. Johnson and R.N. Zare, Far. Diss. Chem. Soc., 67 124 (1979).
55. D.C. Jacobs, R.J. Madix and R.N. Zare, J. Chem. Phys., 85 5469 (1986).

CHAPTER 2
EXPERIMENTAL DETAILS

2.1 INTRODUCTION

It is the object of this chapter to give a description of the apparatus and methodologies used in this thesis for the production and experimental study of the transient species of interest. Detailed accounts are given on the two 'cornerstones' of the apparatus i.e. the laser system and the flow reactor. Also, descriptions will be given on coupling of the LIF and REMPI techniques to the flow reactor.

2.2 Laser System

The laser system used throughout this thesis was a Nd:YAG (Neodymium Nd^{3+}, Yttrium Aluminium Garnet: $Y_3Al_5O_4$) [1] pumped dye-laser and wavelength extender system.

2.2.1 Nd:YAG Laser

The Nd:YAG laser was a Spectron Laser Systems Ltd type SL801 'Q'-switched laser. The laser consists of an oscillator and amplifier arrangement each being pumped by its own flash lamp. The doubling crystal, DCDA, (see later for a discussion of frequency doubling) produced a higher conversion efficiency, for frequency doubling the infrared (ir) 1064 nm fundamental to green 532 nm radiation than a traditional KDP crystal. The laser normally operated at 10 Hz and delivered ~ 6-10 ns pulses with 0.5 ns root mean square (RMS) jitter and an approx 2% pulse to pulse intensity instability. The beam had an approximately gaussian profile.

In order to pump the dye laser, the horizontally polarized 532 nm beam was rotated by 90° by a mica sheet half wave retardation plate. The plate was fitted to the Nd:YAG head exit port.This procedure reduced the available pump power by approximately 20% to ~ 130 mJ per pulse.

The Nd:YAG laser fundamental is obtained by producing gain on the $^4F_{3/2}$ - $^4I_{11/2}$ transition of the Nd^{3+} ion [2]. The ground state electronic configuration of the ion is $[Kr]4d^{10}4f^3 5s^2 5p^6$, which correlates in the Russel-Saunders coupling approximation to ^4I_J (L=6, S=$^3/2$) terms. The ion is a normal multiplet and thus the ground state term is $^4I_{9/2}$. However, in the crystal the atomic terms are split by crystal field interactions into several components: it is these interactions that make the doubly forbidden transition for the Nd^{3+} free ion allowed.

'Q'-switching of a laser entails reducing the Q-factor [2] of the laser cavity for a short period of time, thus reducing the feedback in the cavity. When the Q factor is reduced, the upper state population of the two levels involved in the laser transition can build up to a much higher level. The Q factor is then rapidly increased, producing a very rapid upsurge in photon density followed by a rapid decay i.e. a pulse. 'Q'-switching produces much higher peak powers in a pulsed laser system. 'Q'-switching in the Nd:YAG was obtained by using an electro-optic material (KDP), which becomes birefringent when a voltage is applied across it.

2.2.2 Dye Laser

The dye laser used throughout the thesis was a Quanta-Ray PDL2. This system operates in the Hänsch configuration [3]. Laser operation proceeds by initially splitting and focussing ~ 5% of the incident 532 nm pump beam to transversely pump the dye laser oscillator dye solution. The cuvette containing the dye is inside

the laser cavity, which also contains an output coupling mirror, a beam expanding telescope and a diffraction grating. Placing the telescope on the optical axis inside the cavity serves two purposes:

1) The resolving power of a grating is proportional to NM, the product of the number of grooves on the grating illuminated N, times the diffraction order M [4]. Hence illuminating more grooves reduces the resulting laser linewidth.
2) The power density without beam expansion might be high enough to damage the grating surface.

Wavelength selection was therefore obtained by angle tuning the grating. A combination of the initial polarisation of the pump beam and the diffraction grating implies that the dye laser produces a vertically polarised multi-mode beam. Having selected the laser output with the oscillator the power is then amplified by passing the oscillator beam into the amplifier cuvette. The amplifier cuvette contains its own (less concentrated) recirculating dye solution. Amplification is achieved by overlapping the residual 532 nm beam with the oscillator beam in the cuvette. The bandwidth of the dye laser was $\geq 0.2\ cm^{-1}$.

The tunable wavelength range that could be generated by the laser system was limited by the availability of pump energy and the necessary frequency doubling crystals. The ranges listed below represent all wavelengths that were generated in this thesis.

Dye	Wavelength range/nm	Frequency doubled wavelength range/nm
DCM	615-648	307.5-324
Sulforhodamine 640	600-612	300-306
Kiton Red	582-592	291-296
Rhodamine 590	556-572	278-286
Fluorescein 548	543-557	271.5-278.5

All Dyes were from Exciton.

In the middle of the dye tuning range between 10-20% energy conversion was typically achieved. Hence, at this point, dye laser pulse energies varied between 15 and 25 mJ. The long term stability was found to be good being $\leq \pm$ 5% after a 15 minute warm-up period.

The dye laser could be easily reset to within 0.01 nm, while its absolute accuracy measured relative to a set of optogalvanic lines [5] was found to be within $\pm$ 0.02 nm across all the dye wavelength ranges.

The dye molecules represent the active laser medium in a dye laser. Typically the pump radiation will excite the dye molecule from its normally singlet ground state to its first excited singlet state, $S_1 \leftarrow S_o$. Dye molecules are normally large organic molecules that contain some form of conjugation and that have large absorption cross sections in the region of the pump radiation. Because of the nature of the dye and its interactions in solution it will have essentially continuous absorption and emission bands. Following excitation very rapid vibrational relaxation will take place between the dye and the solute, leaving the dye in the lowest levels of the S_1 state. The fluorescence lifetimes of these excited states is normally short (few ns) and thus fluorescence occurs with a high quantum yield; often near unity. Due to the Franck-Condon principle fluorescence will occur from the lower levels of the S_1 state to some excited levels in the S_o state. Population inversion can occur between S_1 and S_o and an essentially continuously tunable laser source can be achived by having the dye in a laser cavity with a wavelength selective device. Since absorption and fluorescence occur at different wavelengths there are no associated problems of reabsorption.

The only problem associated with dye lasers arises from the fact that in most molecules the $T_2 \leftarrow T_1$ (T = triplet) absorption bands often strongly overlap those of the singlet states. Thus, dye laser efficiency can be reduced if there is significant triplet population.

The problem is minimised in a pulsed excitation system since the $T_1 \leftarrow S_1$ process is spin forbidden and hence is much less likely than fluorescent decay. Thus, any T_1 molecules formed should have a sufficiently long time to relax before the next pulse. The problem is further reduced by having continuously recirculating dye solutions.

2.2.3 Wavelength Extension

Frequency doubled radiation was produced by a Quanta-Ray WEX1A (wavelength extender) module. This module containined two KD*P frequency doubling crystals, either a 58° or 74° cut to the optical axis, that could produce tunable uv light between 330 - 270 nm. The uv pulse was nominally 4 - 5 ns long [6], horizontally polarised and had a typically pulse energies varying between ~ 0.5 - 1.0 mJ at the middle of the dye tuning curves. The quoted bandwidth of the WEX was $\geq$ 0.3 cm^{-1}. However, an experimental measure of this was made from a series of non-power and non-instrumentally broadened spectral lines with an average value nearer 0.4 cm^{-1} being obtained.

It was found that the WEX could maintain acceptable 'auto-tracking' over a dynamic uv energy range of about 10. 'Auto-tracking' implies angle tuning the KD*P doubling crystal and associated quartz compensator, as the dye laser wavelength is tuned, such that optimal doubling efficiency is maintained. The tracking mechanism works on a bi-photodiode servo based mechanism which functions by splitting a small fraction of the generated uv light onto the bi-photodiode for intensity monitoring. Optimal doubling efficiency is maintained by ensuring that equal amounts of uv light fall on both the photodiodes. Tracking efficiency was found to be enhanced when minimal amplified spontaneous emission (ASE) produced by the dye laser was passed into the WEX. To minimise ASE an optical delay line (~ 2.5 ns) was fitted between the oscillator and amplifier stages of the dye laser.

Separation of the second harmonic radiation from the dye laser fundamental was achieved by a Pellin-Broca dispersing quartz prism [7], with the residual dye fundamental being dumped into a series of ceramic stops.

In order to produce efficient frequency doubling it is necessary to have a material exhibiting significant non-linear optical susceptibility. Generally the material must be birefringent (i.e. it necessarily exits in a non-centrosymmetric space group); KD*P is a typical example. It can be shown that for such materials the induced dielectric polarisation can act as a source of new waves with the second harmonic frequency [1]. The new waves will have a polarisation perpendicular to the incident wave. The microscopic contributions generated by the molecules at different positions in the crystal will only result in appreciable second harmonic intensity if the phase velocities of the incident inducing waves and polarisation waves are matched, i.e.'phase-matched'. The condition is met for birefringent crystals where the incident and second harmonic waves may propagate through the crystal as ordinary and extraordinary waves respectively. Birefringent crystals have different phase velocities (refractive indices) for the ordinary and extraordinary waves. Phase matching can be achieved because the phase velocity of the second harmonic (extraordinary) wave depends on the angle of propagation of the wave relative to the unique optical axis of the crystal and to the electric field. The condition is especially simple for collinear propagation of all three waves, as is the case with a laser beam. Harmonic generation is most efficient in this case since it entails the maximum overlap for phase matching to occur. In this case the phase velocities of the incident and second harmonic waves must be equal.

Generally, for a defined range of frequencies it will be possible to find angles in the crystal, over which the phase velocities of the incident and second harmonic waves are sufficiently matched that

constructive interference of the waves at all points in the crystal can occur. A typically doubling efficiency is between 5 - 10% for KD*P. To maintain the second harmonic generation it is necessary to angle tune the crystal as the incident wavelength (of the laser) is tracked. Doubling efficiency is found to scale as the square of the incident intensity and is also strongly dependent on the polarisation of the incident beam. Thus, Nd:YAG pumped dye lasers which produce almost exclusively plane polarised light (Quanta-Ray PDL2 > 95% for all dyes) are excellent sources for frequency doubling.

2.3 Flow Tube

The design of the flow tube was such that it could satisfy all the normal gas dynamical constraints for a kinetic study (see Section 2.3.1) but still be experimentally versatile [8]. A modular design was chosen which facilitated rapid interchange of components and thus the experiments that could be performed.

The tube consisted of three main sections: a radical generation zone, a reaction zone and a detection zone. Subsequent to the detection zone a large bore Springham 25 mm Tap allowed isolation of the tube from the pump or the atmosphere.

The tube except for the discharge arms was of pyrex glass construction. Each module was fitted with suitable cone/socket joints and vacuum was maintained by using a silicone vacuum grease (Dow Corning). The grease was chemically very inert, had a vapour pressure of $< 10^{-6}$ Torr at room temperature and helped maintain the tube leak rate to ~ 0.5 Torr overnight.

Pressure readings within the tube were taken with an MKS Baratron type 222BA gauge (0 - 100 Torr). This gauge was calibrated several times throughout the course of the various studies against an MKS baratron transfer standard [9].

The tube had a uniform 2.5 cm internal diameter throughout its length. With all sections fitted it was 1m in length. The middle section was optional (being required only for rate constant determinations) and was 60 cm in length with a pressure port mounted halfway down its length and perpendicular to the flow axis. The initial section contained inlets for both a sliding injector and a discharge side arm, these formed the routes via which all gases entered the reactor. The detection zone was roughly equivalent for both REMPI and LIF experiments and consisted of a six-way cross: the main axis carrying the flow constituents, the second axis allowing unimpeded passage of the laser beam with the third axis being the detection axis.

Typical pressures for the REMPI experiments were between 1-2 Torr, while for the LIF experiments values ranged between 1 and 6 Torr.

Probably the most serious limitation of the flow tube technique is heterogeneous effects. Under typical reactor conditions: pressure of 1 Torr and a tube diameter of 3 cm, every species present in the reactor makes ~ 1000 collisions in 0.05 s with the tube walls [10]. Therefore, it is important to minimise heterogeneous effects: this is normally achieved by coating the tube walls with a surface recombination inhibiting reagent. Such reagents, which have all achieved varying degrees of success include: Borax, $HClO_4$, sulphuric acid, phosphoric acid, teflon and halocarbon wax (a polyfluorinated wax) [11] [12] [13] [14].

Two agents were found to be universally good inhibitors during the course of these studies, these were phosphoric acid and halocarbon wax (KMZ Chemicals Ltd). Halocarbon wax was the choice agent for coating the reactor walls both because of its inert nature and the ease with which it could be applied in its molten state to yield a uniform thickness of wall coating. Halocarbon wax softens at ~ 60°C and becomes brittle below -30°C thus to prevent heterogeneous

effects in discharge cavities where electron temperatures may approach several thousand Kelvin, a different agent, such as phosphoric acid must be used. To produce the coating in the side arm a small amount of syrupy phosphoric acid was introduced into it before heating to ~ 600°C in a cool (extended blue) Bunsen flame. The heating produced a fairly vigorous reaction at the surface. By slowly rotating the side arm a uniform thin white coating could be achieved quite quickly. The tube was then baked overnight at 400°C to thoroughly dry the surface. The side arm was then washed with water and methanol before a final treatment with discharges of both CF_4 and O_2 for two hours each. This treatment was found to significantly enhance radical concentrations of some of the species dealt with in this thesis.

A high throughput pump, Alcatel 2063 (1100 litres per minute), was used to evacuate the tube for all the studies carried out in this thesis. The pump was an oil sealed two stage (high and low pressure) vane pump that could maintain a base pressure (zero gas flow) of ~ 7×10^{-3} Torr. The base pressure limit being controlled by the choice of oil in the pump. The relative operating efficiency of the pump was periodically checked by noting how the pressure in the flow tube varied as a function of known mass inputs of nitrogen gas (see section 2.4).

2.3.1 Dynamical Restraints in Flow Reactions

It is important when considering the use of flow reactors to be aware of any restrictions under which they should operate. This point is of relevance to studies carried out in this thesis where the production of isotropic gas samples was experimentally important.

A mathematical description of the dynamical properties of the gas flow is based purely on the flow regime present in the reactor. A description of any flow regime follows from three unifying principles [15].

1) Conservation of mass

2) Momentum balance or equation of motion

3) Conservation of energy

An optimal situation in terms of analysis of data occurs when the pressure is high enough such that the mean free path of the gas is negligibly small compared to the radius of the tube (no slip flow). Then, provided that the velocity of transport is not so great that the flow becomes turbulent, the steady state motion of the gas will be similar to the laminar flow of a liquid and will be governed by the viscosity (viscous flow). However, any discussion of laminar flow is based on the assumption of an incompressible fluid, thus the arguments may be applied to gases but only at low speeds, that is up to a Mach number of less than about 0.3 [15].

For a tubular reactor which is considered to be long enough to have negligible end effects and for which the viscosity is governing the flow, a description first derived by Poiseuille becomes appropriate. Poiseuille flow implies a parabolic velocity distribution, with species near the walls remaining in the reactor longer than those in the centre. However, at low enough pressures radial diffusion is sufficiently rapid to entail the establishment of flat velocity and concentration profiles. It is particularly easy in this case to show how residence time in the reactor can be related to flow velocity. The two extreme cases of the flat flow profile [16] [17] [18] and the fully developed laminar flow [17] [18] [19] have been reviewed extensively.

To obtain the well behaved gas flows outlined above consider initially a short cylinder of fluid of radius r and length dx with a transport velocity being given as u and is a function of the radial distance r from the tube axis. In steady flow the pressure drop dp, for a gas of viscosity η, across its ends is balanced by the viscous drag over its curved surface.

The viscous shearing stress T is given by [20].

$$T = \eta \, {du}/{dr} \tag{1}$$

While the viscous drag on the curved surface is,

$$2\pi r dx . \eta \, {du}/{dr} \tag{2}$$

and hence the condition for steady flow is

$$2\pi r dx . \eta \, {du}/{dr} + \pi r^2 \, dp = 0 \tag{3}$$

On rearranging and integrating and applying the boundary condition for viscous flow that at the wall, u(a) = 0, it is found that

$$u = \frac{a^2 - r^2}{4\eta} \, \frac{dp}{dx} \tag{4}$$

Where the radius of the tube is, a.

Equation (4) indicates a parabolic velocity profile. The molecular flow in the cylinder shell between r and r + dr is

$$nu . 2\pi r dr \tag{5}$$

Where n is the number density of the gas. Hence, the number of molecules F, passing through the tube per unit time is

$$F = n \int_o^a u . 2\pi r dr \tag{6}$$

Hence, on integrating and using $n = P/kT$ at constant volume

$$F = \frac{\pi a^4}{8\eta kT} \; p \frac{dp}{dx} \tag{7}$$

Integrating over the tube length from $0 \longrightarrow l$ at the respective pressures of P_1 and P_2 yields

$$F = \frac{\pi a^4}{8\eta kT} \; \frac{P_1^2 - P_2^2}{2} \tag{8}$$

Provided $\Delta P = P_1 - P_2$ is small and defining $\bar{P} = (P_1 + P_2)/2$

$$F = \frac{\pi a^4 \bar{P} \Delta P}{8\eta kTl} \tag{9}$$

and the molar flow rate is

$$F = \frac{\pi a^4 \bar{P} \Delta P}{8\eta RTl}$$

Where R is the gas constant.

Since $F = \delta n/\delta t$ and invoking $n = PV/RT$ where $V = Ar$ and $A = \pi r^2$ with v the mean axial flow velocity then,

$$\Delta P = \frac{8\eta l r}{v^2} \quad \text{(expressed in Pascals, Pa)} \tag{10}$$

Taking typical values used throughout these studies:

For argon at 20°C $\eta = 2.21 \times 10^{-4}$ poise ($gcm^{-1}s^{-1}$) [21]

Tube length $l = 100$ cm

average flow velocity $v = 1000$ cms^{-1}

the radius $r = 1.25$ cm

A value of $\Delta P \sim 0.08$ Torr is obtained. Hence it is normal practice to mount the pressure sensor halfway down the tube and perpendicular to the direction of the flow.

A flat flow profile is often present near the entrance duct of the reactor then, because of the growth of the boundary layer the entrance flow profile will gradually change over to laminar flow. The length of tube required for complete development Le is given by [22]

$$Le = 0.144\ l\ Re \qquad (11)$$

Re is the Reynolds number of the flow, expressing in c.g.s. units

$$Le = 6.5 \times 10^{-6}\ (MQ_m/\eta)\ (cm) \qquad (12)$$

For T = 290K $\eta = 2.21 \times 10^{-4}$ poise, M = 40g $mole^{-1}$, Q_m is the bath gas flow rate (STP) $cm^3\ s^{-1}$ (~ 10)

Le $\sim$ 10 cm and hence end effects are negligible.

Heterogeneous reactions can be a serious problem in flow systems especially for excited or metallic species. For chemically reactive species wall recombination is often thought to occur via reaction of a gas phase species with a surface adsorbed one. Surfaces typically

exhibit high degrees of coverages [23] and on energy grounds alone [24] such a mechanism is plausible. To remove the radial concentration gradients caused by viscous flow and surface effects it is necessary for the radial diffusion process to be sufficiently rapid.

The deactivation rate at the wall can be calculated from a knowledge of the probability γ, defined as the fraction of wall collisions that remove radicals.

The number of radicals striking the wall is given by kinetic theory [20] as

$$\frac{n\bar{c}}{4} \quad A \tag{13}$$

While the number of radicals reacting will be:

$$k_w.n.V \tag{14}$$

$\bar{c}$, is the mean molecular speed

A, is the wall area
n, is the number density
V, is volume
k_w, is the deactivation rate constant

Hence for a cylinder of length l

$$\gamma = \frac{2k_w\ r}{\bar{c}} \tag{15}$$

Or

$$k_w = \frac{\bar{c}\gamma}{2\ r}$$

The value of k_w for any species will depend on the particular wall coating chosen and on the temperature of the chamber. For example for a reactive species such as OH values of γ in the range 1-3 x 10^{-3} [29] are expected.

Random walk theory can be rigorously applied to diffusional problems [20]. The one dimensional diffusion of a gas molecule is given by:

$$\bar{r}^2 = 2Dt \tag{16}$$

Where $\bar{r}^2$ is the mean square displacement during time t for a molecule with a diffusion coefficient D. For radial diffusion to be sufficiently rapid to remove all concentration gradients then:

$$t < \frac{1}{k_w} \tag{17}$$

That is

$$r < \frac{4D}{\gamma c}$$

For a pressure of 1 Torr a typical value of a diffusion coefficient would be approximately 250 $cm^2\ s^{-1}$. Hence, for the case of a reactive species such as OH, c ~ 6 x 10^4 cm s^{-1}, the condition for rapid diffusional flattening of the concentration and flow profile is

$$r < 5 \text{ cm}$$

And is not very severe.

The discussion so far has asserted that under appropriate conditions the flow velocity is the same for all species, and hence that the residence time in the tube t, can be related to an average flow velocity v and position in the tube z.

$$t = z/v \tag{18}$$

Normally the gas composition will be such that any reactive species will be present in trace amounts, hence a pseudo first order analysis is normally presented for any study of bimolecular reactions, such that the concentration c of the species of interest is given by:

$$\frac{dc}{dt} = - kc \qquad (19)$$

$$k(s^{-1}) = k'' \ (cm^3 \text{ molecule } s^{-1}) \ A \ (\text{molecule } cm^{-3})$$

for a steady flow

$$k = - v.\frac{d(\ln c)}{dz} \qquad (20)$$

However, when a reaction does occur the above assumption of uniform flow rates is invalid, as can be seen from:

$$\frac{dc}{dz} = - \frac{kc}{v} \qquad (21)$$

That is the axial concentration gradient causes the radicals to have an additional velocity component down the flow axis of the system. The additional velocity component is given by Ficks first law [20].

$$J = - D\frac{dc}{dz} = v_d \ c \qquad (22)$$

J is the molecular flux down the tube (molecules cm^{-2} s^{-1}) and v_d is the diffusion velocity associated with the reaction.

$$v_d = \frac{Dk}{v} \qquad (23)$$

Thus

$$\frac{-kc}{v} = \frac{dc}{dz} = \frac{k_c c}{v+v_d} \qquad (24)$$

Where k_c is the corrected rate constant allowing for the additional velocity term. Rearranging (23) yields:

$$k_c = k \frac{(1 + v_d)}{v} \tag{25}$$

and from (22)

$$k_c = k \left\{1 + \frac{Dk}{v^2}\right\} \tag{26}$$

Where k is the observed uncorrected rate constant defined in (20). Hence, axial diffusion is negligible provided $v^2 >> kD$. Assuming typical values for a reactive species, such as OH. $k \sim 200\ s^{-1}$, $D \sim 250\ cm^2\ s^{-1}$, $v = 1000\ cm\ s^{-1}$ (which would occur at approximately 1 Torr pressure). The condition is satisfied.

A more rigorous approach to establishing the validity of assuming uniform flow and concentration profiles starts by constructing the one dimensional continuity equation for a uniform flow rate U, with a flat concentration profile with first order homogeneous and heterogeneous reactions, and is given by [16]:

$$U \frac{dc}{dz} - D \frac{d^2c}{dz^2} = - \left[k + \left\{ {}^{2D}/_{\delta R^2} \right\} \right] C \tag{27}$$

δ is the wall catalysis parameter $\delta \sim \frac{4D}{2\gamma R}$ and R the tube radius.

The equation is solved in terms of the dimensionless quantities

$\nu = {}^{UR}/_{D}$, $B^2 = {}^{kR^2}/_{D}$ and $z^* = z/R$

where the solutions have the general form:

$$c = c_o \exp (\pm \lambda z^*) \tag{28}$$

The roots $\lambda \pm$ can be compared to those for the three dimensional continuity equation for fully developed Poiseuille flow with first order homogeneous and heterogeneous reactions for which only numerical solutions are available. The range over which the one dimensional analyses is found to be valid (i.e. within 5% of the 3D analysis) can be expressed in terms of the quantities:

$\delta > 10$ i.e. $k_w < 30$ and reflects radial concentration effects

$B^2 < 1$ and is an insensitive parameter except for the fastest reactions

$\nu < 10$ and again reflects flattening the flow profiles

Similar comparisons have also been drawn by other authors, e.g. [26].

2.4 Gas Handling

In order to introduce various component gases in a controlled manner into the flow tube an attendant gas handling line was constructed. The vacuum line was of standard pyrex glass design and construction, with a liquid nitrogen trapped single stage mercury diffusion pump backed by a rotary pump. The base pressure in the line was found to be typically $\sim 8 \times 10^{-3}$ Torr. The line contained four independentaly isolable arms such that different gaseous components could be metered separately. Young's greaseless taps were used throughout.

Each arm of the vacuum line contained a mass flow controller (Advanced Semiconductor Materials int, type AFC-260). The mass flow control system operated by measuring the mass flow rate of a gas relative to a calibrated standard, N_2 (the units of flow being: standard cubic centimeters per minute, SCCM, standard implies S.T.P.). The following controllers were available: 0-20, 0-50, 0-100, 0-500 and 0-1000 SCCM.

The controllers operate by varying the size of the pathway of the gas to the flow tube. The measurement of the flow is based on a thermal sensor. The controller contains a bridge circuit, with a differential amplifier; the bridge is balanced with no flow. However, with flow, the rate of internal heat exchange is altered, this produces a temperature profile within the controller that causes a bridge output signal.

Given the simple description of the device above it is obvious that the flow rate of any gas is related by the ratio of the heat capacity, C of that gas and the standard gas (nitrogen):

$$\frac{\text{Actual flow of gas X}}{\text{Actual flow of } N_2} = \frac{C(X)}{C(N_2)}$$

The typical accuracy of the flow meters when used with N_2 was between 2 - 4% while for other gases the flow rate was always accurate to within $\pm$ 6%. Calibration of the controllers was carried out regularly. The procedure entailed measuring the time taken for a given volume to be passed, in for example, a bubble burette.

The various gas flows passed from the vacuum line to the flow tube via either teflon or nylon hoses depending on the nature of the gas. When more than one gas or gas mixture was to be introduced into the same flow tube inlet, the hoses carrying the gases were joined well before the gases were introduced into the flow tube. This procedure ensured a completely homogeneous gas mix entered the tube.

2.5 Radical Source

An essential requirement of all experiments carried out in this thesis was the production of a radical or radical generating species. This task is best performed in flow tube experiments by using a gas discharge. Considering the nature of the detection techniques used in this thesis a microwave discharge was the choice route (see below).

The first use of microwave frequencies to excite a discharge was performed in 1948 [27]. However, subsequent experimentation readily found that improved lifetime and stability characteristics of discharges could be obtained at frequencies between 10-3000 MHz [28]. Microwave discharges have been used to peform two important functions: as light sources and as a means of producing excited and free radical species for kinetic studies in the gas phase. The use of microwaves as a source of a discharge can present significant advantages over other conventional sources:

1) The cavity is electrodeless and is thus free of the problem of introducing additional impurities. Normally the cavity will also have a much longer lifetime than one which contains electrodes.

2) A microwave cavity is relatively safe since it produces only weak leak fields.

3) The discharge is typically efficient, producing a high degree of dissociation even at low powers. This leads to minimal heating of the bath gas.

4) The microwave generator produces very little electrical interference, unlike for example a radiofrequency discharge.

Point (4) was of most importance when considering REMPI experiments, since these are very sensitive to radiofrequency interference (RFI).

An EMS Microtron mk III microwave power supply producing microwaves at 2450 MHz was used exclusively in this thesis. The discharge cavity, EMS 214L, was operated at a power of between 15 - 75 watts depending on the radical precursor. The reflected power from the cavity was measured using an EMS reflected power meter, this typically showed that between 20 - 25% of the incident power was being reflected.

The degree of dissociation induced in the reagent gas by a discharge has been extensively studied [29] [30] [31]. There is general agreement that the degree of dissociation will depend on the following factors:

1) The total pressure and flow rate of the gas

2) The purity of the gas

3) The temperature and chemical nature of the walls of the discharge tube

4) The power being coupled into the discharge

Within experimental limitations efforts were always made to optimise radical production by varying the parameters outlined above.

2.6 Fluorescence Spectroscopy

A diagramatic representation of the apparatus used in all fluorescence experiments described in this thesis is shown in Figure 2.1. Two aspects are worthy of further discussion: optimising the fluorescence signal and calibration of the wavelength dependent response of the optical chain.

FIGURE 2.1: Schematic of the experimental configuration of the discharge flow apparatus with a LIF detection methodology.

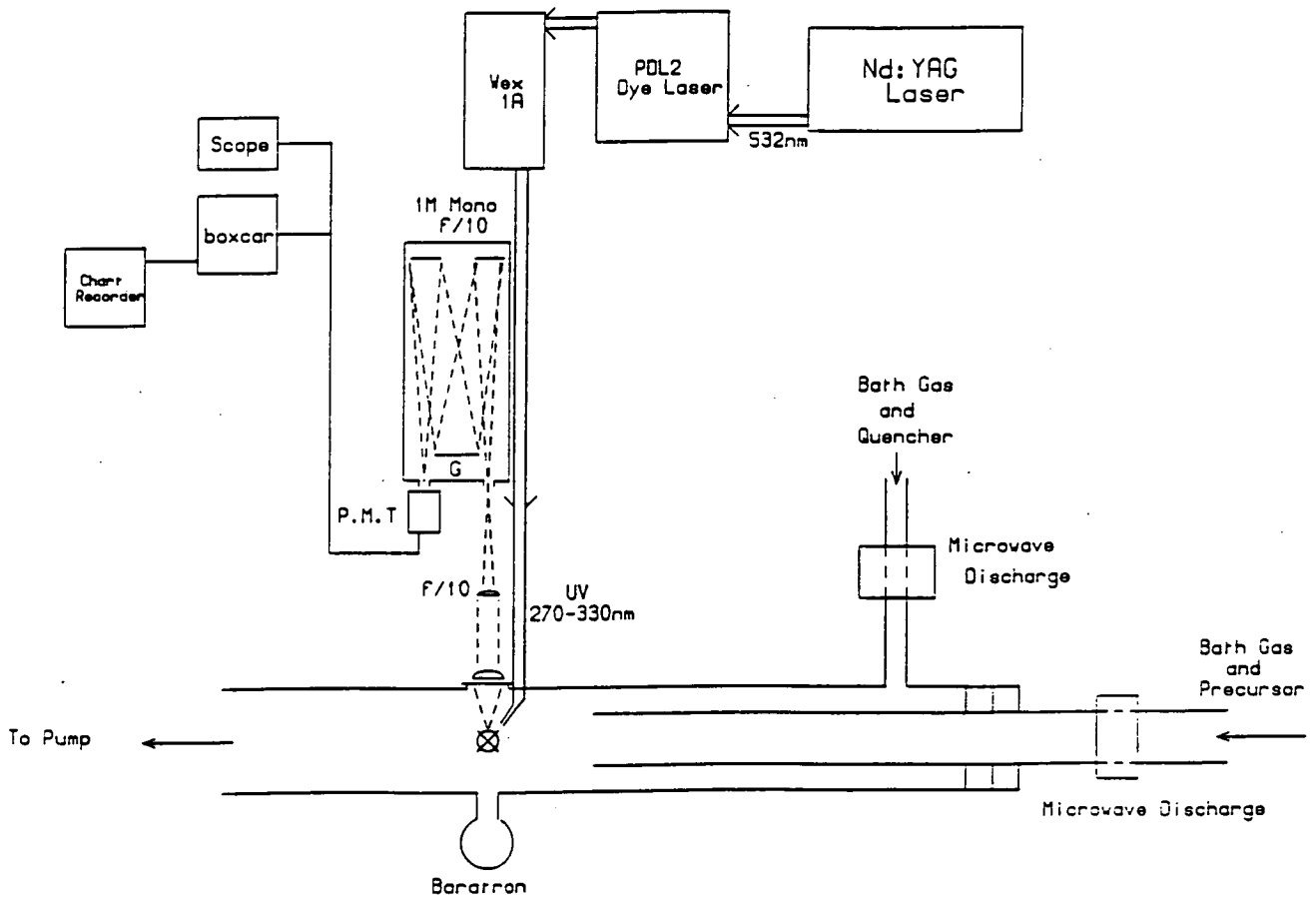

2.6.1 Light Gathering

To optimise the signal to noise ratio in the fluorescence experiments it is necessary to optimise the photon gathering from the region of interaction of the light source with the molecules of interest and to optimise the throughput of this light through the wavelength dispersive instrument (monochromator). The procedure for such a process is well established and is based on a two component telescope [32].

Fluorescence from an isotropic gas sample is emitted to all solid angles. Thus, to gather as much light as possible a 'condensing' lens with as high a relative aperture as possible is placed at a distance, equal to its focal length, f from the interaction zone (in this case an f/2 lens was used). This first lens produces a collimated beam of light, the second lens then images the light onto the detection system. The second 'field' lens is chosen and positioned to focus the collimated beam onto the entrance slit of the monochromator and to simultaneously image the 'condenser' lens onto the first (collimating) mirror of the monochromator. It is necessary to ensure that the field lens fully fills the collimating mirror, this then ensures that the diffraction grating is fully illuminated and optimal resolution of the monochromator is achieved. By matching the relative aperture of the field lens to that of the monochromator and focussing onto the entrance slit, in line with the monochromator optical axis, a focussed image should be produced at the exit slit.

The monochromator used for all LIF experiments in this thesis was a Monospek 1000 D400 grating spectrometer (Hilger and Watts). The Monospek 1000 had a focal length of 1000 mm, an approximate relative aperture of f/10 (102 x 102 mm grating) and was set up in the Czerny-Turner configuration [4]. The grating, which was kinematically

mounted, was of the holographic type (Jobin-Yvon) with 1200 'lines' per mm. From the relevant test data a 'blaze-angle' of around 220 nm seemed most likely. The absolute wavelength accuracy of the monochromator was initially measured against the accurately known wavelengths of a group of low pressure mercury lamp emission lines [33]. However, during the course of normal experimental work, wavelengths were measured relative to the accurately known laser wavelength. The monochromator was found to consistently read wavelengths 5.0 Å too low. The restability of the grating was however, excellent being ~ 0.01 nm.

The slits were precision engineered, bi-lateral opening, with a resetability close to 1 μm and with little absolute offset (this was determined while determining the resolution of the instrument).

The alignment and performance of the monochromator was checked by measuring the resolution factor. The resolution factor was defined as the average over forward and reverse scans of the mean of the recorded peaks heights, of the well-known Hg doublet emission line at 313.2 nm, divided by the trough depth between the lines. The experimental value of 0.97 indicated the monochromator was aligned extremely well. Under these conditions, when operated in first order, the reciprocal dispersion of the instrument with the grating mentioned above was 0.82 nm/mm.

A single photomultiplier tube (PMT) was used for all the LIF experiments (Thorn EMI 9789QB). The tube was chosen because its response curve over the wavelength range of interest i.e. 275 - 340 nm was an approximately linear function, rising monotonically from a quantum efficiency of ~ 20% to 25%. The 9789QB had a 10 ns response time and an ~ 20 ns full width half maximum (FWHM) pulse width at normal operating temperatures. The tube had a venetian blind dynode system (13 stages) and an effective 10 mm CsSb photocathode diameter. The relatively small photocathode diameter produced low dark currents at low light levels.

Signals from the PMT were directed into a gated integrator system, (Stanford Research Systems, model SR250), this device was used throughout the thesis.

2.6.2 Measurement of Spectral Response

The calibration of the optical system, i.e. monochromator, optical components and PMT used in the LIF experiments was measured by using a lamp standard of known spectral irradiance (Optronic Laboratories Inc, model 245A, 45W quartz tungsten-halogen coiled coil filament lamp standard). The total irradiance of these lamps is known to closely follow the radiance of a blackbody and thus closely fits the Stefan-Boltzmann radiation law:

$$I_T = \sigma T^4 \quad (T \sim 3000K \text{ for this lamp; } \lambda_{max} \sim 1.0\ \mu m) \qquad (29)$$

Each lamp has its own tabulated set of irradiance data as a function of wavelength. The assigned values of the irradiance have an estimated uncertainty of $\pm$ 2% relative to National Bureau of Standards (NBS) reference data. Stability tests indicate that a typical lamp should hold its calibration for more than 50 hours of use.

In measuring the response function of the apparatus it was only necessary to measure the relative change in the transmission of the apparatus as a function of wavelength and not the absolute value. Thus, it was necessary only to measure the relative number of photons at each wavelength and compare these to the specified absolute value.

The calibration test was done in accordance with the manufacturers instructions. In particular however, setting the current was critical when using the standard for calibration in the uv, e.g. a 1% error in current setting results in a 12% error in spectral irradiance at 250 nm. To overcome this problem a Farnell B30/10

stabilised power supply was used to power the lamp and a Fluke 75 digital multimeter was used to constantly monitor the current being drawn.

In order to measure the response function of the optical system, the calibration experiment was carried out in a fully darkened room. Light was detected by the PMT only when the aperture of the optical system was open. It was necessary to ensure that the phototube did not become 'saturated' at any wavelength. By examining the wavelength dependent output signal of the PMT in a 50Ω socket of an oscilloscope (Tektronix 2445A) the maximum signal was adjusted such that it never exceeded 65 mV. A signal of 65 mV was well within the linear response range of the tube.

The response function was then calculated simply by taking the ratio of the measured signal intensities to those of the lamp standard calibration points.

2.7 Ionisation Spectroscopy

A diagramatic representation of the apparatus used in all ionisation experiments described in this thesis is shown in Figure 2.2. Two aspects are worthy of further discussion: ion collection and accurate wavelength calibration.

2.7.1 Ion Collection

Ionisation signals were detected using an operational amplifier first described by Grant [34]. This amplifier was chosen because it is an intrinsically noise resistant circuit. It is also rather convenient to use with a conventional sample and hold (boxcar) signal averager. The circuit consists essentially of a balanced bias differential current amplifier buffered by a unity gain differential amplifier which drives a single ended output.

FIGURE 2.2: Schematic of the experimental configuration of the discharge flow apparatus with an ionisation detection methodology.

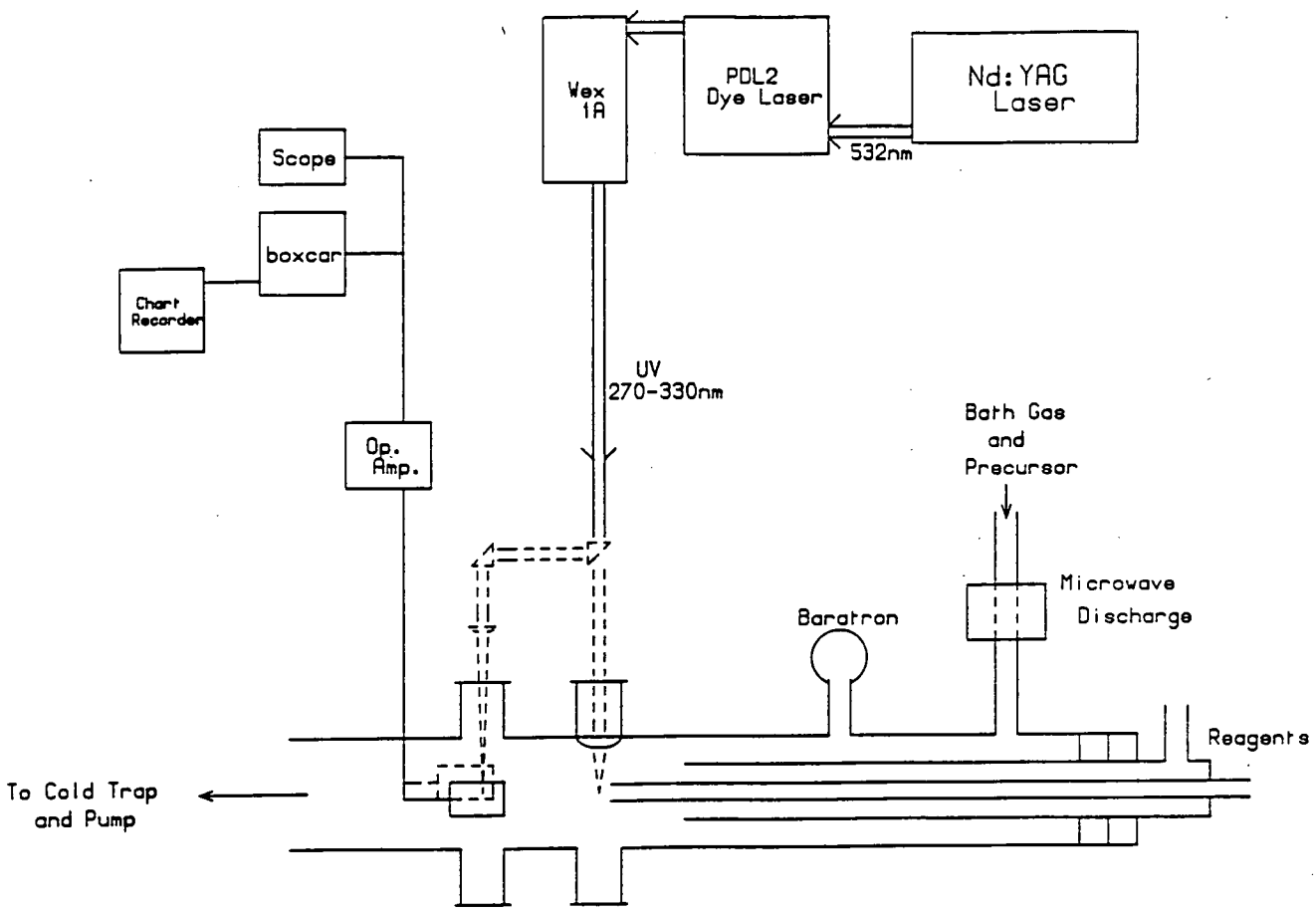

Laser laboratories are notoriously 'noisy' (i.e. the coupling into electronic circuits of extrenuous floating voltages) the most common noise being 50 Hz signals produced by electric and magnetic fields in the mains. Other noise sources such as nearby laser discharge lamps may also cause problems. The advantage of the Grant amplifier is that by using symmetrically biased plates, producing a differential signal, allows the entire circuit (including the detector plates), to be shielded all the way to the single ended output. To further enhance the shielding a grounded conducting ferromagnetic cage which enclosed the flow reactor and detection circuit was made. This shield worked by minimising the stray electric fields which would capacitatively induce voltages in the detection circuit. To reduce 50 Hz noise a 'notch' filter was placed between the single ended output of the amplifier and the signal averager. A notch filter is essentially an RC circuit whose characteristic frequency is such that it will not pass floating voltages with that frequency.

The parallel plate electrode arrangement for detection of the ion signal was chosen. However, this arrangement is by no means ideal and it will fail under certain conditions of pressure and species composition [35]. The electrodes will provide a signal voltage that is proportional to the number of electron-ion pairs produced by the laser, but only within limits that must be found experimentally. The temporal and spatial resolution of the parallel plate design is adequate for the purposes of a REMPI experiment in a flow tube.

While it would be desirable to directly determine from the strength of the ionisation signal the number density of species present, this is very difficult and tedious [35]. The problem arises that there will always be certain phenomena which will set limits on the operating characteristics of the probe these include:

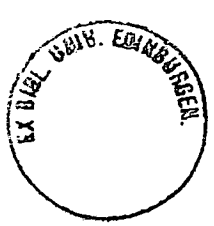

1) electron-ion recombination

2) electron attachment leading to negative ion recombination

3) electron induced avalanche ionisation

2.7.2 Wavelength Calibration

The REMPI studies that were carried out in this thesis were of sufficiently high resolution that it was necessary to accurately calibrate the laser wavelength. This task could be met by using an etalon and several readily assigned atomic resonances found in the REMPI spectra [36]. These atomic resonances are known to at least 7 significant figures. The etalon was made of solid quartz (Technical Optics, finesse ~ 7). By directing a small fraction of the laser at normal incidence onto the etalon, regular energy-spaced transmission fringes were produced as the dye laser was tuned. The transmitted light was detected by a photodiode. The free spectral range of the etalon was slightly wavelength dependent being 3.372 cm^{-1} at 600 nm and 3.336 cm^{-1} at 480 nm [37].

REFERENCES

1). W. Demtroder in 'Laser Spectroscopy - Basic Concepts and Instrumentation', 2nd edition (Springer-Verlag, 1982).

2. J.M. Hollas in 'High Resolution Spectroscopy', (Butterworths, London 1982).

3. T.W. Hänsch, Appl. Optics, 11 895 (1972).

4. F.A. Jenkins and H.E. White in 'Fundamentals of Optics', 4th edn. (McGraw Hill, New York 1976).

5. M.I.T. Wavelength tables (John Wiley and Sons, New York).

6. Quanta Ray reference manual.

7. W.M. McClain, Appl. Optics, 11 895 (1972).

8. J.P.T. Wilkinson private communication.

9. Chell Instruments Ltd, Norfolk.

10. C.J. Howard, J. Phys. Chem., 83 3 (1979).

11. M.A.A. Clyne and W.S. Nip in 'Reactive Intermediates in the Gas Phase. Generation and Monitoring', ed. D.W. Setser (Academic Press, New York 1979).

12. J.G. Anderson, J.J. Margitan and F. Kaufman, J. Chem. Phys., 60 3310 (1974).

13. P.E. Debely, Rev. Sci. Instrum., 41 1290 (1970).

14. M.A.A. Clyne and P.M. Holt, J. Chem. Soc. Far. Trans. II, 75 569, 582 (1979).

15. W.F. Hughes in 'An Introduction to Viscous Flow', (McGraw Hill, New York 1979).

16. R.E. Walker, Phys. Fluids, 4 1211 (1961).

17. E.E. Ferguson, F.C. Fehsenfeld and A. Schmeltkopf, Adv. At. Mol. Phys., 5 1 (1969).

18. F. Kaufman, Prog. React. Kins, 1 1 (1961).

19. P.J. Ogren, J. Phys. Chem., 79 1749 (1975).

20. R.D. Present in "Kinetic Theory of Gases" (McGraw Hill, New York 1956).

21. H.L. Johnson and E.R. Grilly, J. Phys. Chem., 46 948 (1942).

22. A. Fontijn and W. Felder in 'Reactive Intermediates in the Gas Phase. Generation and Monitoring', ed. D.W. Setser (Academic Press, New York 1979).

REFERENCES (Cont/d.)

23. J. Langmuir, J. Chem. Soc., 511 (1940).
24. K.J. Laidler, J. Phys. Chem., 53 712 (1949).
25. J.G. Anderson and F. Kaufman, Chem. Phys. lett., 10 375 (1972).
26. R.V. Poirier and R.W. Carr Jr., J. Phys. Chem., 75 1593 (1971).
27. N.F. Meggars, J. Opt. Soc. Am., 38 7 (1948).
28. E. Jacobsen and G.R. Harrison, J. Opt. Soc. Am., 39 1054 (1949).
29. I.M. Campbell and B.A. Thrush, Ann. Rep. Chem. Soc., 67 17 (1965).
30. T.M. Shaw, J. Chem. Phys., 30 1366 (1959).
31. F.D. Coffin, J. Chem. Phys., 30 593 (1959).
32. J.F. James and R.S. Sternberg in, 'The Design of Optical Spectrometers', (Chapman and Hall Ltd, London 1969).
33. C.R.C. 'Handbook of Chemistry and Physics', 65th ed. R.C. Weast (1984 - 1985) (CRC Press Inc).
34. T.E. Adams, R.J. Morrison and E.R. Grant, Rev. Sci. Instrum. 51 141 (1980).
35. T.A. Cool, Appl. Optics, 23 1559 (1984).
36. NBS 'Atomic Energy Levels' vol. I - III ed. C.E. Moore (1971).
37. M.A. Brown 'Multiphoton Laser Spectroscopy and Photochemistry of Electronically Excited HCl' Edinburgh University Thesis (1987).

CHAPTER 3

AN INVESTIGATION OF THE SPECTROSCOPY AND COLLISION DYNAMICS OF THE CHLOROSILYLIDYNE (SiCl) RADICAL BY LASER INDUCED FLUORESCENCE

3.1 INTRODUCTION

It has long been recognised that atoms and radicals are far more chemically reactive than most molecules. However this fact was not specifically commercially utilised until the early 1960's with the development of dry processing techniques such as plasma etching [1] (and plasma deposition). Applications of these techniques soon included the etching of silicon by fluorine and chlorine containing gaseous compounds [2]. Plasma deposition is now a well-established technique, for example, in producing doped and undoped silicon films for photoelectric and photothermal devices which can be used in solar energy convertors [3]. The starting material for such devices is generally silicon tetrafluoride (SiF_4) [4] or silicon tetrachloride ($SiCl_4$) [5], diluted with argon and sometimes hydrogen.

For many plasma processes the chemically important species are not the feedstock molecules: if this were true, the 'process' would not be enhanced by a plasma. Thus, the plasma dissociates the feedstock molecules into the 'active' species such as atomic or small free radical molecular species, some of which may also be ionised. Detection and concentration measurement of species in plasmas has traditionally relied most heavily upon mass-spectroscopy (ms) and optical emission spectroscopy (oes) [6][7]. Both of these techniques are however limited in terms of their diagnostic ability: ms is invasive and may distort the apparent concentrations of, for example, reactive species, while oes will only detect excited species and thus only monitor a very small part of the total gaseous sample.

Because of the relatively long history of discharges containing $SiCl_4$, the electronic spectra of some of its more important discharge species have become relatively well characterised, e.g. SiCl [8], whereas there has been less certainty about the emission bands of other species, e.g. $SiCl_2$ [9][10][11]. Furthermore, oes and ms have been used to predict various formation and reactivity mechanisms for plasmas containing silicon and chlorine species. Examples include: the production mechanism of SiCl from an $SiCl_4$/Ar plasma [12]; the mechanism of the chemical vapour deposition (cvd) process on Si by $SiCl_4$ [11]; and the ionisation potentials of various $SiCl_x$ species (x = 2-4) [13]. However, postulating formation mechanisms purely on the basis of ms or oes studies can lead to improper conclusions. Mechanism (1) from reference [7], is a case in point and will be noted again in the concluding discussion:

$$SiCl_2 + e^- \longrightarrow SiCl_2^* \longrightarrow SiCl\ (B'^2\Delta) + Cl + h\nu \qquad (1)$$

$$SiCl\ (X^2\pi) + e^- \longrightarrow SiCl\ (B^2\Sigma) + e^- \qquad (2)$$

The manufacture of materials of ever higher specifications is a continuing goal in etching and deposition applications. However, to fully master the production of layered materials, a complete knowledge and understanding of the reactions taking place during production is required, such that the desired (or undesired) surface modification can be optimized [14]. In particular, the most important factors may be:-

1) Identity of the process precursors
2) Measuring the effectiveness of the etch or deposition process
3) The effect of gas phase and surface chemistry on the material properties

These factors can only be answered with quantitative information concerning which species are present in the discharge, what reactions are occurring and what are the rates of these reactions.

A combination of the low pressure conditions found in processing plasmas [15], together with the relatively simple species present within them will often mean that LIF provides a near ideal technique for diagnostic measurements. Thus, consideration of the energies required to access the electronically excited states of the SiCl radical, indicated that the most suitable basis for diagnostic measurements of silicon etching plasmas using SiCl was likely to be through its $B^2\Sigma^+$ and $B'^2\Delta$ states.

Therefore, the investigations carried out in this chapter are centred on elucidating both the spectroscopic and the collisional energy transfer properties of both the $B^2\Sigma^+$ and $B'^2\Delta$ states of SiCl using LIF. Following a resumé of the pertinent data the following investigations will be presented:

1) Excitation spectra of the $B^2\Sigma^+$ and $B'^2\Delta$ states between 275 and 295 nm, section 3.4.
2) Fluorescence spectra from the B state $v' = 0-3$ levels, together with measured vibrational transition probabilities, section 3.5.
3) Fluorescence spectra from the B′ and B states which show typical energy transfer behaviour, section 3.7.
4) Fluorescence spectra, obtained under high resolution, which show the rotational contour of the emission, section 3.8.
5) Measurements of the energy transfer behaviour in the B′ state as a function of collision partner, section 3.9.
6) Discussions and conclusions.

3.2 The SiCl radical

3.2.1 Spectroscopy of SiCl

The electronic spectrum of SiCl was first observed by Jevons in 1913 in the glow produced by the interaction of $SiCl_4$ vapour with active nitrogen [16,17], where he was able to identify several regularities in the spectrum from 223-312 nm. Datta subsequently pointed out that many of these bands were due to a doublet system, in either the upper or lower state, with a separation of about 205 cm^{-1} [18]. In 1936 Jevons suggested that the ground state of SiCl was a $^2\Pi$ state, and that most of the observed bands could be assigned to three electronic systems which he labelled in direct analogy to the isovalent SnCl molecule [19]. There were subsequent studies, carried out under vibrational resolution, which investigated different aspects of the spectrum [20-23]. However, assignment of the various state symmetries was not finally agreed until the first rotationally resolved spectra were obtained by Ovcharenko et.al. [24][25]. These experiments showed that the symmetries of the X, B and C states were respectively $^2\Pi$, $^2\Sigma^+$ and $^2\Pi$.

In his initial work Jevons [19] experienced difficulty in assigning bands in the 277-283 nm region, with the bands tentatively being labelled as the (2,0), (3,0) bands of the B-X system. Garg [20] attempted to assign these bands to a new system, however his analysis was discounted by Barrow [23], who suggested that these bands were possibly due to $SiCl^+$. Thrush [26] confirmed the assignment of Jevons and also reported observing the (2,1) and (3,1) bands. However, it was only when high resolution, rotationally resolved spectra were obtained that these problem bands could be fully explained as being due to SiCl and assigned to the B′ state [27][28].

High resolution, rotationally resolved spectra have now been obtained for most of the lower bound states of SiCl. Table 3.1 lists the important molecular constants of the known bound states. The most important contribution towards fully characterising the nature of the electronic states of SiCl and providing accurate spectroscopic constants has been made by Bredohl and coworkers [29-32]. They have recently carried out a series of extensive studies on the A-X, B-X, C-X, D-X, E-X and F-X electronic transitions. The studies of Bredohl and coworkers provide the only known rotational information for the D and F states and show that the E state is completely rotationally predissociated [32].

Data for the vibrational levels of the ground ($X^2\Pi$) state were until recently available only from emission studies. However, microwave data are now available for the v" = 0 level of the ground state [33], with a favourable agreement existing between the different studies.

The B′ state was found to have $^2\Delta$ symmetry by Verma [27] and independently by Ovcharenko [28]. The emission bands were observed to have the same doublet spacing as the $X^2\Pi$ ground state and the rotational analysis readily yielded $^2\Delta$ symmetry for the excited state.

TABLE 3.1: The principal molecular constants of $^{28}Si^{35}Cl$ (cm^{-1}, except for r_e which is an Å) for the known bound states

State	T_e[a] / cm^{-1}	A_e[b] / cm^{-1}	ω_e[c] / cm^{-1}	$\omega_e x_e$[d] / cm^{-1}	B_e[e] / cm^{-1}	$D_e \times 10^7$[f] / cm^{-1}	r_e[g] / Å	Reference
$X^2\Pi$	0	207.2678	535.482	2.159	0.256154	2.226	2.058	30,36,40
$A^2\Sigma^+$	23010.7		296.9	0.80	0.1990		2.328[i]	29
$B^2\Sigma^+$	34004.1		706.662	3.907	0.278276	2.122	1.971	30,36,40
$B'\ ^2\Delta$	35527.77	-2.729	511.1	5.6	0.2618	3.75	2.035	27,40
$C^2\Pi$	41073.42	10.927	682.7	3.8	0.289899	2.063	1.936	31,39,41
$D^2\Sigma^+$	44843.61		655.98	2.85	0.282792	1.955	1.953[i]	32
E	~45272	Fully Predissociated						32
$F^2\Sigma^+$	46083.4[h]				0.2747[h]		1.982[i]	32

a) T_e: the electronic term value and corresponds to the zero point energy difference between the ground state and the excided state.

b) A_e: the spin orbit interaction energy for the theoretically vibrationless level of the state.

c) ω_e: the wavenumber of vibration of the nuclei with infinitesimal amplitude about their equilibrium positions.

d) $\omega_e X_e$: the vibrational anharmonicity constant.

e) B_e: the rotational constant for the molecule with the atoms being regarded as being in the hypothetical vibrationless condition.

f) D_e: Centrifugal distortion constant.

g) r_e: the value of the internuclear separation when at the zero point of the potential well.

h) Values are T_{00} and B_0 respectively, the values of T and B when in v = 0.

i) Calculated from $B_e = \frac{h}{8\pi^2 IC}$ where I is the moment of inertia of the molecule,

The work of Verma [27] still represents the most complete study of the B'-X bands to date.

The B state was first rotationally resolved by Ovcharenko et.al. [24], with an analysis of the (0,0), (1,0) and (0,1) bands of the B-X system and a correct identification of the B state as having $^2\Sigma^+$ symmetry. Mishra and Khanna [34] were able to improve the vibrational constants of the B-X system. However, their analysis and prediction of a spin splitting constant $\gamma = 0.0098$ cm^{-1} in the excited state was shown by Rai to be incorrect [35]. Bredohl et.al. [30] have performed the most extensive dispersive measurements on these bands. They analysed their data using a model which more fully reflects the coupling of the angular momenta of the states involved. Their study produced accurate spin-orbit, rotational and lambda doubling constants. More recently Meijer et.al. [36,37] have observed the B state under high resolution, using a combination of a molecular beam and either LIF or Lamb dip spectroscopy to detect the radical. A comparison of the data derived from the work of Bredohl et.al. and Meijer et.al. (see Table 1 of reference [36]) reveals a close agreement.

The hyperfine structure revealed by the Lamb dip study of Meijer et.al. [37] is not, in one sense, of direct spectroscopic relevance to the relatively low resolution measurements performed in this thesis. However, the Lamb dip technique can be a highly sensitive measure of the excited state lifetime, which is of interest in this study. In reference [37] the natural lifetime of the excited state was the determining factor in the observed linewidth. The natural lifetime, τ of a particular transition is given by [38]:

$$\tau = \frac{1}{2\pi} \Delta\nu_\tau \qquad (3)$$

Where, $\Delta\nu_\tau$ is the natural linewidth (FWHM)

For $v' = 0$ of the $B^2\Sigma^+$ of $Si^{35}Cl$ lifetimes of 10.0 ± 1.5 ns and 7.8 ± 0.7 ns are reported for levels with N' (the nuclear rotation angular momentum quantum number) equal to 16 and 27. This is good evidence therefore that the excited state lifetime is decreasing with increasing N'. However, Meijer et.al. were unable to distinguish between a shortening of the lifetime due to predissociation or by a change in the coupling of $B^2\Sigma^+$ $v' = 0$ with different ro-vibrational levels in the $^2\Pi$ ground state only. It is possible to compare the lifetimes given above with the lifetime that can be calculated from the measured electronic transition probability for the $B^2\Sigma^+ \longleftarrow X^2\Pi$ transition [39] from which case a lifetime of 10 ns is also predicted.

3.2.2 Potential energy curves for the known bound states of SiCl

To establish a basis for the discussion of the intensities of emission and the collisional transfer properties of the excited states of SiCl, it is useful to have a knowledge of the positions of the excited electronic states and the form of their potential energy curves. The numbers and symmetries of possible electronic states of a diatomic molecule can be derived by considering the appropriate combinations of the separate atomic terms. However, the potential curves can only be obtained either from spectroscopic investigations or ab initio calculations.

Theoretical investigations into the electronic structure of SiCl are very sparse [42]. Also, there is only one previously reported calculation of Franck-Condon factors (related to emission intensities) for SiCl, which was performed for the B to X system and is discussed further in section 3.5.3 [43].

Given the relative energy separations of the ground and excited states of the chlorine and silicon atoms, it is likely that the molecular states of interest in this study arise from the ground state atomic configuration of chlorine and the lower energy configurations of silicon [44], see Table 3.2 below.

TABLE 3.2: Atomic terms and energies of the lowest energy electron configurations in silicon and chlorine

ATOM					
Si I			Cl I		
Configuation	Term	Energy/cm^{-1}	Configuration	Term	Energy/cm^{-1}
$3s^2 3p^2$	^3P_J	0	$3s^2 3p^5$	$^2P^o_J$	0
$3s^2 3p^2$	$^1D_2$	6300	$3s^2 3p^4(^3P)4s$	^4P_J	72000
$3s^2 3p^2$	$^1S_0$	15400			
$3s^2 3p(^2P^o)4s$	$^3P^o_J$	40000			
	$^1P^o_1$				

Following the rules for coupling angular momenta in atomic terms [45][46], the molecular states that are possible for the above cases are:

$^3P + {}^2P^o \Rightarrow {}^2\Sigma^+(2),\ {}^2\Sigma^-,\ {}^2\Pi(2),\ {}^2\Delta;\ {}^4\Sigma^+(2),\ {}^4\Sigma^-,\ {}^4\Pi(2),\ {}^4\Delta$

$^1D + {}^2P^o \Rightarrow {}^2\Sigma^+(2),\ {}^2\Sigma^-,\ {}^2\Pi(3),\ {}^2\Delta(2),\ {}^2\Phi$

$^1S + {}^2P^o \Rightarrow {}^2\Sigma^+,\ {}^2\Pi$,

and for the Rydberg states: (states deriving from an atomic electronic promotion which increases the principal quantum number):

$$^3P^o + {}^2P^o \Rightarrow {}^2\Sigma^+,\ {}^2\Sigma^-(2),\ {}^2\Pi(2),\ {}^2\Delta;\ {}^4\Sigma^+,\ {}^4\Sigma^-(2),\ {}^4\Pi(2),\ {}^4\Delta$$

$$^1P^o + {}^2P^o \Rightarrow {}^2\Sigma^+,\ {}^2\Sigma^-(2),\ {}^2\Pi(2),\ {}^2\Delta$$

The number in brackets corresponds to the number of states of that particular symmetry.

It is obvious therefore, that a great many of the possible states remain undetected. However, this observation is not surprising since all the quartet states represent single photon forbidden transitions from the ground state. Similarly it would be expected that at least half of all possible states should be repulsive.

To obtain an idea of the energy ordering of the molecular orbitals (MO's) within SiCl a Linear Combination of Atomic Orbitals (LCAO) approach was adopted. This method starts from the Atomic Orbitals (AO's) of the individual atoms, which are:

$$Si = 1s^2 2s^2 2p^6 3s^2 3p^2 \Rightarrow [Ne]\ 3s^2 3p^2$$

$$Cl = 1s^2 2s^2 2p^6 3s^2 3p^5 \Rightarrow [Ne]\ 3s^2 3p^5$$

The LCAO diagram is shown in Figure 3.1. The AO's of chlorine are assumed to lie deeper in energy than those of silicon. This assumption is based on orbital contraction with increasing atomic number within a given shell. Figure 3.1 therefore shows the ground state molecular orbital configuration. Assuming that the 3s AO's are essentially core orbitals, the MO configuration can be written as:

$$(\pi)^4\ (\sigma)^2\ (\pi^*)^1$$

FIGURE 3.1: Simple LCAO approach to constructing the ground state molecular orbital of SiCl. The LCAO approach is outlined in the text.

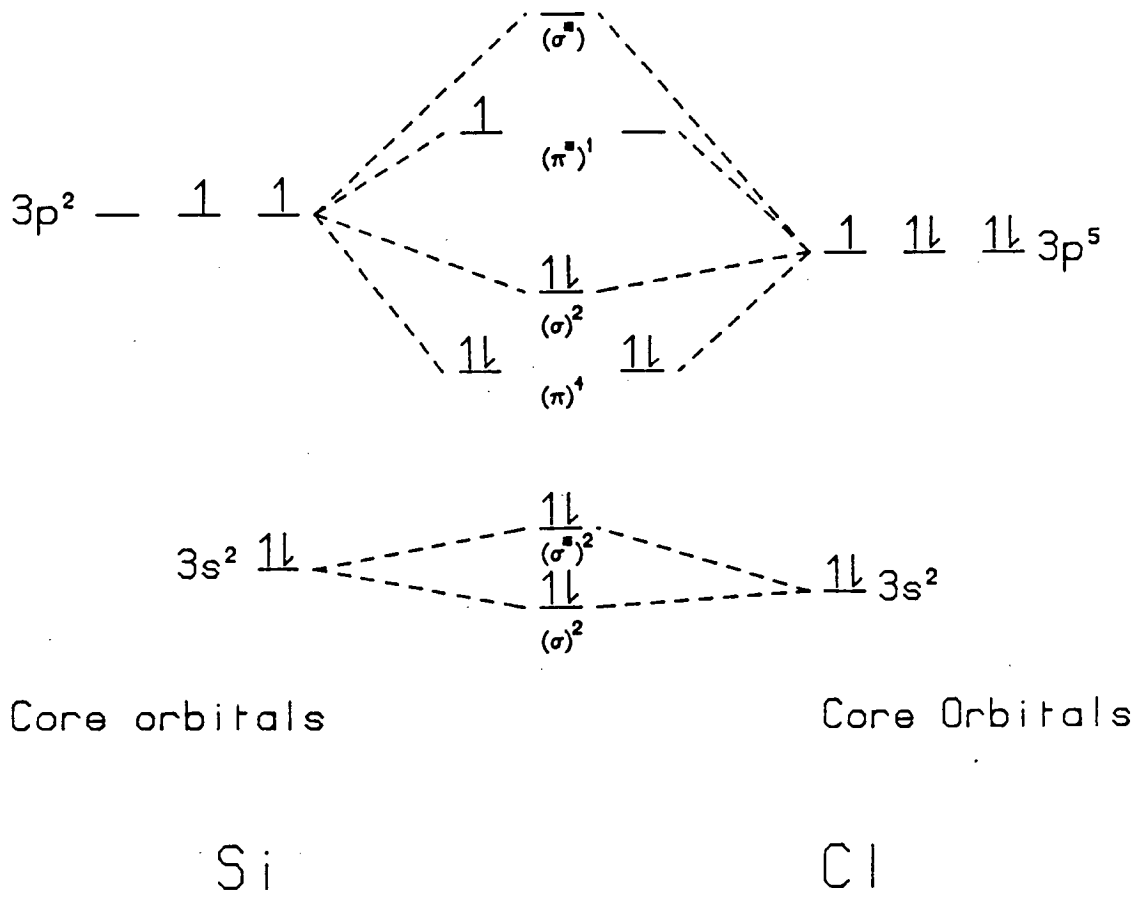

Following the work presented by Verma [27], the first few excited states were derived by considering the terms that arise following electron promotion [45], these are:

1) $(\pi)^4\ (\sigma)^2\ (\sigma^*)^1$ - $^2\Sigma^+$

2) $(\pi)^4\ (\sigma)\ (\pi^*)^2$ - $^2\Sigma^+,\ ^2\Sigma^-,\ ^2\Delta,\ ^4\Sigma^-$

3) $(\pi)^3\ (\sigma)^2\ (\pi^*)^2$ - $^2\Pi_i,\ ^2\Pi_r,\ ^2\Pi,\ ^2\Phi,\ ^4\Pi_i$

4) $(\pi)^4\ (\sigma)^2\ (ns\sigma)$ - $^2\Sigma^+$ (first number of the ns Rydberg series),

then relying extensively on the analogy between the electronic structure of SiF and SiCl, it is possible to assign the known molecular states to these types of configurations. The A state probably belongs to configuration (1) [27][47]. By analogy with the $^2\Delta$ state of CCl [48] and by examining the combinations (1)-(4) the B′ state probably belongs to configuration (2). The B state, like its SiF analogue, is the first member of a Rydberg series and thus belongs to configuration (4) [27]. Analysis of the $C^2\Pi$, $D^2\Pi$ and $F^2\Sigma$ states, indicates that they are all Rydberg states [31][32]. The C state probably has the configuration:

$$(\pi)^4\ (\sigma)^2\ (np\pi),$$

while the D and F states have the following respective configurations:

$$(\pi)^4\ (\sigma)^2\ (np\sigma) \qquad (n = 4)$$

$$(\pi)^4\ (\sigma)^2\ (ns\sigma) \qquad (n = 5)\ .$$

While a reasonable estimate of the dissociation energy and hence dissociation limit may be obtained by a Birge-Sponer

extrapolation [45], this procedure is 'risky' when applied to excited states, the reason being that in the excited state manifold, where the state density has considerably increased, there is a much higher chance of encountering curve crossing phenomena. Hence, the dominant electronic configuration near r_e of a state need not be that near its dissociation limit and hence a simple extrapolation of behaviour from around r_e may be grossly in error. An ab initio study by Karna and Grein [49] indicates that this may well be the situation for the highly analogous isoelectronic SiF molecule.

To characterise the electronic states more quantitatively, especially around the region near the potential minimum, Rydberg-Klein-Rees (RKR) potentials were constructed. While this semi-classical method is excellent for regions in which the spectroscopic constants are well known, care should be taken when extrapolating potentials outside the range of vibronic levels from which the constants were derived.

The RKR method derives the form of the potential from spectroscopic term values without imposing any analytic constraints on it. The method determines the classical turning points r_+ and r_- for a vibrational level of energy U from the expression [50]

$$r \pm (U) = ({}^{f}/_{g} + f^2)^{1/2} \pm f \ , \qquad (4)$$

where

$$f(U) = {}^{h}/_{2\pi(2\mu)^{1/2}} \int_0^{I'} [U - E(I,K)]^{-1/2} dI \qquad (5)$$

and

$$g(U) = {}^{h}/_{2\pi(2\mu)^{1/2}} \int_0^{I'} \frac{\delta E}{\delta K} [U-E(I,K)]^{-1/2} dI \ . \qquad (6)$$

E(I,K) is the sum of the vibrational and rotational energies of the molecule for any level up to U. The variables I,K are defined in quantum terms:

$I = h(v + \frac{1}{2})$ is associated with radial momentum, v is the quantum number.

$K = J(J+1)h^2/8\pi^2\mu$ arises from the quantization of the rotational angular momentum, J is the quantum number and μ is the reduced mass of the molecule.

$I = I'$ when $E = U$.

The semi-classical approach does not restrict the variable of integration I to discrete values. Normally the functions f(U) and g(U) are evaluated for K = 0 to construct the effective potential for the non-rotating molecule.

RKR potentials form a suitable basis for (simulated) fluorescence calculations. Such calculations do however require the potential to be tabulated in very small steps ~ 0.001Å and be accurate to within approximately, $r' - r'' = 0.002$Å [50].

Using the data in the references listed in Table 3.1, RKR potentials were constructed for all the known bound states of SiCl. These potentials are presented in Figure 3.2. The inner limbs of the RKR curves were typically ill-behaved at $\geq {}^1/3\ D_o$. (D_o is the dissociation energy). Hence this limb was modelled by a function which scaled as r^{-12} and joined the RKR data such that the whole potential was continuous and had continuous first and second derivatives. The dashed curve in Figure 3.2 is for the theoretically predicted bound $a^4\Sigma$ state [42]. The curve was positioned at the calculated T_e and r_e values and was assumed to have a valence state character, similar to the B′ state. A Morse function was used to describe its behaviour [45].

FIGURE 3.2: Potential energy curves for the known bound (solid lines) and ab-initio predicted bound (dashed line) states of SiCl. The states were constructed as described in the text.

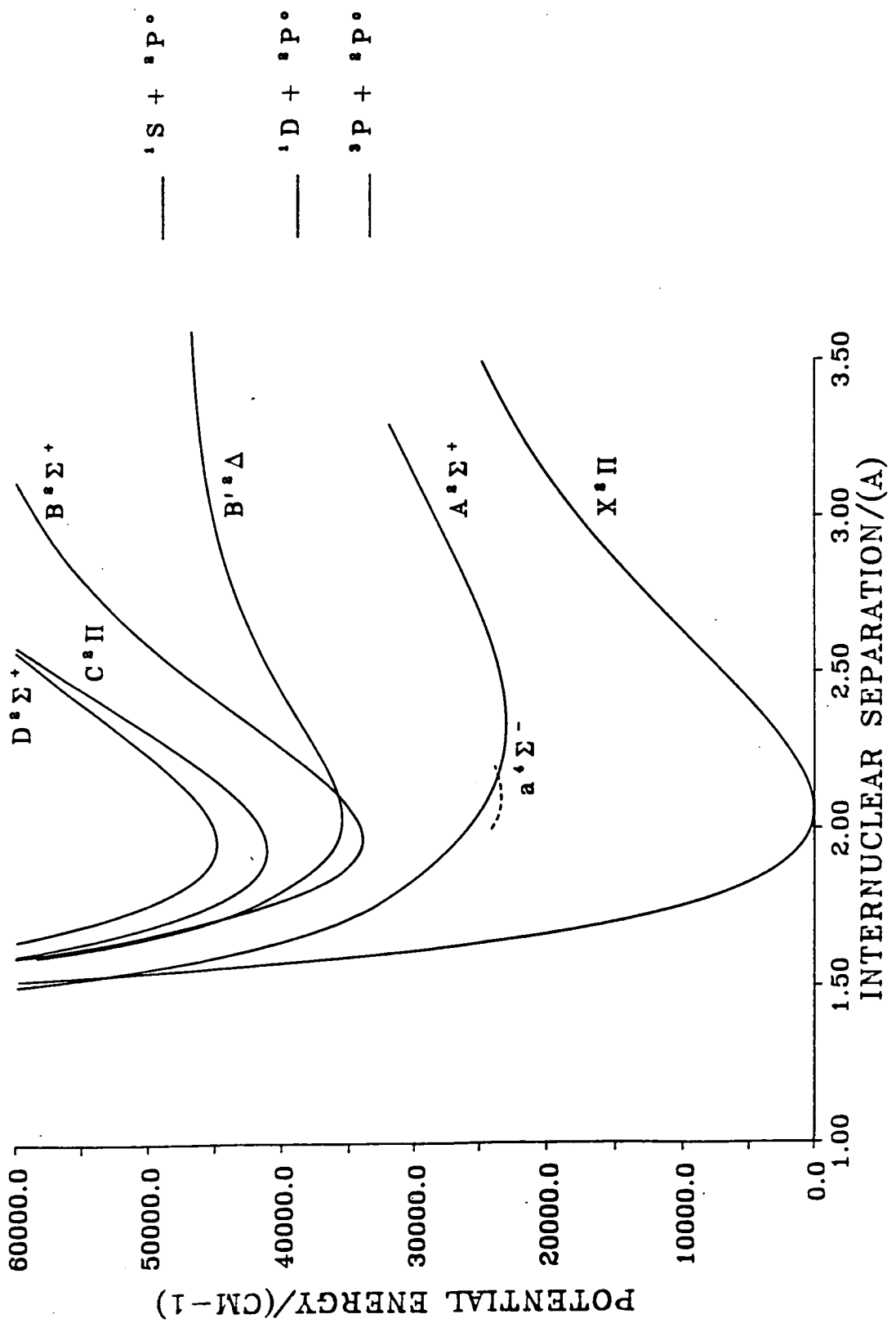

3.2.3 Thermochemistry of SiCl

Thermochemical data are somewhat sparse for the SiCl radical. Values for the dissociation energy of the ground state have been determined mostly by spectroscopic means and lie between 3.3 and 4.5 eV [51]. The only determination of the dissociation energy by thermochemical means yielded a value of 3.84 $\pm$ 0.09 eV [51]. There have been no direct determinations of the ionisation potential (I.P.) of SiCl. However, Hudgens et.al. [47] were able to determine that the I.P. was less than 7.2 eV via a multiphoton ionisation process. By analogy with similar species, Hudgens predicted a value between 7.0 and 7.2 eV. This value compares well to that calculated, using extended Hückel theory, by Hastie and Margrave of 7.36 eV [52].

3.2.4 Reactive and Quenching Studies on SiCl

There have been no reports in the literature, as far as can be determined, of any reaction rate or collisional energy transfer data for SiCl. However, we were aware in the course of this work that similar studies to those reported here had recently been undertaken by Jeffries [53]. The studies of Jeffries included measuring the B-X vibrational transition probabilities from the B v'= 0,1,2 and 3 levels and measuring quenching rates for the B' v' = 0,1 levels using He, Ne and Ar.

3.3 Experimental Methods

For most of the measurements reported in this chapter the SiCl radical was generated by a standard route: flows of argon (500 SCCM) and a 10% $SiCl_4$ in argon mixture (6 SCCM) were premixed well before entering the flow reactor via a 12 mm diameter quartz discharge side arm with a microwave cavity operating at 15 W. Under these conditions the steady state pressure in the flow reactor was ~ 1.1 Torr, with the plasma exhibiting a central white glow and a green tail.

The apparatus used in the LIF experiments was described in Chapter 2, section 2.6 and is represented schematically in Figure 2.1. Briefly, a six way glass cross with three mutually perpendicular axes, painted black, was utilised for the LIF experiments. The first axis constituted the flow axis of the gas sample. A second axis, fitted with two arms ~ 15 cm in length and with Brewster angle windows allowed passage of the interrogating laser beam. Fluorescence was gathered on the third axis, the pressure gauge (MKS Baratron, 0-100 Torr, model 222BA) was also mounted on this axis and hence served the dual purpose of acting as a pressure sensor and light trap.

Low pressure conditions were chosen as standard since subsequent experiments would include investigations into the effects of additional collisional partners. Thus it was desirable to minimise the contribution from the argon carrier gas. When maximum LIF signal was required alternative conditions were used (1000 SCCM Ar, 12 SCCM 10% $SiCl_4$/Ar mixture, 20 - 25 W discharge power and pressure ~ 2.25 Torr). It was found that unlike most radicals, production of SiCl was favoured at relatively low discharge powers. It seems likely therefore that complete fragmentation of $SiCl_4$ to atomic species may occur in 'hot' plasmas.

Initially, experiments were also carried out in which mixtures of only $SiCl_4$ and He passed through the discharge. It was quickly evident, however, that SiCl production was much less efficient when He was used. This observation was consistent with previous investigations [12], where a green emission attributable to the $A^2\Sigma^+ - X^2\Pi$ transition of SiCl could be detected following the introduction of $SiCl_4$ downstream of an argon discharge. Hence, metastable argon species may be important to the efficient production of SiCl.

It was found that only when the discharge was on was there any detectable LIF signal from SiCl, or indeed any signal other than scattered light. When the discharge was on, continuous emission (non-synchronous with the laser pulse) could be detected, but only at the highest flow rates through the discharge. This emission consisted of two isolated sharp features at 300.7 nm and 302.0 nm: and were assigned to transitions in the silicon atom [54]. The remainder of the spontaneous emission 'spectrum' running from 280 - 320 nm showed no detectable features above an essentially zero background.

The mixtures of 10% $SiCl_4$/Ar were prepared in a 10 dm^3 pyrex bulb, fitted with a greaseless tap. The bulb was always made up to an initial pressure of 760 Torr, with the argon being added last, before being left overnight to equilibrate. The mixture of $SiCl_4$/Ar was found to produce condensation of the $SiCl_4$ vapour in the bulb.

Silicon tetrachloride is very sensitive to hydrolysis, with any exposure to moisture yielding HCl, silacious deposits and with the consequent observation in the LIF excitation spectra of lines attributable to the $A^2\Sigma^+ - X^2\Pi$ transition of the hydroxyl radical (OH). Experimentally it was found that exposure of $SiCl_4$ vapour to any 'new' surface which had not been under vacuum or previously exposed to the vapour could yield detectable amounts of OH. Care was always taken, therefore, that the flow reactor and the gas handling line was fully evacuated and passivated before any experimental work commenced, since an incorrect assignment of a line in the OH spectrum as that of SiCl followed by pumping it would obviously yield data relevant to the spectroscopy and energy transfer of OH and not SiCl.

Heterogeneous loss of SiCl was found to be severe on naked glass, especially in the discharge side arm. This is probably due to the constrictive flow within the sidearm. A coating of halocarbon wax (see Chapter 2) was found to considerably reduce these loss effects in the flow reactor. For the discharge side arm a treatment with phosphoric acid (see Chapter 2) was found to enhance the useable lifetime between cleaning by a factor of approximately three. The deposits in the side-arm appeared to be silacious material and were removed by a combination of abrasion and chemical cleaning (NaOH (pellets) and H_2O_2 (80%)). After washing, the side arm was 'passivated' by discharges of CF_4/He, O_2/He and $SiCl_4$/Ar each for two hours. After each cleaning cycle, calibration spectra showed identical but more intense features to those obtained prior to cleaning.

Under typical experimental conditions, a total gaseous flow of 506 SCCM produced a pressure of approximately 1.0 Torr in the reactor. The $SiCl_4$ partial pressure (assuming no dissociation) would be approximately 1×10^{13} Torr or 4×10^{13} molecules cm^{-3}. However, $SiCl_4$ will be almost totally dissociated in a discharge, hence a very approximate estimate of the SiCl concentration can be made by assuming that there is likely to be between 10% and 0.1% dissociation to this radical, i.e. between 4×10^{12} and 4×10^{10} molecules cm^{-3}. An investigation by Rowe [12] has shown that the green glow is likely to be observed in a discharge which was efficiently fragmenting all $SiCl_n$ species (n = 1-4), but was more efficient for large n. Making a gross assumption that thermodynamic calculations could be applied to the non-equilibrium situation found in a discharge, he 'characterised' the green glow conditions with a SiCl population, relative to the $SiCl_4$ mass flow, as approximately 1% and a discharge temperature of 2800 K. The approach of Rowe therefore yields a concentration of approximately 4×10^{11} molecules cm^{-3} and falls between the values obtained from an empirical estimate of the dissociation efficiency.

For a typical $^{S}/_{n}$ ratio in the B state excitation scans of 100:1, total concentrations near 2×10^{9} molecules cm^{-3} should be easily detectable. For the fluorescence scans, due to a superior $^{S}/_{n}$ ratio, a value nearer 5×10^{8} molecules cm^{-3} would be realistic.

To study collisional energy transfer processes quantitatively in a flow reactor it is imperative that the gas under investigation be isotropic. Hence, experiments were carried out where the product state distribution (PSD, see section 3.7) following collisional removal of the $B'^{2}\Delta$ state of SiCl was investigated as a function of time (i.e. distance travelled) and pressure in the reactor. An isotropic mixture was inferred when the PSD was constant with increasing distance travelled.

All gases used throughout this chapter were obtained from BOC and were used without further purification. The gases, together with their stated purities, were: He (99.998%), Ar (99.998%), H_2 (99.99%), N_2 (99.998%), CO_2 (99.8%), CH_4 (99.2%) and CF_4 (Electra II).

3.4 LIF Excitation Spectra

LIF excitation spectra provided the essential basis for all subsequent studies into the spectroscopy and collision dynamics of the SiCl radical. These scans yielded the spectroscopic information such as state symmetries and molecular constants that lead to species identification. Furthermore, they also directly indicate the temperature of the sample under investigation. Under appropriate conditions of resolution, perturbations between excited states may also become evident. These scans therefore indicate the spectral regions which should be exploited for investigations into collisional energy transfer.

Excitation spectra were obtained in the wavelength region bounded approximately by 275 and 295 nm. Excitation was performed mostly

from v" = 0 in the $X^2\Pi$ ground state (both spin-orbit components) to v' = 0,1,2 and 3 in the $B^2\Sigma^+$ state and v' = 0,1 in the $B'^2\Delta$ state. The total fluorescence signal was collected by operating the monochromator in zero order with its slits fully open, see Figure 2.1. Typical energy densities for the spectra were ~ 500 $nJcm^{-2}$, for which it was initially suspected that a degree of saturation for the strong B-X transition may be evident. However, spectra obtained with an energy density of ~ 20 $nJcm^{-2}$ showed no apparent differences in the intensity ratio between the branches.

Simulations are presented with each experimental spectrum, the method of generating these being discussed in Appendix I. Input variables were temperature, for which 302 K was found to yield the best fit and laser bandwidth for which a typical value was 0.5 cm^{-1} and was larger than expected a priori (see Chapter 2). Simulation of the B state using the assumption of full saturation i.e. all linestrengths being equal to one yielded poorer fits. The B state has been shown to have a decreasing lifetime with increasing angular momentum content [37]. However, a function to model this effect (see Chapter 4, for full details) did not significantly improve the fit and was not used in the simulations shown here. The fit of the simulation to the B-X spectra was reasonable in all cases except that the intensity of the Q_1 head was relatively poorly modelled. The difference was not considered serious since the sharp head forming bands were found to be very 'sensitive' to the laser linewidth input of the simulation.

The B-X (0,0) and (1,0) bands are spectroscopically isolated. Also, in both cases the spectral appearance for transitions originating from the $\Pi_{1/2}$ and $\Pi_{3/2}$ components was rather similar. Hence, a typical spectrum for these bands is shown in Figure 3.3. Assignment of the spectrum could be made rather easily, but was obviously facilitated by the availability of the simulation. The B-X bands exhibit P, Q and R branches, which therefore indicates a so-called perpendicular transition. In such a case the transition dipole moment lies in a plane at right angles to the Z axis of the molecule fixed reference

FIGURE 3.3: Excitation scan for the $F_1\ ^2\Pi_{1/2}$ component of the (1,0) band of the $B^2\Sigma^+ - X^2\Pi_r$ system. Assignment of only the band heads has been performed. Separation of the isotopic combinations $^{28}Si^{35}Cl$, $^{28}Si^{37}Cl$ is evident, with their observed intensities being 3:1 (natural abundance). The simulation assumed a laser bandwidth of 0.5 cm^{-1}, T = 302 K.

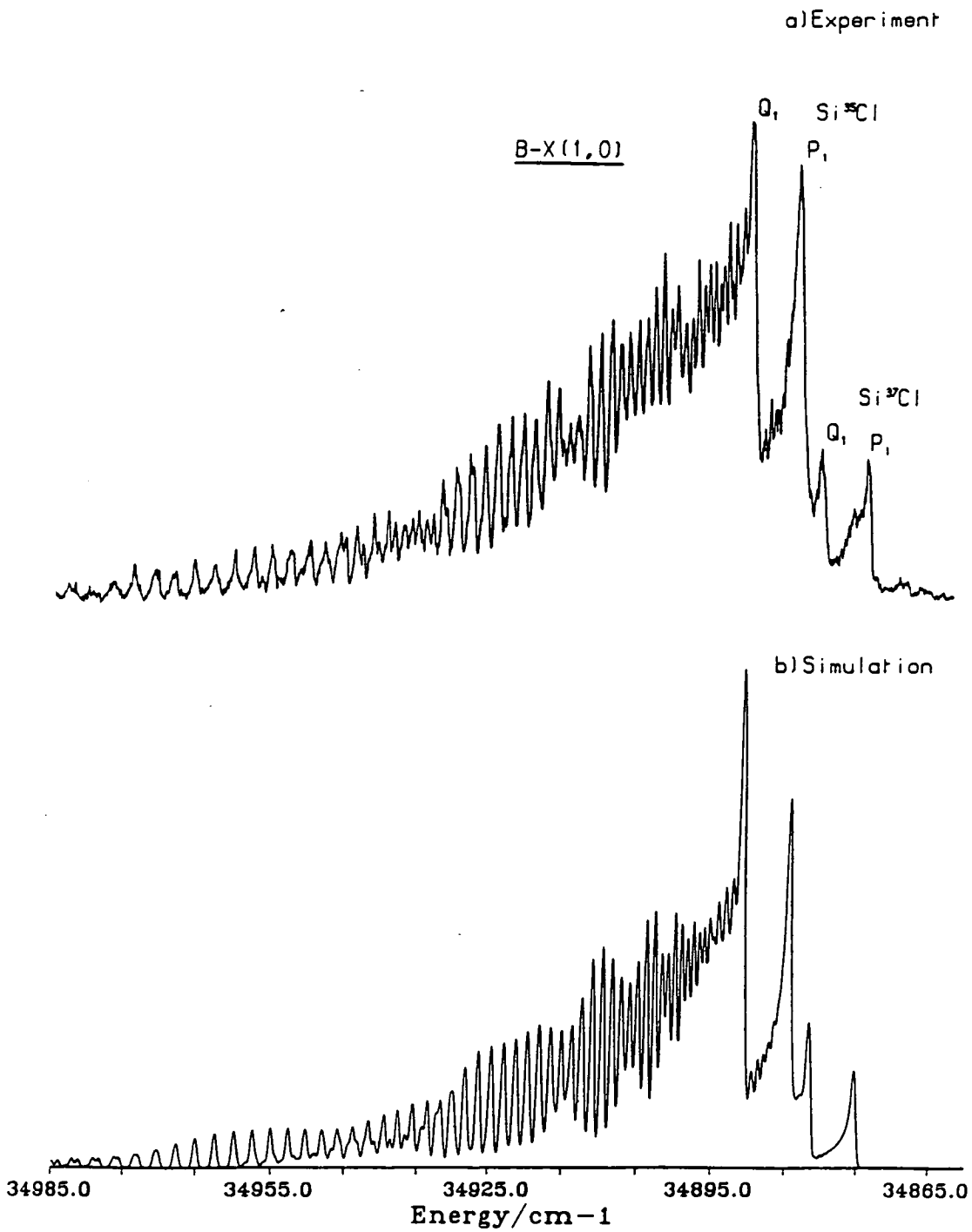

frame [55], while in a parallel transition the transition dipole lies along the internuclear axis. The presence of a large ground state splitting and a strong double headed structure indicates that only $^2\Sigma - {}^2\Pi$, $^2\Pi - {}^2\Pi$ or $^2\Delta - {}^2\Pi$ transitions are possible. However, the presence of a Q branch precludes the $^2\Pi - {}^2\Pi$ possibility. Finally, the absence of any spin orbit coupling in the excited state indicates that the $^2\Sigma - {}^2\Pi$ transition is most likely. The rotational structure of a $^2\Sigma - {}^2\Pi$ transition is outlined in section (i) of Appendix I. All the B-X bands appear shaded to the blue, this implies B' > B" and therefore the head forming branches will be $Q_1(J)$ and $P_1(J)$ for the $^2\Pi_{1/2}$ component and $P_2(J)$ and $^{O}P_{12}(J)$ for the $^2\Pi_{3/2}$ component. Isotopic bands are resolved and appear in the 3:1 ratio of the natural abundance of $^{35}Cl:^{37}Cl$ isotopes. Assuming Boltzmann statistics for the ratio (corrected for laser power) of the spin orbit components separated by 207 cm^{-1}, yields a temperature of 308 $\pm$ 20 K.

The B-X (2,0) and B'-X (0,0) bands were found to be extensively overlapped. However, assignment of a state symmetry to the B' state can again be made purely on the basis of spectral appearance. The B'-X bands again exhibit P,Q and R branches, thus the transition is perpendicular. Assignment to $^2\Delta$ excited state symmetry follows from the realisation that two of the head forming branches, P_2 and $^{P}Q_{12}$, that arise from spin splitting are split by more than would be expected for a $^2\Sigma$ state. The rotational structure of a $^2\Delta - {}^2\Pi$ transition is outlined in section (ii) of Appendix I. For the case where B' > B" in a $^2\Delta - {}^2\Pi$ transition the head forming branches are P_2, $^{P}Q_{12}$, Q_2 and Q_1 [27]. The $\Omega = {}^1/2$ component of the ground state will undergo excitation to the B state and the Ω = 3/2 component of the Δ state, see Figure 3.4, while the Ω = 3/2 component of the ground state will undergo excitation to the B state and the Ω = 5/2 component of the Δ state. Associated with the Ω = 3/2 component of the Π state are the P_2, $^{P}Q_{12}$ and Q_2 head forming branches, see Figure 3.5.

The simulations in Figures 3.4 and 3.5 were produced by a separate 'synthesis' of each transition and then adding these, with appropriate weightings, to yield the best fit spectrum.

FIGURE 3.4: Excitation scan for the overlap region of the $F_1\ ^2\Pi_{1/2}$ component of the (2,0) band of the $B^2\Sigma^+ - X^2\Pi_r$ system and for the $F_1\ ^2\Pi_{1/2}$ component of the (0,0) band of the $B'^2\Delta - X^2\Pi_r$ system. The simulation assumed a laser bandwidth of 0.5 cm^{-1}, T = 302 K.

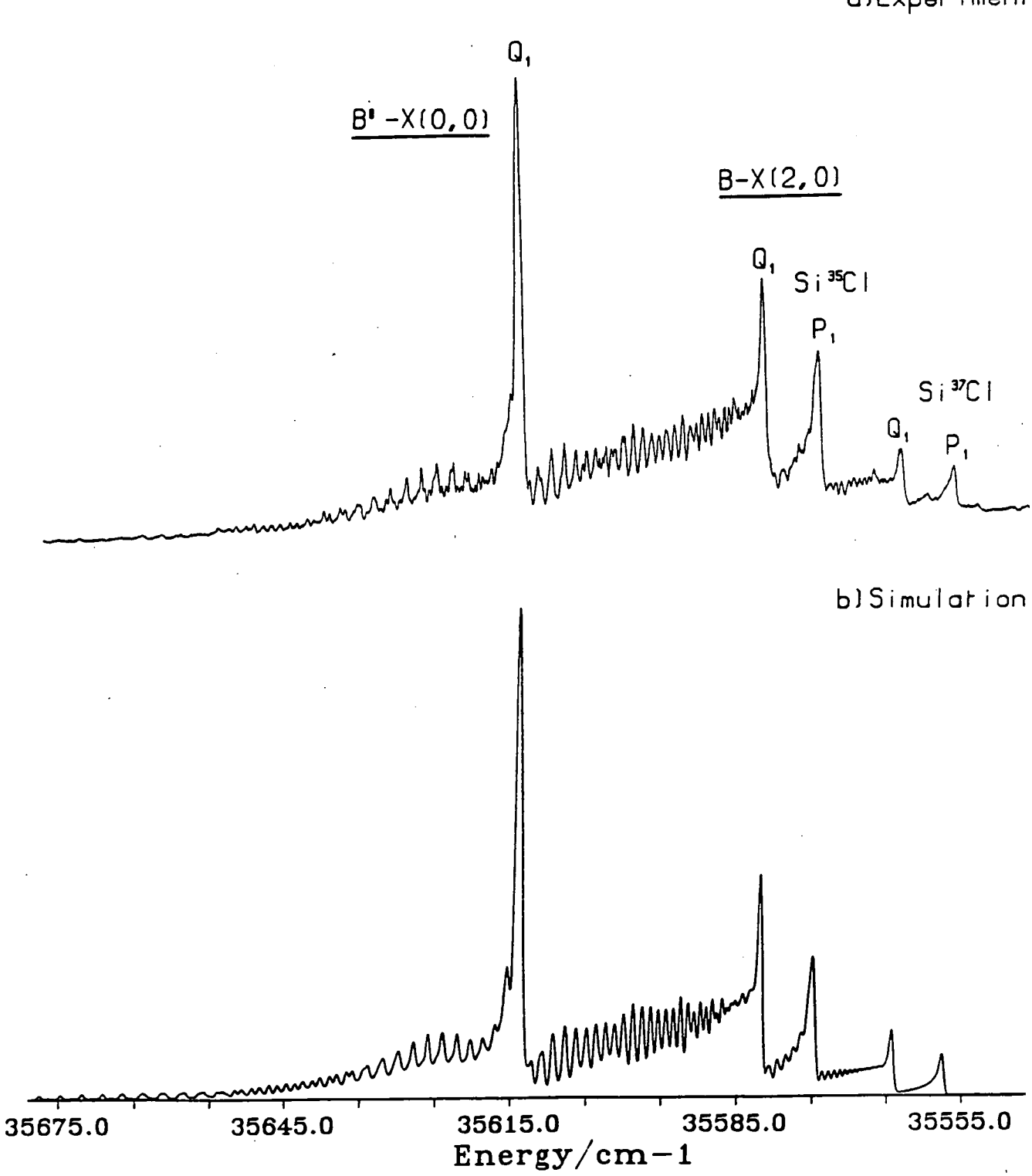

FIGURE 3.5: Excitation scan for the overlap region of the $F_2\ ^2\Pi_{3/2}$ component of the (2,0) band of the $B^2\Sigma^+ - X^2\Pi_r$ system and for the $F_2\ ^2\Pi_{3/2}$ component of the (0,0) band of the $B'^2\Delta - X^2\Pi_r$ system. Simulation assumes a laser bandwidth of 0.5 cm^{-1}, T = 302 K.

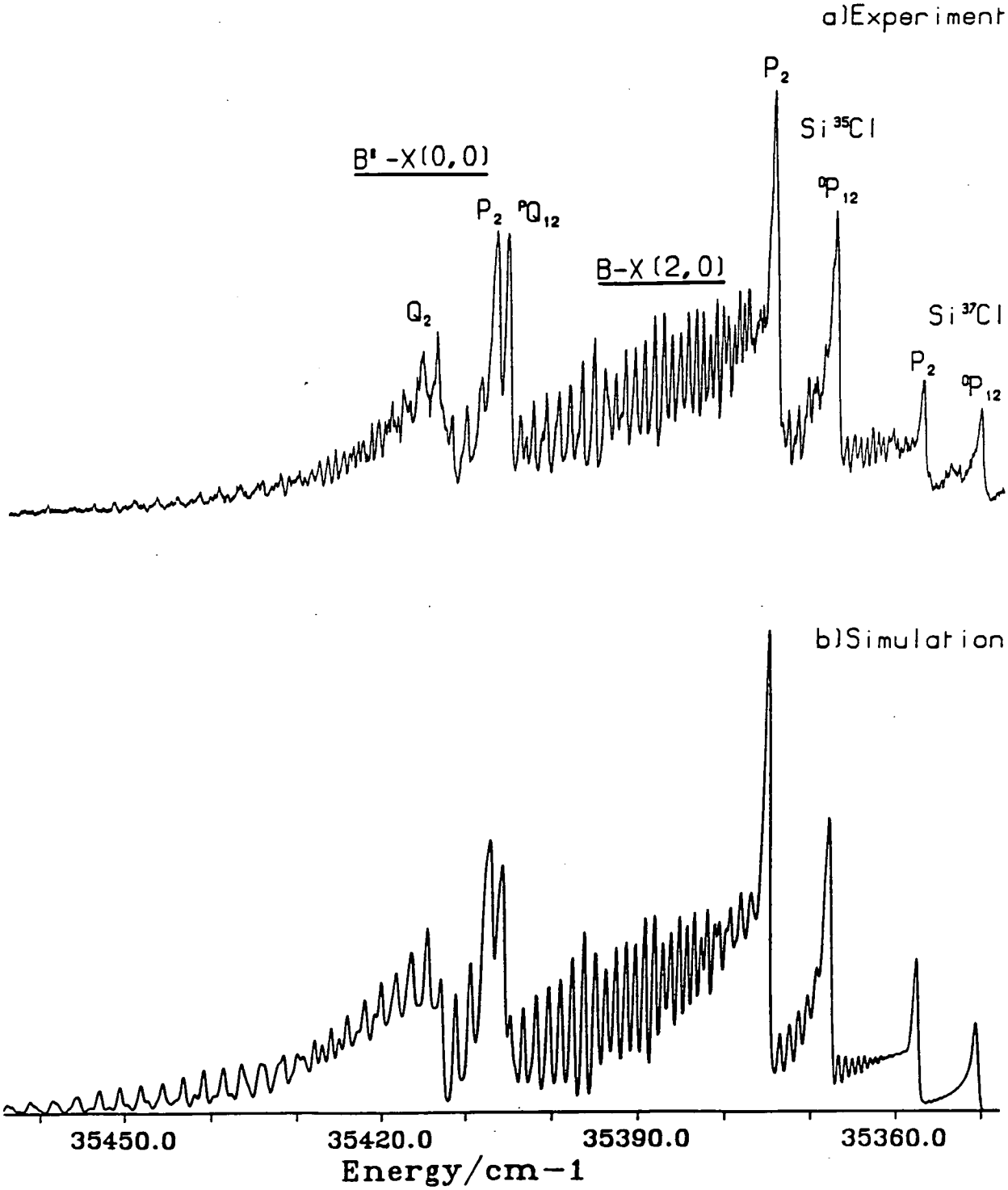

The $^2\Sigma^+$ and $^2\Delta$ states have a difference of 2 in their Λ quantum numbers, where Λ is a 'good' quantum number for both states. Electronic states are normally only expected to interact if there is a difference of zero (homogeneous perturbation) or one (heterogeneous perturbation) in their Λ quantum numbers [45]. Since the spectra of both the states are highly congested and overlay each other it is difficult to tell if there is any interaction between the two. However, no reports from higher resolution studies of any interaction between the states have been made [27][30][36].

The B′ state has a lifetime of ~ 1.0 μs [53], whilst that of the B state is nearer 10 ns [37]. Hence, by arranging that the input impedence of the signal averager is the same as the PMT (50 Ω), the ~ 20 ns temporal resolution of the photomultiplier could be used to discriminate between the emissions of molecules initially prepared in these states. Figure 3.6 shows a scan over the same wavelength region as Figure 3.4. The spectrum shown in Figure 3.6 was obtained by delaying the detector gate 100 ns relative to the excitation pulse, hence the almost complete lack of any B-X emission. Also evident in Figure 3.6 is the (1,1) B′-X hotband transition. This band lies in almost exact resonance with the Q_1 head of the B-X (2,0) band. Assuming that the B′-X bands are almost exclusively diagonal (see section 3.5), then the Franck-Condon factor (FCF) for the B′-X (0,0) and (1,1) bands will be almost identical. Hence, it is possible to estimate the vibrational temperature of the SiCl sample from direct comparison of the intensities of the two bands. Applying Boltzmann statistics to the ratio yields a temperature of 317 $\pm$ 25 K, which agrees reasonably with the temperature estimated by the other routes and with the expectation that the vibrational degree of freedom would be thermalised in the flow reactor. If the detector gate was set to zero delay relative to the excitation pulse, then collection of B state emission was enhanced over B′ state emission and Figure 3.7 was obtained.

FIGURE 3.6: Excitation scan with a delay between excitation and detection of 100 ns, taken over the same region as Figure 3.4. The difference between 3.4 and 3.6 is due to the greater radiative lifetime of the B′ state. Assignment to the $B'^2\Delta - X^2\Pi$ (1,1) hot band transition is made and is almost exactly resonant with the Q_1 head of the (2,0) B-X transition. The simulation assumed a laser bandwidth of 0.5 cm^{-1}, T = 302 K.

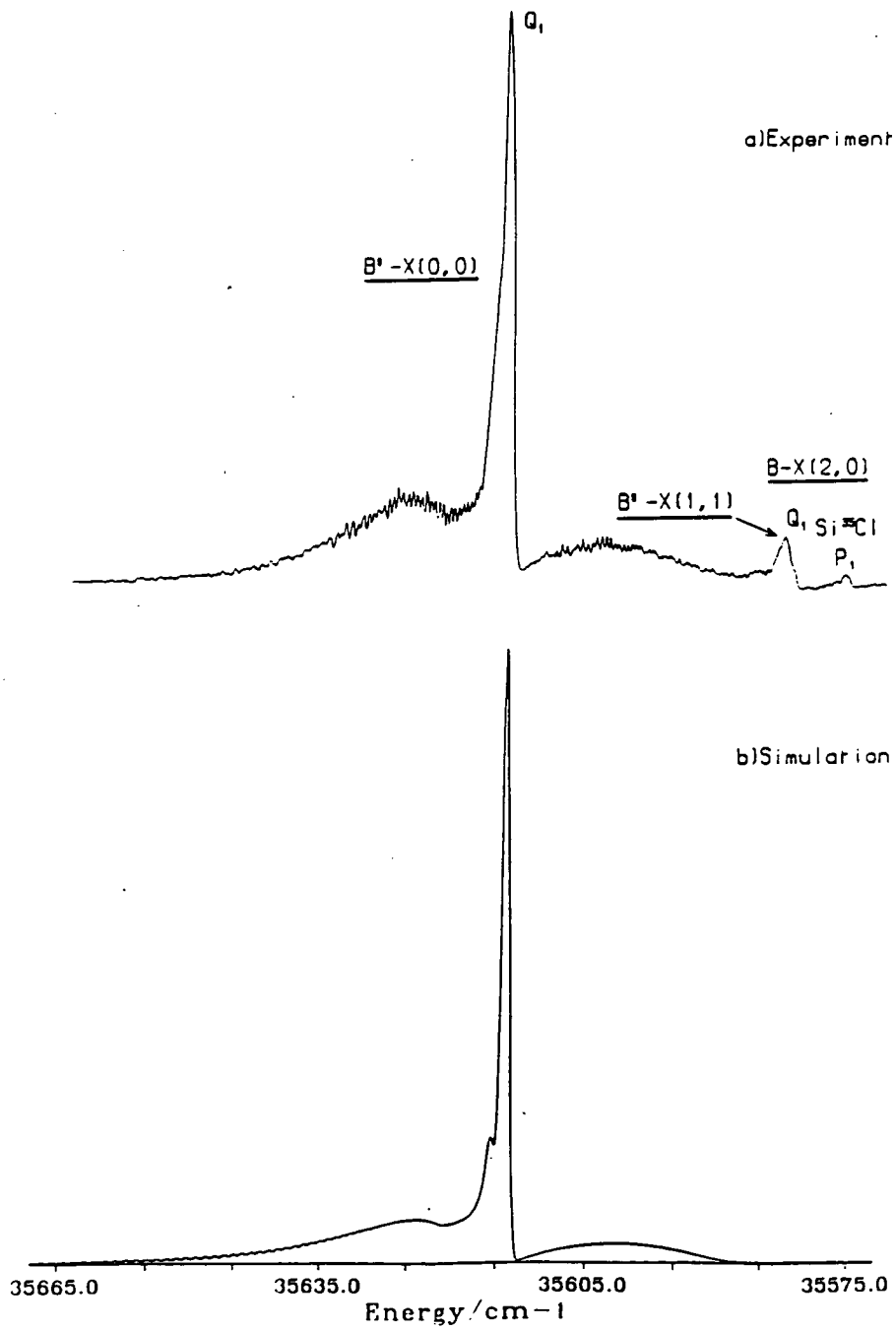

FIGURE 3.7: Excitation scan with no delay between excitation and detection, but with a 10 ns detector gate taken over the same region as Figure 3.6. The simulation assumed a laser bandwidth of 0.55 cm^{-1}, T = 302 K.

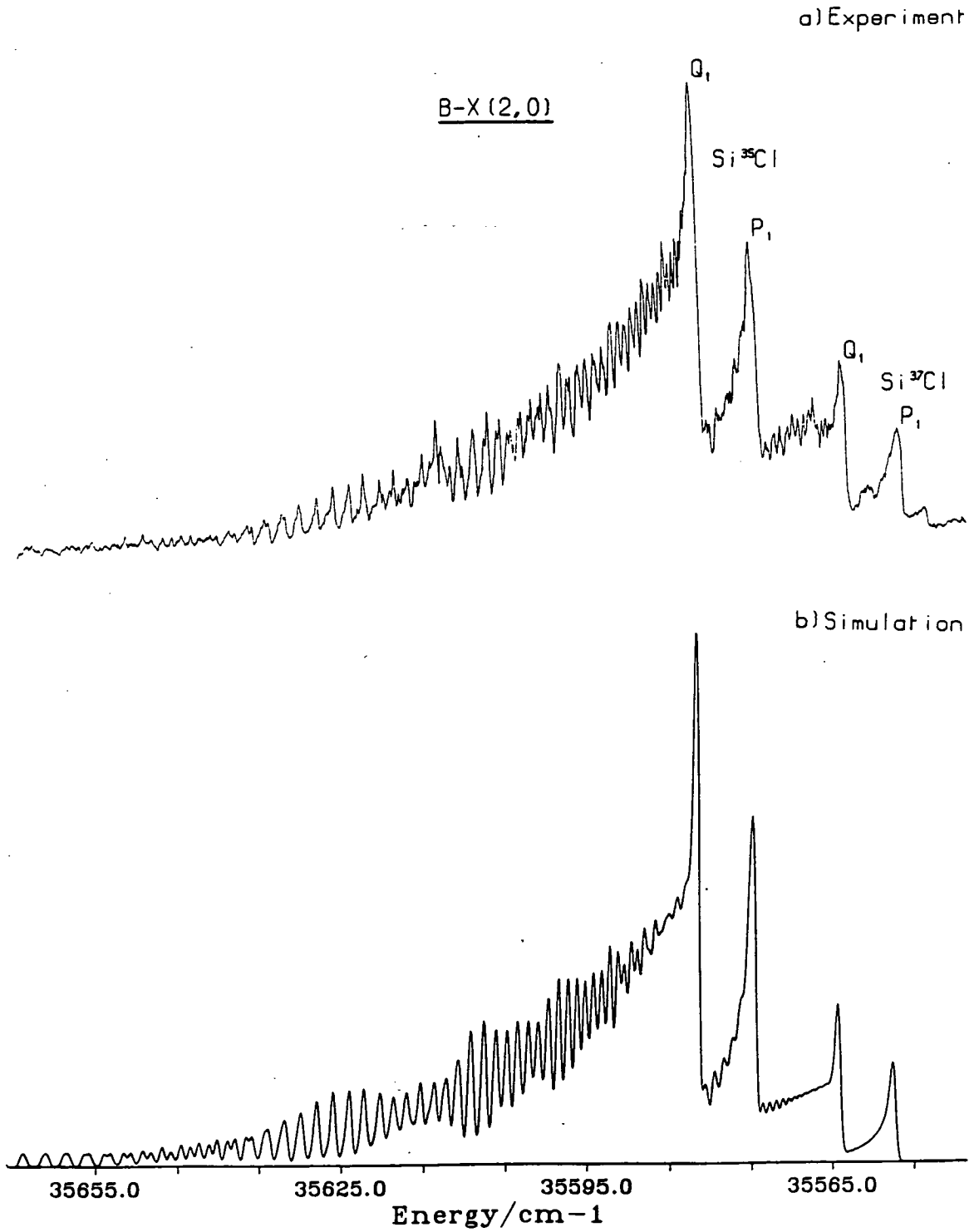

For the B-X (3,0) and B′-X (1,0) bands, spectral overlap occurs between the $B^2\Sigma^+ - X^2\Pi_{3/2}$ transition and the $B'^2\Delta_{3/2} - X^2\Pi_{1/2}$ transition, as is evident in Figure 3.8. It is again possible to temporally discriminate between fluorescence from molecules initially prepared in the B and B′ states, as explained above. If this procedure is carried out such that B′ emission is favoured, with a delay of 150 ns between excitation and observation, Figure 3.9 is obtained. Due to the relatively poor FCF for this transition the s/n ratio is rather poor. For the spectroscopically isolated transition from the $^2\Pi_{1/2}$ component of the ground state to B v′= 3, Figure 3.10 is obtained. In Figure 3.10 assignment could be made to the $^{30}Si^{35}Cl$ isotopomer (^{30}Si is 3% natural abundance of Si). The assignment to this isotopomer was based on the well known relationships between the variation of the reduced mass and the spectroscopic constants [45]. In fact there would also be contributions to the observed spectrum from other isotopomers, these are $^{29}Si^{35}Cl$, $^{30}Si^{37}Cl$ and $^{30}Si^{37}Cl$ and $^{30}Si^{35}Cl$. These species were thought to cause the 'anomalous' rotational contour observed for many of the $^{28}Si^{37}Cl$ B-X bands.

A rotational analysis of the excitation scans is precluded because of the limited experimental resolution. However an analysis of the vibrational term values of the B state was made, see Table 3.3.

FIGURE 3.8: Excitation scan showing isotopic separation between $^{28}Si^{35}Cl$ and $^{28}Si^{37}Cl$ for the overlap region of the F_2 $\Omega = {}^3/2$ component of the (3,0) band of the $B^2\Sigma^+-X^2\ \pi_r$ system and the F_1 $\Omega = {}^1/2$ ($^2\Pi$), component of the (0,0) band of the $B'^2\Delta-X^2\ \Pi_r$ system. The simulation assumed a bandwidth of 0.5 cm^{-1}, T = 302 K.

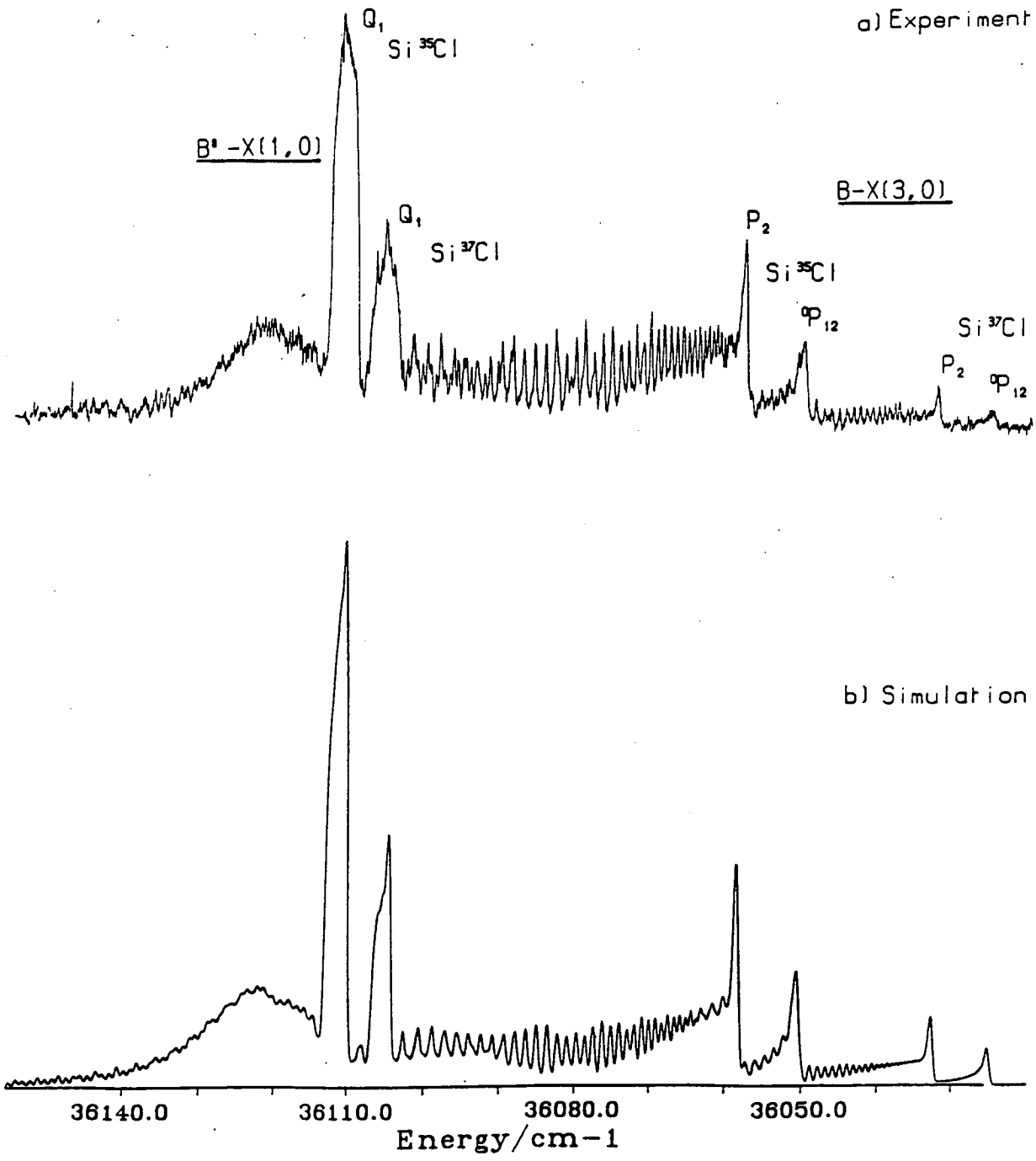

FIGURE 3.9: Excitation scan with a delay between excitation and detection of 100 ns taken over the same region as Figure 3.8. The simulation assumed a laser bandwidth of 0.6 cm^{-1}, T = 302 K.

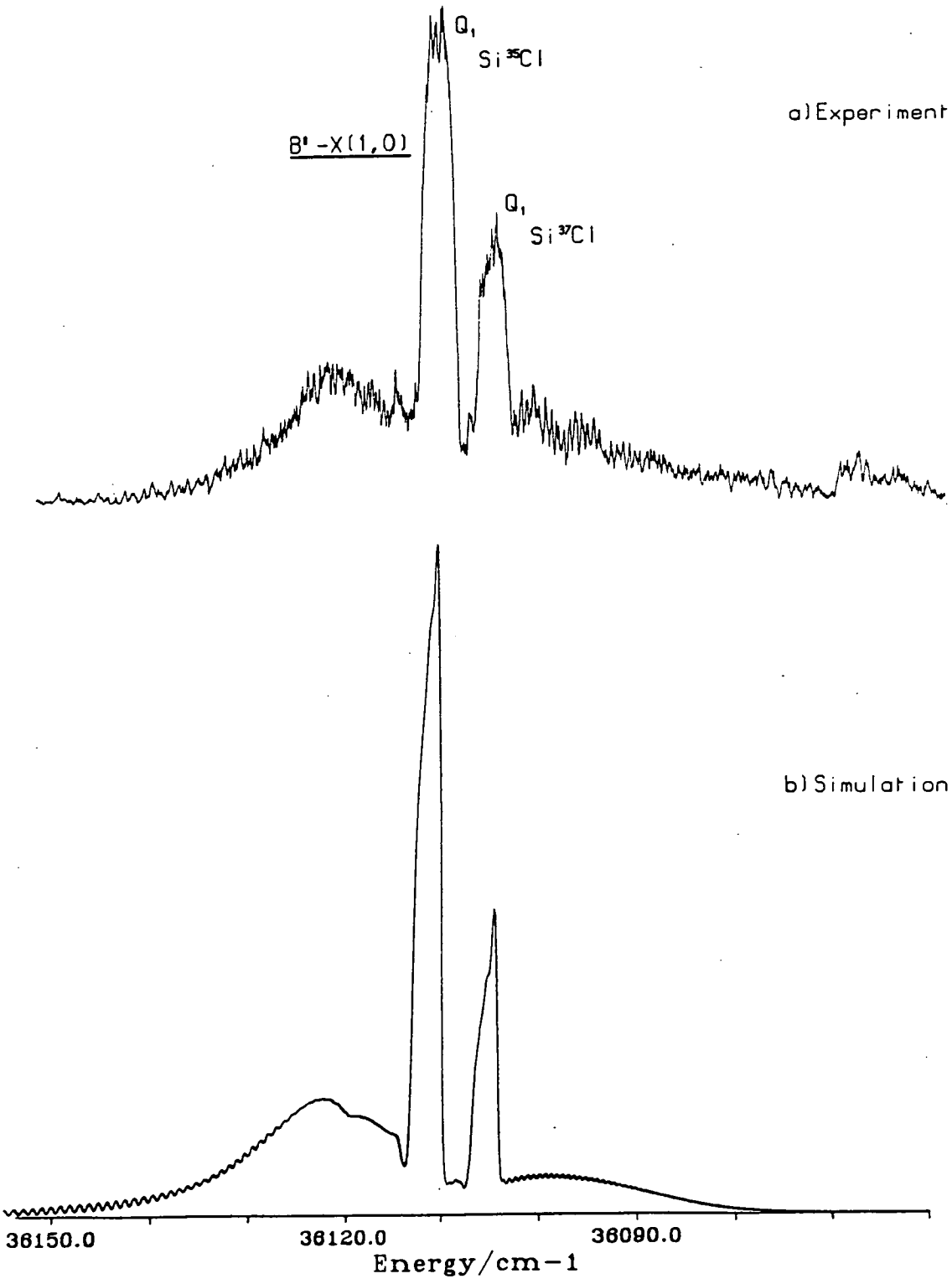

FIGURE 3.10: Excitation scan for the $F_1\ ^2\Pi_{1/2}$ component of the (3,0) band of the $B^2\Sigma^+ - X^2\Pi_r$ system. The Q_1 head of the isotopic combination $^{30}Si^{35}Cl$ is shown, 3% natural abundance. The simulation assumed a laser bandwidth of 0.5 cm^{-1}, T = 302 K.

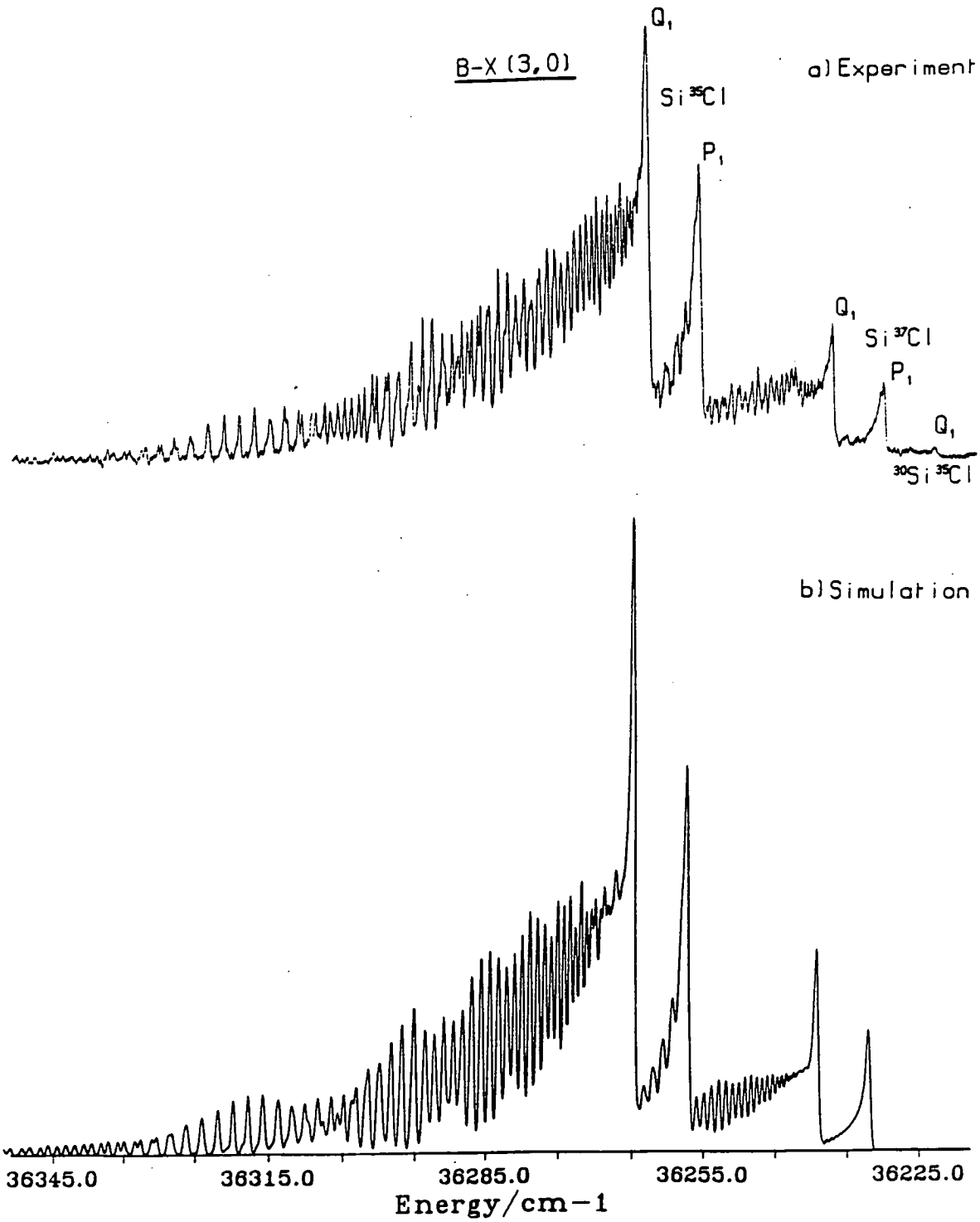

TABLE 3.3: Vibrational term values of the $B^2\Sigma^+$ state for the $^{28}Si^{35}Cl$ and $^{28}Si^{37}Cl$ isotopomers. All values are in cm^{-1}. Values in parentheses represent the uncertainties quoted at the 2σ level and should be applied to the last significant figures.

	Vibrational Constant	
Isotopomer	ω_e/cm^{-1}	$\omega_e X_e/cm^{-1}$
$^{28}Si^{35}Cl$	706.91(72)	3.91(18)
$^{28}Si^{37}Cl$	698.74(78)	4.04(22)

These results present a favourable comparison to previous values [30]. For the Δ state a direct comparison was made to the previously reported band head positions [27], see Table 3.4.

TABLE 3.4: Comparison of band head positions for the (0,0) band of the $B'^2\Delta - X^2\Pi$ transition for $^{28}Si^{35}Cl$. Values are quoted for λ_{air} to allow direct comparison to reference [27].

Band Head	Wavelength/$_{nm}$	Ref [27] Wavelength/$_{nm}$
Q_1	280.705	280.709
$^PQ_{12}$	282.342	282.348
P_2	282.336	282.336
Q_2	282.283	282.293

3.5 Fluorescence Spectra: Collisionless Emission

All fluorescence spectra from which vibronic information was deduced were obtained under essentially identical experimental conditions. The monochromator was operated with a resolution of approximately 0.25 nm (28 cm^{-1} at 300 nm) and the spectra were obtained with the standard gas flow conditions outlined in section 3.3. Any systematic variations of these conditions were noted to change only the absolute signal intensities but not the relative intensities or positions of any of the bands. Spectra were normally obtained following excitation to the Q_1 head of the relevant B-X or B′-X transition. However, excitation to an alternative head or indeed from the other spin orbit component of the ground state showed no noticeable differences, except when spectral overlap was present.

All fluorescence spectra in this and subsequent sections were obtained by expanding the laser beam into the flow reactor to yield a typical power density of approximately 500 μJcm^{-2}.

As has been observed in Figures 3.4 and 3.6 the (0,0) and (1,1) bands of the B′-X transition completely overlap the (2,0) band of the B-X transition. To remove contributing B′ state fluorescence from the B state emission, the P_1 head was pumped and the input impedence of the signal averager adjusted to match that of the PMT (50 Ω). In this configuration, the first 10 ns of the emission could be selected for averaging such that B′ state emission would be strongly discriminated against.

Since the experimental spectra could not be obtained in a digitised form, the simulated spectra, used for comparison purposes, were obtained by applying the correction for the instrumental response function and experimental variations such as laser power to them. The experimental variations were assumed to follow a linear function, between intensity calibrations taken at the start and finish of each spectrum. A measure of the short term fluctuations of the system

was obtained by running identical 1 nm scans immediately after each other. Typically differences of between 2 and 3% were evident. The assumption of monotonic variation was based on several series of spectra taken at regular time intervals. Although the assumption was somewhat arbitrary the drift did approximately follow this behaviour. When fully thermally equilibrated the drift between calibrations was on average near 5% and was similar to that reported in Chapter 2 for the laser stability.

The monochromator and photomultiplier tube formed the experimental basis for fluorescence separation and selection. The bandpass efficiency of light through a monochromator with a fixed slit is proportional to ν^2. Also, the photomultiplier, as used in this thesis, is a device which measures the energy and number of photons emitted by the radiant source. Hence, its current output per photon detected is linearly proportional to the frequency of the incident photon. However, the quantum efficiency for detection of a photon by a PMT varies, often quite strongly with ν, as will for example, the monochromator grating reflectivity. If the various factors such as PMT quantum efficiency and grating reflectivity are gathered together and summarised by an instrumental response function R (ν), the experimental spectrum S_{exp} (ν) is then a convolution given by:

$$S_{exp} (\nu) = R (\nu) A. \nu^3 . \qquad (7)$$

A is the rate of spontaneous emission of photons as a result of a transition between two rovibronic states, see section 3.5.2. R (ν) was obtained by using a calibrated, near black body, light source as described in Chapter 2. The function R (ν) was approximated by a polynomial function which was then applied to 'correct' the simulation to allow comparison with experiment. The polynomial approximation to R (ν) fitted to better than 5% across the whole range of the fluorescence collection region, that is, approximately 270 to 335 nm. It should therefore be carefully noted that the fluorescence spectra

and simulations presented in this thesis have units of energy per unit wavelength interval. Thus, unless otherwise stated, the intensity of a spectral simulation, S_{sim}, is given by:

$$S_{sim}(\nu) = R(\nu) .A.\nu^3 \qquad (8)$$

Fluorescence spectra for the B-X transition following excitation to B v' = 0,1,2 and 3 are shown in Figures 3.11 to 3.14. All spectra were obtained by pumping from v" = 0 of the $\Pi_{1/2}$ component of the ground state with the fluorescence being collected only to the red of this band. The ground state component used to excite to the B state was marked in all spectra with the word 'laser'. The 'doubling' of each band in Figures 3.11 to 3.14 is due to fluorescence from the excited B state level back to the $^2\Pi_{1/2}$ and the spin orbit excited $^2\Pi_{3/2}$ components of the ground state. Each spectrum is presented with a simulation, the simulation procedure being discussed in section 3.5.2.

There was no evidence of any vibrational relaxation in any of Figures 3.11 to 3.14. This observation is consistent with the radiative lifetime of the B state (10 ns) and the pressure at which these spectra were obtained (1 Torr) (see Appendix II); which indicates that on average a radical in the B state will undergo 0.11 gas phase collisions before emitting.

3.5.1 Vibrational Term Values

Using the positions of the bands measured in Figures 3.11 - 3.14, with the monochromator calibrated against the dye laser wavelength, ground state vibrational term values were extracted. The vibrational progressions were followed to slightly higher v" than previous studies: up to v" = 10 compared to v" = 7 in ref. [30].

FIGURE 3.11: Fluorescence spectrum of v'=0 of the $B^2\Sigma^+$ state. Excitation occurs from v"=0 at the Q_1 head of the B-X transition, which is marked on the figure by the word 'Laser'. Fluorescence is collected to the red of this band. The spectrum was collected at a total reactor pressure of ~ 1.1 Torr. Both the spectrum and the simulation contain information on the detection system response with wavelength.

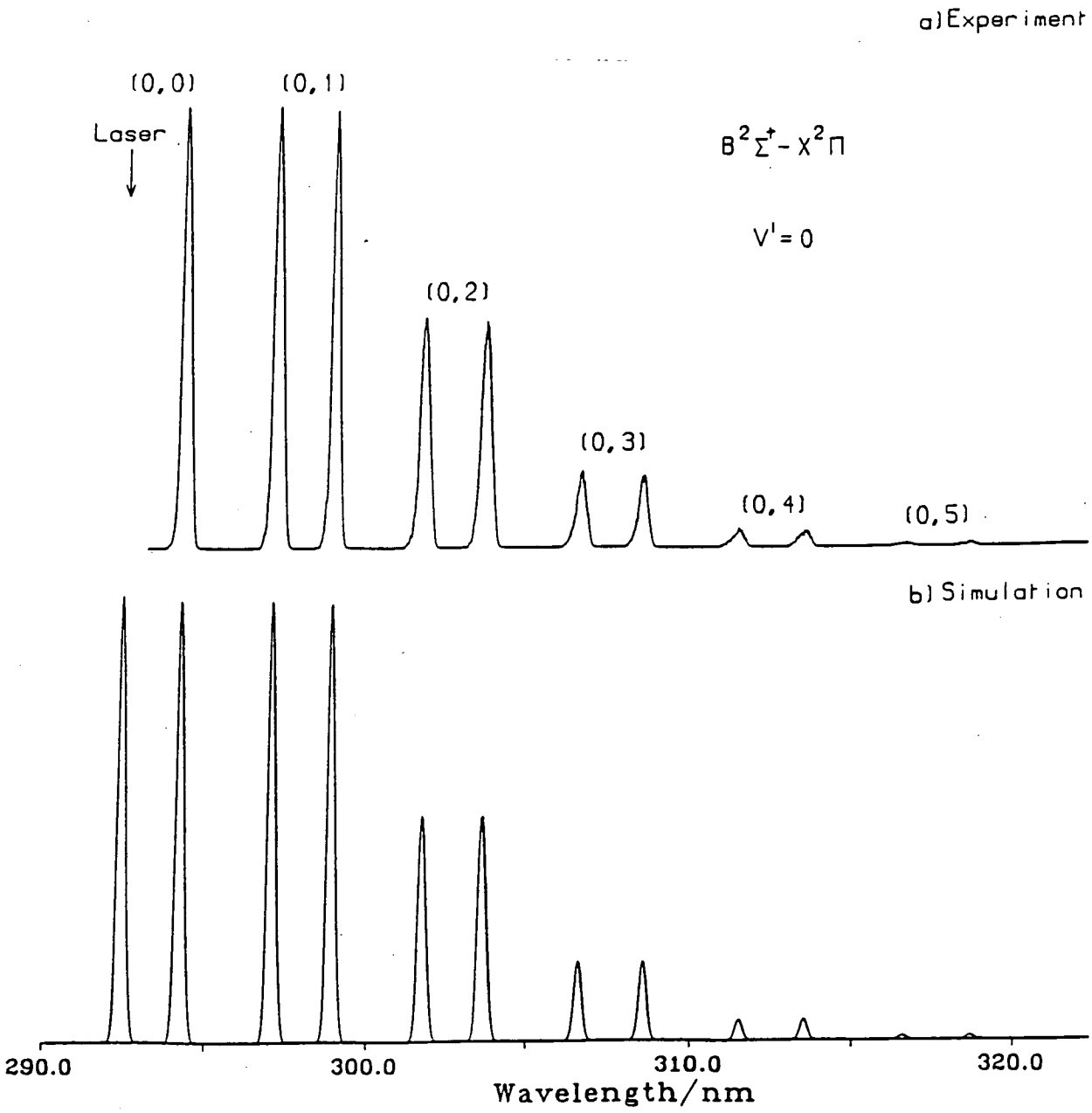

FIGURE 3.12: Fluorescence spectrum of v′=1 of the $B^2\Sigma^+$ state. Conditions were similar to those given in Figure 3.11.

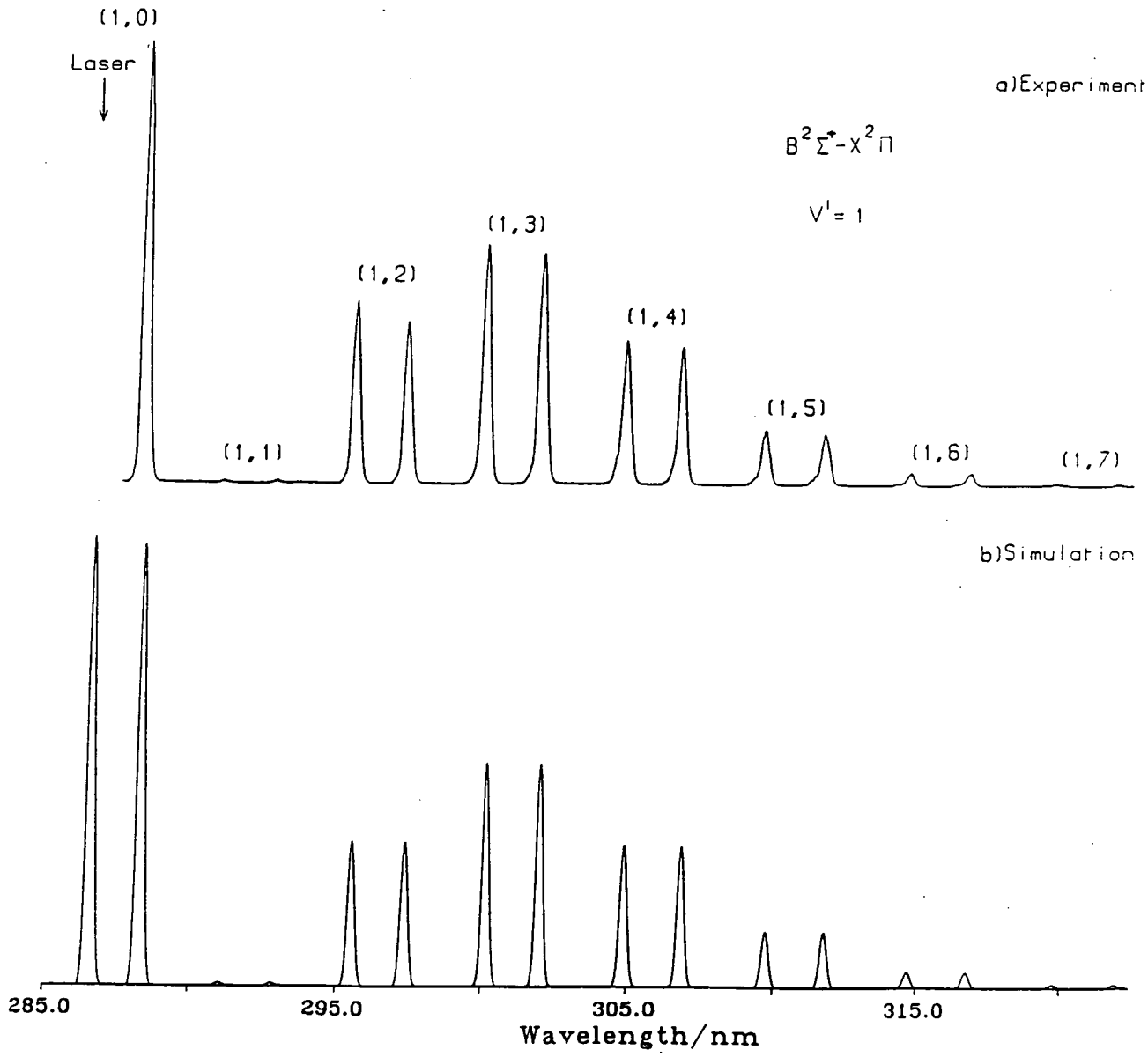

FIGURE 3.13: Fluorescence spectrum of v′=2 of the $B^2\Sigma^+$ state. Conditions are similar to those given in Figure 3.11 except excitation was at the P_1 head of the B-X transition and only the first 10 ns of the emission was collected.

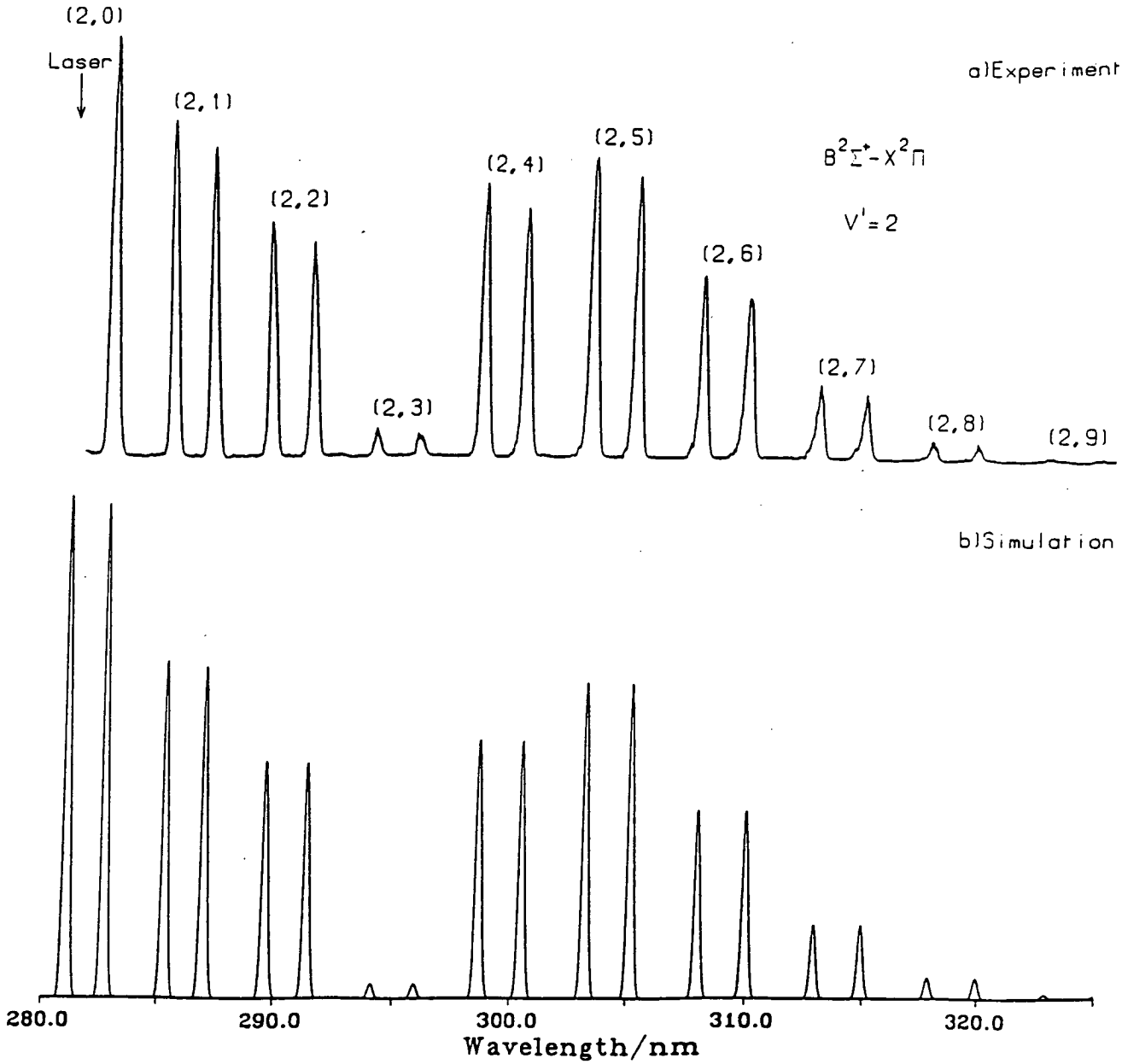

FIGURE 3.14: Fluorescence spectrum of $v'=3$ of the $B^2\Sigma^+$ state. Conditions were similar to those given in Figure 3.11.

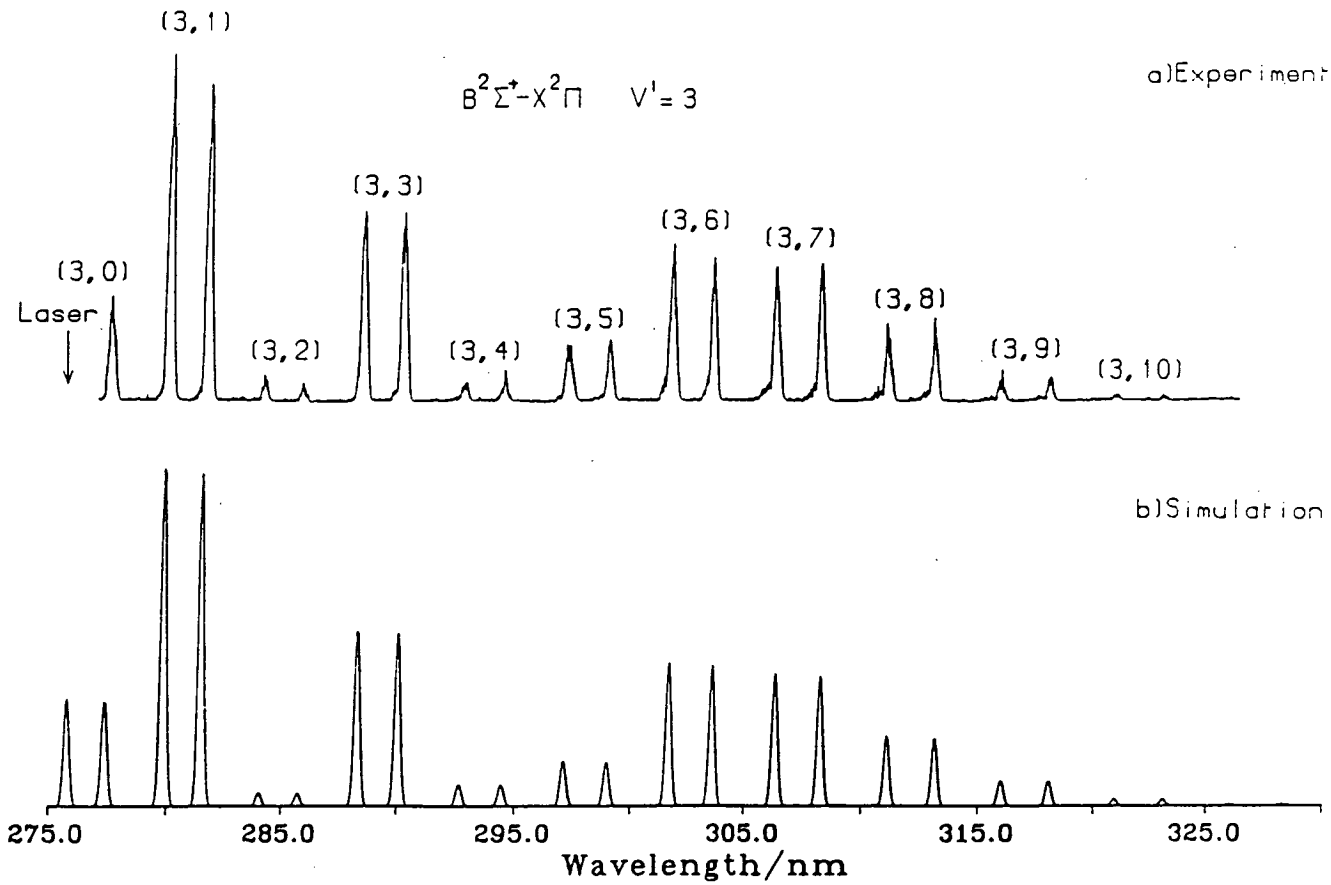

The precision of measurement ~ $5cm^{-1}$, was however significantly poorer than in ref [30]. The vibrational band frequencies were taken as the mid-point between the resolved spin-orbit peaks. To obtain the vibrational constants from the vibrational term expression, G(v):

$$G(v) = \omega_e (v + 1/2) - \omega_e X_e (v + 1/2)^2 \qquad (9)$$

a plot of [G(v")-G(v"=0)]/v" versus v" was constructed. The plot has a slope of $-\omega_e X_e$ and an intercept of $\omega_e - \omega_e X_e$. A straight line was fitted to the points in a least squares manner and yielded the spectroscopic constants shown in Table 3.5.

TABLE 3.5: Vibrational constants for $Si^{35}Cl$ $X^2\Pi$. All values are in cm^{-1}. Values shown in parentheses are the uncertainties quoted at the 2σ level and should be applied to the last significant figures.

Vibrational Constant	Value/cm^{-1}	Values from ref [30]/cm^{-1}
ω_e	535.7(1.4)	535.482(196)
$\omega_e X_e$	2.2(0.3)	2.159(62)
$\omega_e Y_e$	-	0.0054(54)

The reduced Chi-squared (χ^2/ν) from 27 data points was, $\chi^2/\nu = 0.52$.

The reduced Chi-squared effectively defines the quality of the fit of an approximating function to the actual data values. A value near 1 indicates a good fit.

When the data were fitted by a polynomial of degree 3 the value of χ^2/ν was significantly poorer. Hence, up to v" = 10 a quadratic expansion reproduced the vibrational levels more satisfactorily.

3.5.2 Simulation of Fluorescence Spectra

The Einstein coefficient for spontaneous emission, $A_{v'J'v''J''}$, characterises the rate of spontaneous emission of photons as a result of a transition between two rovibronic states [45]:

$$A_{v'J'v''J''} = (64\pi^4/3h)\,[S_{J'J''}/(2J'+1)]\,\nu^3\,[\int \psi_{v'}\, R_e(r)\, \psi_{v''}\, dr^2] \,, \qquad (10)$$

where ψ_v is the vibrational wavefunction characterising the vibrational state v

$S_{J',J''}$ is the rotational linestrength factor given by the Honl-London formulae [45].

The function $R_e(r)$ is called the electronic transition moment and is given by:

$$R_e(r) = \int \psi^{*\prime}_e\,(q_e,r)\, M_e\,(q_e,r)\, \psi''_e\,(q_e,r)\, dq_e \qquad (11)$$

ψ'_e, ψ''_e are respectively the upper and lower state electronic wavefunctions

q_e designates the electronic coordinates

M_e is that part of the electronic transition dipole moment that depends only on the coordinates of the electrons.

With the experimental resolution normally utilised for measurements of vibrational band intensities it is customary to neglect rotational effects (sum over all lines of the band). This leads to:

$$A_{v'v''} = (64\pi^4/3h)\,\nu^3[\int \psi_{v'}\, R_e(r)\, \psi_{v''} dr]^2. \qquad (12)$$

Under this assumption, it is possible to define the vibrational transition probability $p_{v',v''}$ as:

$$p_{v',v''} = (\int \psi_{v'}, R_e(r)\ \psi_{v''}\ dr)^2 \qquad (13)$$

In certain circumstances the values of $p_{v',v''}$ can be related to the well-known Franck-Condon factors, $q_{v',v''}$. If $R_e(r)$ is a slowly varying function of r then $R_e(r)$ may be replaced by an average or effective value R_e and it may be taken outside the integral to yield:

$$A_{v',v''} = (64\pi^4/3h)\ \nu^3\ \bar{R}^2_e\ (\int \psi_{v'}, \psi_{v''}\ dr)^2 \qquad (14)$$

The square of the vibrational overlap integral, the Franck-Condon factor is:

$$q_{v',v''} = (\int \psi_{v'}, \psi_{v''}\ dr)2 \qquad (15)$$

This procedure is exact if R_e is constant or a linear function of r.

Given an adequately characterised potential (see section 3.2.2), then vibrational wavefunctions appropriate to the potential are found by solving the radial Schrödinger equation [50]:

$$\left\{ \frac{\delta^2 \psi_{vJ}}{\delta r^2} \right\} + [E_{vJ} - U_{(r,J)}]\psi_{vJ} = 0, \qquad (16)$$

where E_{vJ} is the eigenvalue for the wavefunction ψ_{vJ};

$U_{(r,J)}$ is the effective potential and hence includes any rotational contribution.

The program used to solve equation (16) and to evaluate equation (12) was written by Lawley and Wheeler [56]. It is not

necessary to give an account, in this thesis, of the mathematics required to evaluate these equations as this has been dealt with adequately by the above authors.

The program required as input, in the form of evenly spaced points, the upper and lower state curves and the approximation to the electronic transition dipole moment. It is obvious that if the vibrational transition probabilities predicted by the program are to be meaningful it is necessary that the potentials used to represent the electronic states be accurate. The input potentials were those derived by the RKR method in section 3.2.2. It was possible to test the input potentials by comparing the term values and turning points calculated by the simulation program with those derived from the spectroscopic constants of the isotopomer ($Si^{37}Cl$). The test was based on the assumption, which is normally valid for heavy diatomics such as SiCl, that the Born-Oppenheimer approximation [57] is valid. The term values, $< 1/r^2 >$ value and the turning points were all found to agree closely with the values obtained from the B and X state spectroscopic constants [30] of the $Si^{37}Cl$ isotopomer.

3.5.3 Transition Probabilities from the B-X Fluorescence Spectra

The measured vibrational transition probabilities for $v' = 0$-3 of the B-X system are listed in Tables 3.6 - 3.9 respectively. These values are of interest because they can be used to directly relate signal strength to population measurements. The relative $A_{v'v''}$ values were obtained from the intensities of the individual bands (see note 1), this included making the correction for the response of the equipment. The $p_{v'v''}$ values were obtained from the $A_{v'v''}$ by realising that:

$$p_{v'v''} \propto A_{v'v''}/\nu_{v'v''}^{3} \qquad (17)$$

The frequency of each band was taken as being the same as that used in determining the vibrational term values in section 3.5.1.

TABLE 3.6: Vibrational transition probabilities ($p_{v'v''}$), Franck-Condon factors ($q_{v'v''}$) and uncertainties for $v' = 0$ of the B-X system. (Entries in the table are actual values multiplied by 1000).

$v' = 0$					
v''	$p_{v'v''}$ expt	$q_{v'v''}$	$p_{v'v''}$ calc	$\delta p_{v'v''}$	$\Delta p_{v'v''}$
0	335	336	335	9	15
1	364	361	361	9	15
2	205	200	201	6	9
3	72	76	76	4	5
4	19	22	22	2	2
5	4	5	5	2	2

TABLE 3.7: Values of $p_{v'v''}$, $q_{v'v''}$ and uncertainties for $v' = 1$ of the B-X system. (Entries in the table are actual values multiplied by 1000).

$v' = 1$					
v''	$p_{v'v''}$ expt	$q_{v'v''}$	$p_{v'v''}$ calc	$\delta p_{v'v''}$	$\Delta p_{v'v''}$
0	350	366	364	9	17
1	3	3	3	2	2
2	165	141	142	5	8
4	242	236	237	8	13
4	157	160	159	6	9
5	64	68	69	5	6
6	17	21	21	3	3
7	3	5	5	3	3

TABLE 3.8: Values of $p_{v'v''}$, $q_{v'v''}$ and uncertainties for $v' = 2$ of the B-X system. (Entries in the table are actual values multiplied by 1000).

$v' = 2$					
v''	$p_{v'v''}$ expt	$q_{v'v''}$	$p_{v'v''}$ calc	$\delta p_{v'v''}$	$\Delta p_{v'v''}$
0	180	202	198	7	10
1	164	149	148	5	8
2	121	116	115	3	5
3	15	8	8	1	1
4	164	146	146	4	7
3	187	190	191	6	9
6	111	120	122	4	6
7	45	50	51	2	3
8	11	15	15	2	2
9	3	4	4	2	2

TABLE 3.9: Values of $p_{v'v''}$, $q_{v'v''}$ and uncertainties for $v' = 3$ of the B-X system. (Entries in the table are actual values multiplied by 1000).

$v' = 3$					
v''	$p_{v'v''}$ expt	$q_{v'v''}$	$p_{v'v''}$ calc	$\delta p_{v'v''}$	$\Delta p_{v'v''}$
0	65	73	72	4	5
1	231	249	246	7	14
2	16	11	10	2	2
3	161	157	157	6	10
4	21	21	21	2	2
5	58	46	46	4	5
6	161	158	160	6	10
7	162	155	156	7	11
8	89	87	88	5	7
9	29	34	34	4	4
10	7	10	10	3	3

Each table contains entries for the measured values of $p_{v'v''}$ (column 2 in the tables), for $q_{v'v''}$, and for $p_{v'v''}$ calc, the value of $p_{v'v''}$ calculated by the simulation procedure described above. Also included in each table are estimates of the uncertainty associated with each transition $\delta p_{v'v''}$ and $\Delta p_{v'v''}$. The sums of the values of $p_{v'v''}$ and $q_{v'v''}$ entered in the table have all been normalised to 1000.

The term $\delta p_{v'v''}$, is an estimate of the uncertainty of the intensity of a particular (v',v") transition and arises from the instrumental response and the statistical error in measuring the value for each (v',v"). Several runs, never less than 3, were made for each spectrum, from which mean values of intensity and statistical error were obtained for each (v',v"). The value $\Delta p_{v'v''}$ represents the total error arising

from the $\delta p_{v'v''}$ for each v' plus (added in quadrature) the individual value for each $\delta p_{v'v''}$. The term $\Delta p_{v'v''}$ is that pertinent to the calculation of population fractions.

It may be seen from Tables 3.6 - 3.9 that the values of $p_{v'v''}$ and $q_{v'v''}$ agree very closely. The reason for the agreement follows from the fact that the transition dipole moment function was almost flat across the range of r sampled by the fluorescence (1.85 - 2.13 Å, see section 3.5.4). Similarly, the good agreement between $p_{v'v''}$ and $p_{v'v''}$ calc. indicates that both the wavefunctions and the potentials used for the B and X states are a good description of reality. Hence, it may be asserted that the B-X transition of SiCl is reasonably well understood in terms of both spectral line positions and intensities for the range of r bounded by $1.85 < r < 2.13$ Å.

The limited number of $q_{v'v''}$ and $p_{v'v''}$ values calculated by Singh and Dube [43] follow similar trends to those reported here, especially for $v' = 0$ of the B state. However, their estimation of the transition dipole moment function as:

$$R_e(r) = 1 - 0.3856r/A \qquad (18)$$

where r ranged between 1.9 and 2.1 Å is outwith the experimental uncertainty of the dipole moment function measured below. The differences must presumably therefore arise from the approximate methods used by these authors to generate both the Franck-Condon factors and r-centroid for each (v',v") band.

3.5.4 Estimation of the transition dipole moment for the B-X system

If the combining B and X state potentials are well characterised and a reliable estimate of the instrumental response function is known, then the remaining variation of successive spectral peaks in the lower state vibrational progression, of intensity I_n, will depend only

on the strength of the transition dipole moment function at the positions at which fluorescence occurs. This function is of interest since it reveals information on the nature of the electronic wavefunctions for both states.

A preliminary estimate of the transition dipole moment function $R_e(r)_{ref} = 1.0$ was made. Calculation of the actual dipole moment function then follows by defining the ratio between the observed, I_n^{obs}, and the simulated I_n^{sim}, spectral intensities:

$$\frac{I_n^{obs}}{I_n^{sim}} = \frac{R_e(r)^2}{R_e(r)^2_{ref}} \tag{19}$$

The values of r corresponding to the fluorescence maxima, I_n, were obtained from the simulation program. The ratios were then fitted by a least mean squares procedure with the best fit being obtained for a linear function:

$$R_e(r) : 1.0 - 0.05r/A, \tag{20}$$

$$\chi^2/\nu = 0.51 \text{ for 33 data points,}$$

r ranged between 1.85 and 2.13 Å.

Equation (20) was then used directly in determining the values of $p_{v'v''}$ calc. Equation (20) is a very slowly varying function of r and in fact when a function, $R_e(r) = 1.0$ was used, the measured $p_{v'v''}$ values fitted almost equally well, within the uncertainties of the measurements.

For the case of an ideal experiment with an unbiased instrumental response at all frequencies, the B-X fluorescence spectra would appear as those given in Figure 3.15.

FIGURE 3.15: Simulation of dispersed fluorescence spectra for the $B^2\Sigma^+ - X^2\Pi$ system with v′=0-3. Spectra are those that would be obtained for an ideal monochromator/pmt detection system which had no variation in detector response with wavelength.

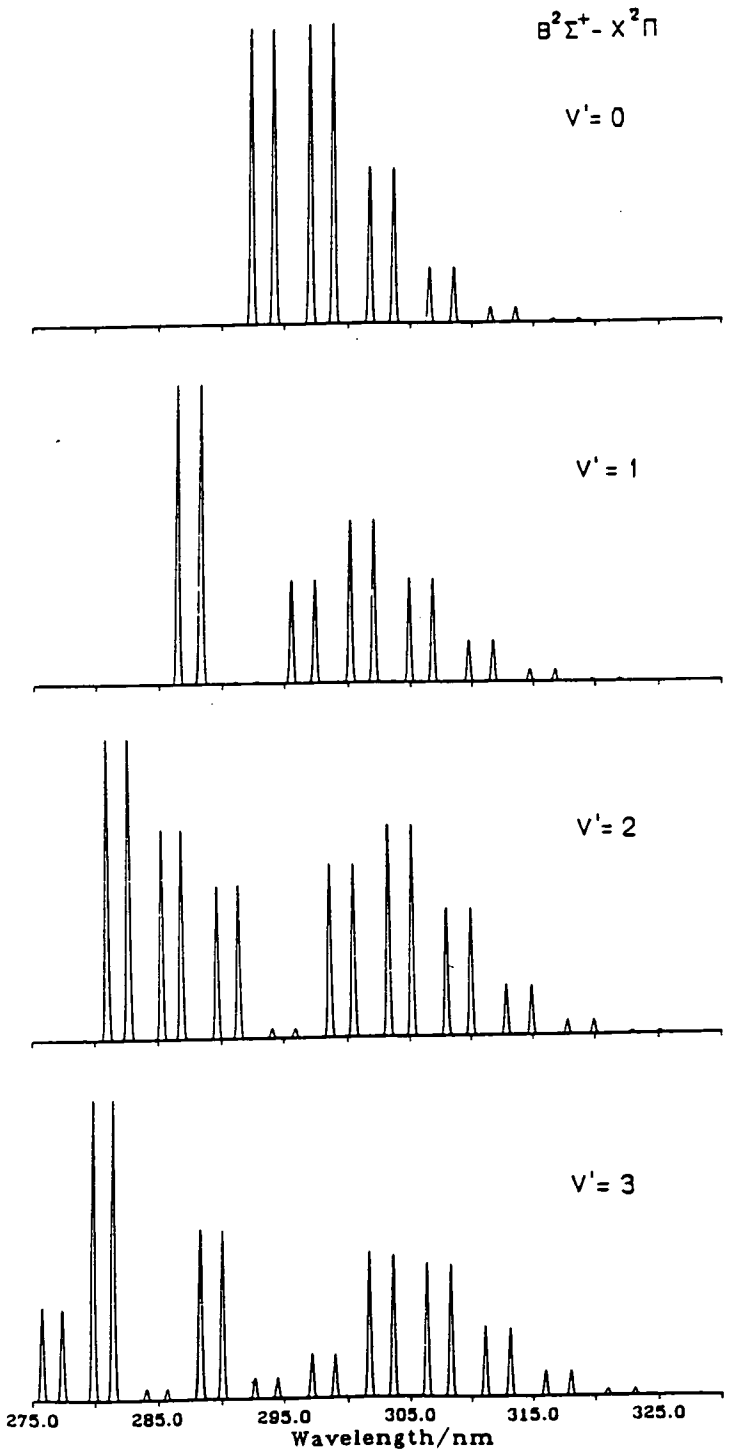

3.5.5 Transition probabilities for the B′-X bands

In principle, a similar procedure to that described in section 3.5.3 for the B-X bands could be applied to the B′-X bands. However, as a consequence of the relatively long radiative lifetime of the B′ state collisional energy transfer to various B state levels was always observable. The B state fluorescence then often overlapped the B′ state fluorescence. [A typical example of this process is shown in Figure 3.21 (section 3.7), where following excitation to v′ = 1 of the B′ state collisional transfer by Ar occurs to various B state levels.]

Because of the possibilities of overlapped bands within fluorescence spectra [such as Figure 3.21], it was difficult to reliably measure vibrational transition probabilities for the B′ v′ = 0,1 levels. However, it was possible to determine the approximate values of the $p_{v'v''}$ and the transition dipole moment for the B′-X transition.

Fluorescence on the (1,0) band of the B′-X transition is only partly overlapped by the (3,0) B-X band. Hence, by pumping from v″ = 0 of the $X^2\Pi_{3/2}$ component, population of only B′ v′ = 1 could be achieved. However, emission from the B′ state to any X state level other than v″ = 0 will be overlapped by emission from collisionally populated B state. The (1,1) band of the B′-X transition is the most intense of the v′ = 1 bands: it is also overlapped by fluorescence only from the (2,0) B-X band. Hence, the B′:B intensity ratio is greatest for this band. The method used therefore, was to extrapolate the pressure sensitive B′-X (1,0): [B′-X (1,1) + B-X (2,0)] ratio to zero pressure, where only (1,0) and (1,1) emission would be observed. Making the reasonable assumption that the RKR potentials for the B′ and X states were accurate, the transition dipole moment was then varied until the desired (1,0):(1,1) ratio was obtained.

To produce the desired ratio of the B'-X (1,0):(1,1) bands, the transition dipole moment function, when expressed as a linear function between the two points had a negative slope, with a gradient equal to 3.12Å^{-1}. The positions of the fluorescence for the (1,0) and (1,1) B'-X bands corresponded to values of 2.098 Å and 2.124 Å respectively. An uncertainty of $\pm$ 0.2 in the slope was estimated purely on the basis of its effect on changing the (1,0):(1,1) ratio.

The best fit simulations of the hypothetical collision-free fluorescence spectra for the B' v' = 0 and B' v' = 1 levels are shown in Figure 3.16. The spectra contain no correction for instrumental response. As expected from the relative positions and shapes of the potentials, the B'-X bands are very diagonal.

Using the procedure outlined above the calculated $q_{v'v''}$ and $p_{v'v''}$ are given in Table 3.10.

TABLE 3.10: Calculated Franck-Condon factors and vibrational transition probabilities for v' = 0 and 1 of the B' - X system. (Entries in the table are actual values multiplied by 1000).

	v' = 0		v' = 1	
v''	$q_{v'v''}$	$p_{v'v''}$	$q_{v'v''}$	$p_{v'v''}$
0	946	995	55	139
1	49	5	860	856
2	6	1	71	3
3	-	-	15	2

FIGURE 3.16: Predicted fluorescence spectra for the $B'^2\Delta - X^2\Pi$ system with $v' = 0,1$. The spectra are those that would be obtained in a collision free environment.

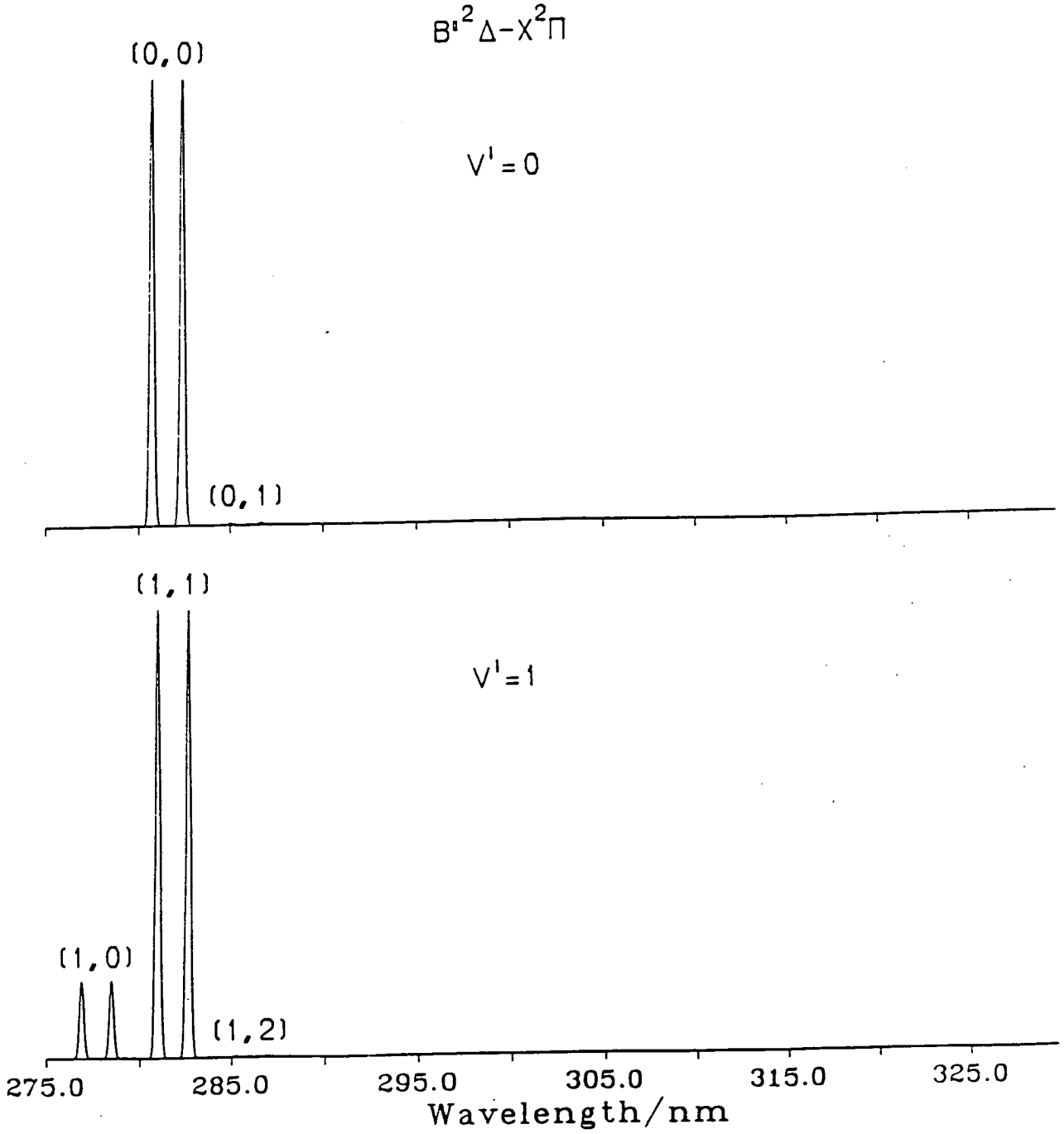

3.6 Radiative Lifetimes of the B and B′ States

As noted previously, the radiative lifetime of the B state is approximately 10 ns [37][39], while that of the B′ state is near 1.0 μs [53]. A satisfactory explanation for the difference was derived solely from the molecular orbital (wavefunction) structure of the diatomic. Such an argument should, therefore, also be consistent with the transition dipole moment functions derived in section 3.5.

The LCAO approach in Figure 3.1 assumed a minimal basis set. That is, it is assumed the molecular wavefunctions ψ_{SiCl} could be obtained from simple atomic orbitals, such that:

$$\psi_{SiCl} = C_1\Phi_{Si} + C_2\Phi_{Cl} \cdot \qquad (21)$$

C_1, C_2 are the coefficients of each atomic orbital.

Given that the ground state electronic configuration of SiCl is $(\pi)^4\ (\sigma)^2\ (\pi^*)^1$, this was constructed as follows:

$(\pi)^4$ will be mostly Cl $3p_{x,y}$, $C_2 > C_1$
$(\sigma)^2$ will be mostly Cl $3p_z$, $C_2 > C_1$
$(\pi^*)^1$ will be mostly Si $3p_{x,y}$, $C_1 > C_2$
(σ^*) will be mostly Si $3p_z$, $C_1 > C_2$.

For the B-X Rydberg transition it is safe to assume that the electron promotion occurs to an essentially pure atomic orbital [45], a silicon Rydberg orbital in this case. Thus the B-X transition essentially involves an electron jump: $(n\sigma) \longleftarrow (\pi^*)$. Both these orbitals are largely centred on the silicon atom, hence orbital overlap should be good and the radiative lifetime will be short. Also, variation of the SiCl bond length should not drastically affect orbital overlap and the transition dipole moment should be a slowly varying function of r, as was found above.

The B′-X transition essentially involves an electron jump: $\pi^* \leftarrow \sigma$. This transition involves the transfer of an electron between the silicon and chlorine atoms. It is expected therefore that overlap will be poor and the radiative lifetime will be relatively long. As the SiCl bond length decreases the overlap should substantially increase. Hence, the transition dipole moment function should be a rapidly increasing function with decreasing r, again as was found above.

3.7 Energy Transfer in the B′ and B States

The interaction of a species in a specific excited state with a collision partner will produce a definite range of collisionally populated states. This distribution of states, known as the product state distribution, is characteristic of the collision partner. As the amount of collision partner present is varied, there is a change in the ratio of the emission from the initially excited state to the final product state, which is known as the branching ratio.

Energy transfer studies were feasible for both the excited states of interest. However, there was a crucial experimental difference between the B′ and B states, that is their respective lifetimes were of the order of 100:1. Hence, on average, see Appendix II, at a pressure of 1 Torr a radical in the B′ state would make ~ 11 collisions during its radiative lifetime (~ 1μs), while a radical in the B state would make only 0.11. It should be noted therefore that while LIF studies (at these pressures) of the B state will appear almost collisionless, those of the B′ state will always appear to be 'contaminated' by emission from levels populated by energy transfer processes.

Within this section the B′ state was almost invariably populated by pumping the Q_1 head of either the $v' = 0$ or 1 levels, while for the B state either the P_1 or Q_1 heads could equally be used.

The fluorescence emission was collected as a function of wavelength, by scanning the monochromator, with the collection conditions being identical to those outlined in section 3.5. The signal averager was normally operated with an input impedance of 1 MΩ and a long detector gate (~ 15μs). Hence measurements were made of the integrated intensity of emission of both the B and B′ states (because of its short radiative lifetime measurement of B state emission represents, to a good approximation, the fraction of the B′ state population transferred to the B state).

For v′ = 0,1 of the B′ state extensive energy transfer studies were carried out for He, Ar, H_2, N_2, CO_2, CF_4 and CH_4. Initial investigations were also made for the additional gases N_2O (99.94), CF_3Cl (99.95), C_2H_6 (99.0) and C_4F_8 (99.9); the numbers in brackets represent the purities (%) of the gases. For gases such as O_2 (99.5), NH_3 (99.96), NO_2 (99.5) and CH_3Br (99.0) no LIF could be detected following excitation to the B′ state, which was believed to be due to bimolecular reactions occurring between ground state SiCl radical and the collision gas.

3.7.1 Product state distribution from initially prepared B′ state

Representative fluorescence spectra following excitation to v′ = 0 of the B′ state are shown in Figures 3.17-3.20. Each spectrum is presented with a simulation and shows the fluorescence distribution obtained from the respective gases Ar, CO_2, H_2 and and CH_4. Corresponding spectra following excitation to B′ v′ = 1 are shown in Figures 3.21-3.24. All spectra were obtained when the partial pressure in the flow reactor of the quenching gas was 1.5 Torr. On each spectrum the position of the transition that was being pumped was marked by 'laser'. Fluorescence from the B′ state and the collisionally populated B state could occur to both the $\Omega = {}^1/2$ and $\Omega = {}^3/2$ components of the ground state, hence the apparent doubling of the spectrum. Transitions to the $\Omega = {}^3/2$ component of the ground state occur to longer wavelengths, these transitions were therefore labelled in all spectra, in this section, with a '+' post-superscript.

FIGURE 3.17: Dispersed fluorescence spectrum following excitation to v′=0 of the B′ state. The pressure in the reactor was 1.5 Torr of argon. The excitation position is shown by 'laser'. Fluorescence occurs to both the spin orbit components of the $^2\Pi$ ground state, transitions terminating on the $\Pi_{3/2}$ component are marked by a '+'.

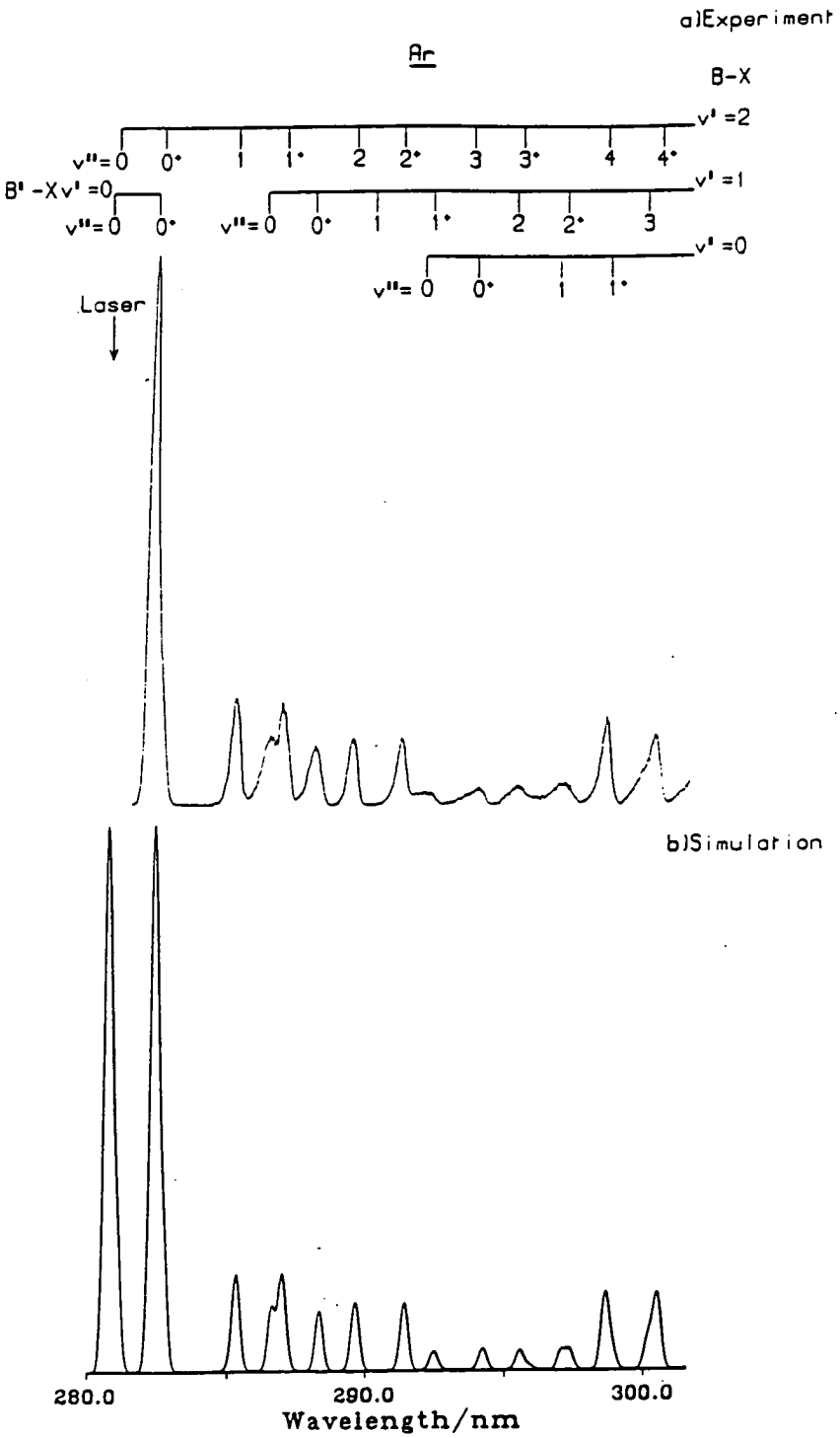

FIGURE 3.18: Fluorescence intensity distribution in the B state following excitation to v′=0 of the B′ state with CO_2 as the quenching gas. The partial pressure of CO_2 was 1.5 Torr and the total pressure in the reactor (argon carrier gas) was near 2.25 Torr. A propensity to transfer to v′=2 of the B state was observed.

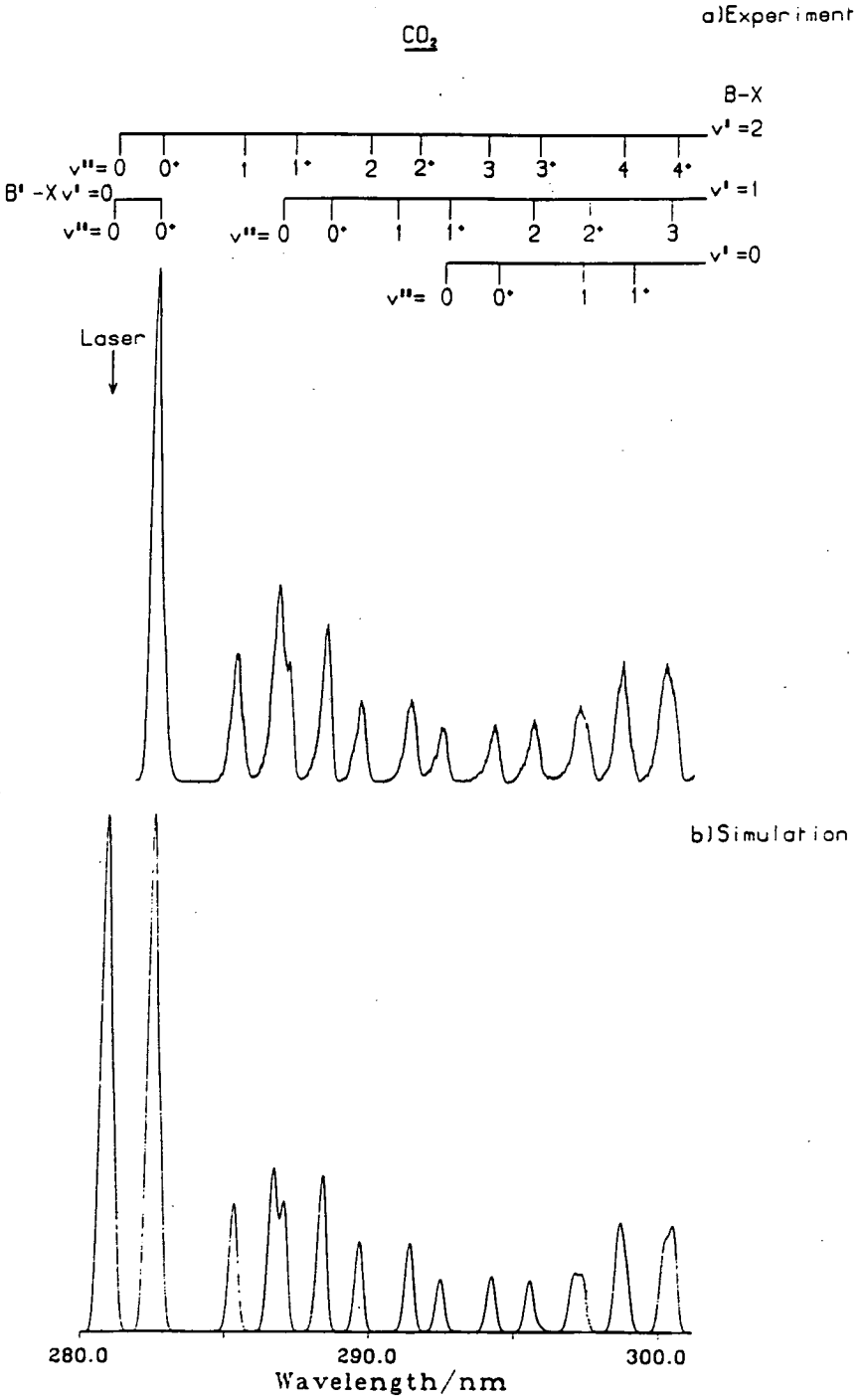

FIGURE 3.19: Fluorescence intensity distribution following excitation to v=0 of the B′ state with 1.5 Torr partial pressure of H_2 quenching gas. A strong propensity to transfer to B v′=1 was observed.

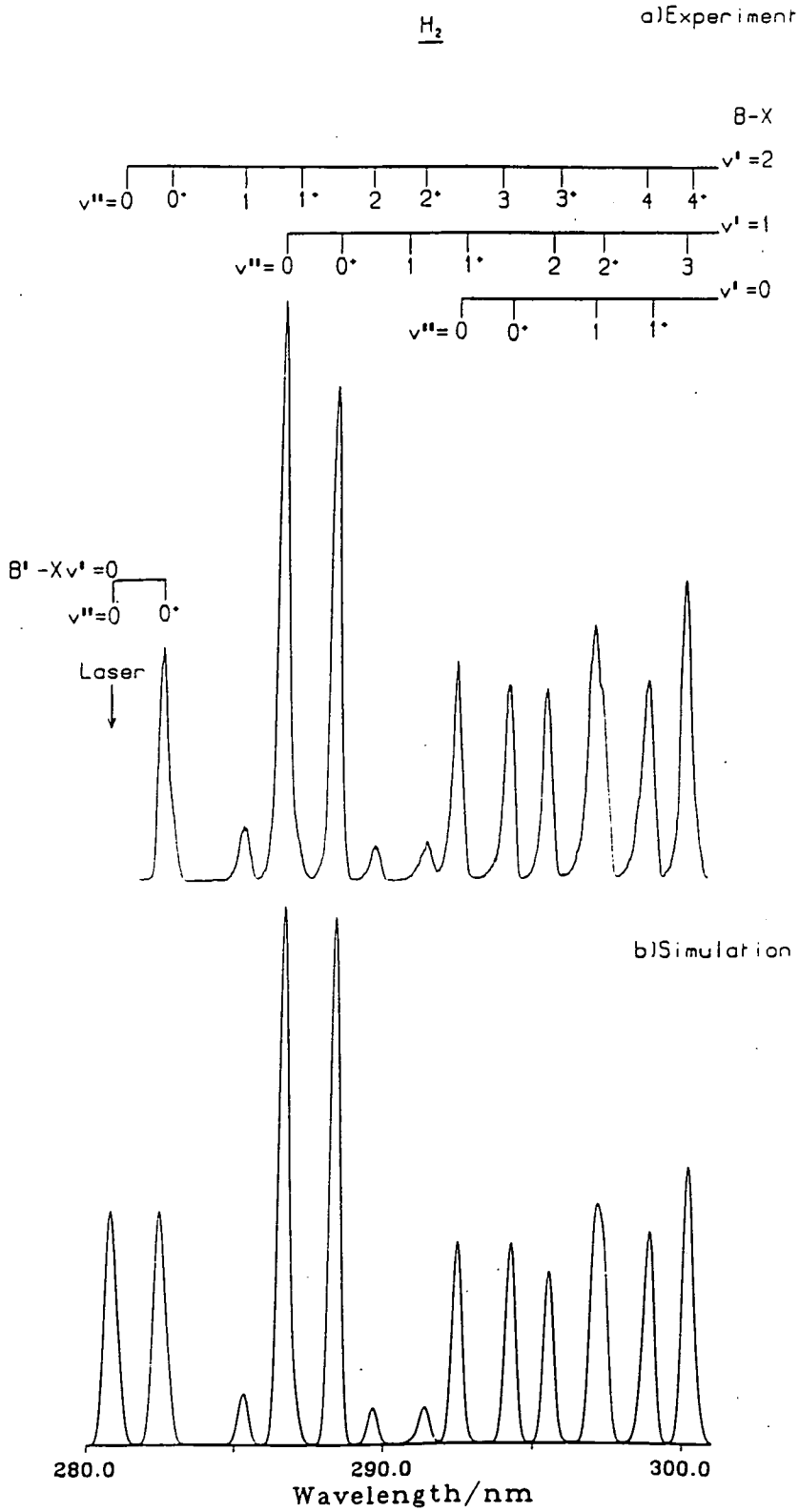

FIGURE 3.20: Fluorescence intensity distribution following excitation to v′=0 of the B′ state with 1.5 Torr partial pressure of CH_4 quenching gas. A strong propensity to transfer to B v′=0 is observed.

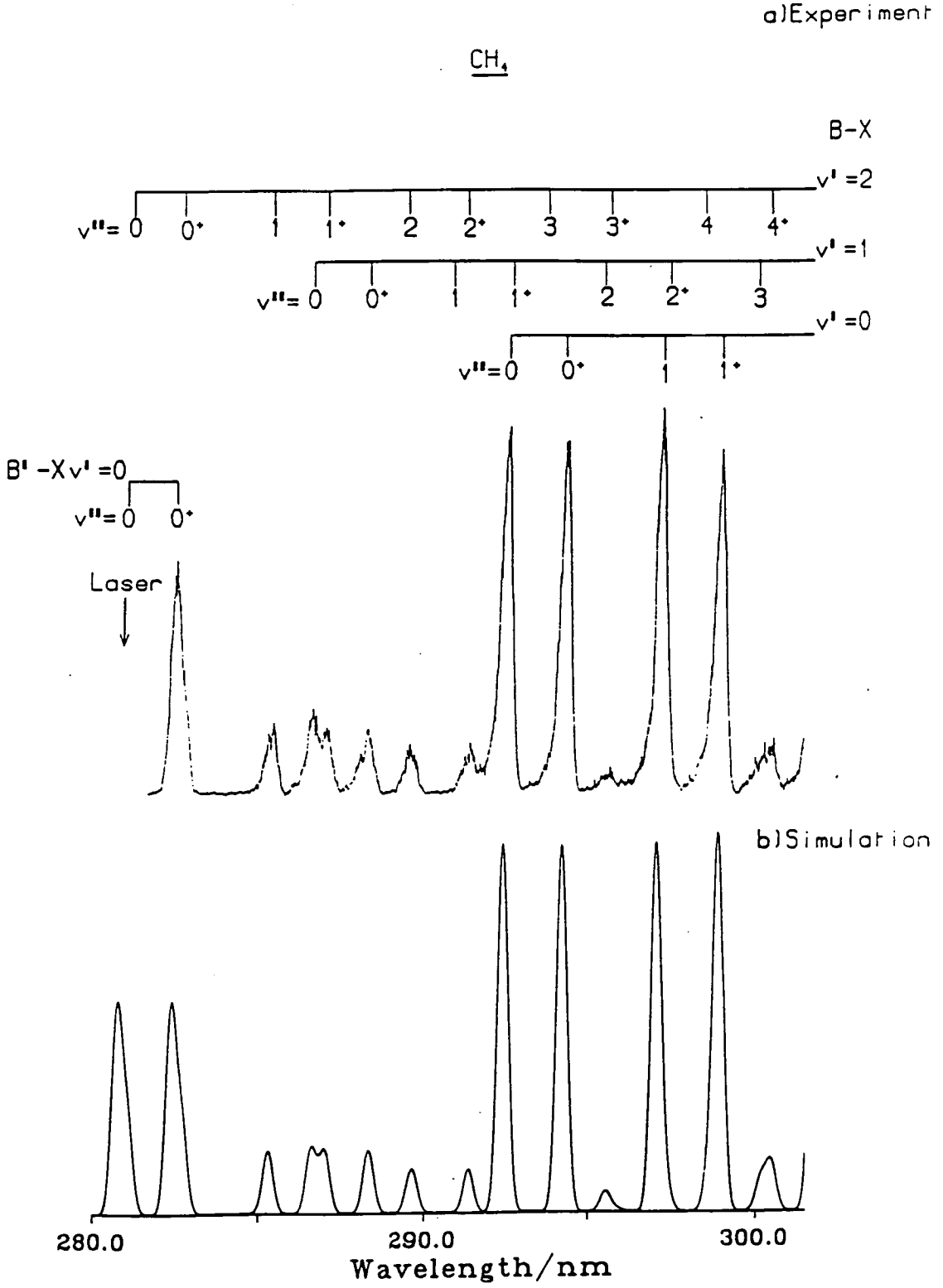

FIGURE 3.21: Fluorescence intensity distribution following excitation to v′=1 of the B′ state with 1.5 Torr total pressure of argon gas. Emission from directly pumped B v′=3 was just observable.

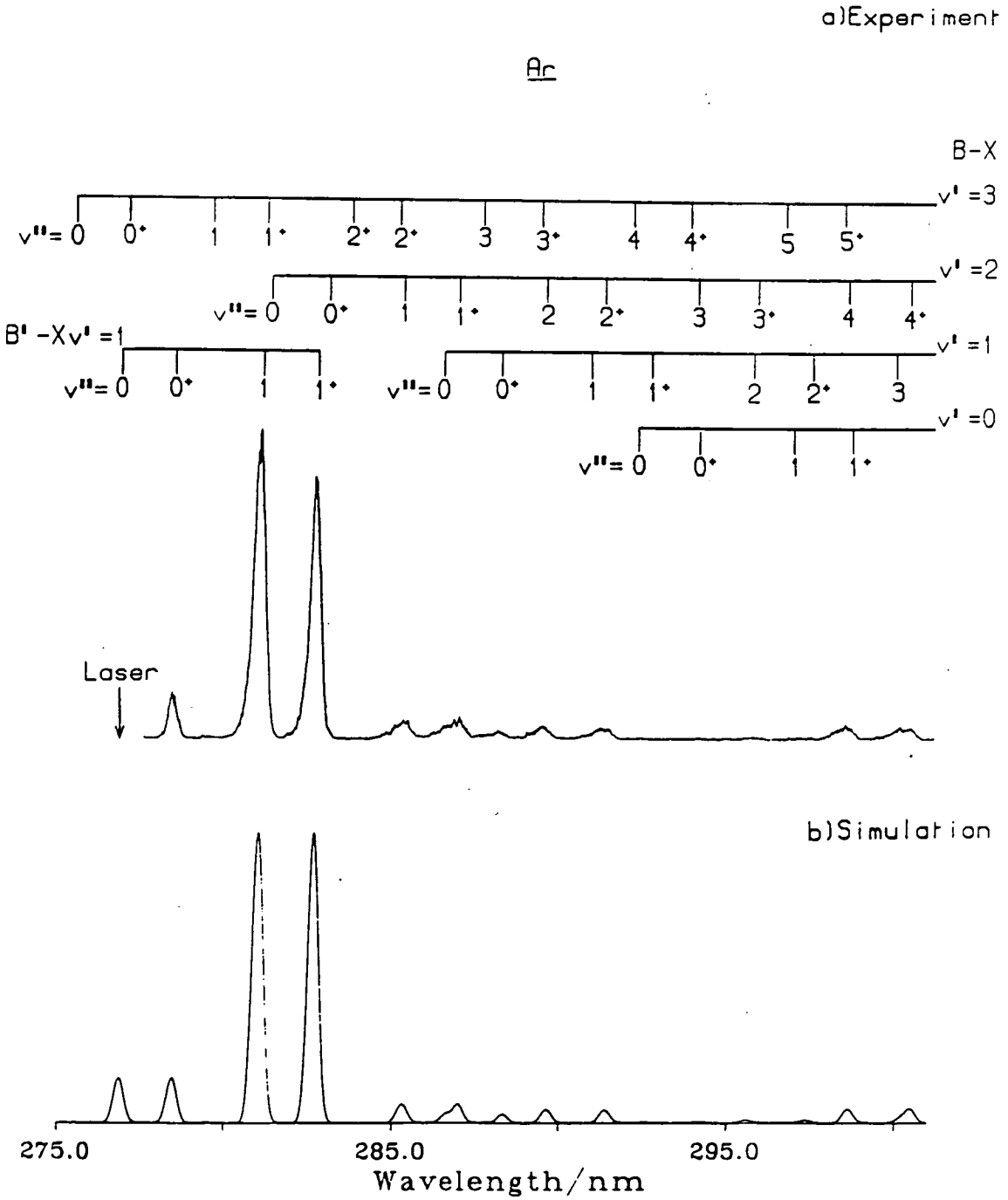

FIGURE 3.22: Fluorescence intensity distribution following excitation to v′=1 of the B′ state with 1.5 Torr partial pressure of CO_2 quenching gas.

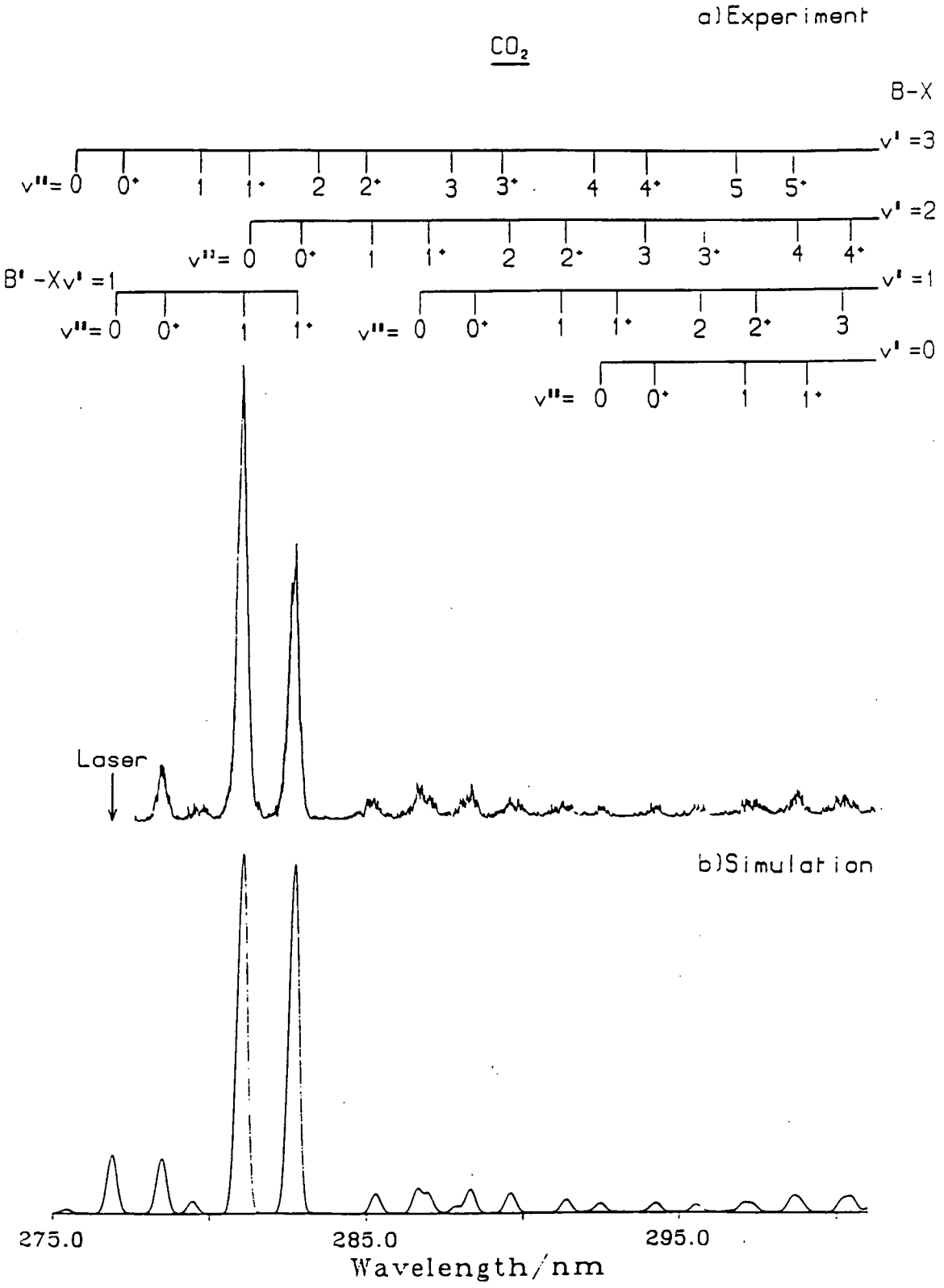

FIGURE 3.23: Fluorescence intensity distribution following excitation to v'=1 of the B' state with 1.5 Torr partial pressure of H_2 quenching gas.

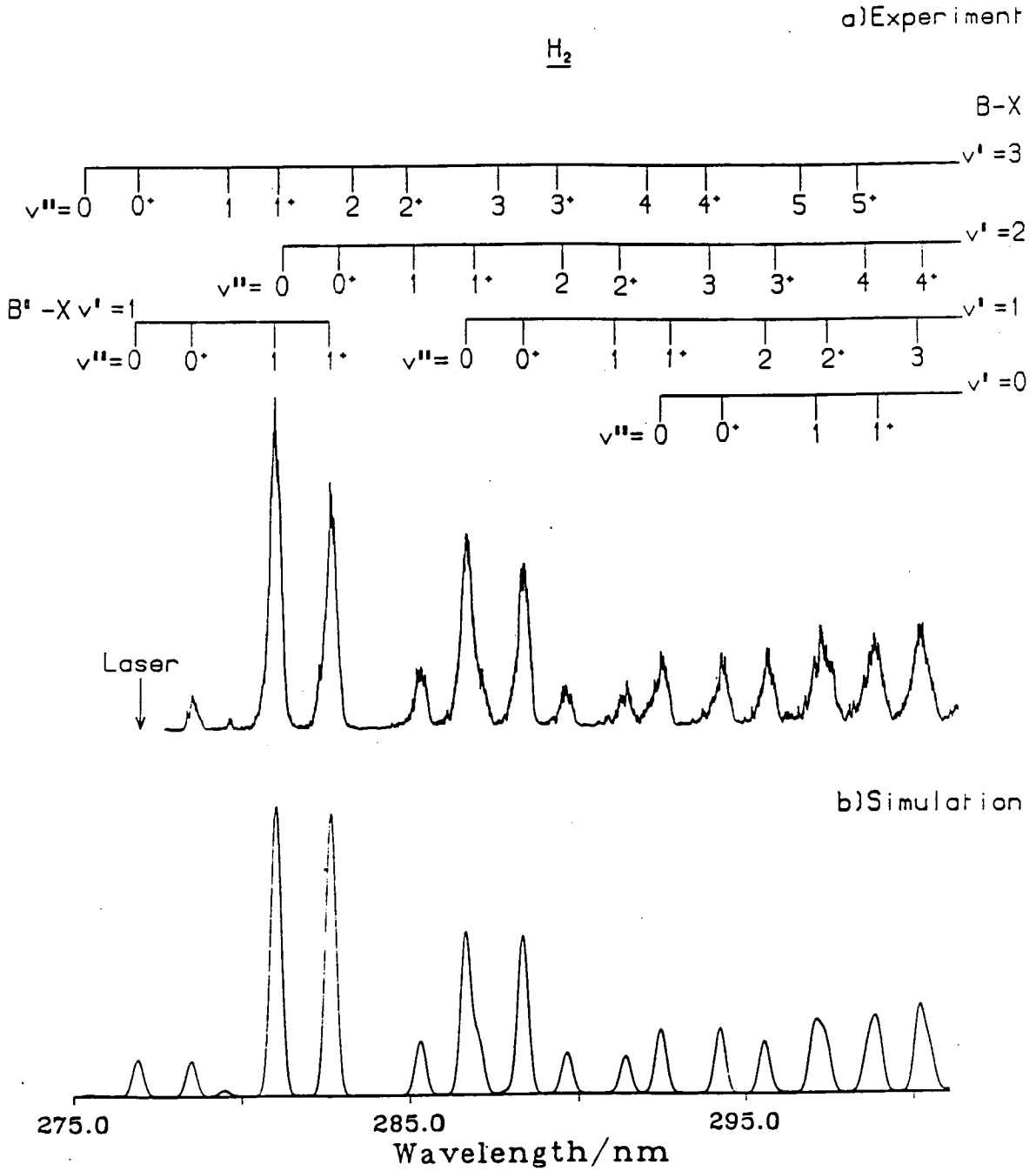

FIGURE 3.24: Fluorescence intensity distribution following excitation to v′=1 of the B′ state with 1.5 Torr partial pressure of CH_4 quenching gas.

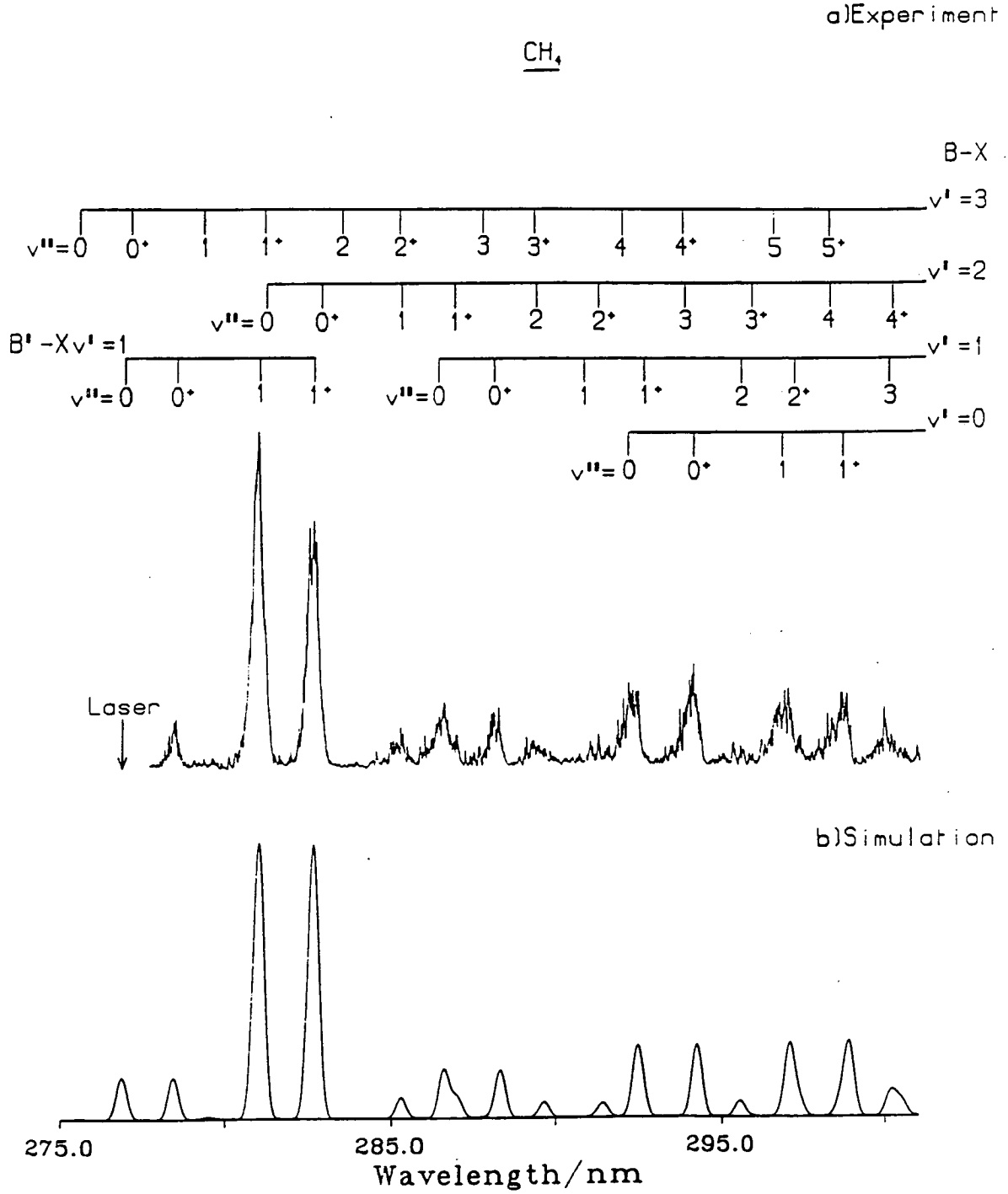

In all cases the simulation fits the observed spectrum reasonably well except for the (1,1) band of the B'-X transition. A possible explanation could be that the monochromator was partially resolving the head forming branches in the $B'-X^2\Pi_{3/2}$ transition.

The various Figures were chosen to illustrate the product state distribution 'propensities' that were found for the differing collision partners. Figure 3.17 shows that for argon, the carrier gas (necessary to maintain the discharge plasma) for all experiments from which data was extracted. A typical example when CO_2 was the collisional transfer agent is shown in Figure 3.18. Carbon dioxide was observed to have a propensity to transfer predominantly to B v' = 2, and thus exhibited behaviour similar in this respect to Ar. Hydrogen, see Figure 3.19, had a very strong propensity to transfer to B v' = 1. He and N_2 produced similar but less strongly peaked distributions. Figure 3.20 shows a typical spectrum when methane was the quencher, for which B v' = 0 was predominant. Methane and CF_4 produced highly analogous distributions.

For excitation to v' = 1 of the B' state, see Figures 3.21-3.24, two general comments could be made in comparison to B' v' = 0.

1) Overall v' = 0 of the B' state showed a larger B' to B transfer rate.
2) The propensity to populate both v' = 0 and 1 of the B state was reduced.

To obtain the relative populations in each B state level, the following expression was used:

$$I_{v'v''} = \frac{N_{v'} R(\lambda)\, p_{v'v''}}{\lambda^3_{v'v''}} \quad , \qquad (22)$$

where $I_{v'v''}$ are the measured (see note 1) integrated (over all time) intensities of the bands that characterise each B state level

$N_{v'}$ is the B state population and is the parameter of interest in this section.

$R(\lambda)$ is the correction term for the wavelength response of the instrument, see Section 3.5.

$p_{v'v''}$ are the vibrational transition probabilities described in section 3.5.

$\lambda_{v'v''}$ are the transition wavelengths.

The population transferred into any B state level i.e. (v' = 0,1,2) may be obtained, in theory, from measurements of any particular (v',v") combination between the B and X states. Figure 3.15 shows all the (v',v") combinations from v' = 0,1,2 and 3 of the B state. It was clear therefore that even with the resolution (~ 0.25 nm) used in these experiments many bands were overlapped at longer wavelengths. Therefore, initial estimates (usually accurate to ~ 90% of the final values) of the various B state populations were taken from the least overlapped B-X bands, which were the (2,1) and (2,2) bands for v' = 2; the (1,0) band for v' = 1 and the (0,0) band for v' = 0. Best estimates of the product state distribution were then obtained from iteratively comparing the experimental and simulated spectra.

Measurements of $I_{v'v''}$ were made at relatively high quencher partial pressure in order to minimise the contribution from the argon carrier gas. For v' = 0 of the B' state partial pressures near 4 Torr were normally used, while for v' = 1 partial pressures near 3 Torr were used. For the additional gases only single measurements were taken at a collider partial pressure of 1.5 Torr and only for v' = 0 of the B' state.

The separate $N_{v'}$ for B v' = 0, 1 and 2 obtained from each gas, were renormalised to represent the percentage of the total population in the v' = 0, 1 and 2 levels and tabulated in Tables 3.11-3.13.

TABLE 3.11: Percentage B state populations following quenching of $v' = 0$ of the B′ state. Numbers in brackets represent the estimated uncertainty in the populations and should be applied to the last significant figures.

	Percentage Population		
Gas	$v' = 0$	$v' = 1$	$v' = 2$
He	9(2)	60(5)	31(3)
Ar	9(3)	27(3)	64(6)
H_2	27(2)	65(4)	8(1)
N_2	11(1)	52(5)	37(4)
CO_2	11(2)	34(3)	56(5)
CF_4	76(4)	13(2)	11(1)
CH_4	71(5)	12(3)	17(3)

TABLE 3.12: Percentage B state populations following quenching of $v' = 0$ of the B′ state. Each of the populations in Table 3.12 should be regarded as having a relative error of 25%.

	Percentage Population		
Gas	$v' = 0$	$v' = 1$	$v' = 2$
N_2O	7	21	72
CF_3Cl	46	22	32
C_2H_6	71	11	18
C_4F_8	51	15	34

TABLE 3.13: Percentage B state populations following quenching of $v' = 1$ of the B′ state. Numbers in brackets represent the error in the fractional populations and should be applied to the last significant figures.

	Percentage Population		
gas	$v' = 0$	$v' = 1$	$v' = 2$
He	6(2)	23(4)	71(9)
Ar	1(1)	12(3)	87(12)
H_2	22(3)	54(5)	25(2)
N_2	12(3)	49(6)	39(5)
CO_2	21(5)	49(8)	30(6)
CF_4	36(4)	44(4)	25(3)
CH_4	52(5)	28(3)	20(4)

The product state distributions following energy transfer from $v' = 0$ of the $B'^2\Delta$ state were summarised in Table 3.11. The numbers in brackets represent the uncertainties for each B state level. Table 3.12 tabulates the data for $B'^2\Delta$ $v' = 0$, for the additional gases while Table 3.13 presents the data for $v' = 1$ of the $B'^2\Delta$ state.

The uncertainties for the entries in Tables 3.11 and 3.13 were calculated in the following manner. For each spectrum the individual $I_{v'v''}$ were measured (normally the (2,1), (2,2), (1,0) and (0,0) bands), then a correction was made to each spectrum for experimental drift. Average values of $I_{v'v''}$ (from at least 3 spectra) were then calculated together with the statistical error. The $N_{v'}$ values then followed from rearrangement of equation (21). The uncertainty in $N_{v'}$ therefore contains terms in $I_{v'v''}$ and $p_{v'v''}$ (the $p_{v'v''}$ carry the uncertainty in $R(\lambda)$). The error for the total B state population is the 'sum' of the absolute errors of the $N_{v'}$. Hence, the uncertainty (entered in the tables) is the error associated with each $N_{v'}$ and with the total B state population, these values being added in quadrature.

3.7.2 Systematic errors in the measurement of the product state distributions

The interpretation of individual band intensities in terms of relative populations may, provided sufficient care is taken, yield reliable results: in this subsection some of the difficulties inherent in this process will be highlighted.

For the additional gases, e.g. N_2O etc., the experiments were carried out only once and at a relatively low collider partial pressure. Hence, the data presented in Table 3.12 was regarded as having a larger uncertainty i.e. 25% of the respective values.

In conjunction with Tables 3.11 and 3.13 the product state distributions are presented diagramatically in Figure 3.25.

1) The vibrational transition probabilities and the experimental response function had been reasonably well characterised. Hence, the method of iteratively comparing experimental and simulated spectra (which utilises all bands in the spectrum) minimises any effects caused by the accidental overlap or random intensity fluctuation inherent in using only single bands as the basis of population measurement.

2) All fluorescence spectra in this section contained a contribution to the measured B state populations from the argon carrier gas. It was possible to minimise this effect experimentally by measuring the product state distributions at a high quencher pressure such that the fractional number of collisions with argon by a radical in the B′ state would be reduced.

Changing the quencher pressure would lead, experimentally, to an apparent change in the B state product state distribution. However, for $v' = 0$ of the B′ state it was nearly always possible to reach a

FIGURE 3.25: Diagramatic representation of the relative B state product state distributions following quenching of the B′ v′=0 and 1 levels. The abscissa axis shows the B state vibration level while the ordinate axis shows the relative populations in each level. The data symbolised by '□' represent quenching from B′ v′=0, while the symbol 'Δ' represents quenching from B′ v′=1. Uncertainties in the data are shown.

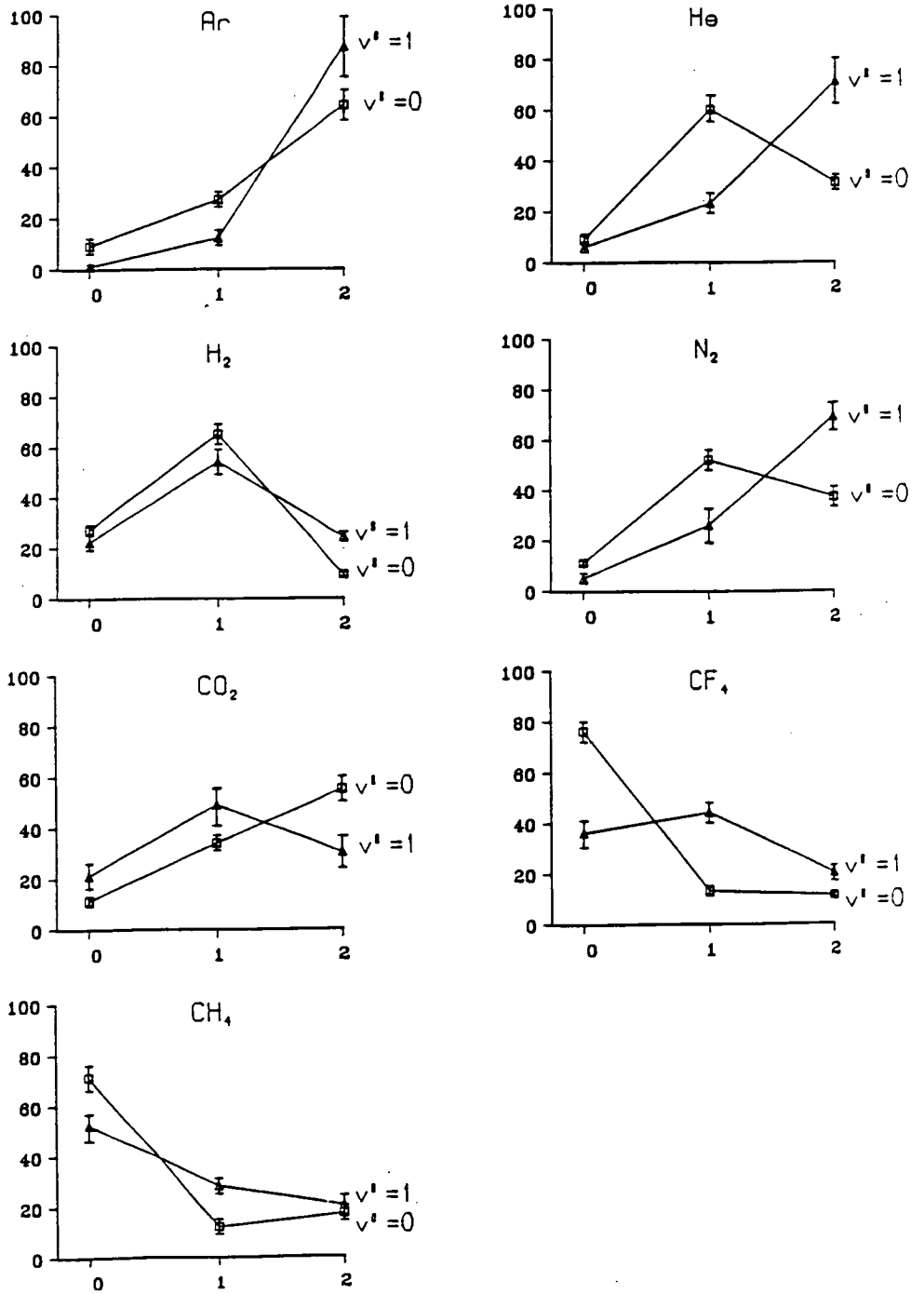

sufficiently high quencher pressure ($\geq$ 4 Torr) that the distribution appeared invariant with addition of more quencher. Additionally, since the relative rates of B′ to B transfer were known (see section 3.9) it was possible by taking simple ratios, to remove the proportion of the measured $I_{v'v''}$ due to argon. For v′ = 0 of the B′ state this correction proved to be negligible in most cases. However, for v′ = 1 of the B′ state it did affect the final product state distributions. Since argon had a very strong propensity to populate v′ = 2 of the B state, the correction to v′ = 2 for the quencher was significant for weak B′ to B quenching gases such as CO_2 and N_2.

3) Excitation on the Q_1 head of v′ = 0 of the B′ state will also accidentally directly populate high J levels of v′ = 2 of the B state, see Figure 3.4, while for v′ = 1 high J levels of v′ = 3 of the B state will be populated; see Figure 3.8.

However, following excitation from the Ω = 3/2 component of the ground state to the B′ state no emission from v′ = 3 of the B state was observed. This transition does not accidentally overlap any B-X bands, in excitation. Hence, the presence of the weak B-X (3,n) bands in the fluorescence spectra, Figures 3.21-3.24 is confirmed to not be due to any energy transfer processes and was therefore considered of no importance.

Excitation to B′ v′ = 0 from both spin orbit components of the ground state leads in either case to bands overlapped by B v′ = 2 emission. However, it was possible to estimate the contribution nascent B v′ = 2 population would make to the total integrated emission intensity of v′ = 2 by delaying the detector gate 100 ns relative to the excitation pulse (as described previously). The population averages of fluorescence spectra for the gases Ar, CH_4 and H_2 obtained under these conditions were then compared to those obtained from the time integrated emission intensities. The values obtained were identical to within the error limits of each method.

This observation was reasonable since examination of the relevant excitation spectrum, Figure 3.4, indicated that the B′:B intensity ratio was approximately 20:1. Furthermore, the fluorescence spectra were obtained at much higher power densities (~ 500 μJ cm^{-2}) than the excitation scans and since the B state would saturate at much lower power densities than the B′ state, the B′:B ratio will be much greater than 20:1. Therefore, no effort was made to directly correct the measured B v′ = 2 population for the contribution from directly excited B state levels.

4) For v′ = 1 of the B′ state there was the additional complexity of B′ v′ = 1 $\longrightarrow$ B′ v′ = 0 transfer. The possibility of this energy transfer route was investigated more fully in Section 3.8. However, it may be stated that, if present, vibrational relaxation appears not to have a major effect on the observed product state distributions.

Therefore, it was felt that the entries in Table 3.11 are reasonably close to those that might be obtained in a hypothetical experiment free from complications while those in Table 3.13 are more uncertain.

3.7.3 Variation of the excitation wavelength: rotational effects

Experiments were performed, with argon as the quencher, such that emission 200 ns after the excitation pulse from v′ = 0 of the B′ state was monitored as a function of excitation wavelength, up to 20 cm^{-1} from the Q_1 head on the 'R' branch. The notation 'R' is used to indicate that the 'R' branch is actually composed of several branches, see Appendix I, Figure AI.ii. As shown in Figure 3.6 pumping the Q_1 head will produce much stronger emission than the 'R' branch, hence the limited excitation ranges used.

Using a simple rotational term expression for the 'R' branch $\Delta J = +1$, the levels which were pumped were characterised by J values of:

$$J \sim {}^{33}/_{2},\ {}^{47}/_{2},\ {}^{57}/_{2},\ {}^{65}/_{2}$$

For all pump positions the observed product state distribution in the B state and the B′:B branching ratio appeared constant. Since the experiment was performed only once at each pump position and because of the relatively poor signal to noise ratio, an estimate of the sensitivity to measurable differences between the $I_{v'v''}$ and the branching ratio at each pump position was approximately 25%.

The experiment described above was rather crude since the bandwidth and intensity of the laser was such that a range of J levels would be directly pumped. Also, the spectra were observations after a considerable time delay between excitation and emission: on average each molecule in the B′ state would have undergone ~ 2.2 gas phase collisions (see Appendix II). Furthermore, rotational energy transfer is normally very efficient for non-hydride diatomics [59][60]; with an energy transfer probability per collision near one and multiple quantum transfers being common.

The conclusion that was drawn, therefore, was that there was no strong rotational dependence on the branching ratio or the product state distribution.

3.7.4 Energy transfer within the B state

In Section 3.5, see Figures 3.11-3.14, it was observed that under the 'base conditions' of 1.15 Torr of argon there was no apparent energy transfer from the various B state levels. Furthermore, addition of various collision partners to initially prepared v′ = 0 and 1 of the B state indicated no transfer. However, close examination of the fluorescence spectra following excitation from the $\Pi_{1/2}$ component of the ground state to v′ = 3 of the B state, with various collision species see Figure 3.26, indicated the presence of an additional weak spectral feature at 282.5 nm. This feature was assigned as the B′ - X (1,1) band, as discussed below. However, excitation from the $\Pi_{3/2}$ component of the ground state could not be utilised as a comparison since v′ = 1 of the B′ state would also be produced.

FIGURE 3.26: Fluorescence spectrum following excitation to v'=3 of the B state. The partial pressures of the quenching agents H_2 and N_2 were both 3.0 Torr. The position of the weak spectral feature assigned to the B'-X (1,1) band is marked.

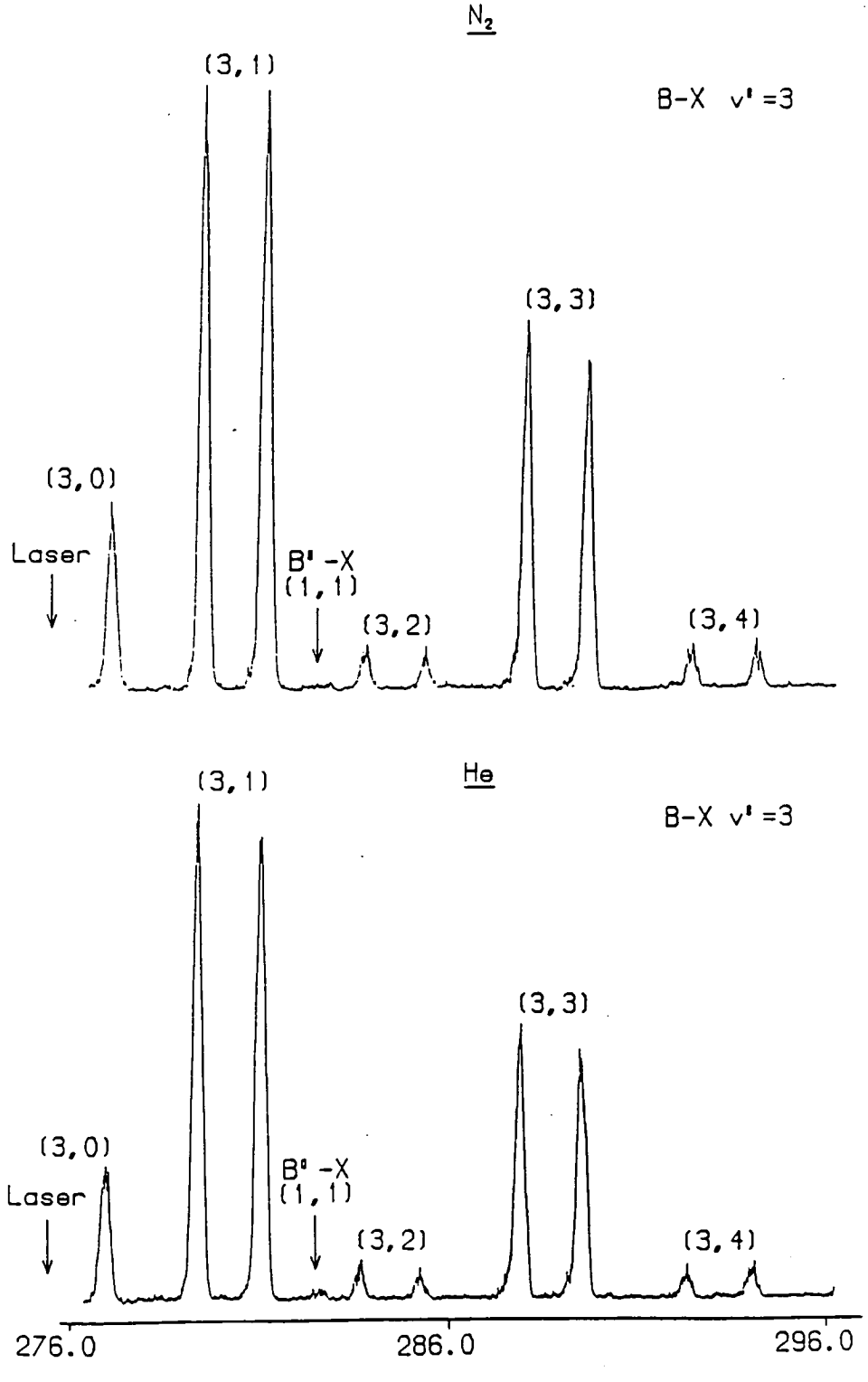

Estimates of the emission intensity of the B'-X band were made relative to the B-X (3,1) band having a normalised intensity of 100. All spectra were obtained at a collision partial pressure of 3.0 Torr. The results for the various gases were summarised in Table 3.14. The error term in the intensity measurements arose from the statistical error in the measured intensity (values being an average of two spectra).

TABLE 3.14: Intensity of the B'-X (1,1) band relative to the B-X (3,1) band which was normalised for all gases to have an intensity of 100. The numbers shown in brackets correspond to the uncertainty in the relative populations and should be applied to the least significant figure.

Gas	Relative Intensity
He	1.0(3)
Ar	0.4(3)
H_2	1.4(4)
N_2	0.8(3)
CF_4	0.4(2)
CH_4	1.1(5)

Assignment to the B'-X (1,1) band was based on the observation that no other additional spectral features, of comparable intensity and correct wavelength position, were ever observed for any of the gases used. Hence, assignment of the spectral feature to either B-X v' = 2 or B'-X (0,0) emission could be rejected with reasonable confidence.

Hence, although the B state radiative lifetime is short under 'high' pressure conditions energy transfer is observed (as would be expected).

3.8 High Resolution Fluorescence Spectra

In conjunction with the previously described low resolution fluorescence studies (sections 3.5 and 3.7), a number of studies at higher resolution were also performed. These studies were important since they revealed the form of the rotational distributions that arose from prompt collisionless emission or following collisional transfer in the excited states.

Within this section high resolution is defined as the ability to resolve, in a fluorescence spectrum, rotational contour or band information. The monochromator had a reciprocal dispersion of 8.2 Å/mm and was normally operated with slit widths between 30 and 90 μm. At wavelengths near 300 nm this corresponded to a resolution of between approximately 3 and 10 cm^{-1}.

3.8.1 Initial preparation of v' = 0 and 1 of the B state

Both v' = 0 and 1 of the B state were spectroscopically isolated, hence the effect of collisions on their rotational envelopes could be easily investigated.

By pumping the Q_1 head of $B^2\Sigma^+ - X^2\Pi_{1/2}$ (0,0) transition the spectrum shown in Figure 3.27 together with a simulation (which will be discussed in section 3.8.2) was obtained. To avoid complications due to scattered light, fluorescence was dispersed on the $B^2\Sigma^+ - X^2\Pi_{3/2}$ (0,0) transition. The choice of which spin-orbit component to pump and which to disperse could be made freely since both components were observed to produce equivalent spectra. The Q_1 head contains mostly low J values with the position of the band reversal occurring at approximately $J = {}^{11}/_2$. Excitation on the Q_1 head therefore populates several rotational states with similar J values. Fluorescence (in a collision free environment) may then occur on any one of six branches, that is a P,Q and R branch to each spin orbit component. These branches may be deduced from Figure AI.i (Appendix I). The P and R branch transitions will occur with small energy shift relative to the Q branch. Hence, the fluorescence spectrum would be expected to yield a narrow distribution, as observed.

The fluorescence spectrum following excitation to the (0,0) band of the B-X transition, approximately 35 cm^{-1} to the blue of the Q_1 head position, is shown in Figure 3.28. This wavenumber shift corresponds, for a Q branch transition, to pumping a J value near ${}^{81}/_2$. Therefore, in this case mostly high J states are being accessed, hence P and R

FIGURE 3.27: High resolution fluorescence spectrum following excitation of the Q_1 head of the B-X (0,0) transition. Fluorescence was dispersed on the $\Omega = {}^3/2$ component of the B-X (0,0) transition. The simulation assumed a laser bandwidth of 0.6 cm^{-1} and a monochromator bandwidth of 3.5 cm^{-1}.

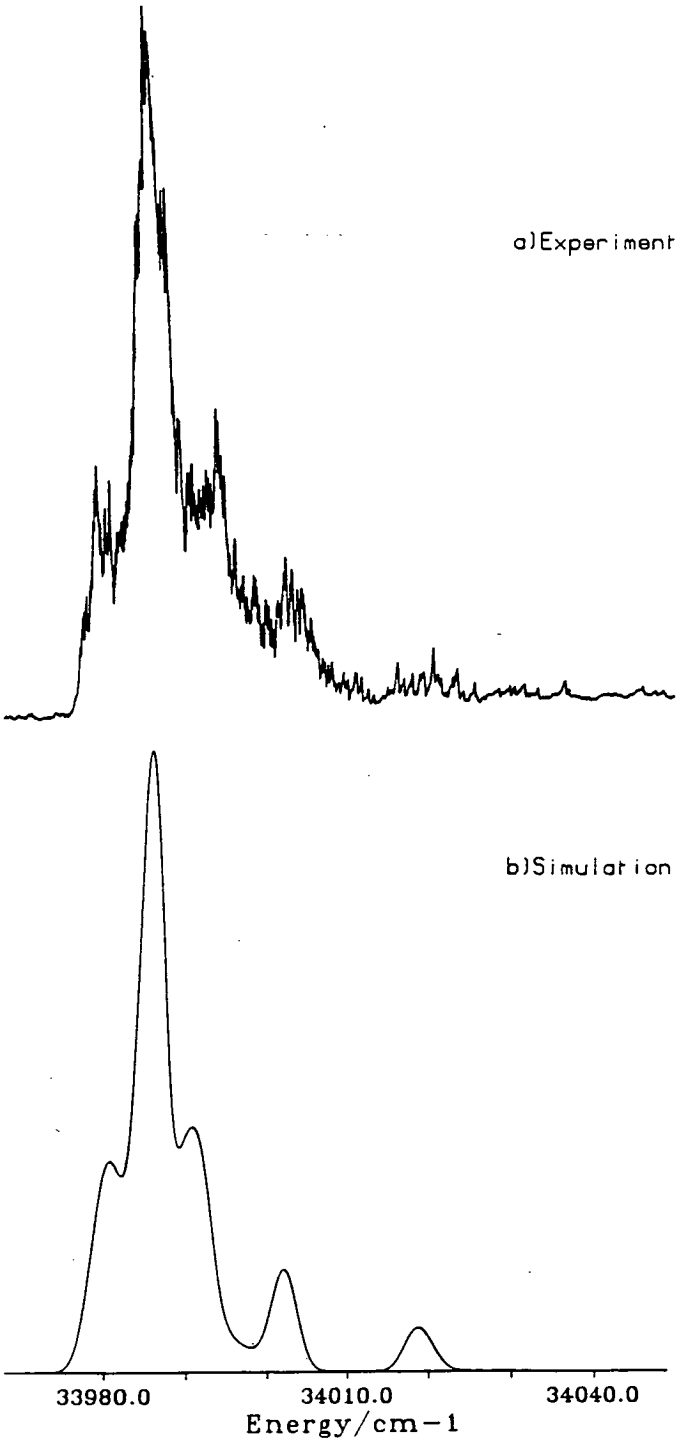

FIGURE 3.28: High resolution fluorescence spectrum following excitation 35 cm^{-1} to the blue, and hence to higher J values than those found in the Q_1 head, of the B-X (0,0) transition. Fluorescence was dispersed on the $\Omega = {}^3/2$ component of the B-X (0,0) transition. The simulation assumed a laser bandwidth of 0.6 cm^{-1} and a monochromator bandwidth of 9.5 cm^{-1}.

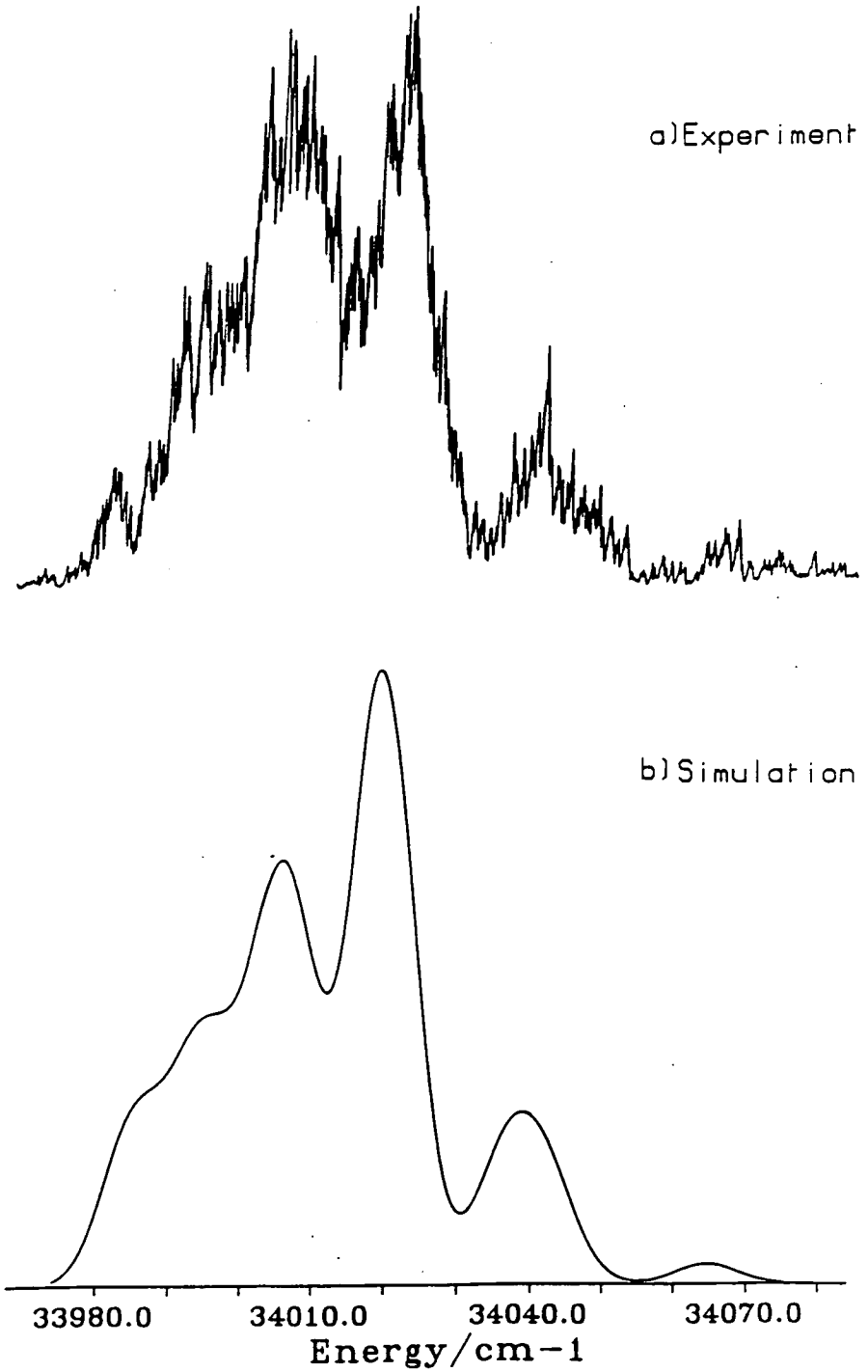

branch transitions back to the ground state will occur with a relatively large energy shift relative to the Q branch. It seems reasonable therefore that a more extended spectrum should be obtained, as observed.

The rotational contours evident in Figures 3.27 and 3.28 were clearly dissimilar to the excitation scan obtained for the B-X (0,0) transition, which was shown to have a thermal rotational distribution.

Similar studies to those outlined for the (0,0) band were carried out for the (1,0) band, see Figures 3.29 and 3.30. The results for pumping the Q_1 head and for the high J study (shifted in this case by 32 cm^{-1}) of the (1,0) band resemble closely those obtained for the (0,0) study. The similarity of the results should not be surprising since identical reasoning for the form of the rotational distribution holds for both the B-X (0,0) and (1,0) bands.

Hence, it was concluded that, under typical experimental conditions where only argon was present there was no evidence for rotational relaxation in the B state.

Collisional quenching partners were added to the gas stream and the high resolution fluorescence experiments were repeated for both the B-X (0,0) and (1,0) bands. For the (0,0) band a partial pressure of CF_4 of 2.5 Torr was added, while for the (1,0) band partial pressures of He and N_2 up to 3.5 Torr were separately added. Within the experimental resolution the intensity pattern of the observed spectra appeared to be identical to the experiments where no additional quencher was added. These observations corroborate the conclusion that at typical experimental pressures rotational relaxation is not significant in the B state. Hence, it may also be reasonably concluded that the B state rotational distributions observed from an initial preparation of the B′ state would be nascent.

FIGURE 3.29: High resolution fluorescence spectrum following excitation to the Q_1 head of the B-X (1,0) transition. Fluorescence was dispersed on the $\Omega = {}^3/2$ component of the B-X (1,0) transition. The simulation assumed a laser bandwidth to 0.6 cm^{-1} and a monochromator bandwidth of 3.0 cm^{-1}.

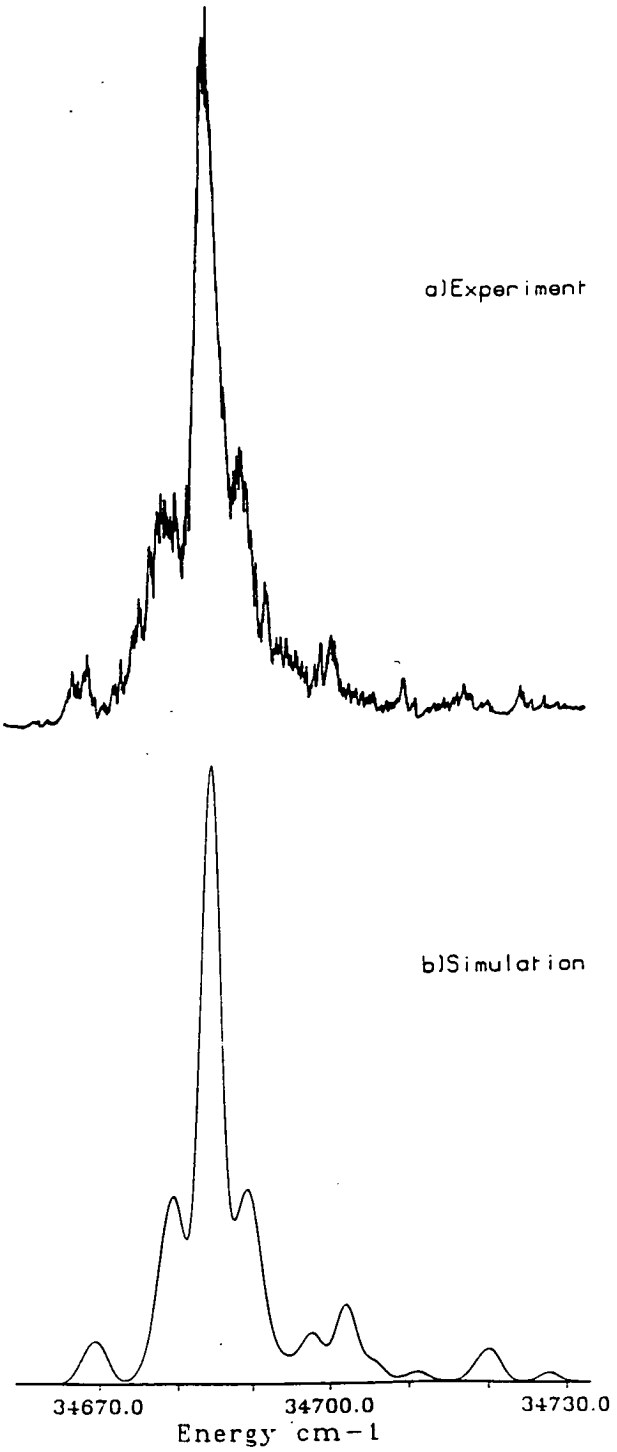

FIGURE 3.30: High resolution fluorescence spectrum following excitation 32 cm^{-1} to the blue, and hence to higher J values than those found in the Q_1 head. Fluorescence was dispersed on the $\Omega = {}^3/2$ component of the B-X (1,0) transition. The simulation assumed a laser bandwidth of 0.6 cm^{-1} and a monochromator bandwidth of 9.0 cm^{-1}

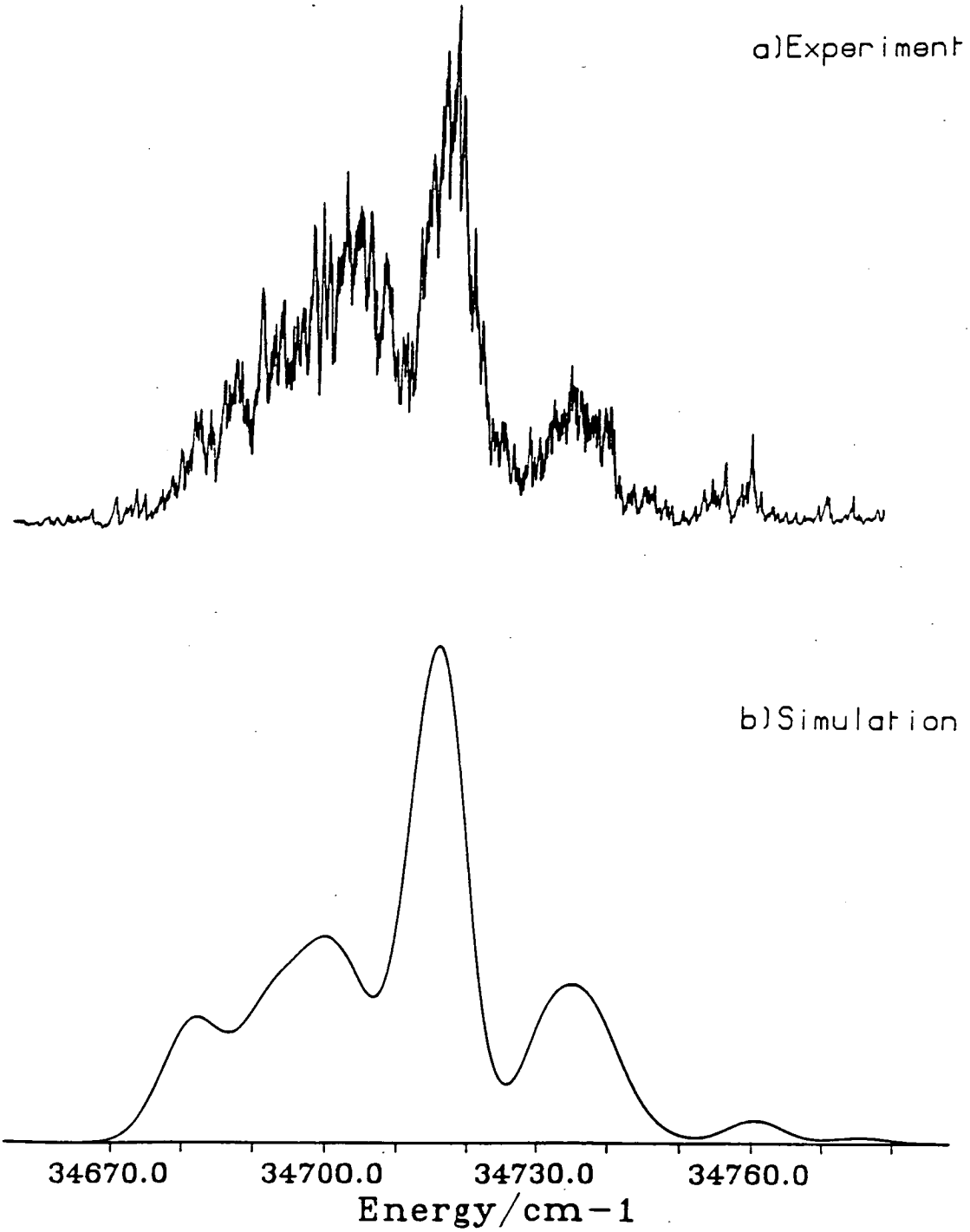

3.8.2 Simulation of B state fluorescence

The simulation procedure followed a purely spectroscopic basis and was thus simply an extension of the program used to generate the B-X excitation spectra. The simulations proceeded by inputting a known photon energy, finding all J's in the excited B state that fell within 4σ (4 laser bandwidths) of the excitation energy and then determining the frequencies of the P, Q and R branch transitions that returned to the $\Pi_{3/2}$ component.

Experimentally it was thought that the excitation stage would suffer from strong saturation effects (i.e. all linestrengths tending to 1.0). However, the simulation process revealed that the spectra obtained at total saturation in the excitation step or when excitation occurred in the linear intensity regime were very similar. This observation was explained in terms of the laser exciting mostly on one branch and to a few similar J's, such that the linestrengths would be relatively invariant over the restricted range of J's populated. In the linear intensity regime the linestrength formulae of Earls [58], were applied for the excitation and fluorescence stages.

The slit function for the monochromator was assumed to be Gaussian in nature and have a constant frequency bandpass. Over the relatively small wavelength ranges scanned, this assumption represents a valid approximation.

3.8.3 Initial preparation of v' = 2 and 3 of the B state

These bands presented significantly different possibilities from the B-X (0,0) and (1,0) bands, in that energy transfer from the B to the B' state is either thermoneutral or exoergic.

Investigations of collisional transfer for v′ = 2 of the B state were more difficult since the rotational envelopes of both spin orbit components of the B-X (2,0) band were overlapped by transitions from the B′-X (0,0) and (1,1) bands. However, since the B′-X system is almost entirely vertical, it was possible to investigate a spectroscopically isolated band in the B-X (2,n) (n = 1,4) fluorescence progression. Fluorescence spectra obtained by this method, both with and without the presence of additional collision gas showed a close resemblance to Figures 3.27 and 3.29 when the respective heads were pumped. Similarly, excitation to v′ = 3 of the B state allowed, in theory, exoergic energy transfer to both the B′-X (0,0) and (1,0) bands. However, for all cases studied (pumping only the spectroscopically isolated Q_1 head of the B-X $(3,0)_{1/2}$ transition) rotational distributions similar to those in Figures 3.27 and 3.29 were obtained.

These observations further reinforce the conclusion that, under these experimental conditions, B state emission occurs without significant rotational relaxation. This fact is readily explained by the short (~ 10 ns) radiative lifetime of the state.

3.8.4 Initial preparation of v′ = 0 and 1 of the B′ state

The v′ = 0 and 1 levels of the B′ state were observed to produce similar rotational contours in the B state following energy transfer. However, since v′ = 0 exhibited the strongest collisional transfer propensities and had a large Franck-Condon factor for excitation most studies utilised this level.

By pumping the Q_1 head of the B′-X (0,0) transition both B′ and B state emission could be observed, see Figure 3.31. The band head positions were measured and are given, together with appropriate comparisons in Table 3.15. In Figure 3.31 the B state emission appears to show (even for the $Si^{37}Cl$ isotopomer) a rotational envelope characteristic of the excitation scan shown in Figure 3.5. Hence, the B state rotational distribution appears approximately thermal.

FIGURE 3.31: High resolution fluorescence spectrum following excitation of the head of the $B'^2\Delta$–$X^2\Pi$ (0,0) transition. Fluorescence was dispersed on the $\Omega = {}^3/2$ component of B–X (2,0) transition and indicated collisionally populated B state, with fluorescence being attributable to the B–X ($\Omega = {}^3/2$) v"=0 state. Total argon pressure was 1.1 Torr. Monochromator bandwidth 2.5 cm^{-1}

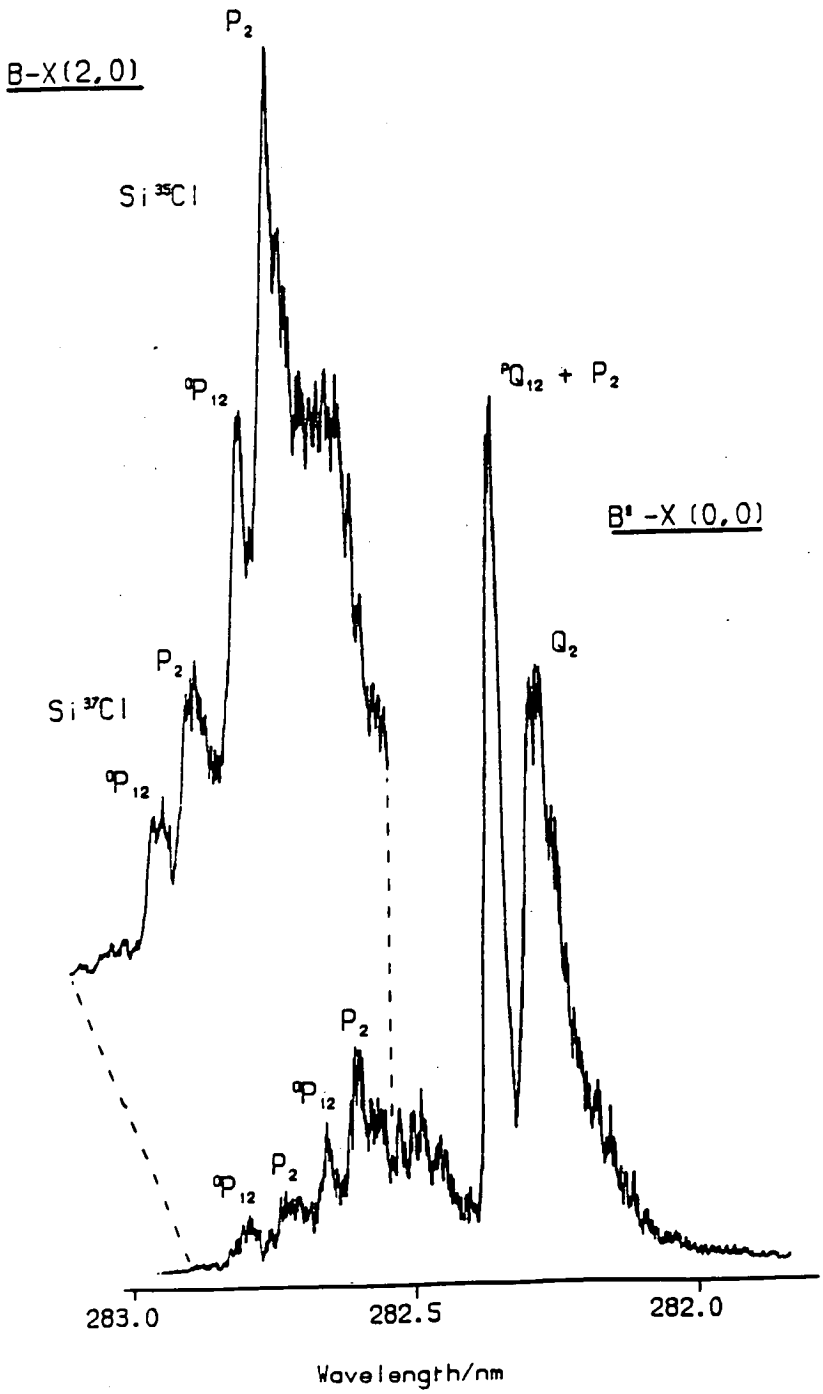

TABLE 3.15: (i) Band head measurements of the B′-X (0,0) band following pumping of the Ω = 1/2 component of the ground state to the B′ state. Values are compared against those of Verma [27], being quoted as air wavelengths to allow a direct comparison

		λ_{air}/nm	
Band	Head	This Study	Ref. [27]
B′-X (0,0)	Q_2	282.30	282.293
	$P_{Q_{12}}$ + P_2	282.35	282.338 - 382.348

(ii) Band head measurements of the B-X (2,0) band, which are compared against the simulated (Sim) values. All values are in vacuum wavenumbers.

Band	Isotope	Head	Head Position/cm^{-1}	Sim/cm^{-1}
B-X(2,0)	$Si^{35}Cl$	P_2	35378	35375.11
	$Si^{35}Cl$	$^oP_{12}$	35370	35367.89
	$Si^{37}Cl$	P_2	35362	35357.53
	$Si^{37}Cl$	$^oP_{12}$	35353	35350.50

By pumping the Q_1 head of v′ = 0 of the B′ state a few high J levels of v′ = 2 of the B state must also accidentally be excited. However, the expected contour for pumping high J levels in the B state has already been established (see Figures 3.28 and 3.30) and does not appear thermal. Also, it was possible to collect the emission after a 200 ns delay from the excitation pulse, such that all nascent B state emission should have disappeared. Under these circumstances the observed spectrum matched very closely that obtained by integrating over all time.

Therefore, the initial conclusion from the experiments outlined directly above and from sections. 3.8.1 and 3.8.3 must be that the observed thermal B state emission was due to rapid thermalisation in the B′ state followed by transfer to the B state and subsequent prompt emission.

By resolving the emission from the spectroscopically isolated B-X (2,n) n= 1,4 bands following excitation to B′ v′ = 0, thermal distributions again appeared and with the expected intensity ratio between the isotopomer bands as well. Such an observation again represents good evidence for B′ to B transfer since to directly excite the $^{28}Si^{37}Cl$ B-X (2,0) band with the fixed pump position would imply high J states were being pumped and hence negligible emission should be observed.

In Section 3.7 it was found that the addition of a quenching gas to the B′ state produced characteristic and strong emission from the B state. In particular, for v′ = 0 of the B′ state CF_4 produced a very strong emission from B v′ = 0 while gases such as He and N_2 favoured populating B v′ = 1. Addition of CF_4 (partial pressure 1.5 Torr) with excitation to v′ = 0 of the B′ state produced the emission contour from v′ = 0 of the B state shown in Figure 3.32. This contour should be compared with those in Figures 3.27 and 3.28 where it had been proven that the direct addition of CF_4 to initially prepared B state levels did not lead to rotational relaxation. The rotational contour shown in Figure 3.32 was modelled by a B-X excitation simulation, with a rotational temperature of 300K.

Similar experiments were carried out for the collision partners He and N_2 (partial pressure of 2.5 Torr) and emission from the B-X (1,0) band was dispersed. The rotational envelopes from these experiments are similar to those of Figure 3.32.

It was concluded therefore that for v′ = 0 of the B′ state rotational relaxation and transfer to the B state occur with high efficiency and that when populated the B state emission is nascent, with no strong propensity for particular rotational levels.

FIGURE 3.32: High resolution fluorescence spectrum following excitation of the Q_1 head of $B'^2\Delta - X^2\Pi$ (0,0) transition in the presence of 2.0 Torr partial pressure of CF_4. Fluorescence was dispersed on the $\Omega = {}^3/2$ component of the B-X (0,0) transition. Monochromator bandwidth was 4.0 cm^{-1}. Clearly resolved are the P_2 and $^oP_{12}$ heads of the B-X (0,0) transition. The simulation assumed a 300 K population and purely B and X state rotational constants.

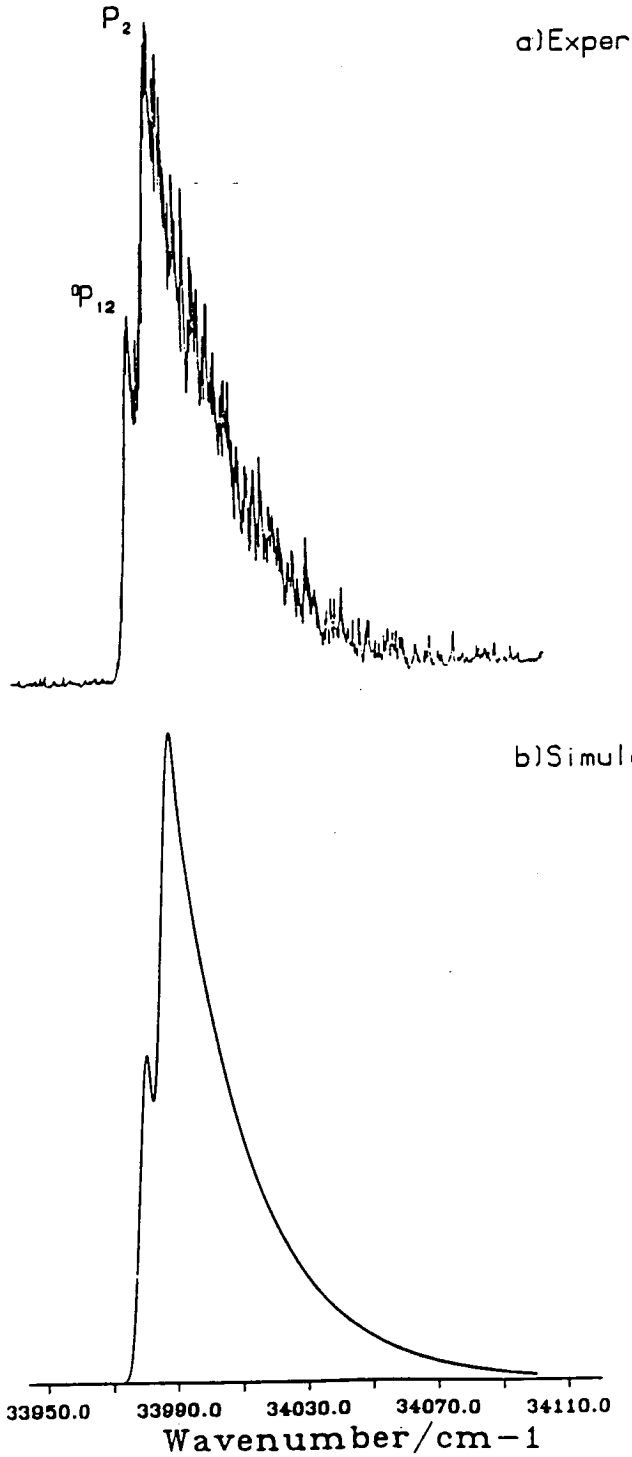

For $v' = 1$ of the B′ state similar if less easily measurable behaviour was observed in the high resolution spectra. However, vibrational energy transfer, i.e. B′ $v' = 1$ to B′ $v' = 0$ transfer was also possible. Since the B′-X transitions were mostly diagonal and the ω_e constants of the B′ and X states were similar only a high resolution study was capable of detecting any vibrational energy transfer. A fluorescence spectrum of the B′-X (1,1) band is shown in Figure 3.33 and also shows B-X (2,0) band. The predicted position of the possible B′-X (0,0) emission is indicated on the figure. The experiment was repeated, inconclusively, several times. It was possible however to set an approximate limit on the intensity of this predicted band as being $3 \pm 3\%$, relative to the B′-X (1,1) band.

No investigations into the variation of the intensity of this 'band' with other collision partners were made. Also, no positive conclusions were drawn as to the presence or otherwise of this 'band'.

3.9 Measurement of B′ State Quenching Rates

Relative rate constants for total removal of the B′ state and partial removal (B′$\longrightarrow$B) were obtained from measurements of the pressure sensitive total B′ intensity and the B′:B intensity ratio. However, if the B′ state radiative lifetimes are known, these relative rates may be converted to absolute values. An outline of the model used to extract the rate constant data is presented in Appendix III. To obtain the absolute rates, the radiative lifetimes measured by Jeffries were used [53]. The values for the lifetimes for $v' = 0$ and 1 of the B′ state, were respectively 1.0 and 0.8 μs. The uncertainty of these values was not reported.

The model presented in Appendix III was based on what were considered to be two reasonable assumptions:

FIGURE 3.33: High resolution fluorescence spectrum following excitation to the Q_1 head of the $^{28}Si^{35}Cl$ isotopomer of the $B'^2\Delta - X^2\Pi$ (1,0) transition. Fluorescence was dispersed on the $\Omega = {}^3/2$ component of the B'-X (1,1) band. Contributing signal was also detected for B-X (2,0) which indicated direct collisional transfer to the B v'=2 state. Also indicated was the expected position of any fluorescence resulting from B' v=1 $\longrightarrow$ B' v=0 transfer followed by B'-X (0,0) fluorescence. The monochromator resolution was ~ 6 cm^{-1}. The pressure in the reactor was 1 Torr of argon.

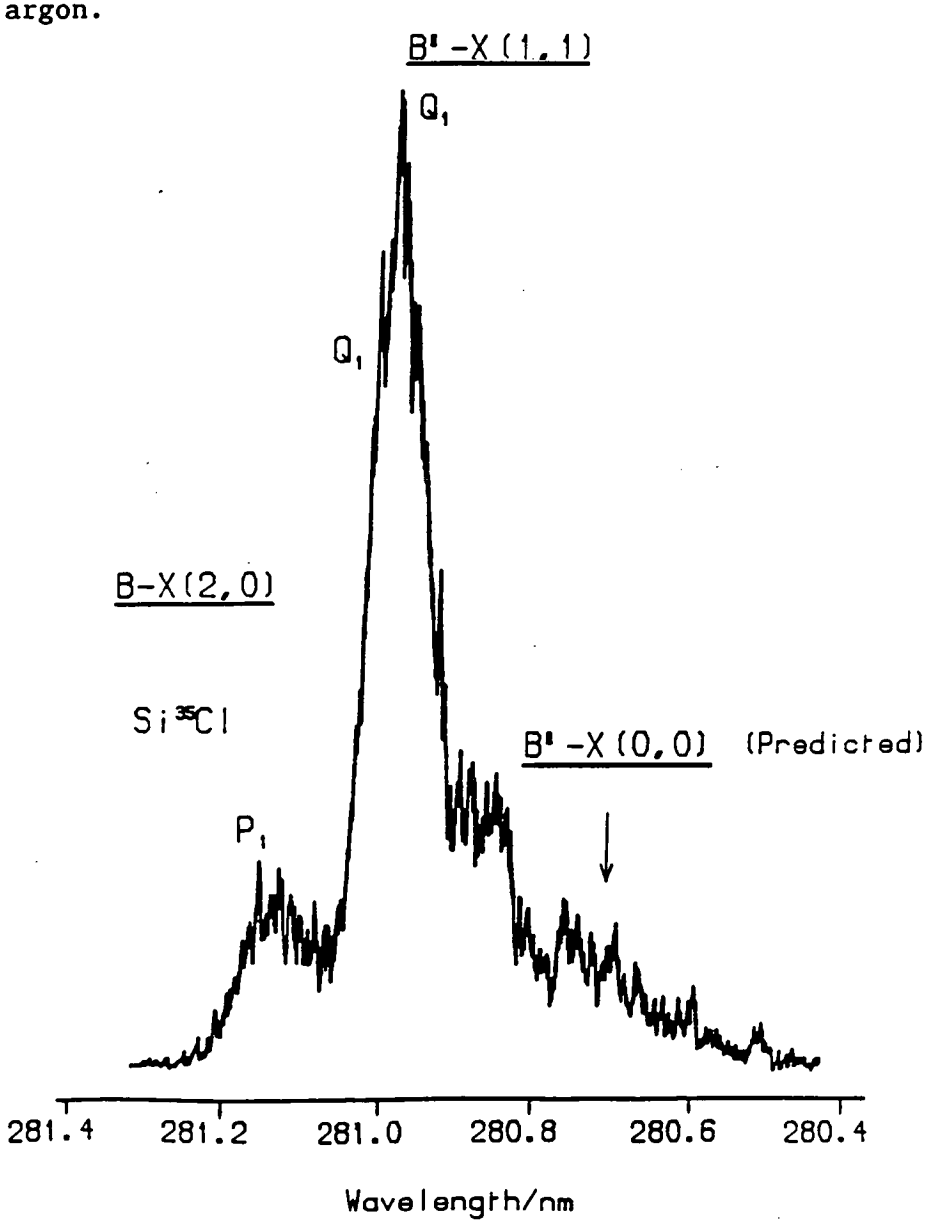

1) Instantaneous B′ state population: this was reasonable since a typical laser pulse (~ 10 ns) was approximately one hundred times less than the B′ state radiative lifetime.

2) Loss of B state by a radiative mechanism only: it was assumed that following energy transfer to the B state, fluorescence would be observed promptly. That is, collisional transfer out of the B state was much slower than the radiative rate. Since the B state radiative decay rate is $10^8 s^{-1}$ the assumption was reasonable at the relatively low pressures of these experiments. Hence the integrated fluorescence intensity from any B state level directly reflects the population transferred to it.

3.9.1 Measurement of the B′ to B quenching rate

The model in Appendix III indicates that by taking the ratio of the integrated emission intensities (i.e. the B and B′ state populations) $I(B)/I(B')$ and plotting against the quenching gas partial pressure a straight line of slope $k_B/\tau_B'^{-1}$ should result: k_B is the total B′ to B quenching rate constant and $\tau_B'^{-1}$ is the radiative decay rate of the B′ state level.

Since the ratio $I(B)/I(B')$ was determined at each pressure, the absolute signal intensities which were crucially dependent on gas dynamical effects in the flow reactor were not required.

To extract the B and B′ state populations, the method outlined in section 3.7 was used. Hence, the B state population was determined provisionally from the B-X (2,1),(2,2),(1,0) and (0,0) bands. The (0,0) band of the B′-X transition is overlapped by the B-X (2,0) band. Hence, it was necessary to subtract an appropriate amount from the overlapped band to determine the B′-X (0,0) intensity. For $v' = 1$ of the B′ state the (1,0) band was used to monitor the B′ state population.

The calculation of the B′ state population assumed that the previously estimated $p_{v',v''}$ values (section 3.5.5) were accurate. While this assumption was not serious for v′ = 0 it was significant for v′ = 1 since a 10% error in the estimated $p_{v',v''}$ value would result in an equivalent error in the B′$\longrightarrow$B quenching rate constants.

The rate constants for quenching of v′ = 0 and 1 of the B′ state are presented in Table 3.16, where the values shown in parentheses represent the uncertainty in the data quoted at the 2σ level. In conjunction with Table 3.16 representative plots for Ar and CF_4 for both v′ = 0 and 1 of the B′ state are shown in Figure 3.34.

The rate constant data presented in Table 3.16 include implicitly the dependence of translational velocity on the transfer probability. Such an effect may be partly removed by expressing the data in terms of a reaction cross section, σ_r. The reaction cross section is defined as [60]:

$$\sigma_r = {}^{k_T}/_{\langle v \rangle} \qquad (23)$$

where σ_r has dimensions of area (Å^2);

k_T is the rate constant at temperature, T;

$\langle v \rangle$ is the average thermal velocity of the collision and is defined as:

$$\langle v \rangle = \left\{\frac{8kT}{\pi \mu}\right\}^{1/2} \qquad (24)$$

k is the Boltzmann constant;

μ is the reduced mass of the collision pair.

Table 3.17 presents the data shown in Table 3.16 in terms of cross sections, the values shown in parentheses are the uncertainties (2σ) in the data.

TABLE 3.16: Quenching rate constants for transfer from v′ = 0 and 1 of the B′ state to the B state (v′ = 0,1,2). Absolute rates were derived on the assumption that the radiative lifetimes of v′ = 0,1 of the B state are 1.0 and 0.8 μs, respectively. Uncertainties are shown in parentheses and are 2σ, but do not include any contribution from the systematic error in the measurement of the radiative lifetimes.

	v′ = 0	v′ = 1
Gas	$k/(10^{11}$ cm^3 molecule^{-1}s^{-1})	$k/(10^{11}$ cm^3 molecule^{-1}s^{-1})
He	2.3(0.6)	1.2(0.3)
Ar	2.7(0.6)	0.6(0.2)
H_2	24(4)	7.4(1.2)
N_2	6.6(1.5)	1.8(0.2)
CO_2	5.0(1.6)	0.7(0.3)
CF_4	18(3)	2.3(0.5)
CH_4	23(4)	3.5(1.0)

TABLE 3.17: Quenching cross sections for transfer from v′ = 0 and 1 of the B′ state to the B state (v′ = 0,1,2). Uncertainties are shown in parentheses and are 2σ.

	v′ = 0	v′ = 1
Gas	$\sigma_r/(Å^2)$	$\sigma_r/(Å^2)$
He	1.8(0.5)	0.9(0.2)
Ar	5.3(1.2)	1.2(0.4)
H_2	13.3(2.2)	4.1(0.7)
N_2	11.6(2.6)	3.2(0.4)
CO_2	9.9(3.2)	1.3(0.6)
CF_4	43.5(7.3)	5.6(1.2)
CH_4	32.7(5.6)	5.0(1.4)

FIGURE 3.34: Representative plots of the ratio of B:B′ intensities against quenching gas pressure. Plots are shown for argon and CF_4, for both v′=0 and 1 of the B′ state. The plots have a slope of $k_B/\tau_{B'}^{-1}$, where $\tau_{B'}^{-1}$ is the radiative decay rate for each vibronic level.

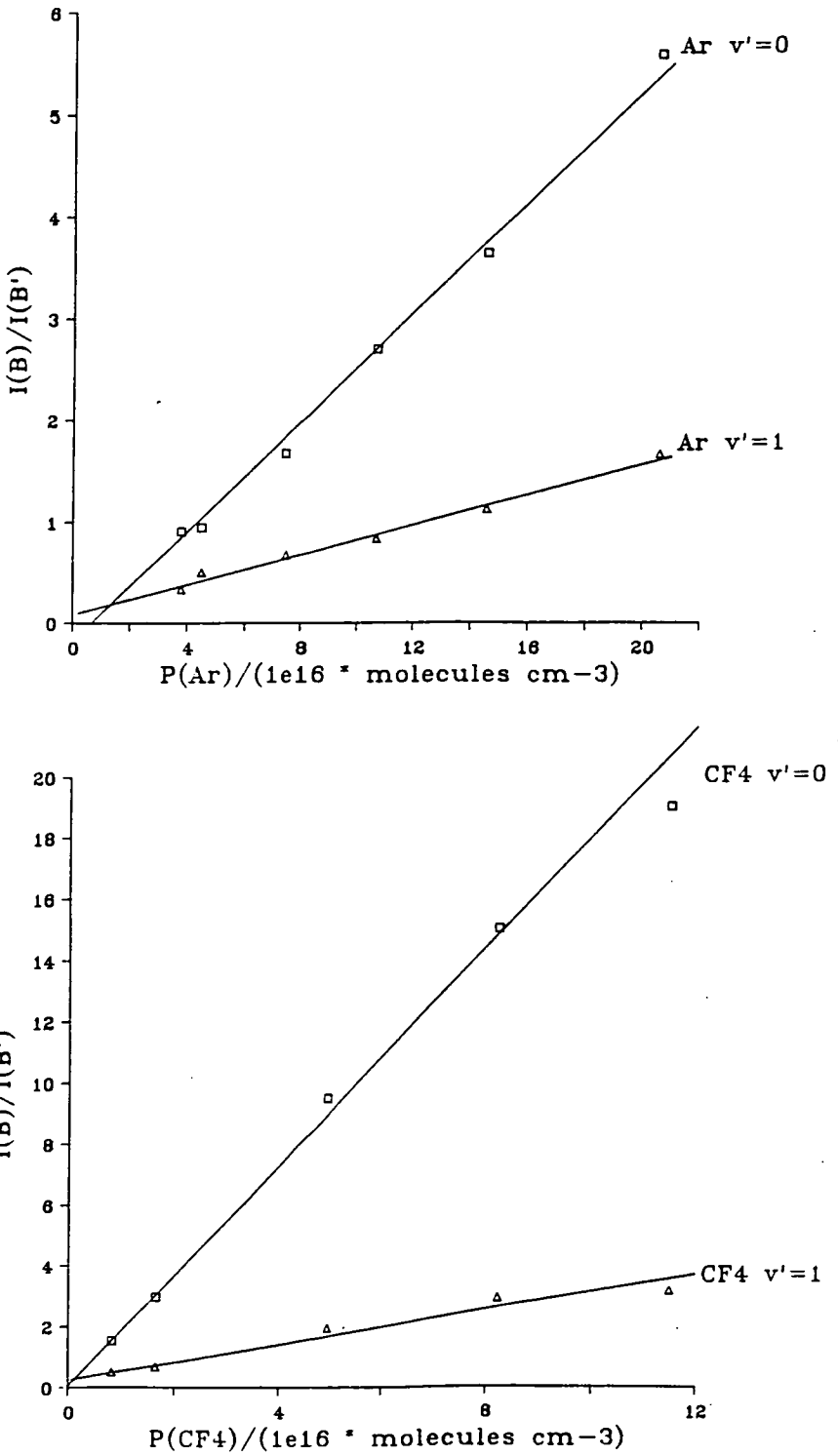

3.9.2 Measurement of total B′ quenching rate

The model in Appendix III indicates that by plotting the reciprocal of the integrated emission intensity from the B′ state, $^{1}/I(B')$, against pressure, P, of the quenching gas a straight line of slope

$$\frac{k_B + k_D}{B'_o \; \tau_{B'}^{-1}}$$ should result,

where: k_B is the B′ to B quenching rate constant.

k_D is the 'mass balance' rate constant and includes all other non-radiative loss mechanisms from the B′ state.

B'_o is the total B′ state population immediately after the laser pulse.

$\tau_{B'}^{-1}$ is the radiative decay rate of the B′ level.

When argon is the only quenching gas present in the reactor the intercept is given by $^{1}/B'_o$. However, when other quenching gases are present the intercept includes a term for the contribution from the argon carrier gas.

The total B′ removal rate may be determined, for the argon only case, simply by dividing the slope of the aforementioned plot by its intercept and the radiative decay rate.

However, implicit in the construction of the $^1/I(B')$ vs. pressure plots lies the assumption that the total radical density, in the interrogation zone of the reactor, was constant with pressure. Such an assumption will be invalid because of gas dynamical effects such as the variation of pumping speed, and hence residence time in the reactor, with pressure. To overcome this problem fluorescence spectra of $v' = 2$ of the B-X band were obtained under identical experimental conditions of pressure to those of the B'-X spectra for each gas. Thus, since the B state has been shown to produce collisionless emission, any variation in the total B state fluorescence intensity as a function of pressure must, to a good approximation, be due to the varying number density of the ground state radical at the interrogation zone.

The intensity of the B' state fluorescence was measured, for B' $v' = 0$, by using the (0,0) band, while for B' $v' = 1$ the (1,0) band was used. For the B'-X (0,0) band, allowance had to be made for the contribution from the overlapped B-X (2,0) band. All B' state intensities, for each quenching gas, were then normalised: firstly for effects such as laser power fluctuations and secondly for the gas dynamical effects by using 'power normalised' B state intensity data. Hence, because of the extensive normalisation procedure the parameter B'_0 was the same constant within any vibrational level but should differ by at least the ratio of the $p_{v'v''}$ values for B'-X (0,0) and (1,0).

The constraints of the experiment imposed by gas dynamics and the discharge plasma implied that, for argon, pressures below approximately 1.0 Torr could not be utilised. To overcome the problem of extrapolation to find the intercept many spectra, including several B-X calibration spectra, were carefully measured for $v' = 0$ and $v' = 1$ (for which less data was available) at reactor pressures near 1 and 2 Torr. For the other pressures and other quenching gases measurements were normally carried out only once.

For $v' = 0$ of the B′ state the total removal rate constant for Ar was determined relatively well, hence the total removal rate constants from $v' = 0$ for the other gases were determined simply by taking the ratio of the slopes of the $^1/I$ (B′) against P plots. For $v' = 1$ of the B′ state the total removal rate constant for Ar was less well determined and hence only relative rate constants were determined.

In Table 3.18 the relative rate constants for $v' = 0$ and 1 of the B′ state are summarised, while Table 3.19 presents the relative total removal cross sections. In Tables 3.18 and 3.19 the numbers in parentheses represent uncertainties quoted at the 2σ level. The absolute values for the total removal cross sections were summarised in Table 3.20. The major contribution to the uncertainties in Table 3.20 was the total removal rate for argon i.e. ~ 40%. Hence, the uncertainties were quoted at the 1σ level. No cross section could be reported for the total removal by CF_4 (due to a lack of B-X calibration points) hence it was not entered in any of Tables 3.18 - 3.20. In conjunction with Table 3.19 representative plots for Ar and CO_2 for $v' = 0$ of the B′ state are shown in Figure 3.35.

It was possible to compare some of the values for the total removal of the B′ state obtained in this work with those obtained independently by Jeffries [53]. Table 3.21 presents a comparison of the cross sections deduced by Jeffries and in this work.

The method of Jeffries was different to the work reported here in that he was able to resolve, in a temporal manner, the time rate of decay of emission from the B′ state. Hence, his experimental methodology was superior to that reported here, in that the extensive normalisation procedures were not required in his analysis.

As may be observed in Table 3.21 the total B′ state removal cross sections reported by Jeffries and in this work agree to within the estimated uncertainties in the data.

TABLE 3.18: Relative rate constants for total removal from v′ = 0 and 1 of the B′ state. Values were measured relative to that of argon which was assumed to have a relative rate of 1.0. Values in parentheses are the uncertainties quoted at the 2σ level and should be applied to the last significant figures.

	v′ = 0	v′ = 1
Gas	Relative rate	Relative rate
He	0.55(28)	0.87(26)
Ar	1.00(24)	1.00(52)
H_2	3.57(96)	6.53(1.58)
N_2	1.02(32)	1.97(78)
CO_2	2.36(90)	2.55(1.00)
CH_4	2.40(1.72)	5.00(2.36) a)

TABLE 3.19: Relative cross sections for total removal from v′ = 0 and 1 of the B′ state. Values were normalised against the relative rate constant for removal by argon being equal to 1.0. Values in parentheses are the uncertainties quoted at the 2σ level and should be applied to the last significant figures.

	v′ = 0	v′ = 1
Gas	Relative Cross Section	Relative Cross Section
He	0.42(22)	0.67(20)
Ar	1.97(48)	1.97(1.02)
H_2	1.99(54)	3.62(88)
N_2	1.79(56)	3.46(1.36)
CO_2	4.68(1.78)	5.06(1.98)
CH_4	3.41(2.44)	7.11(2.36) a)

a) No data were produced for CF_4

TABLE 3.20: Absolute cross section for removal from v′ = 0 of the B′ state. The absolute values were based on the assumptions that the radiative lifetime of v′ = 0 of the B′ state was 1.0 μs and that for all the other gases the absolute cross section for removal from v′ = 0 by argon was the measured value of 15(A^2). The uncertainties, shown in parentheses are 1σ and include the uncertainty in the cross section for argon but not for the systematic error in the measurement of the radiative lifetime.

Gas	Cross Section/($Å^2$)
He	3(1)
Ar	15(6)
H_2	15(6)
N_2	14(6)
CO_2	36(16)
CH_4	26(14)

TABLE 3.21: Total removal quenching cross sections for v′ = 0,1 of the B′ state with Ar and He quenching agents. All values have units of ($Å^2$). The data are compared with those of reference [53]. Numbers in brackets represent the uncertainties quoted at the 1σ level and should be applied to the last significant figures.

	v′ = 0		v′ = 1	
	Ar	He	Ar	He
This work	15(6)	3(1)	11(7)	-
Reference [53]	16	4.3	8	5.1

FIGURE 3.35: Representative plots for the total removal of v'=0 of the B' state by argon and carbon dioxide. The plots have a slope of $(k_B+k_D)/(B'_o\tau_{B'}^{-1})$ where the terms are defined as in Appendix III. The relative slopes indicate the relative total decay rates.

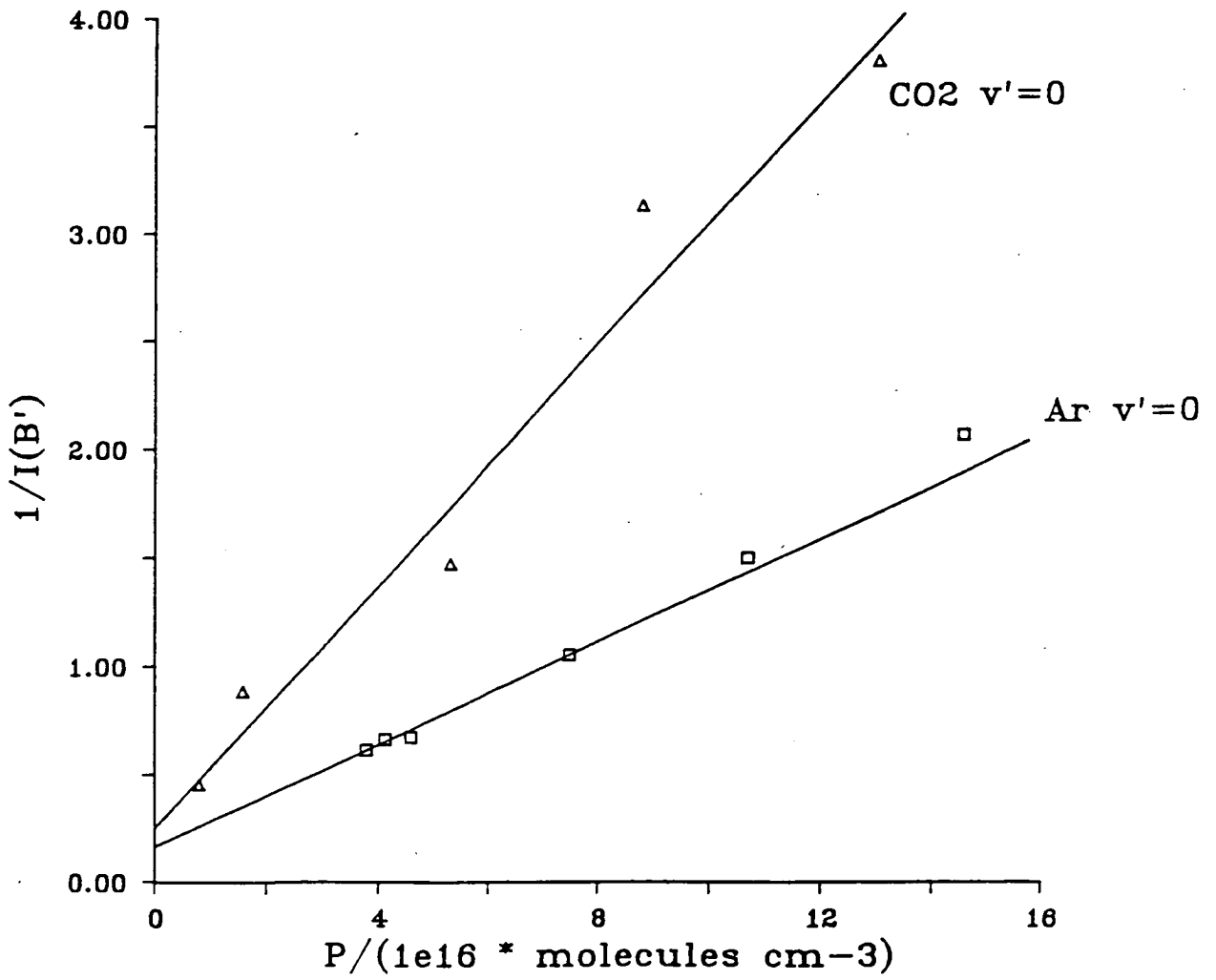

3.10 Energy Transfer in Excited States of Simple Molecules

Any complete discussion of energy transfer in excited states presents a rather formidable task since there are generally several transfer channels to consider. These include spontaneous and collision-induced predissociation, pure electronic quenching, rotational and vibrational relaxation and radiative decay. However, within this section most emphasis will centre on electronic quenching.

At first sight electronic quenching appears to be a fertile ground for the theoretical interpretation of experimental investigations. This expectation is encouraged by the apparent simplicity of the process of two species coming together in a single collision event to yield products. At this level, simple arguments might then be proposed to explain any observed behaviour. For example, an appealing model presented by Freed [61] and Katayama [62] proposed a linear dependence of the electronic quenching cross section $\sigma(Ex)$, on the Franck-Condon factor and an exponential energy gap dependence between the interacting states (Ex,Ex'), that is:

$$\sigma(Ex,v) \longrightarrow (Ex',v') \sim \sigma_{el} | < v \mid v' > |^2 \exp(-\Delta E/kT) \qquad (25)$$

Where: σ_{el} designates an 'intrinsic' cross section for electronic quenching;

ΔE is the energy separation of the initial and final vibrational levels;

T is the translational temperature.

Such a model had a degree of phenomenological success when applied to collision induced transitions in CN [62]. However, from a collision dynamics viewpoint such a model cannot be justified simply because the vibrational motion will not be frozen during the time scale of a typical collision.

Electronic quenching has been investigated for many diatomic molecules: ranging from simple hydrides such as OH [63][64][65], NH [66], CH [67] and PH [68] to heteronuclear diatomics such as CO [69] and CS [70] to homonuclear diatomics, including the halogens, e.g. Br_2 [71].

For the electronically excited $A^2\Sigma^+$ state of OH, which is known to be unperturbed, quenching studies have indicated that it undergoes relatively facile quenching from all its (v',J') levels.

Quenching has also been observed in perturbed systems, with a seminal example being energy transfer between the $X^2\Sigma^+$ and $A^2\Pi$ states of CN. Certain vibrational levels within the A state manifold show strong perturbations (by the X state) in their rotational structure. Early work proposed that transfer was facile between the individual perturbed levels accompanied by thermalisation of the populations in both states. However, it is now accepted, see for example Dagdigian [72][73], that CN A-X transfer is equally facile from both the perturbed and unperturbed levels. Similar observations were also made for the interelectronic transfer between the $A^2\Pi$ and $X^2\Sigma^+$ states of N_2^+ [74][75], where rapid electronic energy transfer occurs even in the absence of non-Born Oppenheimer perturbations, since the permutation-inversion symmetry of the molecular Hamiltonian prohibits any mixing between gerade and ungerade molecular electronic states.

Collision induced intersystem crossing is a well-known phenomenon in the quenching of excited electronic states, and is understood in terms of the appropriately named gateway model, for which the $A^1\Pi$ state of CS is a good example [70]. This model is understood in terms of rapid collision induced rotational energy transfer throughout the initially excited electronic state, but transfer to the nearby state will be inefficient except through particular perturbed rotational levels which therefore have a character which is a mixture of both states.

The approach of a collision partner to an excited diatomic molecule will result in a mutual interaction. The particular angle of approach (except for collinear geometry) will result in the degradation of the cylindrical symmetry of the diatomic. Hence, the description of an isolated molecule with some electronic symmetry must be reformulated for the 'collision system' in terms of, in general C_s (or lower) symmetry with either A' or A" character. The forces between the diatomic and collision partner will be dominated by the electrostatic interaction and it is this interaction which is enough to couple the initial excited and product states and cause a transition between them.

The form of the electrostatic interaction has been derived in detail for rotationally inelastic collision-induced transitions between $^2\Pi$ and $^2\Sigma$ electronic states for an atom-diatomic collision by Alexander and Corey [76]. In general they have shown how to formulate the electrostatic coupling matrix elements between two diabatic states with arbitrary projections of the electronic orbital angular momentum.

The magnitude of the possible matrix elements leads to the form of the potential surfaces in the C_s (or lower) point group and hence governs the observed quenching behaviour.

It appears therefore that to obtain a rigorous description of the quenching process fully 3-dimensional potential energy surfaces for the interacting species are needed. To avoid such a degree of complexity, but still gain a qualitative understanding of the quenching process several simple models have been proposed (see 3.10.1 below) based on various physical parameters thought to be important in governing the interaction process.

An important corollary to the above discussion lies in the investigation of the the quenching behaviour of isotopomers of the species of interest and the quenching partner. The discussion presented above asserts that the most important facet of quenching is the dependence on electronic structure. Therefore, isotopic variation of the quenching agent or the excited species should not affect the observed quenching cross section. For the A state of OH, OD (which is spectroscopically isolated) this has been thoroughly investigated with various species, and such behaviour was observed in these cases [63-65].

If a large variation in quenching rates is found with vibrational level or isotopic substitution, particularly if it is not a monotonic variation for changing vibrational level, then there is an extremely high likelihood of the involvement in the quenching of an additional bound state near the excited one. Examples of this type of behaviour have been reported for the $A^1\Pi$ state of CO by Fink [69] and most recently for the $B^2\Pi$ state of NS by Jeffries and coworkers [77].

3.10.1 Interactions inducing energy transfer

There have been two approaches to the description of energy transfer phenomena, which are based respectively on the alternative assumptions that the dominant energy transfer interaction is either repulsive at small internuclear separation or attractive at long range. This statement may be reformulated in terms of which part of the interaction potential has the largest matrix elements for coupling the two states.

3.10.1.1. Long range attractive force control

Models based on this assumption were inspired by the experimental observation that many energy transfer cross sections were much larger than could be estimated by assuming a hard sphere collision,

i.e. approximately ~ 10 $Å^2$. Examples of quenching processes attributed to long range interactions include the work by Crosley and coworkers on the $A^2\Sigma^+$ state of OH [63-65], and the studies by Stuhl and coworkers on various diatomic hydrides [66][67][68]. Also, Leone found that the collision induced intersystem crossing in the $B^3\Pi(0^+_u)$ state of Br_2 could be correlated with long range control [71].

In all cases experimental verification of long range force control was gained by the magnitude of the quenching cross section and by varying the angular momentum content of the excited species. For any attractive interaction there will be particular orientations which readily lead to the quenching interaction. Hence, as the rotational momentum (velocity) of the excited species is increased these preferred orientations will become washed or averaged out. This results in a lowering of the quenching cross section with increasing J. Similarly, the thermally averaged quenching cross section should decrease as temperature increases.

Apart from the experimental observations listed above the presence of a dominant long range interaction may be deduced by comparing the magnitudes of the quenching cross sections for a series of gases to various empirical models which have a parametric dependence on terms related to long range intermolecular interactions.

1) One of the first models to be developed was that of Selwyn and Steinfeld [78], which was based on the assumption that dispersion forces dominate the quenching process. They predicted that the quenching cross section σ, would vary as:

$$\sigma \propto \mu^{1/2} I_m \alpha_m R_c^{-3} , \qquad (26)$$

where, μ is the reduced collision mass,
I_m is the ionisation potential of the quencher,
α_m is the polarisability of the quencher,
R_c is the hard sphere collision radius.

2) A more sophisticated model to the one above, developed by Thayer and Yardley [79], considered both polar-nonpolar (pn) and polar-polar (pp) interactions. Their model predicted that the cross section would vary as:

$$\sigma_{pn} = A\mu^{1/2} I_A^{\,2} I_m^{\,2} (I_A + I_m)^{-2} \alpha_m^{\,2} R_c^{\,-9} + C \qquad (27)$$

$$\sigma_{pp} = \sigma_{pn} + B\mu^{1/2} D_m^{\,2} R_c^{\,-3} \qquad (28)$$

The terms defined for equation (26) retain the same meaning in equations (27) and (28). Additionally, D_m represents the permanent dipole moment of the quencher. The constants A,B and C are adjustable by empirical fit to the data.

3) A model based purely on the well depth of the interaction between the collision pair, and dependent solely on empirical information, was developed by Parmenter and Seaver [80] and predicts that the quenching cross sections σ_m for species m, scale as:

$$\ln(\sigma_m) = \ln C + \varepsilon_{A^*M}/kT \qquad (29)$$

Where: C is an arbitrary constant,

ε_{A^*M} is the intermolecular well depth between A* and M and is calculated by assuming a geometric combining relationship such that:

$$\varepsilon_{A^*M} \sim (\varepsilon_{A^*A^*}\varepsilon_{MM})^{1/2} \qquad (30)$$

Thus, the intermolecular well depth is derived from the A*-A* and M-M pair potentials. Assuming the validity of such a combining relationship it is possible to approximate further. Since the A*A* contribution will be identical in all cases for which various M are involved, equation (29) simplifies to

$$\ln(\sigma_M) = \ln C + \beta\,(\varepsilon_{MM}/k)^{1/2} \quad , \tag{31}$$

where β is a constant given by

$$\beta = (\varepsilon_{A^*A^*}/kT^2)^{1/2} \quad . \tag{32}$$

Provided there are no resonant energy transfer processes or chemical reactions specific to a particular M gas, then for energy transfer which is governed by attractive forces, equation (31) should always hold.

4) Crosley and co workers have attempted to define the nature of the total interaction potential (estimated empirically in model 3) in terms of all possible intermolecular physical interaction parameters [81]. The one dimensional A*-M interaction is therefore given by a potential V(r) of the form

$$V(r) = -\frac{C_3}{r^3} - \frac{C_4}{r^4} - \frac{C_6}{r^6} - \frac{C'_6}{r^6} \quad , \tag{33}$$

where r is the collision pair separation and the coefficients C_3, C_4, C_6 and C'_6 represent the dipole-dipole, dipole-quadrupole, dipole-induced dipole and dispersion interactions, respectively. To simplify the calculation these terms are evaluated at the orientation of their maximum interactions hence the coefficients are:

$$\text{dipole-dipole } C_3 = 2\mu_1\mu_2 \tag{34}$$

$$\text{dipole-quadrupole } C_4 = {}^3/_2\,(\mu_1 Q_2 + \mu_2 Q_2) \tag{35}$$

$$\text{dipole-induced dipole } C_6 = 2\,(\mu_1^2\alpha_2 + \mu_2^2\alpha_1) \tag{36}$$

$$\text{dispersion } C'_6 = {}^3/_2\,\left(\frac{I_1\,I_2}{I_1 + I_2}\right)\alpha_1\alpha_2 \tag{37}$$

In this model μ refers to the dipole moments of the interacting species.

However, the collision will take place within an effective potential V_{eff}:

$$V_{eff} = V(r) + {}^{Eb^2}/_{r^2} \quad , \tag{38}$$

where b is the impact parameter of the collision and E is the kinetic energy of the collision. For the classically allowed 'orbiting collision', $E = V_{eff}(r_o)$, where the 'o' subscript refers to the orbiting condition. Hence, there exists a value of b_o which defines the classical cross section $\sigma^c(E)$ by

$$\sigma^c(E) = \pi b_o^2(E) \tag{39}$$

The thermally averaged cross section $\sigma_m^c(T)$ at a temperature T is then given by:

$$\sigma_m^c(T) = \frac{1}{(kT)^2} \int_o^\infty \sigma^c(E).\ E.\ \exp\left({}^{-E}/kT\right) dE \tag{40}$$

The value of r_o at which a complex may just form can be calculated using the virial theorem, as shown by Hofzumahaus and Stuhl [82] to be given by

$$r_o^6 - \left(\frac{C_3}{2E}\right) r_o^3 - \left(\frac{C_4}{E}\right) - \left(\frac{2C''_6}{E}\right) = 0 \quad , \tag{41}$$

where $C''_6 = C_6 + C'_6$. Equation (41) can readily be solved numerically. The value of r_o then determines b_o by

$$b_o^2 = r_o^2 \left[1 - V(r_o)/E\right] \quad . \tag{42}$$

The value of b_o can then be used to calculate $\sigma^c(E)$ and hence $\sigma^c{}_m(T)$. A comparison of the calculated $\sigma_m{}^c(T)$ values with the experimental values for highly polar OH [81] and NH [82] radicals in quenching with a wide variety of species, yields acceptable agreement.

The model is limited since a purely one dimensional potential which assumes all the physical interaction mechanisms are in their optimal orientations is calculated. Also, a common quenching probability is assumed once the complex has formed.

3.10.1.2 Repulsive interaction

A theory first developed by Schwartz, Slawsky and Herzfeld (SSH) has gained universal acceptance as a basis for describing energy transfer processes, in simple molecules, that are governed by a repulsive interaction.

For a linear system A + BC where A is the collision partner and BC is the diatomic of interest, the probability P_{nm} of a transition between two levels is given by [60]

$$(P_{nm})_{SSH} = \left(\frac{4A^2BC}{(B+C)(A+B)^2}\,\mu\right) \cdot 1/2 \cdot \left(\frac{2\pi}{3}\right)^{1/2} \cdot \left(\frac{\Theta'}{\Theta}\right) \left(\frac{\Theta'}{T}\right)^{1/6}$$

$$\cdot \exp\left(-3/2 \left(\Theta'/T\right)^{1/3}\right) \cdot \exp\left(\Theta/2T\right) \cdot \exp\left(\varepsilon/kT\right) \quad , \qquad (43)$$

where n,m are respectively the upper and lower levels
A,B,C are the masses of the respective atoms, A,B,C

$$\Theta' = 4\pi^2\,\mu L^2\,\omega^2/k \qquad (44)$$

$$\Theta = \frac{h\omega}{2\pi k} \qquad (45)$$

ε is the well depth of the interaction

ω is the (diatomic) oscillator frequency (s^{-1})

L is the distance of approach at which energy transfer will occur

μ is the collision reduced mass.

Under isothermal experimental conditions the probability of transfer will be dominated by the term $\exp(-\,{}^{3}/2\,(\,\Theta'/T)^{1/3})$ and the probability should scale as

$$\ln \langle p \rangle = A - \mu^{1/3} \quad , \qquad (46)$$

where A is an arbitrary constant.

3.11 Energy Transfer in the B and B′ States of SiCl : Comparison of Experiment and Theory

The numerous experimental observations in this work and all other spectroscopic investigations on SiCl have indicated that both the $B^2\Sigma^+$ and $B'\ ^2\Delta$ states are unperturbed. This observation is reinforced by the cumulative evidence that the dissociation limit of the ground state is below T_o of the B state; as determined by the various spectroscopic and thermochemical estimates of D_o and the possibility of spontaneous predissociation in $v' = 0$ of the $B^2\Sigma^+$ state.

In section 3.9 both the total quenching of the B′ state and the B′ to B partial quenching cross sections were shown, for several gases,

to be at least as large as those that may be estimated from the hard sphere collision diameter. Such efficient quenching strongly indicates that the dipole matrix elements for quenching are large. Hence the interaction potential produced by the 'collision transient' of low symmetry must contain surfaces that will correlate with Δ, Π and Σ^+ symmetry in the 'quenching' products and 'reactants'.

3.11.1 Energy transfer from the B state

It was observed in section 3.7.4 that a very small amount of quenching from $v' = 3$ of the B state did occur to $v' = 1$ of the B' state. The data was considered sufficiently uncertain not to attempt an analysis. This is a result of the very small number of collisions suffered, on average, by a molecule in the B state.

However, given the large cross sections for transfer from the B' to B states, observation of the reverse B to B' process is entirely consistent with the principle of microscopic reversibility (although, in particular in this case, transfer from B' $v' = 1$ to B $v = 3$ was not observed).

3.11.2 Energy transfer from the B' state

At first sight the B' state appears to show quite nefarious energy transfer behaviour. However, considerable insight may be gained by tackling the observed quenching and product state distributions from two different viewpoints:

1) What is it that is controlling the total quenching behaviour observed for each collider and for each v'?
(See Tables 3.18 - 3.20)

2) What is it that is controlling the observed product state distributions (i.e. partial cross sections) in the B state for each v′ and each collider?
(See Tables 3.16,3.17,3.11,3.13 and Figure 3.25).

These two questions will now be tackled separately with considerable emphasis being placed on trying to find correlations predicted by the energy transfer models outlined in sections 3.10.1.1 and 3.10.1.2. To this end the relevant data necessary for the calculation of the theoretical 'cross sections' as predicted by the models were gathered into Table 3.22. The theoretically predicted quenching magnitudes are presented in Table 3.23.

As an aid to the subsequent discussions on the energy transfer processes an approximate energy level diagram was constructed and is presented in Figure 3.36. Labelled on the diagram are the approximate energy defects for transitions between the various B and B′ state levels.

3.11.2.1 Discussion of total quenching behaviour in the B′ state

The experimentally determined relative cross sections for v′ = 0 and 1 of the B′ state were plotted against the theoretical quenching magnitudes presented in Table 3.23. In fact, both the numerical values and the values including the error bar associated with each datum were plotted. It was found that the plot against the well depth parameter $(\varepsilon/k)^{1/2}$ gave a poorer correlation as measured by the linear correlation coefficient, r, when the statistical errors were included in the plot but that for all other cases a much better correlation was achieved. For the cases, not including the well depth model, the correlation coefficient when the statistical error was not included was less than or equal to 0.55, this implies that the data had only an approximately 60% chance that they were correlated.

Therefore, as expected, the inclusion of additional uncertainty improved the overall fits. For the case of the well depth parameter the correlation coefficient dropped from 0.9 to nearer 0.7 when the uncertainties were included. This observation was taken to indicate that there was a datum which was relatively certain but which was clearly anomalous relative to the rest of the data. Examination of Table 3.19 readily indicated this datum to be the cross section for H_2.

The data in Table 3.19 were then replotted, without the datum for H_2, against the various models. Since the number of data points had reduced the correlation coefficient improved for each case. However, for the plot against the well depth parameter $(\varepsilon/k)^{1/2}$ the correlation coefficient was now ~ 0.99, which indicated that their was a probability of at least 99% that the data were correlated.

TABLE 3.22: Data used to calculate the theoretical quenching magnitudes from the 4 models outlined in Section 3.10.1.1. The numbers in square brackets represent the relevant reference from which the data were obtained.

Gas	$(\varepsilon/k)^{1/2}$ [80]	$\mu/(D)$	$Qx10^3/esu\ m^2$ [84]	$\alpha/(Å^3)$ [85]	I.P/(eV) [44][8][86]	
He	3.2	0	0	0.20	26.6	
Ar	11.0	0	0	1.63	15.8	
H_2	6.1	0	+0.66	0.79	15.43	
N_2	9.7	0	-1.52	1.76	15.58	
CO_2	14.0	0	-4.3	2.65	13.77	
CF_4	12.1	0	0	2.90	13	a)
CH_4	12.1	0	0	2.60	12.71	

a) A value of 13 eV was assumed.

TABLE 3.23: Calculation of various quenching magnitudes using the models outlined in sections 3.10.1.1 and 3.10.1.2. Calculations using the model of Selwyn and Steinfeld are tabulated as σ_{SS}. For the approach of Thayer and Yardley the data are tabulated as σ_{TY}. For SSH theory the data were tabulated as σ_{SSH}. The quenching magnitudes estimated by σ_{TY} and σ_{SS} have arbitrary units while those for σ_{SSH} are $(amu)^{1/3}$.

Gas	$(\varepsilon/k)^{1/2}$	$\sigma_m^{calc}(T)/(Å)^2$ a)	σ_{SS}	σ_{TY} b)	$\sigma_{SSH}/(amu)^{1/3}$
He	3.2	24	0.78	0.60	1.85
Ar	11.0	47	4.16	6.40	3.45
H_2	6.1	40	0.84	1.40	1.48
N_2	9.7	43	2.92	3.16	3.19
CO_2	14.0	40	2.66	1.35	3.51
CF_4	12.1	57	2.85	1.22	3.95
CH_4	12.1	55	2.74	3.68	2.77

a) The calculation of the classical quenching cross section requires the dipole moment of the excited state, SiCl (B′), which was calculated to be 1.0D [42]. Also, since the polarisability was required, a very approximate estimate based on an approximate bond order of 2 for the radical was made, this yielded via a comparison to other diatomics [85] a value of 2 $Å^3$. The polarisability is common to calculation for all gases. The I.P. of the radical in the B′ state was estimated from the term energy and the I.P. of the ground state radical given by Hudgens [41] from which a value of 3.0 eV was obtained.

b) As may be seen from Table 3.22 the polar-polar interaction term in the model of Thayer and Yardley does not enter into these calculations.

FIGURE 3.36: Approximate energy level diagram of the B and B′ states, with approximate energy defects for transitions between the various B and B′ state levels indicated.

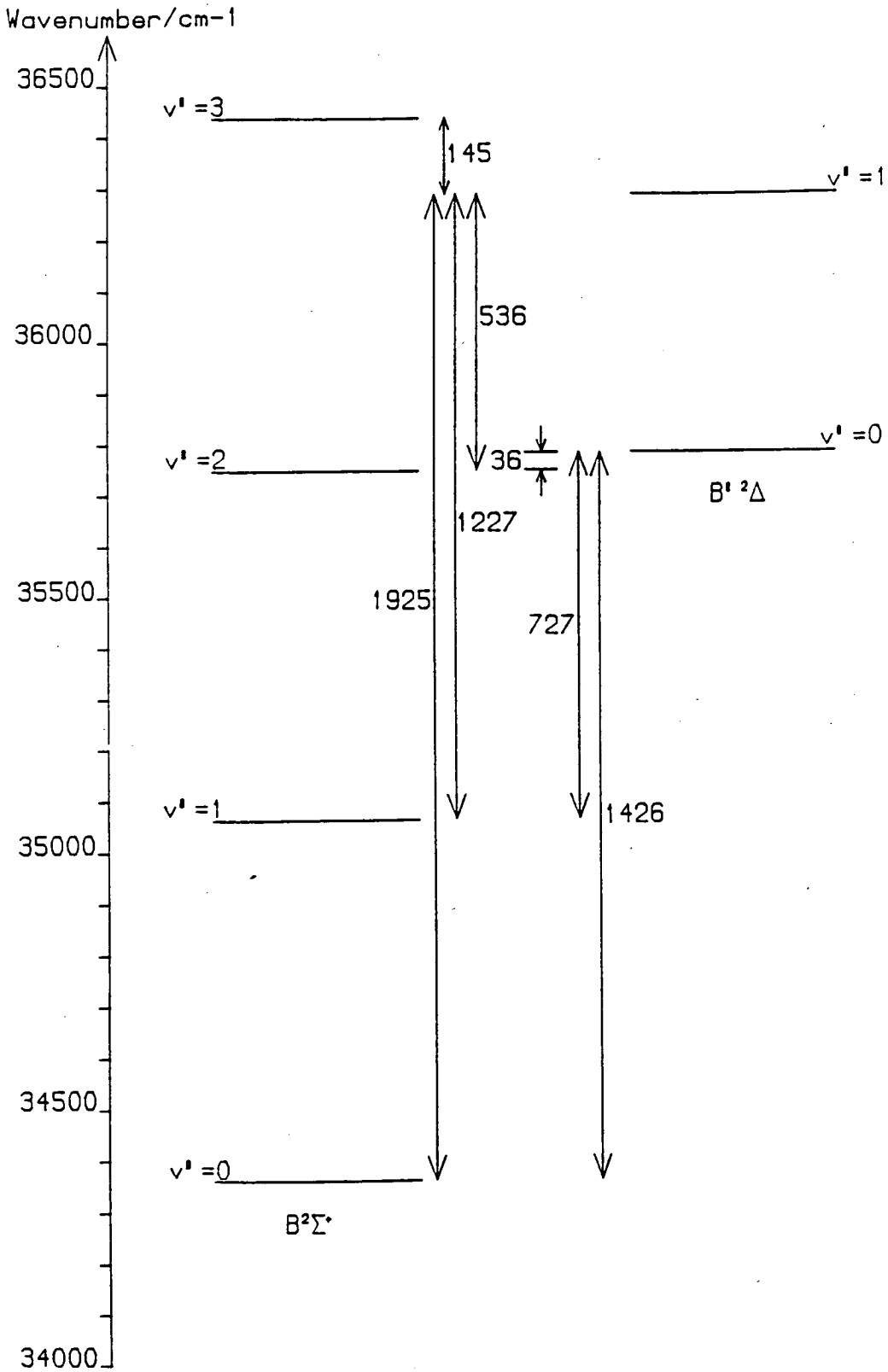

For v′ = 1 a similar procedure was followed, with a similar conclusion being drawn that the best correlation between the experimental and predicted quenching magnitudes was obtained for the well depth parameter, excluding the datum for H_2. In this case r ~ 0.94.

The data for v′ = 0 and 1 of the B′ state are presented in Figure 3.37. The logarithm of the relative total removal cross sections σ_r were plotted against the well depth parameter $(\varepsilon/k)^{½}$. For v′ = 1 all the data were displaced by +2.0 on the ordinate axis to allow a separation of the data sets.

It was concluded therefore that the total removal of the B′ state was governed by long range attractive forces. While this conclusion is somewhat at odds with the observation in section 3.7.3 where variation of the excitation wavelength did not lead to apparent change in the removal rate, the conclusion drawn in section 3.7.3 was made with sufficient circumspection as not to be viewed as contradictory.

Hydrogen has a rotational constant near 60 cm^{-1} [8] and at room temperature most of the rotational population will be in J = 0 and 1. Hydrogen exists in two forms, ortho and para-H_2, determined by the nuclear spin orientation of the nuclei. Hence, only transitions in which ΔJ is even are allowed. Rotational energy transfer has, for several cases, been found to be governed by statistical energy gap power laws of the form [87] [88]

$$k \propto c \left\{ \frac{\Delta E}{B} \right\}^{-a}, \qquad (47)$$

where, k is the rate constant for a particular transition with exchange of energy ΔE between rotational and translational degrees of freedom, B is the rotational constant and c and a are variable parameters to the fit of the experimental data. Expression (47) indicates that small ΔJ transitions will always be favoured. For a transition J=1 to J=3 an energy of 600 cm^{-1} is calculated while for J=0 to J=4 an energy of 1200 cm^{-1} is calculated.

FIGURE 3.37: Plots for v′=0 and 1 of the B′ state for the relative total removal cross-sections against the well depth parameter of Parmenter and Seaver. The data for v′=1 were displaced by 2.0 relative to their actual positions. The relative cross sections were all measured with respect to the total removal rates for v′=0 and 1 of the B′ state by argon having a normalised rate of 1.0. The data for H_2 were not included in the least squares fit straight lines.

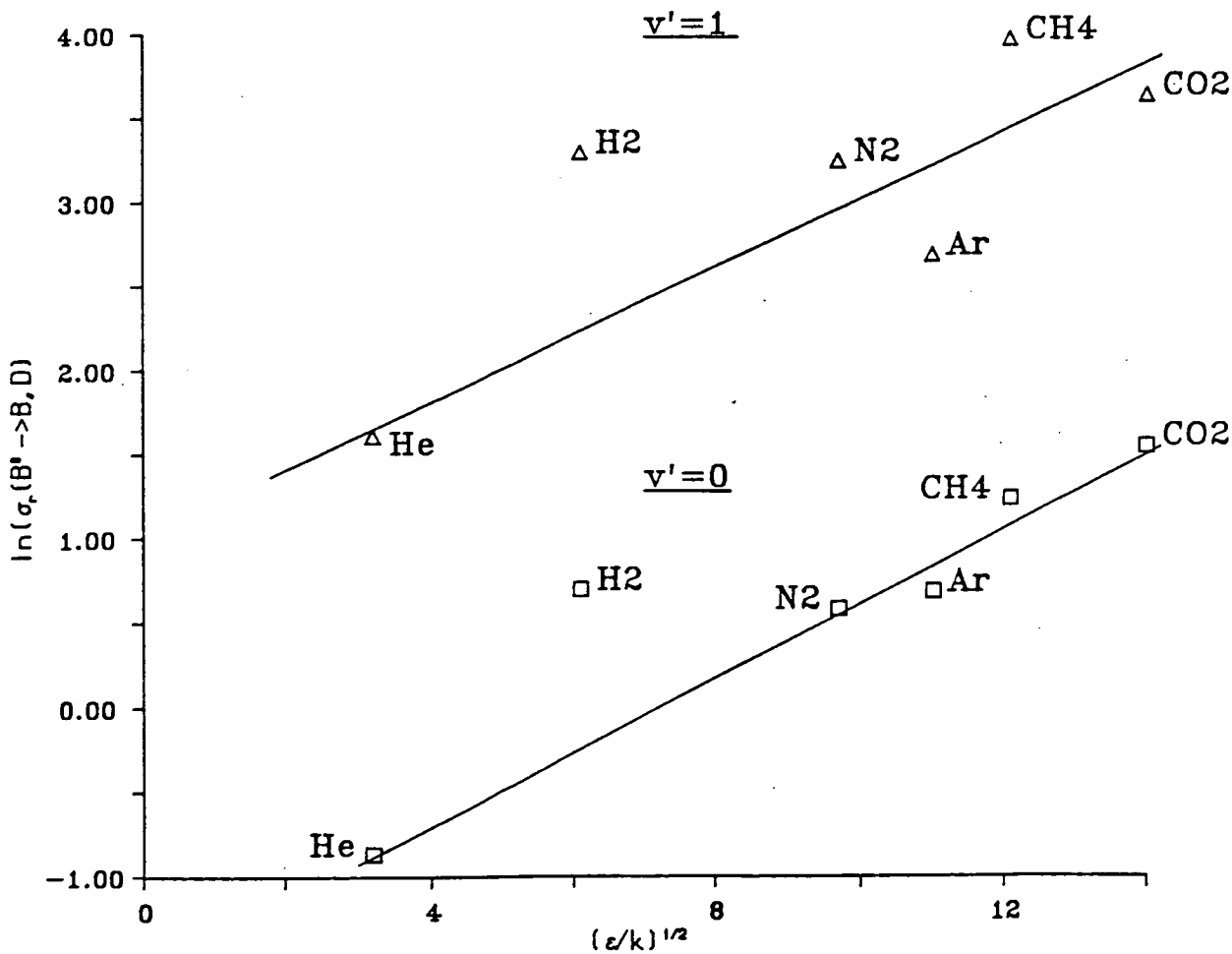

Figure 3.25 indicates that H_2 has a strong propensity to populate $v' = 1$ of the B state from either $v' = 0$ or 1 of the B′ state. Also, Figure 3.36 indicates that the energy defects for these transitions are respectively 727 and 1227 cm^{-1}. Additionally, it should be noted that total removal of the B′ state is derived mostly from the B′ to B process. Hence, it is proposed, that a near resonant energy transfer process for H_2 from electronic to rotational energy may contribute to its apparently anomalously large quenching cross sections.

3.11.2.2 Discussion of the B′ to B quenching behaviour

The energy transfer studies for the $v' = 0$ and 1 levels of the B′ state show similar, but not identical trends, for transfer to the B state. As may be observed from Figure 3.25 the polyatomic colliders CH_4 and CF_4 are very efficient at populating $v' = 0$ of the B state but the simpler species favour much more strongly $v' = 1$ and 2 of the B state. The trend to populate lower vibrational levels of the B state is reduced following initial population of $v' = 1$ of the B′ state. Also, the quenching cross sections for B′ to B transfer are all smaller for initial population of $v' = 1$, by a factor ranging up to about 8 for CF_4. However, CH_4 and CF_4 always show very strong B′ to B transfer rates relative to the other gases.

Following the methodology of the previous section the total B′ to B cross sections (summed over all B state levels) were plotted against the various quenching magnitudes predicted by the models outlined previously. However, in this case no good correlations could be found for any of the models. The best fit was again obtained for the well depth model of Parmenter and Seaver with a correlation coefficient of 0.70, while the other models produced correlation coefficients near 0.5. Figure 3.38 presents the plots for the Parmenter and Seaver model (3.38a), and for the repulsive interaction model SSH, (3.38b).

As in section 3.11.2.1 an examination of the colliders was performed with a view to identifying potential particular resonant energy transfer effects. Because the polyatomic colliders CH_4 and CF_4 showed

FIGURE 3.38: Plots of the total B' v'=0 to B removal cross sections against: a) the well depth parameter of Parmenter and Seaver and b) the collision reduced mass term indicative of a repulsive interaction as predicted by the SSH theory.

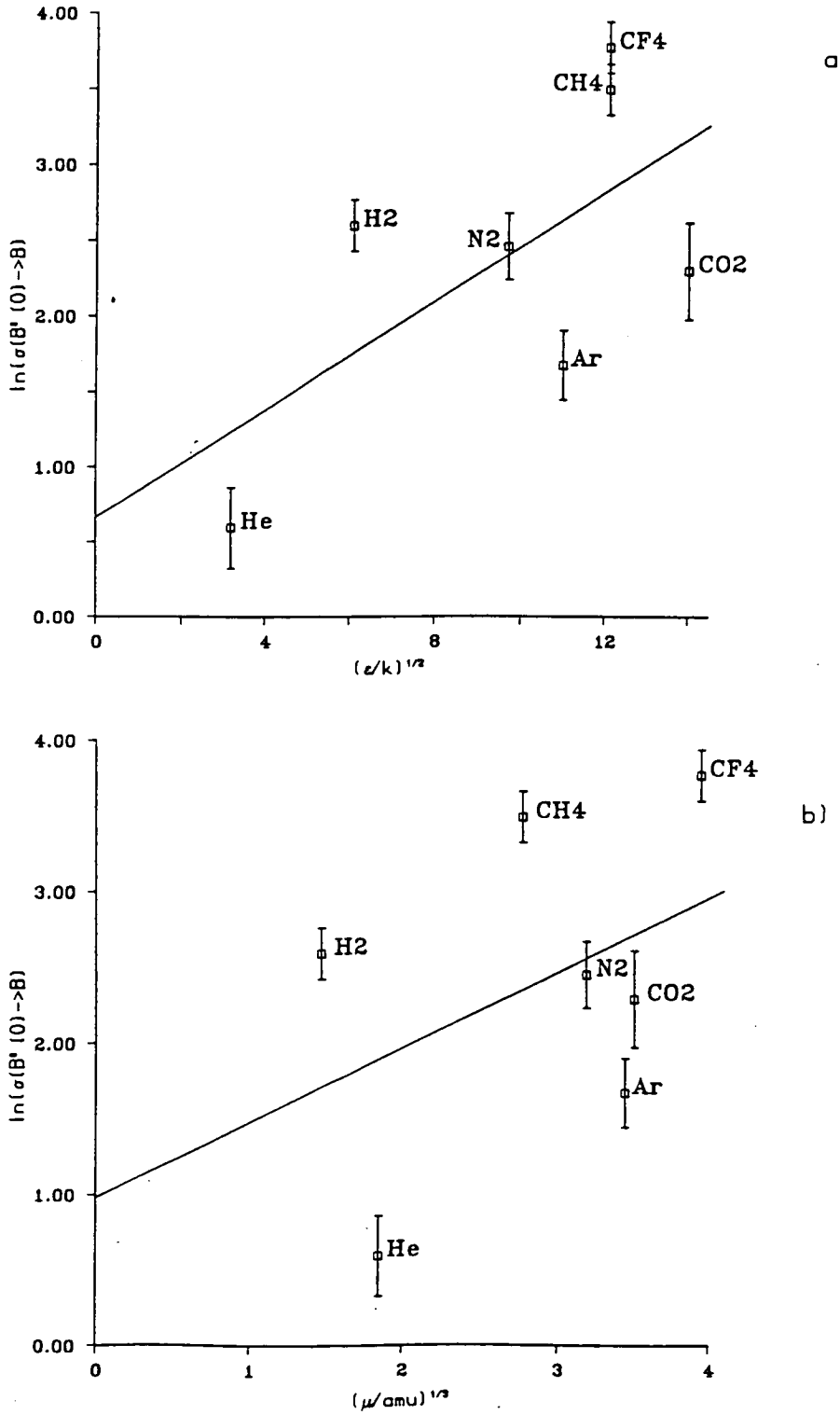

the strongest transfer cross sections an obvious candidate for resonant energy transfer lies with electronic to vibration transfer. The vibrational frequencies of the molecules used as collision partners are summarised in Table 3.24. Examination of Table 3.24 indicates that both CH_4 and CF_4 have a vibrational mode near 1300 cm^{-1}. Also, the B' v' = 0 to B v' = 0 energy defect is approximately 1400 cm^{-1} (see Figure 3.36). Transfer from v' = 1 of the B' state to B v' = 1 has a defect of ~ 1200 cm^{-1} while transfer to B v' = 0 has a defect of ~ 1900 cm^{-1}. For transfer from B' v' = 1 an 'acceptor' vibrational mode for CF_4 can be found but for CH_4 one is not readily evident. Carbon dioxide has a vibrational mode near 1400 cm^{-1} but does not show a strong propensity to transfer to B v' = 0. An important additional observation however is that the 'acceptor' modes of both CH_4 and CF_4 are infrared active while that of CO_2 is not. The important feature of this infrared active mode would be that it may be able to produce the large dipole matrix elements required to produce the observed quenching behaviour between the B' and B states.

It has been observed above and in section 3.11.2.1 that B' to B transfer occurs in an 'anomalous' manner to v' = 0 and 1 of the B state, with this behaviour being most pronounced for v' = 0 of the B' state. Hence, separate consideration was given to near-resonant transfer to v' = 2 of the B state. By using the previously determined product state distributions and the B' to B quenching cross sections, the partial cross sections for transfer to B v' = 0, 1 and 2 were determined for both v' = 0 and 1 of the B' state. For transfer from v' = 0 of the B' state these partial cross sections were found to correlate extremely well to the attractive force model of Parmenter and Seaver, while for transfer from v' = 1 no good correlation could be found. The partial cross sections for transfer to B v = 2 from v' = 0 and 1 of the B' state were summarised in Table 3.25 and the data for v' = 0 of the B' state were presented pictorially in Figure 3.39.

TABLE 3.24: Vibrational frequencies of the collision partners used in this work, with relevant data obtained from references [8][86][89]

Gas	Mode	Symmetry	Frequency/cm^{-1}	Infra-red active
H_2	ν_1		4395	No
N_2	ν_1		2360	No
CO_2	ν_1		1388	No
	ν_2		667	Yes
	ν_3		2349	Yes
CH_4	ν_1	a_1	2917	No a)
	ν_2	e	1534	Yes
	ν_3	f_2	3019	Yes
	ν_4	f_2	1306	Yes
CF_4	ν_1	a_1	909	No
	ν_2	e	435	No
	ν_3	f_2	1281	Yes
	ν_4	f_2	632	Yes

a) Observed in the infrared through Coriolis interaction with ν_4.

TABLE 3.25: Partial cross sections for transfer from initially prepared $v' = 0$ and 1 of the B′ state to $v' = 2$ of the B state. Numbers in parentheses represent the uncertainty in the data and should be applied to the last significant figures.

Gas	$\sigma(B'(0)-B(2))/(Å^2)$	$\sigma(B'(1)-B(2))/(Å^2)$
He	0.56 (16)	0.64 (14)
Ar	3.39 (77)	1.04 (35)
H_2	1.06 (18)	1.03 (18)
N_2	4.29 (96)	1.25 (16)
CO_2	5.54 (1.79)	0.39 (18)
CF_4	4.79 (80)	1.40 (30)
CH_4	5.56 (95)	1.00 (28)

FIGURE 3.39: Plot of partial removal cross section from B′ v′=0 to B v′=2 against the well depth parameter of Parmenter and Seaver.

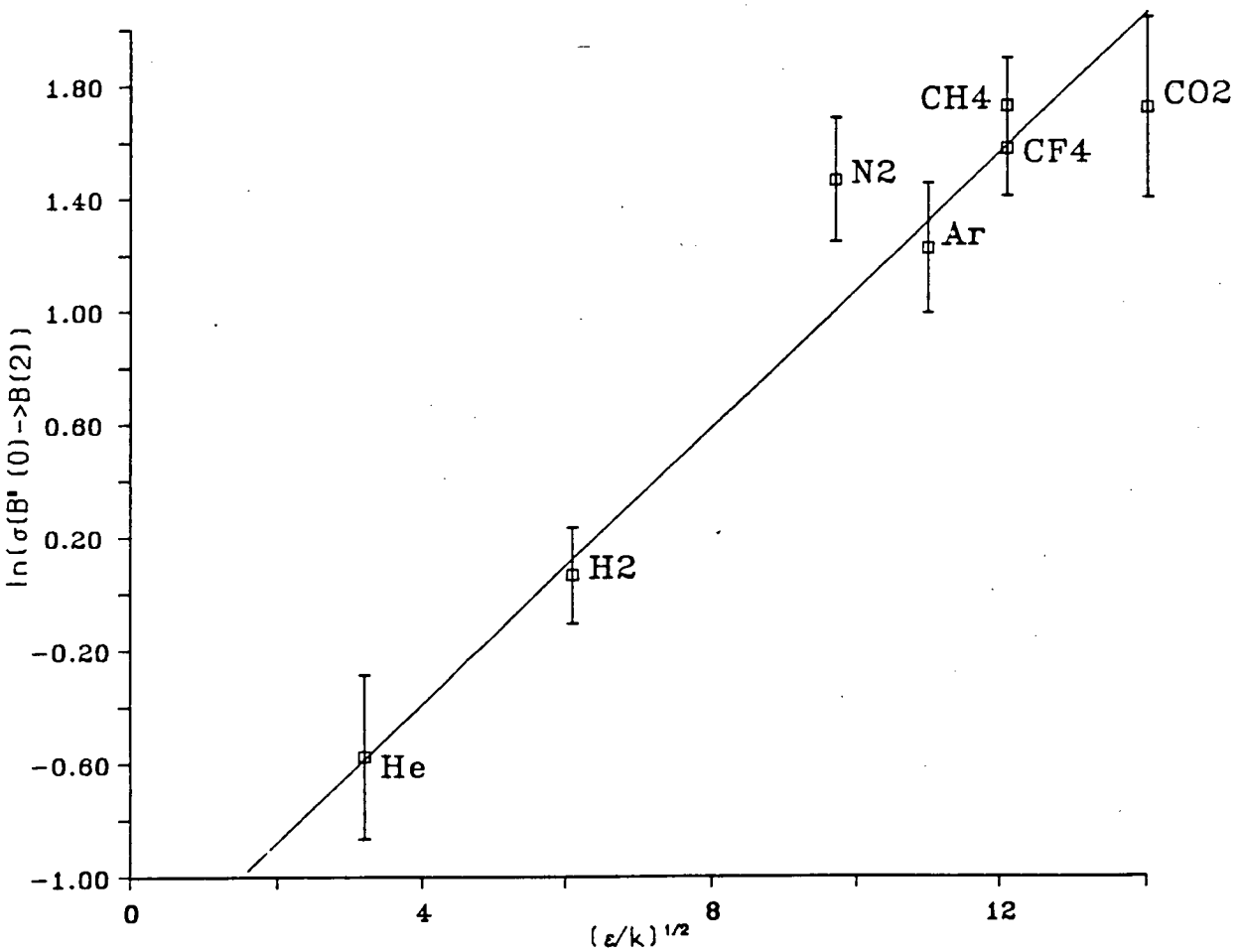

3.11.2.3 Comparison of the total and partial quenching cross sections for the B′ state

Having investigated, separately, both the total removal and the partial removal (to the B state) quenching cross sections a useful comparison may now be drawn.

For the removal to the B state, H_2 and the polyatomic colliders CH_4 and CF_4 were shown to have 'anomalously' large cross sections. Possible mechanisms for these observations have been put forward. An important point however is that the total removal cross section has been found to correlate well with attractive forces. This is partly evidenced by the total removal cross section for CO_2 having a magnitude comparable to those of CH_4 and (probably) CF_4.

For the simple species for which no specific resonant mechanisms could be envisaged the quenching cross section appears to partition with no great propensity between the B state and the other available channel(s).

Hydrogen stands out separately as having a total quenching cross section in excess of that predicted by an attractive interaction. This is viewed as being due possibly to the high efficiency for electronic to rotational transfer.

3.12 CONCLUSIONS

This chapter has covered many aspects of the spectroscopy and collision dynamics of the chlorosilylidyne radical. The most significant observations are summarised below.

1) An examination of the LIF excitation spectra of the radical allowed a ready identification, in agreement with the literature, of the B and B′ states and highlighted the features of interest for subsequent energy transfer studies. Within the bandwidth limitations of the laser system, both states appeared spectroscopically isolated, again in accord with previous results.

2) Measurement of individual transition probabilities, $p_{v'v''}$ for the $B^2\Sigma^+ - X^2\Pi$ transition under collisionless conditions indicated that the transition dipole moment was essentially constant with internuclear separation. These data were then used to determine vibrational populations in the B state in subsequent energy transfer studies.

   Estimates of the $B'^2\Delta - X^2\Pi$ transition probabilities were also reported for $v' = 0,1$ of the B′ state. In this case the transition dipole moment was thought to be a strongly decreasing function of internuclear distance.

3) Energy transfer from $v' = 3$ of the B state was observed but was too weak to allow a reliable discussion.

4) Total quenching cross sections for removal from $v' = 0$ of the B′ state for a variety of gases were reported while only relative cross sections were reported for $v' = 1$. The total quenching cross sections agree, within the experimental uncertainty, to those reported elsewhere for a subset of the gases in this study. The magnitude of the total quenching cross sections appear to be correlated with long range attractive forces between the collision pair.

5) Partial cross sections for transfer to the B state, for the same gases, were measured for v′ = 0 and 1 of the B′ state. A discussion of these cross sections was presented. No consistent interpretation for the total B′ to B cross sections could be found. However the importance of energy resonant transfer effects were highlighted for the polyatomic colliders. For the partial cross sections of near-resonant B′ v′ = 0 to B v′ = 2 transfer a good correlation was again found with long range attractive forces.

In closing this discussion it is clear that a deal of uncertainty still exists as to the interpretation of energy transfer in the B and B′ states of SiCl, which may only be cleared up by a combination of further experimental and theoretical investigations. Thus, the SiCl radical appears to present a challenging yet fruitful molecule for the study of electronic quenching behaviour.

Finally, it appears that LIF studies via the B state of SiCl would present a useful diagnostic methodology for probing ground state SiCl distributions in dry processing plasmas involving chlorine and silicon containing species and that interpretation of emission studies without taking account of quenching processes may be fraught with difficulties [7].

NOTES

i) Determining spectral areas using a method of image analysis.

The method described below details a relatively simple, but fully automated method for measuring band intensities. The work was performed on a Kontron IBAS image analyser available at Unilever Research, Port Sunlight Laboratory, Bebington, Merseyside. The method entails the following:

1) Defining a baseline for each spectral band.

2) Capturing the whole spectrum, in one image, in the image analyser.

3) Identifying as separate objects individual spectral bands.

4) Determining the area (sum of all pixels in the object) of each band.

5) In the case of SiCl, averaging over both spin orbit components to determine the desired band intensity.

REFERENCES

1. S.M. Irving, Solid State Technol., 14 47 (1971).
2. S.M. Irving, K.E. Lemons and G.E. Bobos, U.S. Patent No. 3 615 956 (1969).
3. M.A. Butler and D.S. Ginley, J. Mater. Sci., 15 1 (1980).
4. A. Madan, S.R. Ovshinsky and E. Benn. Phyl. Mag., 40 259 (1979).
5. G. Fortunato, F. Evangelisti, G. Bruno, P. Capezzuto, F. Cramarossa, V. Avgelli and R. Muri, J. Non-Cryst. Solids, 46 95 (1981).
6. N. Mayo, U. Carmi, I. Rosenthal, R. Arni, R. Manory and A. Grill, J. Appl. Phys., 55 4404 (1984).
7. G. Bruno, P. Capezzuto, G. Cicala and F. Cramarossa, Plasma Chem. Plasma Proc., 6 109 (1986).
8. K.P. Huber and G. Herzberg in 'Molecular Spectra and Molecular Structure Vol. IV. Constants of Diatomic Molecules' (Van Nostrand, New York 1979).
9. R.K. Asundi, M. Karim and R. Samuel, Proc. Phys. Soc. (London), 50 581 (1938).
10. R. Cornet and I. Dubois, J. Phys. B., 10 L69 (1977).
11. D. Sameith, J.P. Mönch, H.J. Tiller and K. Shade, Chem. Phys. Lett., 128 483 (1986).
12. M.D. Rowe, J. Chem. Soc. Far. Trans. II, 84 191 (1988).
13. H.R. Ihle, C.H. Wu, M. Miletic and K.F. Zmbov, Adv. Mass. Spec., 7A 670 (1978).
14. J.W. Coburn, Plasma Chem. Plasma Proc., 2 1 (1982).
15. Y. Matsumi, S. Toyoda, T. Hayashi, M. Miyamura, H. Yoshikawa and S. Komiya, J. Appl. Phys., 60 4102 (1986).
16. W. Jevons, Proc. Roy. Soc. (London) Ser. A., 89 187 (1914).
17. W. Jevons, Proc. Roy. Soc. (London) Ser. A., 106 174 (1924).
18. A.C. Datta, Z. Phys., 78 486 (1932).
19. W. Jevons, Proc. Phys. Soc. (London), 48, 563 (1936).
20. S.N. Garg, Pro. Nat. Acad. Sci. India, A19 23 (1950).
21. K. Wieland, Z. Phys. 133 229 (1952).

REFERENCES (Cont/d.)

22. K. Wieland and M. Heise, Bull. Sci. Fac. Chim. Ind. i Bologna 10 12 (1952).
23. R.F. Barrow, G. Drummond and S. Walker, Proc. Phys. Soc. (London), A67 186 (1954).
24. I.E. Ovcharenko, L.N. Tunitskii and V.I. Yakutin, Opt. Spectrosc. 8 393 (1960).
25. I.E. Ovcharenko and Y.Y. Kusyakov, Opt. Spectrosc. 20 14 (1966).
26. B.A. Thrush, Nature, 186 1044 (1960).
27. R.D. Verma, Can. J. Phys., 42 2345 (1964).
28. I.E. Ovcharenko, Y.Y. Kuzyakov and V.M. Tatesvkii, Opt. Spectrosc. Mol. Spectrosc. Suppl. 2 6 (1963).
29. H. Bredohl, I. Dubois, Y. Houbrechts and H. Leclerq, J. Phys. B., 11 437 (1978).
30. H. Bredohl, P. Demoulin, Y. Houbrechts and F. Mélen, J. Phys. B., 14 1771 (1981).
31. F. Mélen, Y. Houbrechts, I. Dubois, B.L. Huyên and H. Bredohl, J. Phys. B., 14 3637 (1981).
32. H. Bredohl, R. Cornet, I. Dubois and F. Mélen, J. Phys. B., 15 727 (1982).
33. M. Tanimoto, S. Saito, Y. Endo and E. Hirota, J. Mol. Spec., 103 330 (1984).
34. R.K. Mishra and B.N. Khanna, Curr. Sci., 38 361 (1969).
35. S.B. Rai, J. Singh, K.N. Upadhya and D.K. Rai, J. Phys. B., 7 415 (1974).
36. G. Meijer, B. Jansen, J.J. Ter Mullen and A. Dynamas, Chem. Phys. Lett., 136 519 (1987).
37. G. Meijer, W. Ubachs, J.J. Ter Mullen and A. Dynamus, Chem. Phys. Lett., 139 603 (1987).
38. A. Corney in 'Atomic and Laser Spectroscopy' (Clarendon Press, Oxford 1986).
39. A.V. Mandrugin, L.A. Kuznetsova and Y.Y. Kuzyakov, Spectry, Lett., 17 259 (1989).

REFERENCES (Cont/d.)

40. M. Venkataramanaiah and S.V.J. Laksman, J. Quant. Spect. Rad. Trans., 26 11 (1981).
41. R.D. Johnson III, E. Fang and J.W. Hudgens, J. Phys. Chem., 92 3880 (1988).
42. R.K. Gosavi and O.P. Strauz, Chem. Phys. Lett., 131 243 (1986).
43. J. Singh and P.S. Dube, Ind. J. Pure. Appl. Phys., 9 164 (1971).
44. C.E. Moore 'Atomic Energy Levels' vol. I National Bureau of Standards (1971).
45. G. Herzberg in 'Molecular Spectra and Molecular Structure I. Spectra of Diatomic Molecules', (Van Nostrand, New York 1950).
46. A. Maitland and R.D.H. Brown, J. Chem. Ed., 60 203 (1983).
47. R.D. Verma, Can. J. Phys., 40 586 (1962).
48. R.D. Verma and R.S. Mulliken, J. Mol. Spec., 6 419 (1961).
49. S.P. Karna and F. Grein, J. Mol. Spec., 122 28 (1987).
50. R.N. Zare, J. Chem. Phys., 40 1934 (1964).
51. M. Farber and R.D. Srivastava, J. Chem. Soc. Far. Trans. I. 73 1672 (1977).
52. J.W. Hastie and J.L. Margrave, J. Phys. Chem., 73 1105 (1969).
53. J.B. Jeffries, S.R.I. International, Menlo Park, California USA, whom we gratefully acknowledge for the supply of some of his results in advance of publication.
54. 'Wavelengths and Transition Probabilities for Atoms and Atomic Ions', National Bureau of Standards 1980.
55. D.A. Case, G.M. McClelland and D.R. Herschbach, Mol. Phys., 35 541 (1978).
56. K.P. Lawley and R. Wheeler, J. Chem. Soc. Far. Trans. II, 77 1133 (1981).
57. M. Weissbluth in 'Atoms and Molecules', (Academic Press, New York 1978).
58. L.T. Earls, Phys. Rev., 48 423 (1935).
59. J.D. Lambert in 'Vibrational and Rotational Relaxation in Gases', (Clarendon Press, Oxford 1977).

REFERENCES (Cont/d.)

60. J.T. Yardley in 'Introduction to Molecular Energy Transfer', (Academic Press, New York 1980).
61. K.F. Freed, Adv. Chem. Phys., 47 291 (1981).
62. D.H. Katayama, T.A. Miller and V.E. Bondybey, J. Chem. Phys. 71 1662 (1979).
63. R.A. Copeland, M.J. Dyer and D.R. Crosley, J. Chem. Phys. 82 4022 (1985).
64. J.B. Jeffries, R.A. Copeland and D.R. Crosley, J. Chem. Phys. 85 1898 (1986).
65. J.B. Jeffries, K. Kohse-Höinghaus, G.P. Smith, R.A. Copeland and D.R. Crosley, Chem. Phys. Lett., 152 160 (1988).
66. R.D. Kenner, F. Rohrer and F. Stuhl, J. Phys. Chem., 93 7824 (1989).
67. P. Heinrich, R.D. Kenner and F. Stuhl, Chem. Phys. Lett., 147 575 (1988).
68. R.D. Kenner, S. Pfannenberg and F. Stuhl, Chem. Phys. Lett., 156 305 (1989).
69. E.H. Fink and F.J. Comes, Chem. Phys. Lett., 25 190 (1974).
70. T.A. Carlson, J. Copley, N. Durii, P. Erman and M. Larsson, Chem. Phys., 42 81 (1979).
71. K. Yamasaki and S.R. Leone, J. Chem. Phys., 90 964 (1989).
72. G. Jihua, A. Ali and P.J. Dagdigian, J. Chem. Phys., 85 7098 (1986).
73. A. Ali, G. Jihua and P.J. Dagdigian, J. Chem. Phys., 87 2045 (1987).
74. D.H. Katayama, T.A. Miller and V.E. Bondybey, J. Chem. Phys., 72 5469 (1980).
75. D.H. Katayama, J. Chem. Phys., 81 3495 (1984).
76. M.H. Alexander and G.C. Corey, J. Chem. Phys., 84 100 (1986).
77. I.J. Wysong, J.B. Jeffries and D.R. Crosley, J. Chem. Phys., 91 5343 (1989).
78. J.E. Selwyn and J.I. Steinfeld, Chem. Phys. Lett., 4 217 (1969).

REFERENCES (Cont/d.)

79. C.A. Thayer and J.T. Yardley, J. Chem. Phys., 57 3992 (1972).

80. H.M. Lin, M. Seaver, K.Y. Tang, A.E.W. Knight and C.S. Parmenter, J. Chem. Phys., 70 5442 (1979).

81. P.W. Fairchild, G.P. Smith and D.R. Crosley, J. Chem. Phys., 79 1795 (1983).

82. A. Hofzumahaus and F. Stuhl, J. Chem. Phys., 82 3152 (1985).

83. R.P. Wayne in 'Singlet Oxygen Vol.1 Physical-Chemical Aspects', ed A.A. Frimer (CRC Press).

84. D.E. Stogryn and A.P. Stogryn, Mol. Phys., 11 371 (1966).

85. J.O. Hirschfelder, C.F. Curtiss and R.B. Bird, in 'Molecular Theory of Gases and Liquids' 2nd ed (Wiley, New York 1964).

86. G. Herzberg in 'Molecular Spectra and Molecular Structure III. Electronic Spectra and Electronic Structure of Polyatomic Molecules', (Van Nostrand, New Jersey 1967).

87. T.A. Brunner, R.D. Driver, N. Smith and D.E. Pritchard, J. Chem. Phys., 70 4155 (1979).

88. T.A. Brunner, N. Smith, A.W. Karp and D.E. Pritchard, J. Chem. Phys., 74 3324 (1981).

89. Tables of Molecular Vibrational Frequencies, Nat. Stand. Ref. Data. Ser., Nat. Bur. Stand. (U.S), 39 (1972).

CHAPTER 4

RESONANCE ENHANCED MULTIPHOTON IONISATION SPECTROSCOPY OF HYDROGEN IODIDE: A STUDY USING THE REACTION H + I_2 ⟶ HI + I

4.1 INTRODUCTION

At first glance the hydrogen halides HX (X=F,Cl,Br,I) appear to be an almost trivially simple family of molecules, being composed only of the simplest atom, hydrogen and a halogen atom which has a p^5 atomic configuration. As a result of their apparent simplicity and because of the large separation between their individual vibrational and rotational levels, they have been the subject of a wide variety of experimental and theoretical investigations. In particular they have become one of the most widely studied groups of molecules in the field of reaction dynamics, see for example [1][2][3] and references therein.

The interest in these molecules is however also derived from a more practical level. Of current interest is the environmental impact of molecules containing odd atom numbers of chlorine and bromine. These atoms become released into the stratosphere by, typically, the photodissociation of chlorinated and brominated hydrocarbons. They are then active in some of the catalytic cycles of ozone destruction [4]. The major reservoir species for the atoms are HCl and HBr, generated normally by hydrogen abstraction from hydrocarbon species. Hence a precise knowledge of the photochemistry and reaction dynamics of these species is of high importance.

The HX species have all been generated by the simple exchange reaction between hydrogen and the diatomic halogen molecule, with the observation that reaction leads to internal excitation of the products, that is:

$$H + X_2 \longrightarrow HX^{\ddagger} + X \qquad (1)$$

Where, ‡ represents the generation of the HX species in an excited ro-vibronic state. The reactions have been studied using a variety of methods, including: measured relaxation [5], arrested relaxation [5] and crossed molecular beams [6]. While all methods have successfully reported detailed rate constants, k (v',R',T') (v' is the product vibrational excitation, R' the rotational excitation and T' the translational excitation) for the reactions, the crossed beam technique is most reliable since it totally removes relaxation effects which, become very difficult to correct in the other methods for the fastest reactions [7,8].

Following the observation of vibrationally excited products in the exchange reaction (1), prediction of a laser based on vibrational inversion was made in 1960 [9], Subsequently observation of laser action, by chemical reaction, was made by Pimental et.al. [10] from HCl, with laser action at 3.7 μm. Several other vibrational lasers have now been developed, including HF (DF), HBr (DBr) and several others [11].

Typical of many dynamical studies of the reactions characterised by equation (1) was the use of spontaneous ir emission of the products as the means of determining the relative populations of the excited states. However, ir emission methods are incapable of observing the ground vibrational state of a molecule and suffer from very small spontaneous emission probabilities.

As discussed in Chapter 1 the techniques of LIF and REMPI appear to offer an attractive alternative for monitoring population distributions because of their intrinsically high sensitivity and resolution. While LIF has been widely and successfully used to monitor, in considerable detail, the products of reactive events [12] (and references therein) REMPI has been used less frequently [13]; although other examples of its usage may be found in the fields of surface desorption [14] and energy transfer phenomena [15].

Implicit in all studies which utilise excited intermediate states, is an intimate knowledge of their behaviour. Both LIF and REMPI can reveal detailed aspects of the excited state dynamics, however such studies have not been widely reported for the HX family, HCl being the most cited example [16][17][18][19].

Therefore, this chapter is concerned primarily with a spectroscopic investigation into some of the excited states of HI between approximately 67500 cm^{-1} and 73500 cm^{-1} and hence presents a comparison of the results obtained from the single photon vuv studies of Ginter et.al. [20][21][22][23], with those obtained from [2+1]REMPI spectroscopy. Secondly it is concerned with the possibility of probing the product states that arise following generation via the reactive event, although it was realised that probing nascent state distributions, within a 'slow' flow reactor, would not be a realistic goal. The remainder of this chapter presents:

1) A resumé of spectroscopic and dynamical data pertinent to this study.

2) Presentation of the results obtained from the [2+1] REMPI studies and comparison to those of the single photon absorption studies of Ginter et.al.

3) Discussion and interpretation of results.

4.2 Electronic Structure of HI

The electronic structure of the hydrogen halides are expected to show quite general similarities since the main bonding orbitals are all thought to be derived from an atomic p^5 configuration. The atomic configurations may be represented as:

F = [He] $2s^2 2p^5$
Cl = [Ne] $3s^2 3p^5$
Br = [Ar] $4s^2 3d^{10} 4p^5$
I = [Kr] $5s^2 4d^{10} 5p^5$

However, as may be observed from the tables of atomic excitation energies [24], the full d shell may safely be regarded as core orbitals. Ginter et.al. [20-23][25-30] have proposed that the lowest lying configurations and corresponding electronic states for the hydrogen halides could be represented in a general manner, as shown in Table 4.1.

TABLE 4.1: General scheme for the lowest lying electronic configurations and states of the hydrogen halides. (The configurations are meant to represent what may be no more than best estimates or largest contributions to the excited electronic state near the equilibrium internuclear separation).

Electronic Configuration	State
$\ldots(\sigma^2\pi^4)$	$X^1\Sigma^+(0^+)$
$\ldots(\sigma^2\pi^3)a\sigma^*$	$a^3\Pi_i(1,0^-)$, $A^1\Pi(1)$
$\ldots(\sigma\pi^4)a'\sigma^*$	$t^3\Sigma^+(1,0^-)$, V or $B^1\Sigma^+(0^+)$
$\ldots(\sigma^2\pi^3)b\sigma$	$b^3\Pi_i(2,1,0^\pm)$, $C^1\Pi(1)$
$\ldots(\sigma^2\pi^3)c\sigma$	$d^3\Pi_i(2,1,0^\pm)$, $D^1\Pi(1)$
$\ldots(\sigma^2\pi^3)c\pi$	$e^3\Sigma^+(1,0^-)$,$E^1\Sigma^+(0^+)$,$f^3\ \Delta_i(3,2,1)$, $F^1\Delta(2)$
	$g^3\Sigma^-(1,0^+)$, $G^1\Sigma^-(0^-)$
$\ldots(\sigma^2\pi^3)d\pi$	$h^3\Sigma^+(1,0^-)$, $H^1\Sigma^+(0^+)$, $i^3\Delta_i(3,2,1)$, $I^1\Delta(2)$
	$j^3\Sigma^-(1,0^+)$, $J^1\Sigma^-(0^-)$
$\ldots(\sigma^2\pi^3)d\sigma$	$n^3\Pi_i(2,1,0^\pm)$, $N^1\Pi(1)$
$\ldots(\sigma^2\pi^3)a\delta$	$k^3\Pi_r(0^\pm,1,2)$, $K^1\Pi(1)$,$1\Phi(4,3,2)$,$L^1\Phi(3)$
$\ldots(\sigma^2\pi^3)e\sigma$	$m^3\Pi_i(2,1,0^\pm)$, $M^1\Pi(1)$
$\ldots(\sigma^2\pi^3)f\sigma$	$r^3\Pi_i(2,1,0^\pm)$, $R^1\Pi(1)$

In Table 4.1, the Rydberg states are labelled in an alphabetical manner according to the lowest energy first. The additional 'V' label attached to the $B^1\Sigma^+$ (0^+) state was that originally used by Mulliken [31] and subsequently adopted by Ginter et.al. For consistancy the 'V' nomenclature will be followed in this work. Both ΛS (see definitions of angular momenta in Appendix I) and $\Omega\omega$ coupling approximations are presented as state labels. In $\Omega\omega$ coupling [32] there is a strong spin orbit coupling in the 'core' (π^3), between the individual orbital and spin projection quantum numbers, λ_i and s_i for each of the π electrons to form separate ω_i. These ω_i then form a

resultant Ω. This is then followed by a coupling of Ω with the angular momentum ω of the additional (Rydberg) electron. It is useful to retain both ΛS and Ωω notations, since the former is more descriptive in discussions of state ancestry and orbital assignments, while the later (especially for the heavier halogens) is often a better representation of the angular momentum coupling.

Interpretation of the general aσ, bσ, cσ, cπ notation for the particular example of HI yields: 12σ, 13σ, 14σ, 7π orbitals respectively. Similarly, application of conventional one electron Rydberg state taxonomy would correlate, the bσ, cσ, cπ orbitals with the first members of the nsσ, npσ and npπ series respectively. Hence, again for HI, these would be the 6σ, 6pσ and 6pπ orbitals.

The X, a, A and t states of HI are all correlated with the ground state atomic limits i.e. $H(^2S)$ and $I(^2P^o_{3/2})$, or the spin orbit excited term for iodine $I(^2P^o_{1/2})$, with all but the X state having repulsive potential energy curves. These curves have now been estimated, using relativistic configuration interaction calculations, and are able to reproduce the experimentally observed data to a reasonable degree [33].

The $^1\Sigma^+$ ground state of HI was calculated to be 93% $^1\Sigma^+_{0^+}$ $(\sigma^2\pi^4)$ at 3.5 bohr (1 bohr ~ 0.53 Å), which was near the equilibrium internuclear separation r_e, of 1.61Å. At an intermediate separation of 6.0 bohr the ground $^1\Sigma^+$ state contained only 61% $^1\Sigma^+_{0^+}$ $(\sigma^2\pi^4)$. The remaining population being composed of 23% $^1\Sigma^+_{0^+}$ $(\sigma^{*2}\pi^4)$ and a significant contribution from $^3\Pi_{0^+}$ states. At large separations the configuration $(\sigma\pi^4)\sigma^*$ will become dominant because the σ* orbital acquires more and more hydrogen admixture with separation such that dissociation into the ground state atomic terms is achieved naturally. In other words at short and intermediate separations HI possesses strong ionic character

from contributions arising from double occupation of the σ (σ^*) orbitals. However, at larger internuclear separation HI possesses essentially covalent character.

As shown by Peyerimhoff et.al. [34] for HCl (and HF, see references therein) the $V^1\Sigma^+$ state undergoes an essentially complementary change in character to that of the ground state. That is covalent character prevails at small and intermediate internuclear distances while ionic character becomes dominant at large separations, for which dissociation leads diabatically to the products $H^+ + Cl^-$. Hence, it was concluded that for HCl [34], and hence in general here for HI, that the ground and excited states essentially form an 'avoided crossing' [35]. The $V^1\Sigma^+$ state is an example of a so-called 'ion-pair' state and unsurprisingly it exhibits properties not normally found in valence or Rydberg states. The outer limb is governed by the long range Coulomb attraction: $-e^2/r$ (e is the electronic charge (on each ion) and r is the internuclear separation). Also, it has a relatively much wider and deeper potential curve and a larger equilibrium internuclear separation. Hence, it is likely that the inner limb of the ion pair state will pass through most of the Rydberg state manifold and that strong perturbations will be expected with other states of the same electronic symmetry.

In addition to excitation to the σ^* orbital that produces the repulsive and ion-pair states discussed above, excitation to various ns, np, nd and nf members of the Rydberg series may occur. A theoretical description of the higher excited states of HI is not available to aid the experimental interpretation. Instead, briefly, a comparison may be made to theoretical and experimental data pertinent to HCl. In their work Peyerimhoff et.al. [36][19] predicted extensive interaction between the ion-pair and Rydberg states of 0^+ symmetry, with an assymetric double minimum state resulting. Despite the sophisticated nature of the ab-initio calculations the resulting potential supports vibrational and rotational level structure in poor agreement with the known spectroscopic data [19].

The electronic sprectrum of HI consists of absorption continua near 46000 cm^{-1} [37] and 23000 cm^{-1} [38] and discrete absorption bands which originate near 55000 cm^{-1} but which extend to above the first ionisation limit [39,20]. A description of the high energy continuum was presented by Mulliken [40] and for which experimental evidence, obtained by photofragmentation with time of flight analysis [41] and LIF Doppler spectroscopy [42] agree. In his original work Price [39] attempted to arrange his observations into 'Rydberg series'. However, Ginter and coworkers have carried out extensive, rotationally resolved, investigations using vuv absorption spectroscopy of HI and DI [20-23] and discounted Price's explanations. In fact Ginter and coworkers have carried out comparable investigations for the related molecules HCl, DCl [25-27] and HBr, DBr [28-30].

Ginter et.al. have predicted the correlation of the Rydberg electronic states to the relevant molecular ion core ($X^2\Pi_{3/2}$ ($I_{3/2}$) or $X^2\Pi_{1/2}$ ($I_{1/2}$)) limits. The correlation of states from the general configurations $(\sigma^2\pi^3)n\lambda$, where n is the principal quantum number and λ is the orbital angular momentum of the excited state, to the ion core limits $I_{3/2}$, $I_{1/2}$ is analogous to the correlation of states from a Λs coupling description to an $\Omega\omega$ description [43]. Thus, for the relatively low lying excited states, for which multichannel interactions are not too serious; for $(\sigma^2\pi^3)n\sigma$ configurations the $^3\Pi_1$ (1) and $^3\Pi_2$ (2) states are associated with the $I_{3/2}$ core limit while the $^1\Pi$ (1) and $^3\Pi_0$ ($0^{\pm}$) states are associated with the $I_{1/2}$ limit [22]. For the $(\sigma^2\pi^3)n\pi$ configurations $^3\Sigma^+$ ($1,0^-$), $^3\Delta_3(3)$, $^3\Delta_2(2)$ and one 0^+ can be associated with $I_{3/2}$ while $^1\Sigma^-$ (0^-), $^3\Sigma^-(1)$, $^1\Delta_2(2)$, $^3\Delta(1)$ and one 0^+ can be associated with $I_{1/2}$ [22].

The ionisation potentials to the $I_{3/2}$ and $I_{1/2}$ core limits have been accurately determined by photoionisation mass spectroscopy [44] as 10.386 and 11.0495 eV respectively.

There is a tendency for the $\Omega = 1$ states of HI to exhibit predissocation effects, especially below 68000 cm^{-1}. These effects may be attributed most obviously to interactions with the repulsive valence states of $\Omega = 1$ symmetry. Similarly, there is evidence for the $b^3\Pi_0$ $(0^{\pm})$ and $d^3\Pi_0$ $(0^{\pm})$ states to exhibit predissociation in the 0^- component. Hence, interaction with the t (0^-) state may be suggested. Also evident in the b and $d^3\Pi_0$ $(0^{\pm})$ states are two separate band origins. That is the expected degeneracy predicted by a ΛS coupling scheme has been lost and an origin exists for the separate 0^+ and 0^- components. The origin of the 0^- component is observed to be lower. This lowering of the 0^- band origin relative to the 0^+ origin arises from interconfiguration mixing caused by the mixing of states of the same symmetry (within the $\Omega\omega$ coupling scheme) [32].

Within the extensive analysis of the HX family presented by Ginter et.al. [20-23][25-30], the configurations $(\sigma^2\pi^3)c\pi$ have been fully characterised. In general the coupling appears to shift rapidly towards the $\Omega\omega$ limiting case as the number of electrons on the halogen is increased. Also, the states associated with $(\sigma^2\pi^3)d\pi$ in HCl appear to have coupling nearer $\Omega\omega$ than the $c\pi$ configurations. If this observation extends to the less well characterised $d\pi$ configurations of HBr and HI the limiting case of pure $\Omega\omega$ coupling would be very closely approximated.

Furthermore, the trend to $\Omega\omega$ coupling in HI is evidenced by the fact that the most intense spectral features in the vuv work of Ginter et.al. may all be associated with obeying the $\Delta\Omega = 0, \pm 1$ selection rule. Ginter et.al. were able to observe states with values of $\Omega \geq 2$, even though transitions from a 0^+ ground state to states with $\Omega > 1$ are forbidden, regardless of electronic coupling scheme or the magnitude of interconfigurational mixing effects [21]. They attributed the observation of $\Omega \geq 2$ states as being due to rotational mixing in one or both of the states involved in the transition [21].

The electronic states and band origins observed by Ginter et.al. [22] in the vuv absorption spectrum of HI in the range 60000 - 74500 cm^{-1} are presented in Figure 4.1.

4.3 Reaction Dynamics

The mechanism of the production of HI from the mixture of H_2 and I_2 has been one of the most widely discussed subjects in the field of reaction dynamics [45]. However, it was Sullivan who correctly predicted that it was atomic processes that were important [46], including the elementary reactions H + I_2 and H + HI.

The H + I_2 and H + HI reactions have been investigated as a function of temperature by Lorenz et.al. [47], for which the temperature dependent rates between approximately 250 - 400 K were measured as:

$$k_1(H+I_2) = (6.6 \pm 3)10^{-10} \exp(-20\ K/T)\ cm^3\ molecule^{-1}s^{-1} \qquad (2)$$

and is equally well represented by the temperature independent expression:

$$k_1(H+I_2) = (6 \pm 2.5)10^{-10}\ cm^3\ molecule^{-1}s^{-1} \qquad (3)$$

For the HI loss reaction, the temperature dependent rate expression is:

$$k_2(H+HI) = (7.4 \pm 2)10^{-11} \exp(-290\ K/T)\ cm^3\ molecule^{-1}s^{-1} \qquad (4)$$

Subsequently k_2 has been remeasured at room temperature with good agreement existing between the measurements [48].

FIGURE 4.1: Energy level diagram of the previously observed states of HI. Each state is labelled by its vibrational quantum number (right) and electronic assignment (left). All the states derived from a particular orbital occupancy are gathered into specific columns.

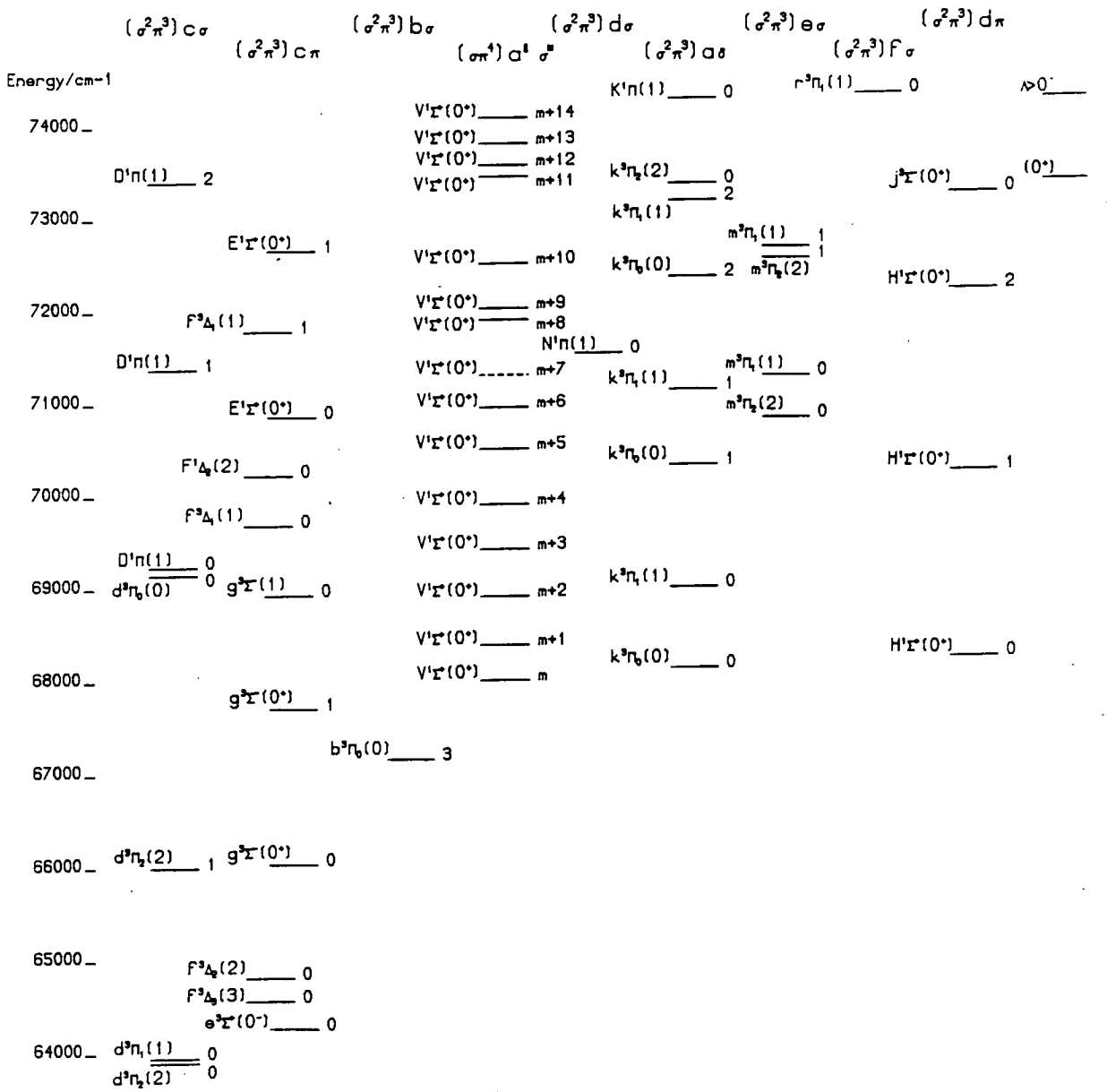

The reaction H + I_2 has been investigated by both trajectory calculations [49,50] and by crossed molecular beam studies [6][51] which have all indicated that the reaction produces substantial internal excitation, with a fraction between 0.6-0.8 of the reaction exoergicity entering the HI product.

The reaction enthalpy ΔH_R, is 147 kJ mol^{-1}, therefore between 90-120 kJ mol^{-1} is available for excitation of the products. Lorenz et.al. [47] observed the spin orbit excited state of the iodine atom I* ($5p^5\ ^2P^o_{1/2}$) under conditions where they considered it to be a direct product of the reaction. Although such an excitation is energetically possible, requiring 90.8 kJ mol^{-1}, Lorenz et.al. were unable to determine the $I^*/_I$ branching ratio. For the comparative reaction H + Br_2 Bly [52] has shown that $Br(^2P^o_{1/2})$ formation is of negligible importance and the crossed beam study of McDonald et.al. [6] did not report the observation of I* from the reaction D + I_2.

Although the energy release for the H + I_2 reaction is the least for all the H + X_2 reactions, it is sufficient to produce HI in the 6th vibrational level, as observed for the isotopic variant D + I_2 in reference [6]. The calculations of Anderson and Kung [50] estimate that relative rate constants, k (v') for production of HI in the interval v' - 1/2 to v' + 1/2 would be: k(0') = 0, k(1') = 0, k(2') = 1, k(3') = 11, k(4') = 26, k(5') = 5, k(6') = 0. They also estimated that the average energy of the product would partition as: vibration $\bar{E}_{v'}$ = 112 kJ mol^{-1}, rotation $\bar{E}_{R'}$ = 9 kJ mol^{-1} and translation $\bar{E}_T$ = 55 kJ mol^{-1}. In the reaction series H + X_2 (X = F,Cl,Br,I) the production of excited HI occurs with most efficiency and is explained in terms of this reaction occurring on a surface with the biggest 'attractive energy release' component [49].

Since the reaction H + I_2 occurs with a large population inversion it presents a near ideal candidate for an initial study of reaction products via REMPI.

Although, other possible reactions were considered e.g. H + ICl and H + ICH_3, because of, respectively, the unfavoured product channel to HI [53] or the lack of generation of excited species [54]; only the reaction between H + I_2 was studied.

4.4 Two Photon Spectroscopy

The methodology for deriving the rotational selection rules, for two photon transitions has been presented by McClain and Harris [55], the rules obtained are presented below for, the experimental situation, absorption of two identical linearly polarised photons.

Within a coupling scheme in which spin orbit coupling is 'tight', besides transitions due to the single photon selection rules, $\Delta\Omega = 0, \pm 1$ transitions due to $\Delta\Omega = \pm 2$ become allowed. While, for situations described by ΛS coupling the rules are $\Delta\Lambda = 0, \pm 1, \pm 2$ and $\Delta S = 0$. However, as spin-orbit coupling becomes more important the transition $\Delta S = \pm 1$ becomes possible, see Kovacs [56].

For a $0^+ - 0^+$ transition, the change in rotational quantum number $\Delta J = 0, \pm 2$ is allowed and hence O, Q and S branches will be observed. Whereas, for a $1 - 0^+$ or $2 - 0^+$ transition, changes of $\Delta J = 0, \pm 1, \pm 2$ are possible and hence O, P, Q, R and S branches should be observed. Table 4.2 summarises the two photon selection rules, for the experimental situation, of absorption of two identical linearly polarised photons.

TABLE 4.2: Allowed electronic and rotational selection rules for which the Ω and (ΛS) quantum numbers describe the interacting states with a ($^1\Sigma^+$) 0^+ ground state

Electronic Selection Rule	Rotational Selection Rule
$(^1\Sigma^+),0^+ \leftarrow (^1\Sigma^+),0^+$	$\Delta J = 0, \pm 2$
$(^1\Pi), 1 \leftarrow (^1\Sigma^+),0^+$	$\Delta J = 0, \pm 1, \pm 2$
$(^1\Delta), 2 \leftarrow (^1\Sigma^+),0^+$	$\Delta J = 0, \pm 1, \pm 2$

Rotational linestrength factors have been reported by several authors, although the most easily interpreted are those of Bray and Hochstrasser [57] and those of Zare et.al. [58], whose differing approaches produce essentially identical results. The line strength formulae of Bray and Hochstrasser were derived in terms of Ω and J and because of their explicit representation could be easily incorporated into the simulation procedure, see discussion later.

By tracing each rotational branch back to its line of lowest J", it is possible to uniquely correlate, to a specific symmetry (Ω or Λ value), the upper and lower states. Such assignment is made considerably easier if the ground state symmetry is known, as is the case for HI with $^1\Sigma(0^+)$. In Table 4.3 the minimum J value associated with each branch for a $^1\Sigma^+(0^+)$ is indicated, these are labelled J min.

TABLE 4.3 The pattern of J min which will appear in a two photon spectrum as a function of upper electronic state symmetry, with $^1\Sigma^+(0^+)$ ground state symmetry.

Electronic State Symmetry		J min of rotational branch				
Upper	Lower	O	P	Q	R	S
$0^+(\Sigma^+)$	$0^+(\Sigma^+)$	2	-	0	-	0
1 (Π)	$0^+(\Sigma^+)$	3	2	1	0	0
2 (Δ)	$0^+(\Sigma^+)$	4	3	2	1	0

The appearance of two photon rotational spectra is also discussed in Appendix I.

4.5 Experimental Section

In this Chapter the [2+1] REMPI spectra of HI were all obtained from the same experimental methodology. In brief, I_2 (BDH Chemicals Ltd, 99.9% purity) was placed in a vacuum tight container. Helium was then flowed over the I_2 such that any nascent vapour was entrained into a gas flow. This flow then passed into a glass sliding injector for

introduction to the flow reactor. Hydrogen atoms were generated via a microwave discharge of a mixture of H_2 in Ar (normally 5%, BOC). Following exit from the injector and reaction, the product HI was probed with the nearby focussed laser beam. The ions generated by the multiphoton ionisation process were detected by two equal but oppositely biased nickel parallel plates within the reactor (see Figure 2.2). Typical experimental conditions under which approximately equivalent experimental results, in terms of signal to noise and bands observed could be obtained were: reaction pressure 1 - 2 Torr, microwave discharge power 35 - 50 Watts, iodine container temperature -5 - 5°C, helium flow over the iodine 5 - 20 SCCM.

While the outline presented above is conceptually simple several experimental features must be mentioned with regard to the limitations of the method.

Microwave discharges are known to generate significant numbers of metastable species, often of high energy, which in the case of argon are $^3P_{0,2}$ [59]. It was found that if the discharge was operated at high powers, with high gas flow rates, that the detector plates would act as efficient energy dumps and hence seriously increased the experimental noise would be observed. Therefore, experiments could not be performed with microwave powers above 50 W and with pressures of more than 2 Torr, although it was possible to increase one at the expense of the other.

The parallel plate arrangement detects the total ion yield as a function of wavelength. It may therefore be readily attached to a flow tube apparatus since, at the moderate pressures at which these experiments were performed, the various factors which led to its rather poor spatial and temporal resolution are unimportant in terms of the experimental observable (total ion signal). Hence, provided the detector is operating within a regime of linear response the only factor which would lead to a reduction in relative intensity of a specific ionisation process would be a competing non-ionising intermediate state loss mechanism, such as predissociation.

It was found that the REMPI experiments required a minimum reactor pressure, at least 0.25 Torr but preferably better than 0.4 Torr. The reason for this appeared to be that at low flow rates, large continuum ionisation signals could be detected. This was attributed to either species desorbing from the reactor walls or back diffusion of the pump oil, followed by ionisation and possibly fragmentation.

The total pressure at which the experiment was performed was varied from 0.75 to 2.5 Torr and was found not to be a crucial parameter in terms of the total intensity of the observed HI bands (no upper limit was established). The most typical experimental pressure was near 1.5 Torr, for which the gas flow was characterised by a mean drift velocity of approximately 10 ms^{-1}.

To reduce heterogeneous losses of hydrogen atoms within the flow reactor a coating of halocarbon wax (see Chapter 2) was applied to all its internal surfaces, while the discharge side arm was coated with phosphoric acid (see Chapter 2). The combination of surface recombination inhibiting reagents was found to produce a highly stable and apparently reproducible hydrogen atom concentration. The argon to hydrogen mixing ratio was varied from approximately 100:1 to nearly 1:1 with little difference being observed in the total intensity of the observed HI bands. This observation indicated the hydrogen atom concentration was possibly not a limiting factor in observing the HI bands (hot bands). Hence, an Ar:H_2 mixing ratio of 20:1, obtainable directly from the cylinder (BOC), was used most often.

The sliding injector had a 2 mm internal diameter, while that of the flow reactor was 25 mm. Hence, in order to prevent significant back diffusion of the reactive hydrogen atoms up the sliding injector the He:Ar flows were adjusted such that there would always be a higher flux within the injector. In practice therefore, the helium flows were varied from a minimum of 5 SCCM to about 15 SCCM, although even with a He carrier flow of 25 SCCM the observed relative band intensities (including the hot bands) appeared relatively invariant.

An important experimental parameter was found to be the temperature of the iodine sample; for example at 40°C I_2 has a 1 Torr equilibrium vapour pressure, whereas at a temperature of 0°C it has a vapour pressure near 0.03 Torr [60]. In a regime of flow the actual vapour pressure would be expected to be much lower. Using a sample temperature near 0°C (although variance from -5° to 5°C was acceptable) both stable flows and a reasonable HI:I_2 ionisation signal ratio could be obtained. An approximate estimate of the I_2 number density would be at the 10^{13} molecules cm^{-3} concentration level (extrapolated from a measurement in Appendix IV).

By adjusting the injection to laser probe separation it was possible to probe the ground state HI rovibrational distributions at time scales ranging from approximately 100 μs (1 mm) to several milliseconds, with most experiments being performed with an injector to laser probe 'flight time' near 500 μs. Increasing the injector to detection distance was noted to decrease the total HI signal, as expected, due to the fast HI loss reaction, $H + HI \longrightarrow H_2 + I$ (see section 4.3). Also, the hot bands were observed to relax very rapidly i.e. an approximate 5mm increase of the reactor to probe distance caused the hot band to ground state intensity ratio to drop by approximately 5. Experiments wherein the injector to probe beam distance was reduced produced increasing contributions from unreacted I_2. Also, difficulties were experienced in probing non-turbulent or inhomogeneous gas mixtures at very small separations. Experiments were normally carried out using a 31 cm focussing lens, however repeat experiments using a 6 cm lens (mounted in the reactor), whose ionisation volume was such that maximum ion yield would be obtained from a relatively small region indicated that these comparative rovibrational distributions appeared identical.

A discharge of hydrogen and argon is known to produce trace quantities of nitrogen and oxygen atoms [9]. However in separate studies using discharges of pure N_2 and O_2 none of the observed resonances could be attributed to those observed from the reactive system. Similarly, no observation of transitions attributable to hydrogen atoms or molecules

were made under conditions where the reaction with I_2 was occurring. However, in the absence of I_2 [3+1] REMPI spectra of H_2 and H could be observed using the strongly focussing 6 cm lens. Appendix IV presents typical spectra and appropriate assignments for transitions due to iodine and hydrogen atoms and the hydrogen molecule. Also presented are supplementary assignments for atomic chlorine and bromine which show the generality of the method.

Present in all the experimental spectra was an I_2 pseudo ionisation continuum, which nevertheless, contained specific structure. Hence, because of the possibility of underlying features, little importance was attached to the interpretation of the observed HI rotational envelopes (especially hot bands), except for a few relatively favoured cases or cases of special interest, these will be discussed later. An obvious alternative approach for measuring the rotational intensities would be to perform the REMPI experiments in a glass cell containing only HI. However, HI exists in equilibrium such that:

$$H_2 + I_2 \rightleftharpoons 2HI \qquad K = 55.3 \text{ at } 699K \text{ [62]}$$

Similarly it was found in agreement with [63], that HI appeared to undergo fairly facile metal-surface mediated decomposition into I_2 and H_2. Hence, the static cell was found to produce a time varying background ionisation signal. While cooling the cell helped considerably the varying background signal was still evident. Superior approaches would include buffering the cell with H_2 or to flow a low pressure of HI through the cell.

As was briefly alluded in Chapter 2 the line positions of the molecular features of interest were measured via the accurately known atomic iodine line positions and interpolation between the transmission fringes of the solid quartz etalon. The oscillator strength of the atomic iodine lines relative to any molecule feature was normally large, hence in order to avoid extreme power broadening

(several cm^{-1} FWHM) for some of the atomic resonances, a uv attenuating filter was placed in front of the beam just before scanning over a particular atomic resonance. Very strong absorptions which could be attributed to I* ($^2P^o_{1/2}$) were observed in the experiment, hence given the assumption that I* is not a major product of the reaction various other possibilities exist for the apparently anomalously intense transitions due to I* ($^2P^o_{1/2}$):

1) Photolysis of the $c^3\Sigma^+_1$ state of I_2, which has an absorption maximum near 37000 cm^{-1} and leads directly to $^2P^o_{1/2}$ + $^2P^o_{3/2}$ iodine atoms [64].

2) Photolysis of HI, which has been observed at 266 nm to yield approximately 40% $^2P^o_{1/2}$ and 60% $^2P^o_{3/2}$ [42].

3) A very effcient, V - E energy transfer process between HI and I and could occur only for $v'' \geq 4$ (where $v'' = 4$ is expected to be the most populated level). Such a process has been observed in the reaction F + HI [65].

4.6 Two Photon Spectroscopy of HI

Initially, relatively rapid scans of the [2 + 1] resonance enhanced multiphoton ionisation spectra of HI were obtained, these served to indicate the positions at which the bands of interest could be found and the excited state symmetry. Then, within the stability of the experiment, longer scan times were normally used in order to measure the line positions. Figure 4.2 presents a fairly typical survey and includes transitions from both the ground and excited vibrational levels of HI. The analysis of the observed spectra, in the range 67500 cm^{-1} to 73500 cm^{-1}, has been summarised and is presented in Table 4.4 (together with the attached notes).

FIGURE 4.2: [2+1] REMPI spectrum of HI near 68000 cm^{-1}. Assignments were made to transitions from both v" = 0 and v" = 1. Lines marked by a '+' indicate perturbed lines. Assignment to two two-photon transitions in atomic iodine was also made.

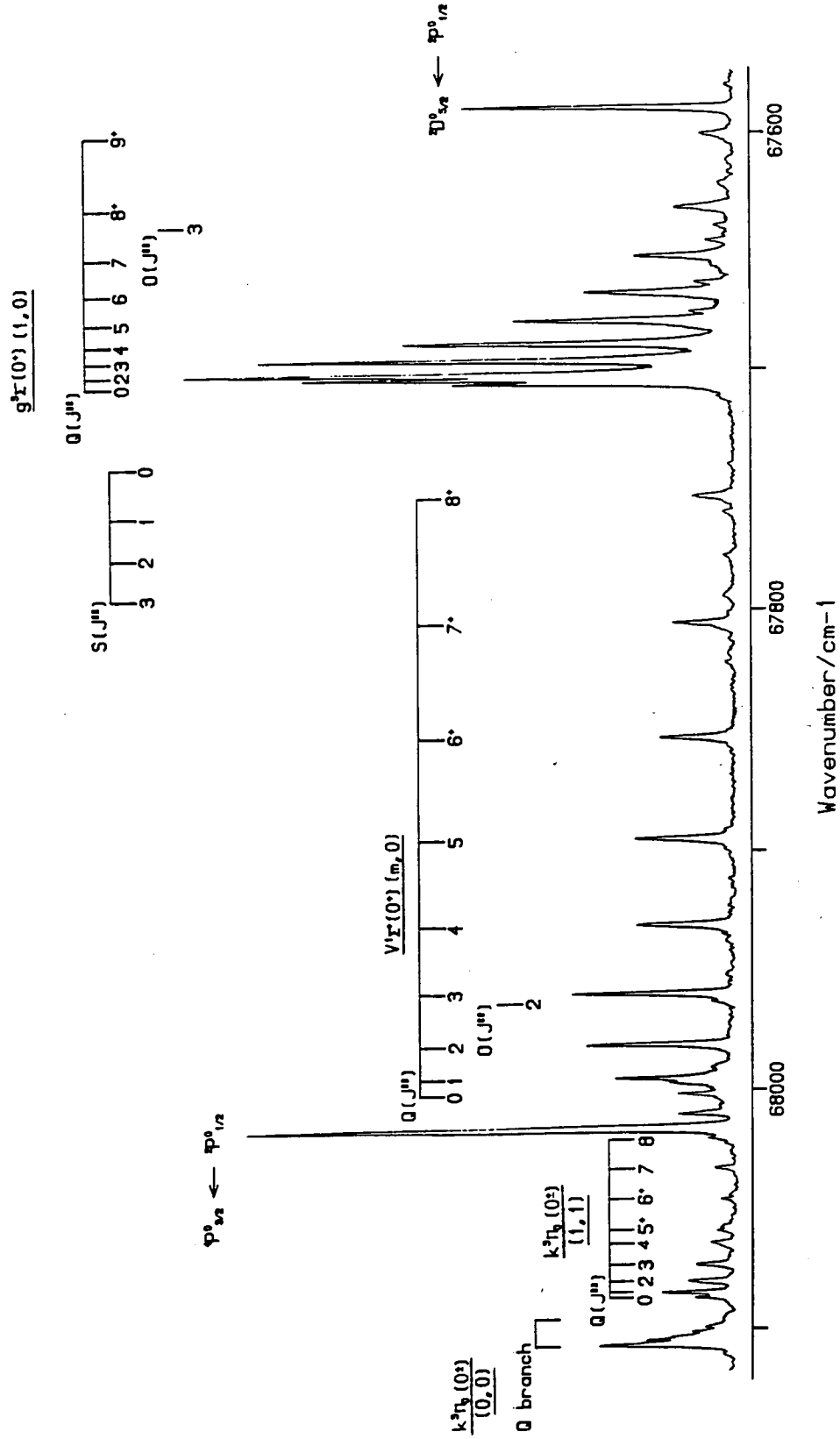

The spectra presented in this chapter were not simultaneously normalised for fluctuations in laser power. For most spectra, which extend over only relatively small wavelength regions this effect was not large (~ 10%). However for the $\Delta(2)$ states which do extend over significant wavelength regions this variation was important. To partially correct for this effect, the change in the square of the laser intensity (see discussion later) was applied to the simulation to allow for comparison with experiment. In this case best (typical) example spectra are presented.

[a]

TABLE 4.4: Observed molecular states and calculated spectroscopic constants from the [2 + 1] REMPI spectra of HI in the region 67500 cm^{-1} - 73500 cm^{-1}

Upper[b] State	(v',v")	$\Lambda(\Omega)$[c] cpts	Band Origin[d]/ cm^{-1}	Absolute[e] Uncertainty/ cm^{-1}	B_v/[f] cm^{-1}	$D_v x10^4$/[g] cm^{-1}	Observed lines, comments
$g^3\Sigma^-(0^+)$	(1,0)		67704.4(6)	0.36	5.59(6)	22(10)	Q(0-9), S(0-3), 0(3) J=8,9 perturbed
$V^1\Sigma^+(0^+)$	(m,0)		68003.5(5)	0.04	2.89(3)		Q(0-8), 0(2) J=6,7,8 perturbed
$k^3\Pi_0(0^\pm)$	(1,1)		68089.9(7)	0.24	5.07(8)	-33(11)	Q(0-8) J=5,6 perturbed J=5 diffuse
$k^3\Pi_0(0^\pm)$	(0,0)		68110.5(6)	0.28	6.24(2)		Q(0-8)
$H^1\Sigma^+(0^+)$	(0,0)		68276.6(7)	0.80	5.81(7)		Q(0-8) $J\geq5$ perturbed, lines increase in diffuseness with increasing J
$E^1\Sigma^+(0^+)$	(0,1)		68619.2(9)	1.80	6.01(16)	121(53)	Q(0-6) J=6 perturbed
$F^1\Delta(2)$	(2,2)	+	69969.5(2.1)	3.04	6.05(20)		Q(3) S(0,1) Q head measurement only
		-	69970.2(9)	3.04	5.97(5)		R(1-4) P(3)

Upper State	(v',v")	Λ(Ω) cpts	Band Origin/ cm^{-1}	Absolute Uncertainty/ cm^{-1}	B_v/ cm^{-1}	$D_v x10^4$/ cm^{-1}	Observed lines, comments
$F^1\Delta(2)$	(1,1)	+	70089.6(6)	2.68	6.08(1)		Q(2-9),S(0-2) Q(2) unresolved
		-	70089.7(6)	2.68	6.12(3)		R(1-3),R(5), P(4-7)
$F^1\Delta(2)$	(0,0)	+	70229.1(5)	2.24	6.321(10)		Q(2-10),S(0-7) Q(2,3,4,5) partially resolved
		-	70229.7(4)	2.24	6.308(11)		R(1-8),P(3-9)
$H^1\Sigma^+(0^+)$	(1,0)		70243.5(1.5)	2.20			band too weak to resolve
$V^1\Sigma^+(0^+)$	((m+5),0)		70513.8(7)	1.40	3.82(9)	-65(22)	Q(0-6)
$E^1\Sigma^+(0^+)$	(0,0)		70852.4(5)	0.40	6.00(9)	120(32)	Q(0-6),S(0-2),O(3-4) J=6 perturbed
$V^1\Sigma^+(0^+)$	((m+6),0)		70950.8(7)	0.24	4.02(7)		Q(0-7) J=5,6,7 perturbed
$j^3\Sigma^-(0^+)$	(0,1)		71024.1(4)	0.40	5.77(8)	69(26)	Q(0-5)
$0^+(I)$ [h]	(0,1)		71153.4(5)	0.08	5.810(14)		Q(0-9)
$0^+(II)$ [i]	(1,0)		71302.2(6)	0.12	5.98(6)	18(8)	Q(0-8),S(1-3),O(2,3)
$V^1\Sigma^+(0^+)$	((m+13),1)		71593.3(3)	0.24	3.77(3)		Q(0-6)

Upper State	(v',v")	Λ(Ω) cpts	Band Origin/ cm^{-1}	Absolute Uncertainty/ cm^{-1}	B_v/ cm^{-1}	$D_v x10^4$/ cm^{-1}	Observed lines, comments
(2) ^{j}	(2,2)	+	71701.6(4)	0.32	5.83(3)		Q(2-6),S(0,1) Q(2) unresolved
		-	71701.1(6)	0.32	5.86(2)		R(1-6),P(3-5)
(2) ^{j}	(1,1)	+	71866.8(9)	0.12	6.08(3)		Q(3-6),S(0,1) Q(2) unresolved
		-	71867.3(9)	0.12	6.10(4)		R(1-4),P(3,5,6)
(2) j	(0,0)	+	71988.9(4)	0.04	6.283(11)		Q(2-7),S(0-7),0(4,6),0(8) Q(2) unresolved
		-	71988.5(5)	0.04	6.295(12)		P(3-10),R(1-6)
$k^3\Pi_0(0^{\pm})$	(2,0)		72353.0(6)	0.28	5.68(4)		Q(0-5)
$V^1\Sigma^+(0^+)$	((m+10),0)		72506.6(8)	0.04	4.07(7)		Q(0-4) Diffuse lines increasing in diffuseness with increasing J
$E^1\Sigma^+(0^+)$	(1,0)		72649.1(6)	0.36	5.20(2)		Q(0-8) J=3,4 perturbed
$j^3\Sigma^-(0^+)$	(0,0)		73255.0(8)	0.40	5.71(8)	38(16)	Q(0-7) J=6,7 'slightly' perturbed
$0^+(I)$ ^{i}	(0,0)		73582±(4)				Insufficient data for analysis, obscured by strong iodine resonance
$V^1\Sigma^+(0^+)$	((m+11),0)		73457.6(8)	0.20	3.28(14)		Q(0-3)

a) Throughout the table the constants of Guelachvili et.al. [66] have been used in the fitting routine. All spectroscopic constants have units of cm^{-1}. The weighting attached to each experimental line varied upwards from 0.5 cm^{-1} and depended on how sharp the line was and whether it was blended or perturbed etc.

b) Both ΛS and $\Omega\omega$ coupling schemes are used to describe the upper state.

c) + and - refer to Ω^+ and Ω^- or equally Λ^+ and Λ^- components respectively.

d) The rotationless or band origin is quoted together with the estimated uncertainty in the origin quoted at the 2σ level. The value in brackets (in this and the columns dealing with the B_v and D_v values) should be applied to the last significant figure(s) in the spectroscopic constant.

e) The absolute uncertainty follows from the uncertainty in the estimated free spectral range of the etalon. The value is taken to scale as n.f, where, n is the number of etalon fringes from the nearest atomic iodine calibration line to the band origin and f is the estimated uncertainty (2σ) in the fsr in the observed spectrum i.e. 0.04 cm-1.

f) B_v (and D_v) are the calculated effective molecular constants, see Appendix I.

g) The centrifugal distortion constant is only shown if the calculated numerical value was greater than twice the estimated uncertainty in the constant. Hence, only bands showing large effects tend to be entered.

h) State with (0^+) symmetry previously observed in the vuv absorption by Ginter et.al. [22].

i) Previously unobserved state with ($0^\pm$) symmetry and will be discussed in section 4.6.4.

j) Previously unobserved state with $\Omega = 2$ symmetry, and will be discussed in section 4.6.2.

4.6.1 Measurement precision and accuracy

Several atomic iodine lines were normally available within each spectrum to allow the calculation of an average free spectral range of the etalon. The mean statistical uncertainty in the estimated f.s.r., quoted at the 2σ level was 0.01 cm^{-1}. This corresponds to an uncertainty of 0.04 cm^{-1} in the absolute position of each etalon fringe, as measured on the spectrum. Hence, for a band next to one of iodine standard lines its absolute position is determined with high accuracy, while a band further from the standard line is less well determined. The uncertainty was taken to scale as the number of fringes from the nearest iodine line times twice the standard deviation in the estimated uncertainty of the f.s.r. In this case most bands were found to have an estimated uncertainty of less than 1 cm^{-1} although for the worst case a value near 3 cm^{-1} was obtained.

The effect of the uncertainty of the f.s.r. on the calculated rotational constants was investigated. Even for the worst situation of the $\Delta(2)$ states, where the bands extend over a few hundred wavenumbers, the effect was only comparable to ± 1 in the least significant figure.

From the experimental spectra the measurement precision was estimated to be 0.5 cm^{-1} for sharp lines, while for diffuse or partially blended lines the estimated uncertainty of each line was appropriately increased.

As was discussed in section 4.2 some of the excited states of HI are influenced by interconfigurational mixing effects. Hence, for states with $\Omega > 0$, assignment must be made not only to the rotational branches that connect the differing $\pm\ \Omega$ components (see Appendix I) but also to separate rotational origins ν_o. Therefore, the procedure was to fit the observed rotational structure to an effective Hamiltonian such that effective molecular constants B_{eff} and D_{eff} could be determined.

$$\nu = \nu_o + B_{eff}\, J(J+1) - D_{eff}\, J^2(J+1)^2 \qquad (5)$$

The constant D_{eff} is only quoted in the fit if its estimated value was greater than twice the estimated uncertainty obtained for the fitting procedure. The difference in the B_{eff} values $|B^+ - B^-|$ gives the Ω doubling constant q, as indicated in Appendix I this constant was expected to be rather small.

The rotational fitting algorithm was based on a linear least squares method outlined by Bevington [67]. The original program for this task was written by a coworker Mr A M James and was subsequently modified to allow the additional complexity arising from two photon excitations. For a series of measured lines: ν_1, ν_2, ν_3.... an initial correction was made for the known ground state rotational term values such that ν'_1, ν'_2, ν'_3... were calculated. The upper state constants were then calculated by using the matrix equation:

$$\begin{bmatrix} \nu'1 \\ \nu'2 \\ \nu'3 \\ : \\ : \\ : \\ \nu'n \end{bmatrix} = \begin{bmatrix} J_1\ (J_1+1)\ (J_1(J_1+1))^2 \\ : \\ : \\ : \\ : \\ : \\ J_n(J_n+1)\ (J_n(J_n+1))^2 \end{bmatrix} \begin{bmatrix} B' \\ D' \end{bmatrix} \qquad (6)$$

Where the problem of finding the coefficients (B',D') reduces to finding the inverse of the matrix in J and the constant ν_o is found by back substitution.

An alternative method to determining the constants could be usefully employed for states with Ω = 2 (1) symmetry. In this case the combination relations were employed. To determine B' for the (-) component of the state using the rotational term value expression, but neglecting terms in D, use:

$$E_{(R,J")} - E_{(P,J")} = R_{(J")} - P_{(J")} = 4B'(J"+½) \qquad (7)$$

and B" follows from:

$$E_{(R,J"-1)} - E_{(P,J"+1)} = R_{(J"-1)} - P_{(J"+1)} = 4B"(J"+½) \quad (8)$$

For the (+) component of the state, use the S and O branches:

$$E_{(S,J")} - E_{(O,J")} = S_{(J")} - O_{(J")} = 8B'(J"+½) \quad (9)$$

and B" follows from:

$$E_{(S,J"-2)} - E_{(O,J"+2)} = S_{(J"-2)} - O_{(J"+2")} = 8B"(J"+½) \quad (10)$$

Similarly by using the term relations it was possible to determine the band origins of the $\pm\ \Omega$ components. For the (-) component use:

$$E_{(R,J"-1)} + E_{(P,J")} = R_{(J"-1)} + P_{(J")} = 2\nu_o + 2(Bv'-Bv")J"^2 \quad (11)$$

Where equation (11) utilises the previously determined Bv' (Bv") constants and ν_o is the rotationless origin. Thus a plot of the sum $R_{(J-1)} + P_{(J)}$ against J^2 yields an intercept of $2\nu_o$.

For the (+) component of the state, the following expression was obtained:

$$E_{(S,J"-2)} + E_{(O,J")} = S_{(J"-2)} + O_{(J")} = 2\nu_o + 2(B'-B")[J"^2-J"+1] \quad (12)$$

Hence a plot of $S_{(J"-2)} + O_{(J")}$ against $(J"^2-J"+1)$ yields an intercept of $2\nu_o$.

In their analysis Ginter et.al. [20-23] used the ground state rotational constants for HI of Palik [68], however in this work the more precise values of Guelachvili et.al. [66] were used. Usefully, reference [66] also reports constants and rotational origins for excited ground state molecules.

4.6.2 Discussion of Ω = 2 states

Examination of Table 4.4 indicates that two very similar Ω = 2 states were observed during the course of this work. One band, the $F^1\Delta(2)$ was found, in agreement with Ginter et.al. [22] to have an origin near 70229 cm^{-1}, while the other band, not observed in the vuv studies, was measured to have a (0,0) origin near 71990 cm^{-1}.

If the bands at 70229 and 71990 cm^{-1} are considered in isolation then an initial conclusion may be that they are the (0,0) and (1,0) bands of the $F^1\Delta(2)$ state. Such bands have been observed in the vuv spectrum of HCl [27], while (0,0) and (1,0) bands have also been observed for the $f^3\Delta_1$ state of HBr [29]. However, if the band at 71990 cm^{-1} was $v' = 1$ of the $F^1\Delta(2)$ state and given the approximately equal oscillator strengths of the two Ω = 2 bands, as observed by two photon absorption, then although weak the band at 71990 cm^{-1} should have been observed interspersed amongst the sparse rotational structure of the $V^1\Sigma^+$ (m+9) band in the vuv study.

The strongest evidence however for these bands deriving from different origins comes by allowing the sliding injector to approach closely ($\lesssim$ 5 mm) the laser beam. For both the bands at 70229 and 71990 cm^{-1} additional bands with a very similar rotational contour (and with R(1) being the first observed line in the R branch), appeared just to the red of them. Since the additional Ω = 2 bands appear between one and two hundred wavenumbers from the excited state origins it is clear that the difference in the vibrational constants between the ground and excited states must be small. This observation is exemplified by the energy difference ~ 2090 cm^{-1} for $v' = 0$ and 1 of the $f^3\Delta_1$ state of HI (which is expected to show highly similar behaviour to the $F^1\Delta(2)$ state). Additionally, Ginter et.al. [23] have shown that the energy separation of the $v' = 0$ and 1 levels of the $F^1\Delta(2)$ state of DI was 1550 cm^{-1}. Hence, given that the ground state vibrational constant of DI is near 1600 cm^{-1}, using the well known relationships between the spectroscopic

constants for isotopic substitution [69] indicates that the vibrational constant for the $F^1\Delta(2)$ state of HI must be similar to the vibrational constant of the ground state of HI. Therefore since the $\Omega = 2$ bands which originate from $v'' = 0$ are separated by approximately 1700 cm^{-1}, the band of 71990 cm^{-1} cannot be attributed to the $F^1\Delta(2)$ state. Finally, throughout Table 4.4 and from the extensive vuv studies of Ginter et.al. (for all the HX molecules) no evidence was found for large vibrational progressions in the Rydberg series. Hence, the band at 71990cm^{-1} cannot easily be attributed to any known $\Omega = 2$ state in HI. It is highly likely therefore, that these additional bands are sequence bands with $\Delta v = 0$. Thus in both cases the observed bands must be the (0,0) (1,1) and (2,2) bands.

The rotational analysis of the $F^1\Delta$ (2) (0,0) (1,1) and (2,2) bands are shown in Tables 4.5, 4.6 and 4.7 respectively. Figures 4.3 and 4.4 show representative spectra of the sequence bands of the $F^1\Delta(2)$ state. The analysis was based on the comparison of spectra taken after long and short residence times in the reactor. In Figures 4.3 and 4.4 branches associated with the (0,0) transition are labelled O,P,Q etc., those associated with the (1,1) band have an additional * label attached; while those associated with the (2,2) band are labelled with an additional # mark.

TABLE 4.5: (a) Line positions and rotational analysis of the $F^1\Delta(2)$ (0,0) band, analysis of the P and R branches. See text for details of the fitting procedure.

Assignment	Observed position/cm^{-1}	Calculated position/cm^{-1}	Residual (obs-calc)/cm^{-1}
R(1)	70254.28	70254.72	-0.44
R(2)	70266.79	70266.88	-0.09
R(3)	70278.82	70278.80	-0.02
R(4)	70290.69	70290.53	0.16
R(5)	70302.29	70302.05	0.24
R(6)	70313.58	70313.43	0.15
R(7)	70324.71	70324.68	0.03
R(8)	70335.82	70335.82	0.00
P(3)	70190.91	70190.48	0.43
P(4)	70177.11	70176.98	0.13
P(5)	70163.21	70163.28	-0.07
P(6)	70149.06	70149.42	-0.36
P(7)	70135.24	70135.43	-0.19
P(8)	70121.69	70121.34	0.35
P(9)	70106.87	70107.21	-0.34

Calculated band origin = 70229.7(4) cm^{-1}
Calculated effective rotational constant = 6.308(11) cm^{-1}
reduced Chi-Squared = 0.28

TABLE 4.5: (b) Line positions and rotational analysis of the $F^1\Delta(2)$ (0,0) band, analysis of the Q and S branches, no O branch was observed.

Assignment	Observed position/cm^{-1}	Calculated position/cm^{-1}	Residual (obs-calc)/cm^{-1}
Q(3)	70227.70	70227.88	-0.18
Q(4),Q(5)	unresolved	-	-
Q(6)	70225.03	70225.05	-0.02
Q(7)	70224.58	70223.85	0.73
Q(8)	70223.08	70223.58	0.50
Q(9)	70221.34	70221.28	0.06
Q(10)	70219.91	70219.99	-0.08
S(0)	70266.79	70267.06	-0.27
S(1)	70292.16	70292.13	0.03
S(2)	70317.04	70316.99	0.05
S(3)	70341.95	70341.66	0.29
S(4)	70366.08	70366.15	-0.07
S(5)	70390.60	70390.47	0.13
S(6)	70414.22	70414.66	-0.44
S(7)	70437.61	70438.75	-1.14

Calculated band origin = 70229.1(5) cm^{-1}
Calculated effective rotational constant = 6.321(10) cm^{-1}
reduced Chi-squared = 0.36

TABLE 4.6: **(a)** Line positions and rotational analysis of the $F^1\Delta(2)$ (1,1) band, analysis of the P and R branches. See text for details of the fitting procedure.

Assignment	Observed position/cm^{-1}	Calculated position/cm^{-1}	Residual (obs-calc)/cm^{-1}
R(1)	70114.01	70113.98	0.03
R(2)	70125.55	70125.71	-0.16
R(3)	70136.60	70137.19	-0.59
R(5)	70159.14	70159.49	-0.35
P(3)	70051.37	70051.46	-0.09
P(4)	70038.49	70038.21	0.28
P(5)	70025.02	70024.76	0.26
P(6)	70011.58	70011.12	0.46
P(7)	69997.59	69997.31	0.28

Calculated band origin = 70089.7(6) cm^{-1}
Calculated effective rotational constant = 6.12(3) cm^{-1}
reduced Chi-squared = 0.52

TABLE 4.6: (b) Line position and rotational analysis of the $F^1\Delta(2)$ (1,1) band, analysis of the Q and S branches, no O branch was observed.

Assignment	Observed position/cm^{-1}	Calculated position/cm^{-1}	Residual (obs-calc)/cm^{-1}
Q(3)	70087.58	70087.57	0.01
Q(4)	70086.15	70086.24	-0.09
Q(5)	70084.36	70084.62	-0.26
Q(6)	70082.57	70082.72	-0.15
Q(7)	70080.67	70080.59	0.08
Q(8)	70078.51	70078.24	0.27
Q(9)	70075.57	70075.75	-0.18
S(0)	70125.75	70126.11	-0.36
S(1)	70150.51	70150.09	0.42
S(2)	70174.51	70173.74	0.77

Calculated band origin = 70089.6(6) cm^{-1}
Calculated effective rotational constant = 6.08(1) cm^{-1}
reduced Chi-squared = 0.31

TABLE 4.7: (a) Line positions and rotational analysis of the $F^1\Delta(2)$ (2,2) band, analysis of the P and R branches. See text for details of the fitting procedure.

Assignment	Observed position/cm^{-1}	Calculated position/cm^{-1}	Residual (obs-calc)/cm^{-1}
R(1)	69993.71	69993.93	-0.22
R(2)	70005.82	70005.44	0.38
R(3)	70016.68	70016.76	-0.08
R(4)	70027.85	70027.90	-0.05
P(3)	69933.07	69933.13	-0.06

Calculated band origin = 69970.2(9) cm^{-1}
Calculated effective rotational constant = 5.97(5) cm^{-1}
reduced Chi-squared = 0.27

TABLE 4.7: (b) Line positions and rotational analysis of the $F^1\Delta(2)$ (2,2) band, analysis of the Q and S branches, no O branch was observed.

Assignment	Observed position/cm^{-1}	Calculated position/cm^{-1}	Residual (obs-calc)/cm^{-1}
Q(3)	69969.01	69969.13	-0.12
S(0)	70005.82	70005.82	0.00
S(1)	70030.06	70029.94	0.12

Calculated band origin = 69969.5(2.1) cm^{-1}
Calculated effective rotational constant = 6.05(20) cm^{-1}
reduced Chi-squared = 0.12

FIGURE 4.3: [2+1] REMPI spectrum of the (0,0) and (1,1) bands of the $F^1\Delta_2(2) - X^1\Sigma^+(0^+)$ transition in HI.

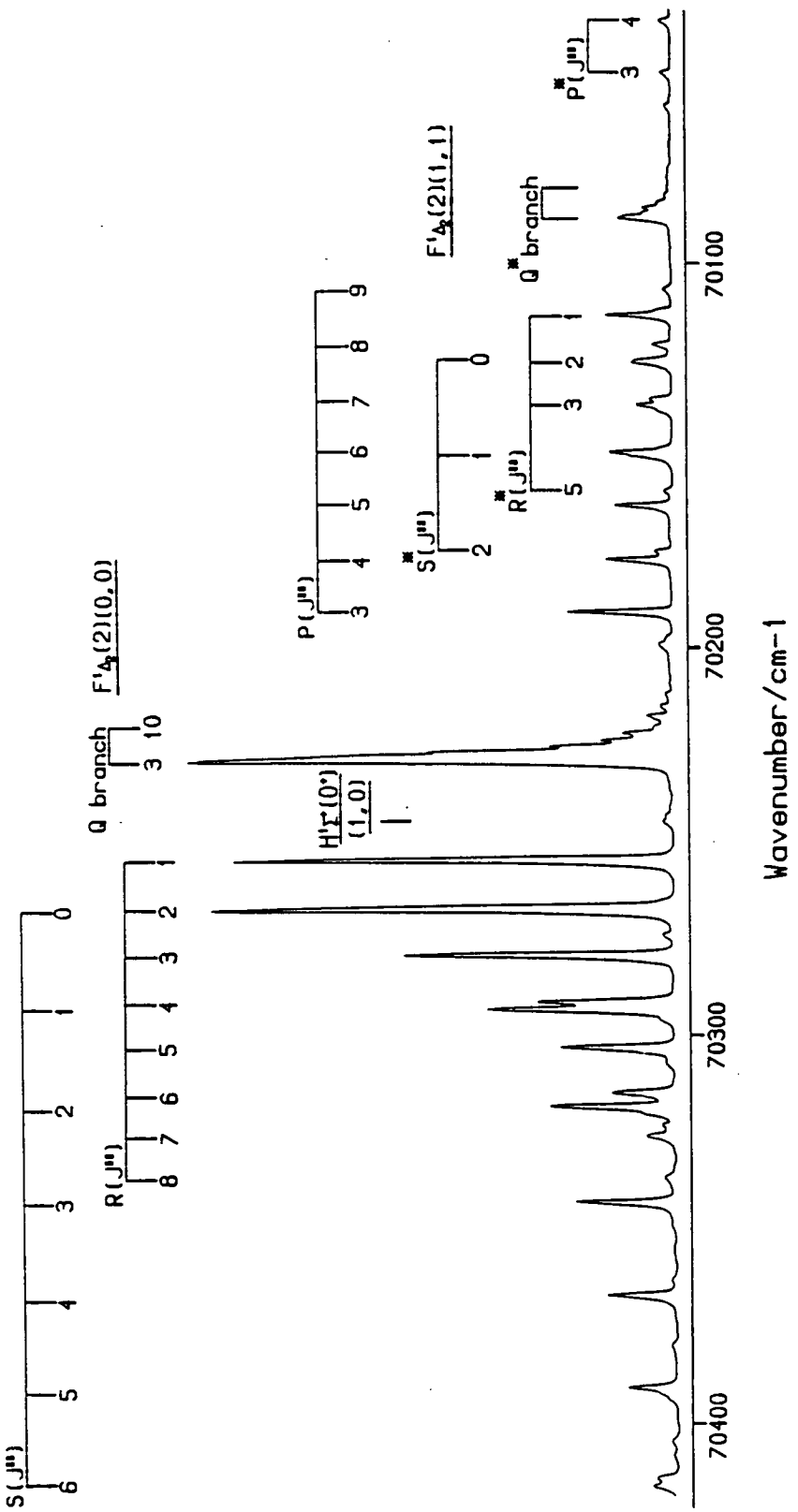

FIGURE 4.4: [2+1] REMPI spectrum of the (1,1) and (2,2) bands of the $F^1\Delta_2(2) - X^1\Sigma^+(0^+)$ transition in HI.

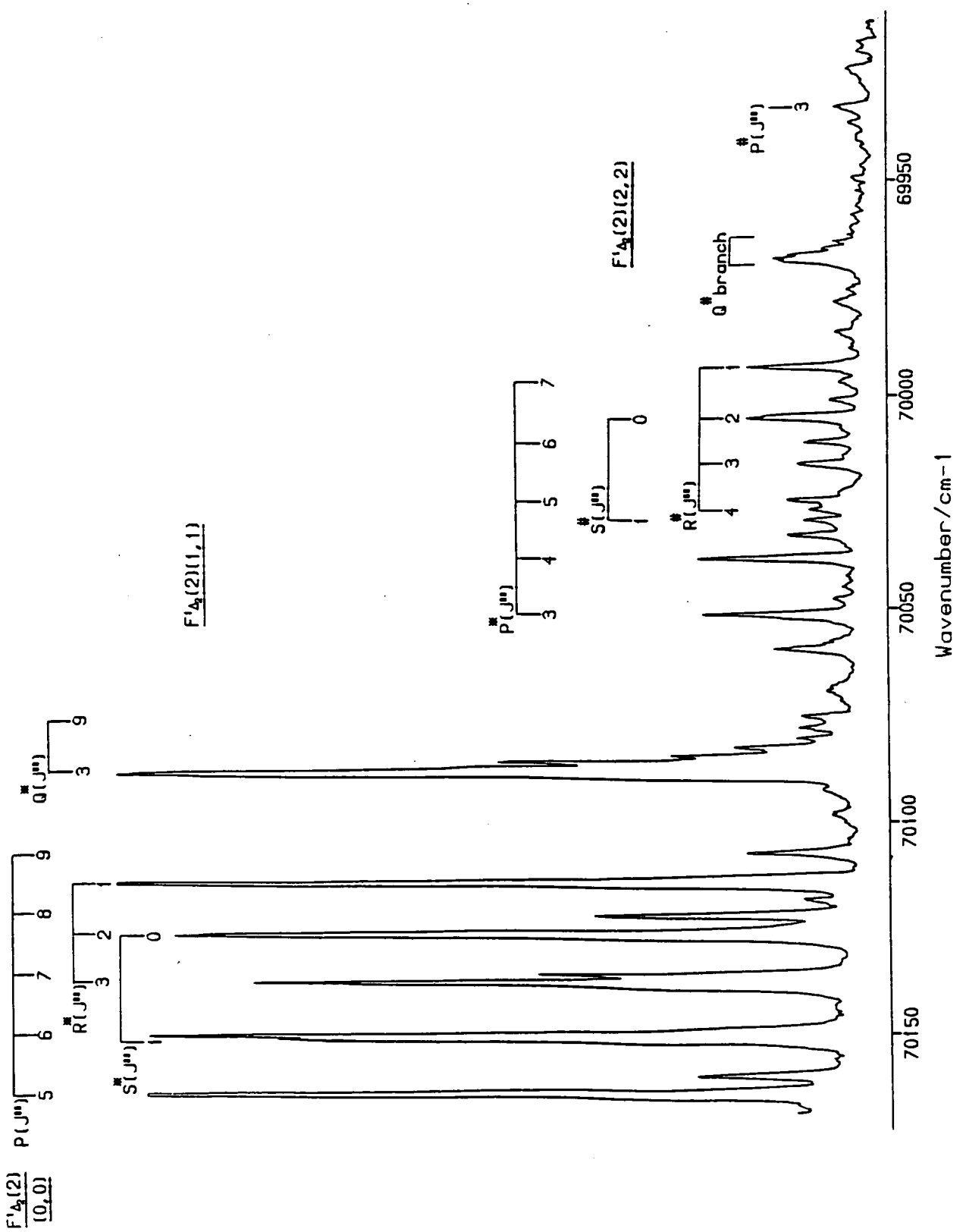

For the $F^1\Delta(2)$ state the Q branches were relatively congested, with Q(2) and Q(3) never being resolved. Hence, in order to help establish the J numbering in the Q branch the constants derived from the S branch could be used and the Q numbering varied until the minimum of the reduced Chi-squared was obtained.

From the three sequence bands it was possible to calculate some additional spectroscopic constants: T_e, ω_e and $\omega_e X_e$, by solving the three available simultaneous equations in the vibrational term value expression. Since the P and R branches produced constants with a slightly higher precision they were used to calculate the vibrational constants. However, since only the P and R branches were used, the estimated additional constants may, again, only be regarded as effective constants. Because only three bands were available for the calculation of the constants a meaningful error analysis was not possible, the quoted uncertainties were therefore derived by propagating the errors obtained from the analysis of the data presented in Tables 4.5 - 4.7. Table 4.8 presents these values.

TABLE 4.8: T_e, ω_e and $\omega_e X_e$ constants for the $F^1\Delta(2)$ state, calculated from the band origin data in Tables 4.5-4.7 from the P and R branches only. The numbers shown in brackets are the estimated uncertainties quoted at the 2σ level and should be applied to the last significant figures.

Spectroscopic constant	Value/cm^{-1}
T_e	70307.5(1.0)
ω_e	2148.2(1.4)
$\omega_e X_e$	29.2(0.6)

Similarly, the three rotational constants obtained from the sequence bands allowed calculation of the equilibrium effective rotational constant and the anharmonic distortion constant, α_e. Table 4.9 presents these values.

TABLE 4.9: Rotational constants for the $F^1\Delta(2)$ state of HI. Values in brackets are the uncertainty in the values quoted at the 2σ level and should be applied to the last significant figures.

Spectroscopic constant	Value/cm^{-1}
B_e	6.39(2)
α_e	0.17(2)

While the results presented in Tables 4.8 and 4.9 were calculated from an 'incomplete' representation of the $F^1\Delta(2)$ state band origins and rotational constants, examination of Tables 4.5 - 4.7 indicates that a 'full' analysis should yield very similar values to those reported, in preference, here.

By combining the calculated vibrational and rotational constants it was possible to estimate the Franck-Condon factors for absorption from v" = 0 and 1 of the $X^1\Sigma^+$ (0^+) state to the $F^1\Delta(2)$ state. These are presented in Table 4.10.

TABLE 4.10:(a) Franck-Condon factors for absorption from v" = 0 of the $X^1\Sigma^+$ (0^+) state to the $F^1\Delta(2)$ state.

Upper state vibrational level	Upper state turning points r_{min}/Å	r_{max}/Å	Franck-Condon factor
0	1.510	1.763	0.989
1	1.469	1.823	0.011
2	1.440	1.882	0.000

Equilibrium internuclear separation 1.624 Å.

TABLE 4.10:(b) Franck-Condon factor for absorption from v" = 1 of the $X^1\Sigma^+$ (0^+) state to the $F^1\Delta(2)$ state.

Upper state vibrational level	Franck-Condon factor
0	0.014
1	0.964
2	0.022

Table 4.10 reproduces the experimental observation that Δv 0 transitions are strongly disfavoured. This arises simply from the fact that the upper and lower state potentials, in the lower vibrational levels, are very similar and hence overlap of the wavefunctions is only significant for $\Delta v = 0$ transitions.

Observation of only $v' = 0,1$ and 2 of the $F^1\Delta(2)$ state was expected since these bands are accessed from the edge of a particular dye tuning curve. This point is however discussed more fully for the next state.

Consideration of the evidence concerning band origins and rotational symmetry leads naturally to invoking a state derived from the next electronic configuration ($d\pi$, see Table 4.1) for the previously unobserved $\Omega = 2$ state. The $d\pi$ configuration produces, in direct analogy with with the $c\pi$ configuration, the electronic states $i^3\Delta_i(3,2,1)$, $I^1\Delta_2$. Hence, it is natural to expect the splitting (that is the energy separation of the $^3\Delta_3$, $^3\Delta_2$ components from the $^3\Delta_1$, $^1\Delta_2$ components [32]) of the states to be approximately equal to the spin orbit coupling, A of the ion ($\sim$ 5350 cm^{-1}) [44]. The $i^3\Delta_3$ and $i^3\Delta_2$ states are associated with the lower ionisation limit $I_{3/2}$ while the $i^3\Delta_1$ and $^1\Delta_2$ states are associated with the upper, $I_{1/2}$ ionisation limit. In their vuv absorption studies Ginter et.al. [22] noted that, for HI, states derived from the $I_{3/2}$ core limit of 'higher' electronic configurations could be found to protrude into spectral regions

associated with states from lower electronic configurations. Also, the two photon selection rules allow transitions to all states but the $i^3\Delta_3$ state.

Following the interpretation of the $\Omega = 2$ HI bands near 70000 cm^{-1} as being due to sequence bands between the $F^1\Delta(2)$ and $X^1\Sigma^+(0^+)$ states, it is asserted, that the band associated with absorption from $v'' = 0$ of the ground state with an origin near 71990 cm^{-1} represents the allowed two photon absorption to $v' = 0$ of the $i^3\Delta_2(2)$ state.

While it was noted for the $c\pi$ configurations of HCl, HBr and HI that for the $f^3\Delta_2$ state $B' > B''$ [26][29][21], for the $i^3\Delta_2(2)$ state of HCl (the only hydrogen halide for which the i state has been observed), $B' < B''$. Ginter et.al. noted that as the number of electrons on the halogen increased the tendency towards $\Omega\omega$ coupling also increased. They also noticed that for HCl the states derived from the $d\pi$ configuration appeared to follow $\Omega\omega$ coupling more closely than those derived from the $c\pi$ configuration. Hence, assuming the previous statements form a trend, then for HBr and especially HI the $d\pi$ configurations should follow essentially pure $\Omega\omega$ coupling. Therefore a possible explanation for the lack of appearance in the vuv experiment may be that when the $\Omega\omega$ coupling scheme is a good description of the excited state, any additional coupling mechanism (such as rotational mixing highlighted in reference [21]), may be sufficiently weak that in the single photon absorption experiment a transition of $\Delta\Omega = 2$ remains unobserved (forbidden).

A more definitive assignment to these bands could be made by using the reaction $D + I_2$ (or even a simple glass cell) such that the effect of isotopic substitution would immediately indicate whether the band at 71990 cm^{-1} derived from $v'' = 0$ was terminating on $v' = 0$ or otherwise.

The initial expectation within any particular atomic iodine or molecule hydrogen iodide Rydberg series might be that the relative energy ordering and defects between the series members would be similar.

Hence, by examining the tables of atomic excitation energies [24] with the same J core states in the $[^3P_J]6p$ and $[^3P_J]7p$ atomic Rydberg series (which is considered to be a good approximation to the molecular situation) the 6p-7p energy splitting is near 10000 cm^{-1} and hence presents an uncomfortably large contrast to the difference reported here for the molecular states ~ 7300 cm^{-1}. The value of 10000 cm^{-1} cannot be considered entirely 'hard' because there is considerable (several thousand cm^{-1}) splitting of the sub-levels of the $[^3P]6p$ atomic configuration. The splitting must be due in some part to the exchange interaction between the 6p and 7p orbitals, which would nevertheless still be present in the molecule such that a similar magnitude of splitting should be observed. However, in atomic iodine the 5d and 7p orbitals are almost degenerate. Hence, it is possible that 5d-7p mixing in the molecule could force down the Rydberg states based on the 7p configuration quite substantially, i.e. to the observed 7300 cm^{-1} splitting in the HI molecule.

Typical spectra of the $i^3\Delta_2(2)$ (0,0) (1,1) and (2,2) sequence bands are shown in Figures 4.5 and 4.6. Several strong atomic iodine lines were available for calibration purposes, but in fact only one, the $^2S^o_{1/2} \longleftarrow {}^2P^o_{3/2}$ was used. The strong iodine line $^4D^o_{3/2} \longleftarrow {}^2P^o_{3/2}$ partially obscured the Q head of the (0,0) band, but otherwise did not appear to seriously degrade the spectral appearance of the head.

In Figures 4.5 and 4.6 branches associated with the (0,0) transition are labelled 0,P,Q etc.; those associated with the (1,1) band have an additional * label attached; while those associated with the (2,2) band are labelled with an additional # mark. The spectral region covered by the (0,0) (1,1) and (1,1) (2,2) bands required a change of both laser dye and frequency doubling crystal, hence a rapidly varying intensity profile is associated especially with Figure 4.6.

The sequence bands associated with this state show very similar behaviour to those of the $F^1\Delta(2)$ state. Hence, the rotational analysis was carried out in accordance with the discussion presented earlier, the derived constants are summarised in Tables 4.11 to 4.13.

FIGURE 4.5: [2+1] REMPI spectrum of the (0,0) and (1,1) bands of the $i^3\Delta_2(2)$ - $X^1\Sigma^+(0^+)$ transition in HI.

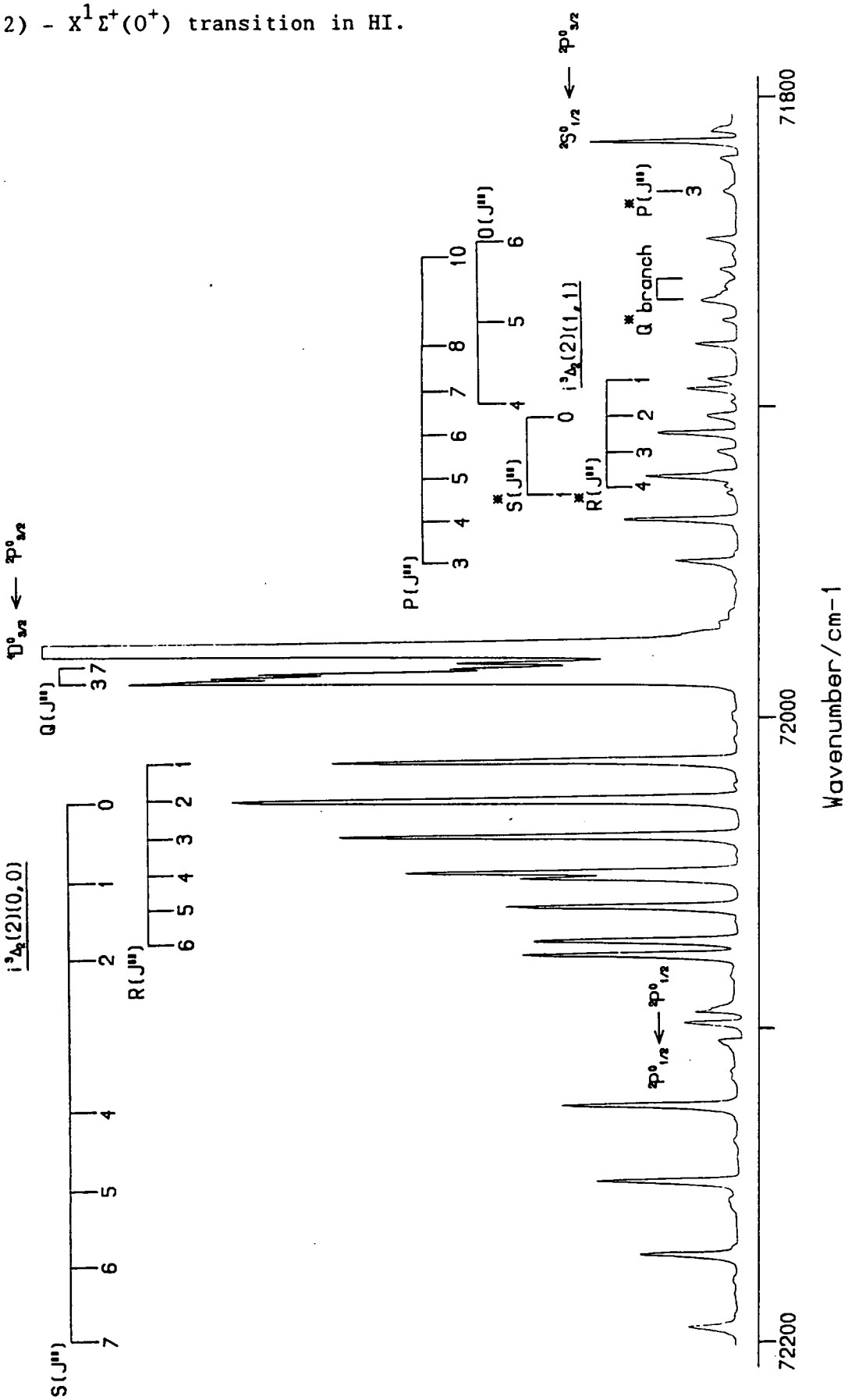

FIGURE 4.6: [2+1] REMPI spectrum of the (2,2) band of the $i^3\Delta_2(2) - X^1\Sigma^+(0^+)$ transition in HI.

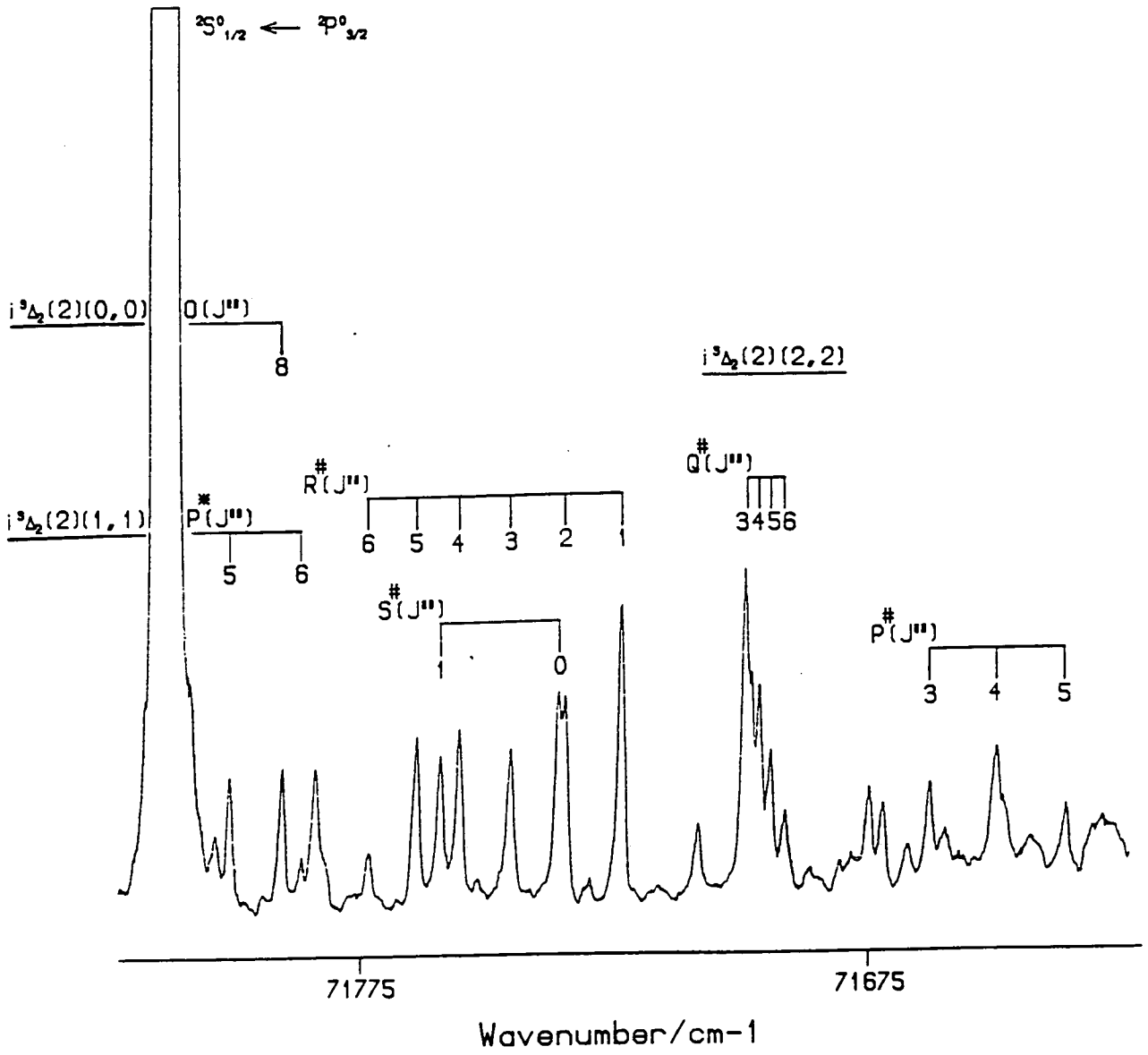

TABLE 4.11:(a) Line positions and rotational analysis of the $i^3\Delta_2$ (2) state, (0,0) band. Analysis of the P and R branches. See text for details of the fitting procedures.

Assignment	Observed position/cm^{-1}	Calculated position/cm^{-1}	Residual (obs-calc)/cm^{-1}
R(1)	72013.02	72013.39	-0.37
R(2)	72025.96	72026.46	0.50
R(3)	72037.44	72037.29	0.15
R(4)	72049.02	72048.88	0.14
R(5)	72060.22	72060.26	-0.04
R(6)	72071.94	72071.45	0.49
P(3)	71948.86	71949.17	-0.31
P(4)	71935.16	71935.57	-0.41
P(5)	71921.91	71921.77	0.14
P(6)	71908.12	71907.78	0.34
P(7)	71893.76	71893.64	0.12
P(8)	71879.38	71878.37	0.01
P(10)	71850.11	71850.62	-0.51

Calculated band origin = 71988.5(5) cm^{-1}
Calculated effective rotational constant = 6.295(12) cm^{-1}
reduced Chi-squared = 0.44

TABLE 4.11:(b) Line positions and rotational analysis of the $i^3\Delta_2$ (2) state, (0,0) band. Analysis of the Q,S and O branches.

Assignment	Observed position/cm^{-1}	Calculated position/cm^{-1}	Residual (obs-calc)/cm^{-1}
Q(3)	71987.33	71987.24	0.09
Q(4)	71986.08	71986.15	-0.07
Q(5)	71984.65	71984.82	-0.17
Q(6)	71983.28	71983.27	0.01
Q(7)	71982.08	71981.54	0.54
S(0)	72025.96	72026.63	-0.67
S(1)	72050.98	72051.48	-0.50
S(2)	72075.93	72076.04	-0.11
S(4)	72124.38	72124.37	0.01
S(5)	72148.36	72148.17	0.19
S(6)	72171.76	72171.74	0.03
S(7)	72194.73	72195.15	-0.42
O(4)	71898.35	71898.19	0.16
O(5)	71871.97	71871.73	0.24
O(6)	71845.92	71845.48	0.44
O(8)	71791.15	71791.18	-0.03

Calculated band origin = 71988.9(4) cm^{-1}
Calculated effective rotational constant = 6.283(10) cm^{-1}
reduced Chi-squared = 0.37

TABLE 4.12:(a) Line positions and rotational anlaysis of the $i^3\Delta_2$ (2) state, (1,1) band. Analysis of the P and R branches. See text for details of the fitting procedure.

Assignment	Observed position/cm^{-1}	Calculated position/cm^{-1}	Residual (obs-calc)/cm^{-1}
R(1)	71890.96	71891.37	-0.41
R(2)	71902.93	71902.96	-0.03
R(3)	71914.58	71914.90	0.32
R(4)	71925.23	71925.27	-0.04
P(3)	71829.31	71828.85	0.46
P(5)	71801.99	71802.16	0.17
P(6)	71787.70	71787.94	-0.24

Calculated band origin = 71867.3(9) cm^{-1}
Calculated effective rotational constant = 6.10(4) cm^{-1}
reduced Chi-squared = 0.38

TABLE 4.12:(b) Line positions and rotational analysis of the $i^3\Delta_2$ (2) state, (1,1) band. Analysis of the Q and S branches, no O branch was observed.

Assignment	Observed position/cm^{-1}	Calculated position/cm^{-1}	Residual (obs-calc)/cm^{-1}
Q(3)	71864.89	71864.77	0.12
Q(4)	71863.20	71863.42	-0.22
Q(5)	71861.95	71861.77	0.18
Q(6)	71859.77	71859.86	-0.09
S(0)	71902.93	71903.31	-0.38
S(1)	71927.68	71927.29	0.39

Calculated band origin = 71866.8(9) cm^{-1}
Calculated effective rotational constant = 6.08(4) cm^{-1}
reduced Chi-squared = 0.25

TABLE 4.13:(a) Line positions and rotational analysis of the $i^3\Delta_2$ (2) state, (2,2) band. Analysis of the P and R branches. See text for details of the fitting procedure.

Assignment	Observed position/cm^{-1}	Calculated position/cm^{-1}	Residual (obs-calc)/cm^{-1}
R(1)	71724.21	71724.07	0.14
R(2)	71734.24	71734.91	-0.67
R(3)	71745.72	71745.32	0.40
R(4)	71755.57	71755.31	0.26
R(5)	71764.75	71764.90	-0.15
R(6)	71773.99	71774.13	-0.14
P(3)	71663.26	71663.28	-0.02
P(4)	71649.81	71649.82	-0.01
P(5)	71636.12	71635.99	0.13

Calculated band origin = 71701.1(6) cm^{-1}
Calculated effective rotational constant = 5.86(2) cm^{-1}
reduced Chi-squared = 0.43

TABLE 4.13:(b) Line positions and rotational analysis of the $i^3\Delta_2$ (2) state, (2,2) band, analysis of the Q and S branches, no O branch was observed.

Assignment	Observed position/cm^{-1}	Calculated position/cm^{-1}	Residual (obs-calc)/cm^{-1}
Q(3)	71699.12	71699.54	0.42
Q(4)	71696.58	71696.77	-0.19
Q(5)	71694.70	71694.39	0.31
Q(6)	71691.41	71691.60	-0.19
S(0)	71736.40	71736.66	0.26
S(1)	71759.41	71759.50	-0.09

Calculated band origin = 71701.6(8) cm^{-1}
Calculated effective rotational constant = 5.83(3) cm^{-1}
reduced Chi-squared = 0.42

For the $i^3\Delta_2(2)$ state all five rotational branches were observed, hence, in this case the combination difference equations shown in section 4.6.1 could be utilised. However, only $v' = 0$ of the state produced a sufficient number of observable rotational transitions for the analysis to be worthwhile. The values of B′ and B" obtained by this method, were calculated by averaging the relevant differences, and are summarised in Table 4.14.

TABLE 4.14: The B′ and B" values for the $i^3\Delta_2$ (2) (0,0) band, calculated from the combination difference equations of section 4.6.1 and the line positions in Tables 4.11 - 4.13. The numbers shown in brackets represent the estimated uncertainties quoted at the 2σ level and should be applied to the last significant figures.

Rotational Branches	B'/cm^{-1}	B''/cm^{-1}
P,R	6.31(4)	6.43(6)
S,O	6.279(8)	6.40(2)

A comparison of Tables 4.14 and 4.11 may be made, with the deduction that the calculated B′ values agree very well. Similarly a comparison of the calculated B" value with that in the literature [66] also presents a favourable comparison.

Additionally the band origins for the $i^3\Delta_2$ (2) (0,0) band were determined from the separate P, R and S,O branches, as shown in section 4.6.1. In this case the values are presented in Table 4.15.

TABLE 4.15: Determination of band origin of the $i^3\Delta_2(2)$ (0,0) band from the P,R and S,O branches using equations (11) and (12). The values shown in brackets represent the estimated uncertainties quoted at the 2σ level and should be applied to the last significant figures.

Rotational Branches	Band Origin/cm^{-1}
P,R	71988.3(7)
S,O	71988.6(8)

Hence, both the estimated band origins and effective rotational constants agree, as expected, for both methods of determination. However, all the estimated spectroscopic constants are sufficiently imprecise that observation of separate band origins or Ω doubling (in the statistical sense) cannot be concluded.

Following the procedure for the $F^1\Delta$ state, the spectroscopic constants T_e, ω_e, $\omega_e X_e$ for the $i^3\Delta_2(2)$ state were calculated. The calculated values are presented in Table 4.16.

TABLE 4.16: T_e, ω_e and $\omega_e X_e$ constants for the $i^3\Delta_2(2)$ state, calculated from the band origin data derived from Tables 4.11 - 4.13 for the P and R branches only. The numbers shown in brackets are the estimated uncertainties quoted at the 2σ level and should be applied to the last significant figures.

Spectroscopic Constant	Value/cm^{-1}
T_e	72932.3(1,2)
ω_e	2232.5(1.8)
$\omega_e X_e$	62.0(0.7)

Hence the $i^3\Delta$ (2) state shows a much large vibrational anharmonicity than the $F^1\Delta(2)$ state.

In addition, the equilibrium effective rotational constant and anharmonic distortion constant were determined for the $i^3\Delta_2(2)$ state, in direct analogy to the $F^1\Delta_2$ (2) state. Table 4.17 presents these values:

TABLE 4.17: Rotational constants for the $i^3\Delta_2(2)$ state of HI. Values in brackets are the uncertainty in the values quoted at the 2σ level and should be applied to the last significant figures.

Spectroscopic constant	value/cm^{-1}
B_e	6.404(16)
α_e	0.217(11)

Comparison of Table 4.17 to Table 4.9 shows, in a similar manner to the vibrational constants, analogous values but significantly higher 'distortion' constants, for the $i^3\Delta_2(2)$ state than the $F^1\Delta_2(2)$ state.

By combining the calculated vibrational and rotational constants it was possible to estimate the Franck-Condon factors for absorption from v" = 0 of the $X^1\Sigma^+(0^+)$ state to the $i^3\Delta_2$ (2) state. These are presented in Table 4.18:

TABLE 4.18: Franck-Condon factors for absorption from v" = 0 of the $X^1\Sigma^+(0^+)$ state to the $i^3\Delta_2$ (2) state.

Upper state Vibrational level	Upper state turning points r_{min}/Å	r_{max}/Å	Franck-Condon factor
0	1.512	1.761	0.987
1	1.473	1.829	0.013
2	1.445	1.886	0.000

Equilibrium internuclear separation 1.625Å

Hence, a comparison of both the Ω = 2 Rydberg state (see Tables 4.8 - 4.10 and 4.16 - 4.18) indicates that they show highly analagous behaviour, are involved primarily in Δv = 0 transitions from the ground state but that the $i^3\Delta_2(2)$ state shows more 'anharmonicity'. The experimental methodology was such that the reaction zone contained in fairly high local concentrations, additional species such as H, H_2, I, I_2. The total number density for any of these species was not determined for the typical experimental situation. Hence, the zone of interest (containing the HI hot bands) was poorly defined. In this context two experimental observations must be explained:

1) since v" = 4 of the ground state is reported to be the most populated level why were transitions from greater than v" = 2 never observed from any band and
2) why were transitions from v" = 0 observed with most intensity.

The hot bands were observed to 'relax' very quickly, however even at a minimum experimental injection to probe distance of ~ 1mm no additional

bands became evident (although this point was not investigated rigorously because of the aforementioned experimental difficulties, it did appear to be generally true). An injection to probe distance of say 2mm corresponds to a 'flight time' of approximately 200 μs and this corresponds to approximately 2000 gas phase collisions for a reactor pressure near 1 Torr. For small molecules SSH theory [70] predicts that the probability of V $\longrightarrow$ T energy trnsfer is very small per gas phase collision, (unless specific resonant transfer processes are available). Hence, for a molecule with a large vibrational spacing such as CO (ω_e = 2170 cm^{-1}) relaxation of v" = 1 by H_2 has a probability near 1 x 10^{-4}, while for relaxation by Ar a value near 1 x 10^{-6} is observed. Therefore, on this simple basis near nascent vibrational distributions should have been observed.

However, it is believed that additional more efficient 'relaxation' mechanisms may be contributing to producing the experimental observations. In particular these mechanisms may be:

$$H + IH^{\ddagger} \longrightarrow HI + H \qquad (13)$$

$$HI^{\ddagger} + I \longrightarrow HI + I\ (I^*) \qquad (14)$$

While it appears that the rates of these processes have not previously been measured, similar processes may be found in the literature. For example the rates of relaxation of v' = 1 of DCl by Cl and Br have been measured at 5.5 x 10^{-12} and 2.3 x 10^{-13} cm^3 $molecule^{-1}$ s^{-1} [71], and are very efficient. For the resonant energy transfer process of deactivation of HF (v" = 1) by Br ($^2P^o_{3/2}$) a rate near 3 x 10^{-11} cm^3 $molecule^{-1}$ s^{-1} was measured [72]. The rate of the exchange mechanism (equation 13) has been measured by Polanyi et.al. [73] for the reaction for HF + D. Although the reaction is thermoneutral it does display (perhaps surprisingly) a high activation barrier which was noted to reduce significantly at higher v".

Since the 'zone' over which reaction took place was not well defined experimentally and because no states with v" > 2 were ever observed

an alternative or contributing explanation may also be put forward. Repulsive valence states with symmetries of Ω = 2,1,0 are known and because higher vibrational levels have turning points at smaller r, a predissociative interaction may well play an important role in preventing observation of high lying vibrational levels of any Rydberg state.

Within the wavelength range studied in this chapter two additional states with Ω = 2 symmetry should have, but never were, observed. These were the transitions to $m^3\Pi_2$ v′ = 0,1 and the $k^3\Pi_2$ v′ = 0. In fact no observations of similar $^3\Pi_2$ bands have been reported in the previous REMPI studies on the HX family. The only possible explanations for this observation are either: a predissociative loss mechanism, for which some evidence may have been expected from the vuv absorption studies; or simply a weak absorption strength in a [2+1] process.

4.6.3 Discussion of Ω = 1 states

Examination of Table 4.4 indicates that no Ω = 1 states were observed during this work. Comparison to previous REMPI experiments with HCl are revealing, Gordon et.al. [17], in analogy to these experiments, observed no Ω = 1 states while Brown [19] obtained fragmentary information from a few bands. Gordon et.al. attributed the lack of any Ω = 1 bands in their spectra to obeyance of the selection rules they derived. However, those rules are spurious as shown in references [57] and [58] and as observed by Brown. A more convincing argument discussed by Brown relates to the likelihood that the states may well be strongly predissociated.

The vuv absorption spectra recorded by Ginter et.al. for HI [20-23] indicates that all Ω = 1 states below 68000 cm^{-1} exhibit predissociation effects, indeed above this energy the $D^1\Pi$ (1) state also exhibits diffuse rotational structure. As shown by the calculations of Chapman et.al. [33] there are several states of the correct symmetry to cause such predissociation effects in the Rydberg series.

Work carried out subsequent to these studies using LIF (REMPI) of HI following two photon absorption, by a fellow worker Mr G.G. McFadyen, detected bands attributable to $v' = 0$ and 1 of the $k^3\Pi_1$ state. These experiments were carried out with HI pressures of greater than 1 Torr and hence indicates the weak absorption strength associated with these bands.

4.6.4 Discussion of $\Omega = 0$ states

The $V^1\Sigma^+(0^+)$ ion pair state of HI was observed by Ginter et.al. [20-23] to dominate the single photon absorption spectrum, since it formed a long vibrational progression, although as discussed earlier it was observed to be extensively perturbed by the other Rydberg states with 0^+ symmetry.

To highlight the rather extensive perturbations present between the 0^+ states, the deviations of the observed ion pair bands from an empirical interpolation equation, similar to that given by Ginter et.al. [22], was used to construct Figure 4.7. The equation used was:

$$\nu = 68000 + 505\ (n) - 5\ (n)^2 \qquad (15)$$

Where n is taken as an integer that runs from 0 to 14 and hence covers the wavelength region investigated in this chapter. Also marked on the spectrum are the positions of all the previously reported states of 0^+ symmetry within this wavelength range. As is evident from the diagram the positions of maximum deviation are nearest the clusters of states of 0^+ symmetry, thus indicating maximal interstate perturbation and mixing.

The rotational constant is normally regarded as determining the expectation value $< r^{-2} >$ and hence the equilibrium internuclear separation. To further highlight the nature of these configurational interactions the rotational constants of the ion pair state (taken from the work of Ginter et al. [22]) were plotted in Figure 4.8. Also indicated in Figure 4.8 are the positions of the previously reported states of 0^+ symmetry, within the wavelength range of these experiments.

FIGURE 4.7: Deviations of the known vibrational level energies for $V^1\Sigma^+(0^+)$ from their interpolated values (see text). The asterix indicates the interpolated position of the v′ = m+7 level. The energies of the non-V-state 0^+ levels previously known to exist in this region are indicated by vertical lines.

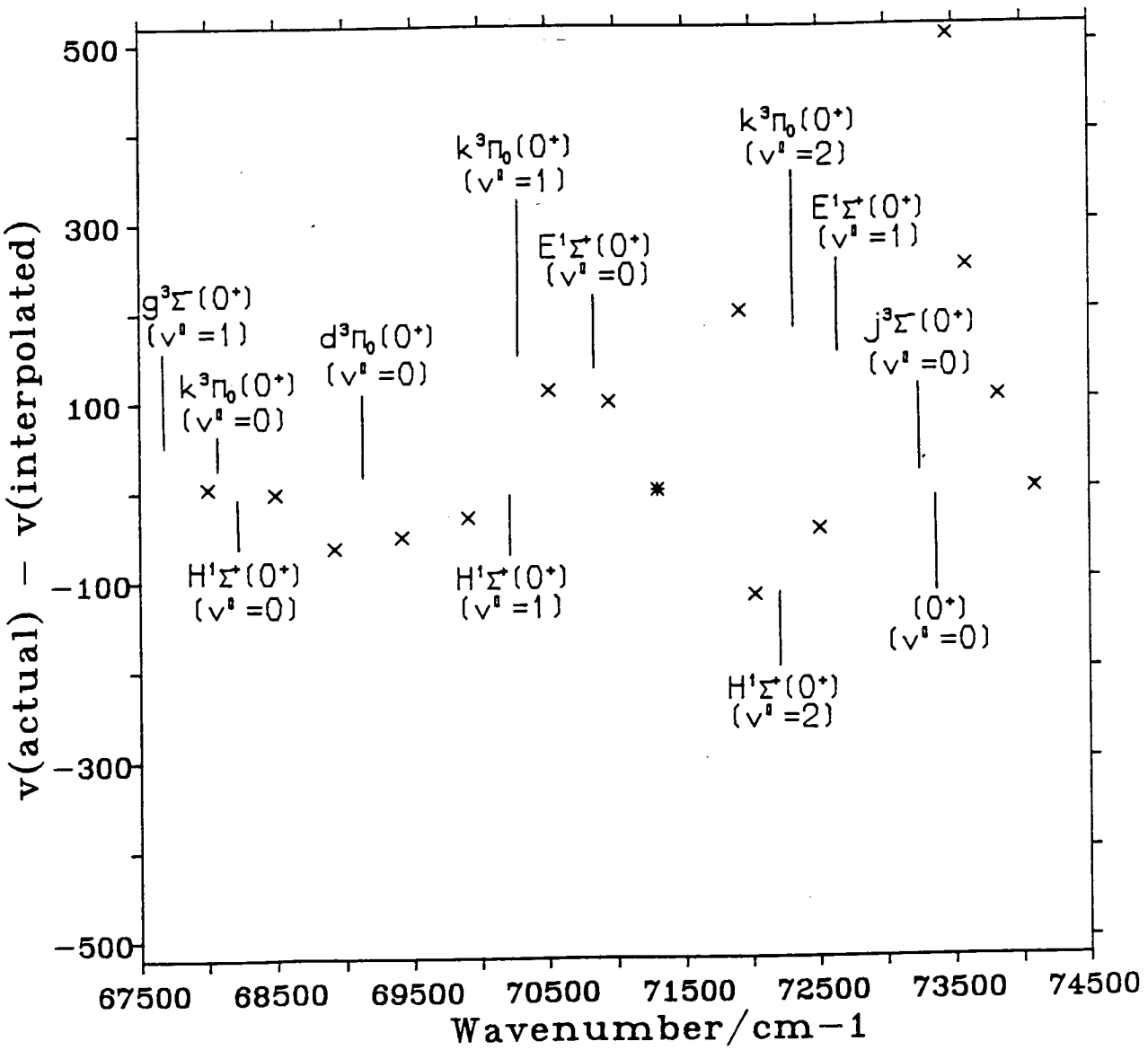

FIGURE 4.8: Rotational constants of the known vibrational levels for $V^1\Sigma^+(0^+)$. The energies of the non-V-state 0^+ levels previously known to exist in this region are indicated by vertical lines.

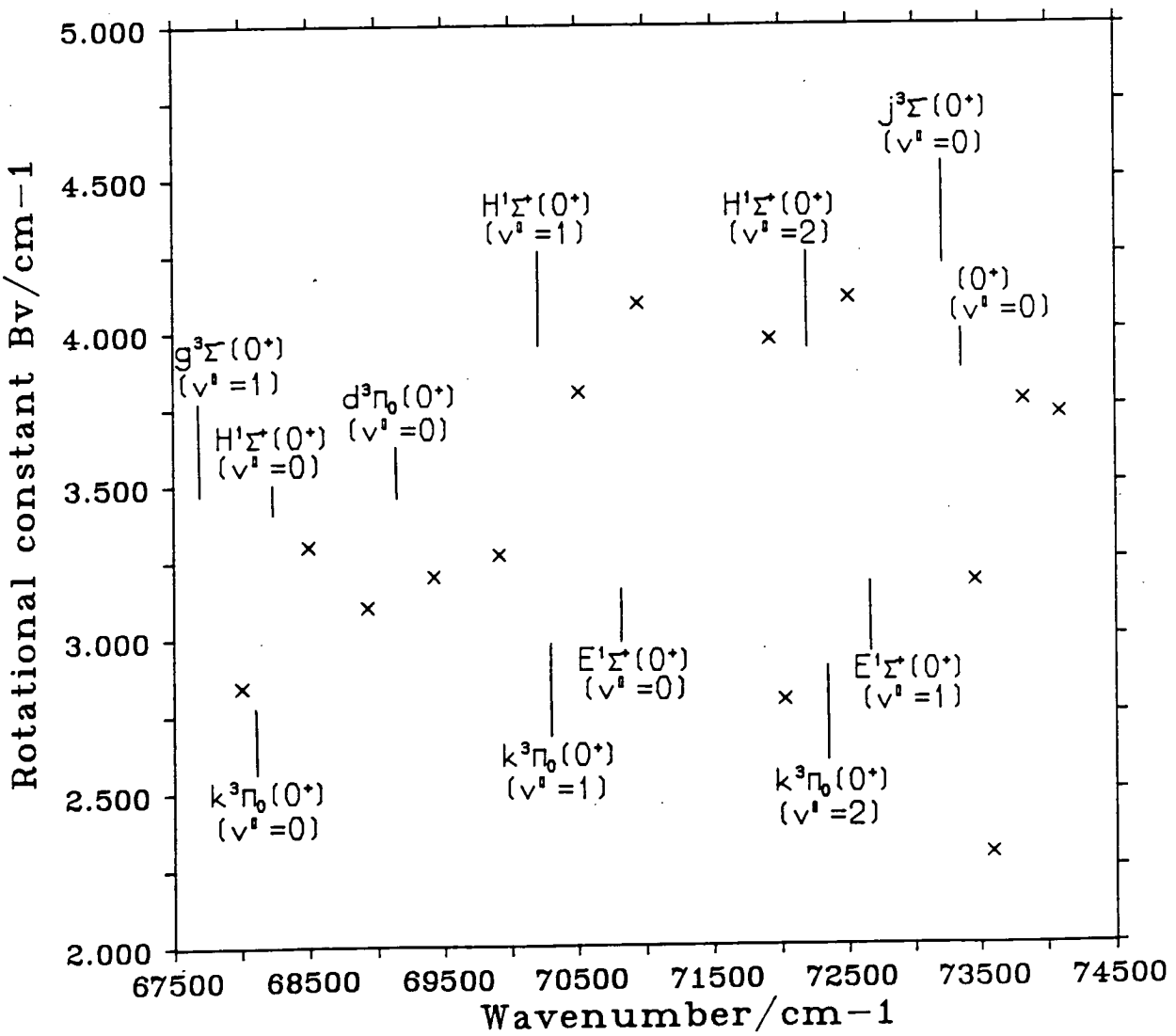

In direct analogy to Figure 4.7 the largest deviations are observed around the culsters of Rydberg states with 0^+ symmetry. In addition to the perturbed B values the centrifugal distortion constants were noted for several of the ion pair levels to possess large negative values.

Perturbation between the various 0^+ states were manifest in the observed spectra in several ways. For example in Figure 4.1 both the intensities and positions of the rotational levels of v' = m of the $V^1\Sigma^+(0^+)$ state near the $g^3\Sigma^-(0^+)$ state were perturbed, while in Figure 4.9 the intensity of J = 6 of the (0,1) band of the $0^+(I)$ state appeared to be anomalous (this could not be checked on the (0,0) band). A more pronounced effect was observed between the E-X (0,0) and V-X ((m+6),0) transitions. For the $V^1\Sigma^+(0^+)(m+6)$ band the J value which had maximum intensity was J = 6 (assuming Boltzmann statistics the J value with maximum intensity should be 4) for a sample of 300 K and was directly adjacent to the Q head of the E state. The (m+6) band was the strongest observed ion pair band and its anomalous intensity distribution indicates that it may be 'stealing' intensity from the E state.

Interpretation of the rotational lines associated with the E-X (0,0) or V-X ((m+6),0) bands was facilitated by observation of the (0,1) band of the E-X transition because no lines attributable to the hot band transition to the (m+6) state were observed. Such an observation was interpreted simply in terms of the differing Franck-Condon factors between the ground and excited states when excitation occurs either from v" = 0 or v" = 1. Similarly while it was observed that v' = 1 of the $k^3\Pi_0(0^\pm)$ band was observed only weakly from v" = 0, the band was observed much more strongly from v" = 1. It is noted in passing therefore that pumping from higher v" could be used to determine if ion pair vibrational levels with a 'quantum number' lower than m can be observed.

In addition to various perturbations, predissociation effects were observed in several bands. For v' = 1 of the $k^3\Pi_0(0^\pm)$ band, not only were J = 5,6 perturbed but J = 5 was diffuse, this observation

FIGURE 4.9: The anomalous rotational contour, especially for J=6, of the (0,1) hot band transition for the previously known but unassigned 0^+ state.

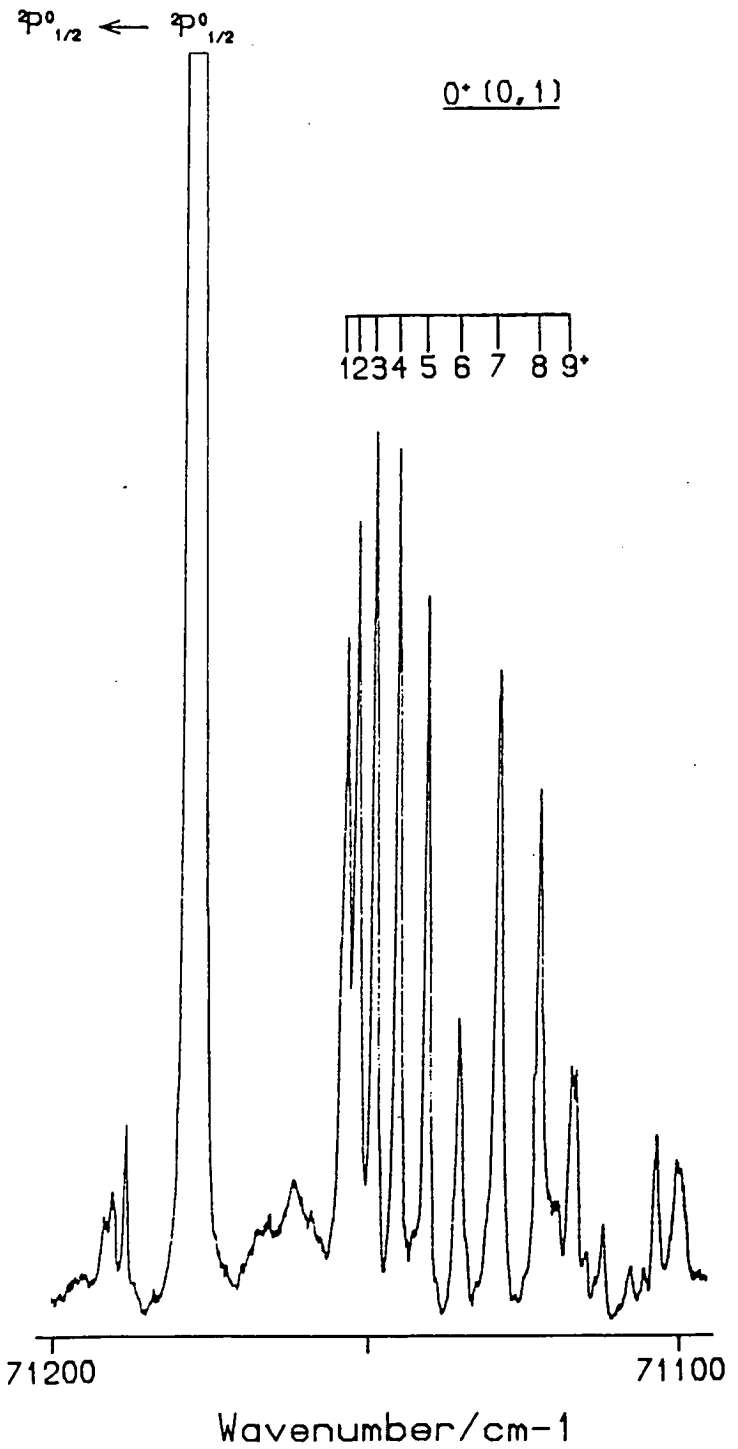

would be consistent with the presence of a local heterogeneous perturbation [73]. The $V^1\Sigma^+(0^+)$ m+10 level was observed to be diffuse for all the observed lines, with a line intensity which decreased rapidly from $J_{max} = 2$. For the $H^1\Sigma^+$ $v' = 0$ band, the effect was so pronounced that for J = 6 a linewidth (FWHM) near 8 cm^{-1} was measured, this corresponds to a lifetime of less than one picosecond.

A previously unobserved 0^+ state was observed in this work, 0^+(II) in Table 4.4. The lack of observation of this state in the vuv absorption studies of Ginter et.al. [22] is, at first glance, surprising since a transition to a 0^+ state is fully allowed in a one photon absorption experiment. However, it was noted that the band origin for this state, ~ 71300 cm^{-1} lies in the rotational contour of the $m^3\Pi_1(1)$ band which Ginter et.al. [22] did observe. The $m^3\Pi_1(1)$ band was reported to be one of the strongest bands in the single photon work, hence it is deduced that this previously unobserved band was simply masked in the vuv absorption experiments.

It was noted from the work of Ginter [22] that the vibrational spacing of the (0,0) and (1,0) bands of the $D^1\Pi(1)$ state was ~ 2138 cm^{-1} and that the difference in the rotational constants was approximately 0.15 cm^{-1}. The (0,0) band of the $d^3\Pi_0(0^\pm)$ state was observed to lie approximately 100 cm^{-1} lower in energy than the $D^1\Pi(1)$ state and to have a similar rotational constant. Therefore, since the (1,0) band of the $D^1\Pi(1)$ state was reported to lie near 71382 cm^{-1}, the (1,0) band of the $d^3\Pi_0(0^\pm)$ state should lie near 71282 cm^{-1}. Similarly the measured rotational constant for the previously unreported band is 5.99 cm^{-1}, and is approximately 0.15 cm^{-1} lower than the (0,0) band of the $d^3\Pi_0(0^\pm)$ state. These observations therefore lead to the conclusion that this previously unobserved band is actually the (1,0) band of the $d^3\Pi_0(0^\pm)$ state. Table 4.19 presents the measured lines positions and rotational analysis of this band while Figure 4.10 presents a typical experimental spectrum.

FIGURE 4.10: The rotational contour of the (1,0) band of the $d^3\Pi_0(0^{\pm})$ state of HI. Just distinguishable were transitions attributable to the O and S branches. The rotational contour shows a non-uniform decrease in line intensity with increasing J.

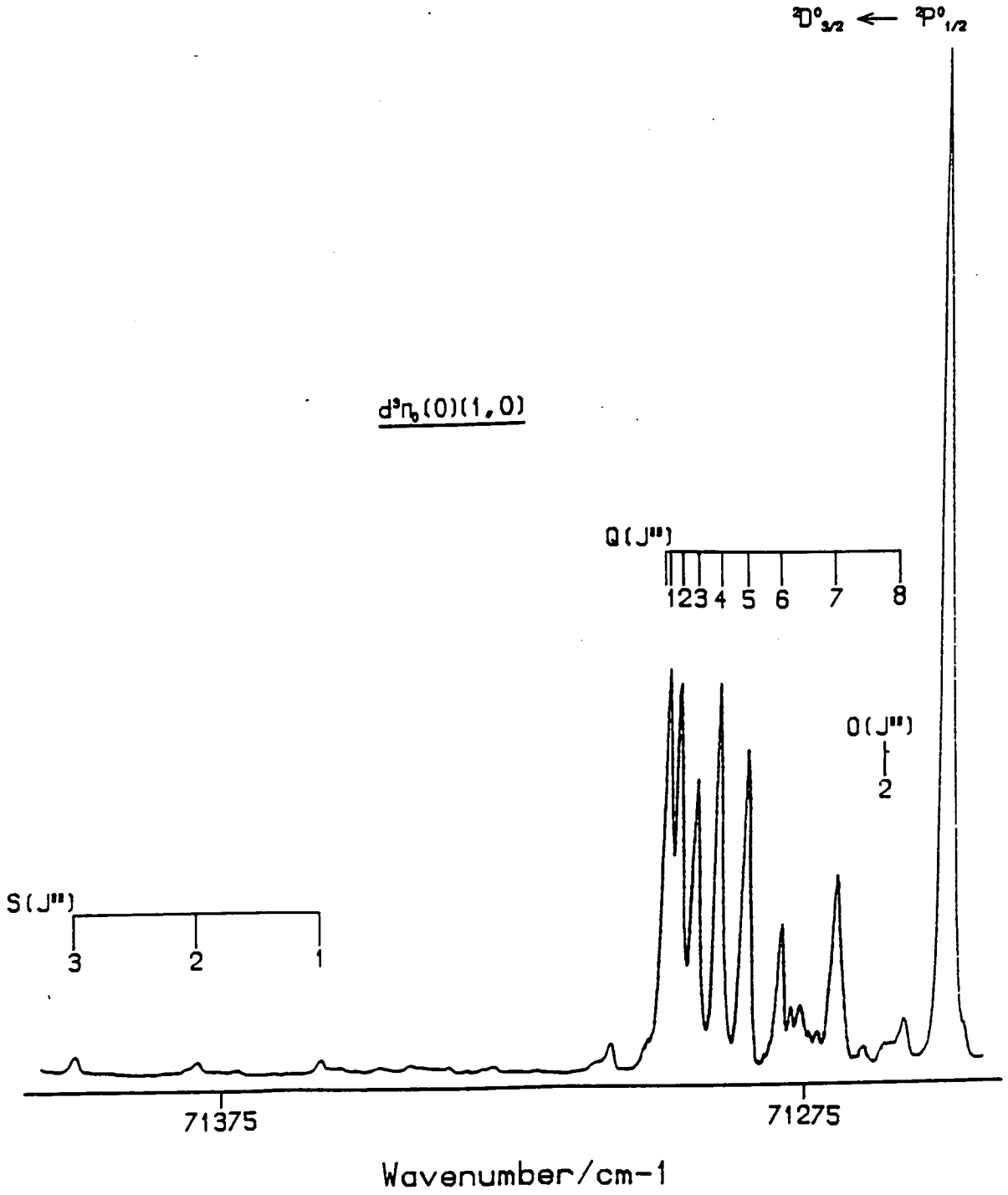

TABLE 4.19: Line positions and rotational analysis of the $d^3\Pi_0(0^{\pm})$ (1,0) band

Assignment	Observed position/cm^{-1}	Calculated position/cm^{-1}	Residual (obs-calc)/cm^{-1}
Q(0)	71301.90	71302.08	-0.18
Q(1)	71301.17	71301.19	-0.02
Q(2)	71299.55	71299.38	0.17
Q(3)	71296.70	71296.56	0.14
Q(4)	71292.39	71292.61	-0.22
Q(5)	71287.36	71287.37	-0.01
Q(6)	71281.15	71280.64	0.51
Q(7)	71272.61	71272.17	0.44
Q(8)	71261.37	71261.68	-0.31
S(1)	71360.56	71360.80	-0.24
S(2)	71382.09	71382.51	-0.42
S(3)	71402.19	71402.89	-0.70
O(2)	71263.89	71264.25	0.36

Calculated band origin = 71302.1(7) cm^{-1}
Calculated rotational constant = 5.99(6) cm^{-1}
Calculated distortion constant = 18(8) x 10^{-4} cm^{-1}
reduced Chi-squared = 0.21

4.7 Simulation of REMPI spectra

The experimental description given in section 4.5 indicates that an isotropic distribution of ground state molecules should result from the rapid thermalisation of the reaction products, with perhaps only the vibrational degree of freedom being non-thermal. Hence, provided alignment of the intermediate state via the initial two photon absorption process is not too important [74] then assuming that absorption of the third photon is independent of wavelength and that it is saturated for all transitions, the individual line strengths should follow from (see Appendix I):

$$I = C\, S_{J',J''} \exp(-E_{rot}/kT) \qquad (16)$$

where $\exp(-E_{rot}/kT)$ is the rotational energy of the particular J", k is the Boltzmann's constant and T the temperature. $S_{J',J''}$ is the two-photon rotational linestrength, see for example [57][58], while C is a constant which reflects the transition dipole between the two

states and is independent of the rotational transition. The'structure' of the constant C has been discussed in [57].

The dependence of the ionisation signal on the laser intensity (power) was determined for the Q head of the $F^1\Delta(2)$ and $i^3\Delta(2)$ states and for R(1) of the $i^3\Delta(2)$ state. In all cases the plot of the log of the intensity against the log of the ionisation signal was found, by a least squares fitting procedure, to have a slope near 2.0 with a typical uncertainty quoted at the 2σ level of 0.2. Thus, at the power levels used (near 500 μJ per pulse with a 31 cm focussing lens), the ionisation step was likely to be close to kinetic saturation, as suggested by Zakheim and Johnson [75]. Similar plots to those just described were not obtained for any other states. In these cases, the behaviour of the state was assumed to be analogous to that of the $\Omega = 2$ states.

Since the initial two photon absorption was observed to be the rate limiting step then equation (16) and the two photon rotational line strengths should form an adequate basis for the interpretation of the observed spectra.

However, examination of the literature indicates, in general, that the two-photon linestrengths do not normally reproduce the observed intensity distributions in the HX spectra [15][17]. For example, Chandler et.al. [15] observed that for the (0,0) band of the $E^1\Sigma^+ - X^1\Sigma^+$ transition in HCl that the measured and calculated linestrengths (using the formulae in reference [57]) fitted poorly, with the quality of the fit decreasing with increasing J. To explain this observation they invoked a declining strength in the transition dipole with increasing angular momentum. However, as already noted, Brown [19] has proposed that predissociation may play an important role in the excited electronic states of HCl; this argument will now be considered for the case of HI.

In general, a predissociative mechanism is predicted to increase the width of the spectral line and decrease its height, both being in

accord with the shortening of the excited state lifetime. Hence since both fluorescence and ionisation experiments occur on timescales that are capable of probing the excited state dynamics, predissociation effects may be manifest in these experimental spectra.

There are two forms of predissociation: homogeneous ($\Delta\Omega = 0$) which affects all lines equally except for a weak dependence of the predissociation rate on the vibrational quantum number and heterogeneous predissociation ($\Delta\Omega = \pm 1$) which normally manifests itself more obviously with the rate of predissociation being proportional to the varying content of the excited state angular momentum. Tellinghuisen [76] has shown that the spontaneous predissociation decay rate k_{pred}, is given by:

$$k_{pred} = k'J(J+1) \qquad (17)$$

where k' is a scaling constant and J is the total angular momentum; with this explanation being successfully utilised by Ashfold and Dixon [77-79].

The observed signal strength for an ionisation (fluorescence) process depends on the quantum yield for that process ϕ as well as the line strength factor and the initial population. Therefore, given the rate of ionisation is independent of wavelength, the quantum yield will be defined as:

$$\phi = \frac{k_i}{k_T} \qquad (18)$$

Where k_i is the rate constant for ionisation and k_T is the sum of the rate constants for loss of the excited state and is given by:

$$k_T = k_i + k_{fl} + k_{pred} \qquad (19)$$

k_{fl} is the 'rate constant' for fluorescence. Hence using equation (18), the quantum yield is:

$$\phi = \frac{k_i}{(k_i + k_{fl} + k_{pred})} \qquad (20)$$

In the case of no predissociative loss, or when J = 0, it is possible to define ϕ_o as:

$$\phi_o = \frac{k_i}{(k_i + k_{fl})} \tag{21}$$

Hence by combining equations (20) and (21)

$$\phi = \frac{\phi_o}{[1 + CJ(J+1)]} \tag{22}$$

Where $C = \frac{k'}{k_i + k_{fl}}$ (23)

or alternatively:

$$\phi = \frac{\phi_o}{F} \tag{24}$$

Where F is the 'damping function' and is given by:

$$F = (1 + CJ(J+1)) \tag{25}$$

Therefore the observed ϕ is reduced from that expected in the absence of predissociation, ϕ_o. The effect on an observed spectrum is two-fold, the observed spectral line height h is reduced from the value h_o, predicted purely from linestrength and population arguments, while the linewidth w, will show a proportionate increase as a consequence of the decreased excited state lifetime. Hence

$$h = \phi\, h_o/F = {}^{h_o\phi_o}/_{F^2} \tag{26}$$

$$w = w_o F \tag{27}$$

The term which is included in the simulation therefore is the ${}^{1}/_{F^2}$ term which controls the spectral line heights. No effort was made to 'correct' the spectral linewidths of the simulation because in this work, except for a very few cases, the observed linewidth was governed by the instrumental resolution, which for these experiments was near 1 cm^{-1}.

4.7.1 Simulation of $\Omega = 0$ transitions

The simulation of any of the $0^+ - 0^+$ transitions proved difficult because the extensive perturbations existing between the 0^+ states were

often all too obvious in terms of the observed rotational envelopes and line positions of the states. In this situation only the least perturbed states were chosen as examples from which to attempt the simulation. Figure 4.11 shows a simulation of the hot band transition ((m+13),1) between the $V^1\Sigma^+(0^+)$ and $X^1\Sigma^+(0^+)$ states. Although weak the band does appear to be relatively free of intensity and positional perturbations at low J.

Simulation of a $0^+ - 0^+$ band requires an estimation of two independent transition dipole moments μ_I and μ_S, as defined in references [57] and [58]. The absolute values of μ_I^2 and μ_S^2 are not required for the simulation, only their ratio. An estimate of the ratio may be obtained simply from the relative intensities between the Q and the O or S branches or alternatively by using linearly and circularly polarised light. However neither of these methods were available in this case and an arbitrary ratio was set such that no O and S branches were observed, as in the experiment. The required value of the damping function was 0.03 and was the largest for any of the simulations shown here and thus indicated that the (m+13) level was strongly affected by predissociation effects. The spectrum and simulation shown in Figure 4.11 have not been normalised for variations in the laser power, however over the relatively small range of the scan this did not vary appreciably.

In Figure 4.12 the simulation for the $g^3\Sigma^-(0^+) - X^1\Sigma^+(0^+)$ (1,0) band is presented. In this case the 'damping function' took a value of 0.02 and hence was significantly less than that of the high lying ion pair state level. An explanation for this behaviour was taken to be simply that the relative coupling of the g state level to its predissociating 'state' was much less efficient than for the V state to its predissociating 'state'. Again however the match of the experimental and simulated spectrum was reasonable. In this case S branch lines were clearly observable in the spectrum, hence an estimate of the ratio μ^2_I/μ^2_S could be obtained as 0.15. Because the S branch lines were observed very weakly this ratio is somewhat uncertain. As for Figure 4.11 the spectrum does not contain the normalisation for the changing laser intensity across the wavelength range covered by the band.

FIGURE 4.11: Simulation of the [2+1] REMPI spectrum of the ((m+13),1) band of the $V^1\Sigma^+(0^+)$ - $X^1\Sigma^+(0^+)$ transition of HI. The simulation assumed a laser bandwidth of 1.0 cm^{-1}, T = 300 K and a 'damping' factor of 0.03.

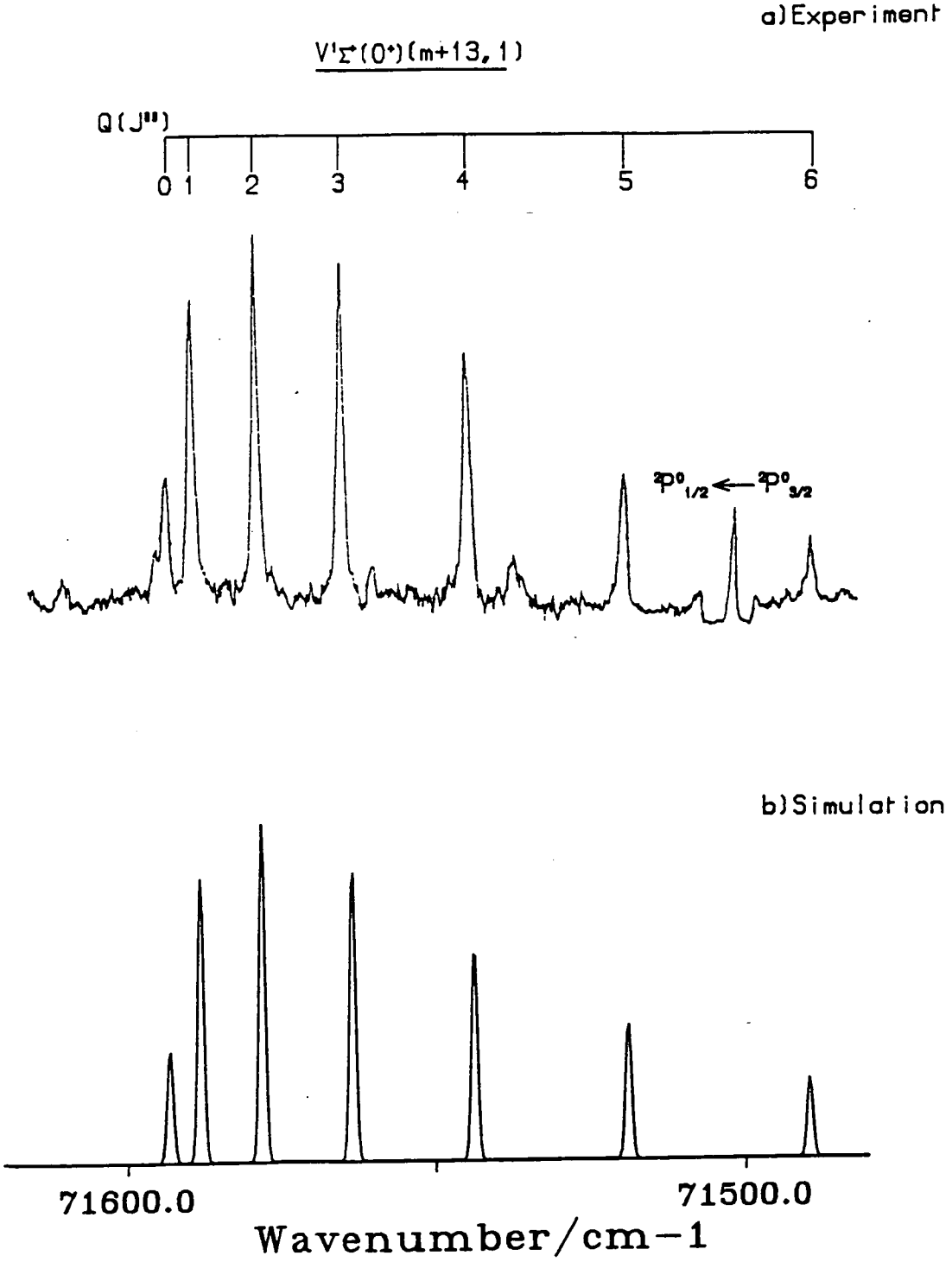

FIGURE 4.12: Simulation of the [2+1] REMPI spectrum of the (1,0) band of the $g^3\Sigma^-(0^+)$ - $X^1\Sigma^+(0^+)$ transition of HI. The simulation assumed a laser bandwidth of 1.0 cm^{-1}, T = 300 K and a 'damping' factor of 0.02.

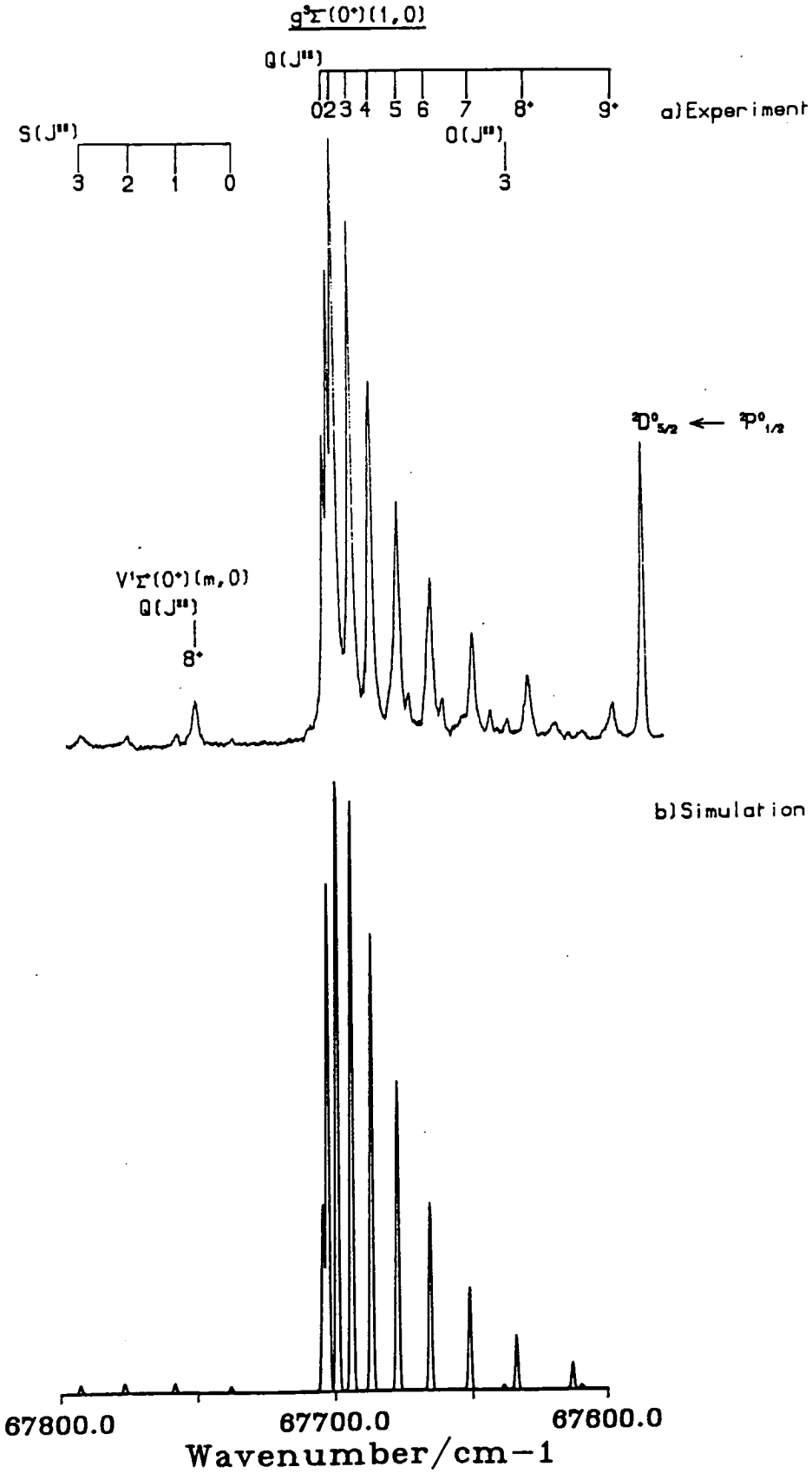

4.7.2 Simulation of Ω = 2 transitions

At first sight the Ω = 2 transitions appear to present ideal candidate states for population monitoring of the ground state. This observation being encouraged by the fact that both the Ω = 2 states observed in this work produced highly regular rotational structure, with the inclusion of all the observed rotational lines in the least squares fitting procedure and the determination of the effective rotational constants with high precision. However, even for these states, the 'damping' term is found to improve the overall fit. Since the $i^3\Delta_2(2)$ state was previously unobserved it was chosen as the basis for which to attempt the simulation but, because of the strong iodine resonance $^4D^o_{3/2} \longleftarrow {}^2P^o_{3/2}$ which overlapped the high rotational structure of the Q branch, relatively less importance was attached to modelling the intensity of this branch in comparison to the others. Figure 4.13 shows the (0,0) and, weakly, the (1,1) bands of the $i^3\Delta(2) - X^1\Sigma^+(0^+)$ transition. In this case the simulation has been corrected for the square of the variation of the laser power, by applying a polynomial approximating function to the variation in laser power and then applying this function to the simulation for comparison with experiment. The intensity of the (0,0) and (1,1) bands have been arbitrarily scaled to fit the experimental observations. In Figure 4.13 a 'damping' function value of 0.005 was used and hence was the state (of those that were simulated) which showed the least spontaneous predissociation effects. However, this simulated spectrum presents the worst comparison to experiment of any of those modelled. The alternative choice, the $F^1\Delta(2)$ state did not fit the simulation to a significantly better degree.

It was concluded from the above paragraph, that for the Ω = 2 cases the simulation was only acceptable. To investigate more rigorously the applicability of the linestrength theory in these cases would require a more carefully defined experimental procedure.

FIGURE 4.13: Simulation of the [2+1] REMPI spectrum of the (0,0) and (1,1) sequence bands of the $i^3\Delta_2(2) - X^1\Sigma^+(0^+)$ transition of HI. The (0,0) and (1,1) bands were arbitrarily scaled to fit the observed intensities. The simulation assumed a laser bandwidth of 1.0 cm^{-1}, T = 300 and a 'damping' factor of 0.005.

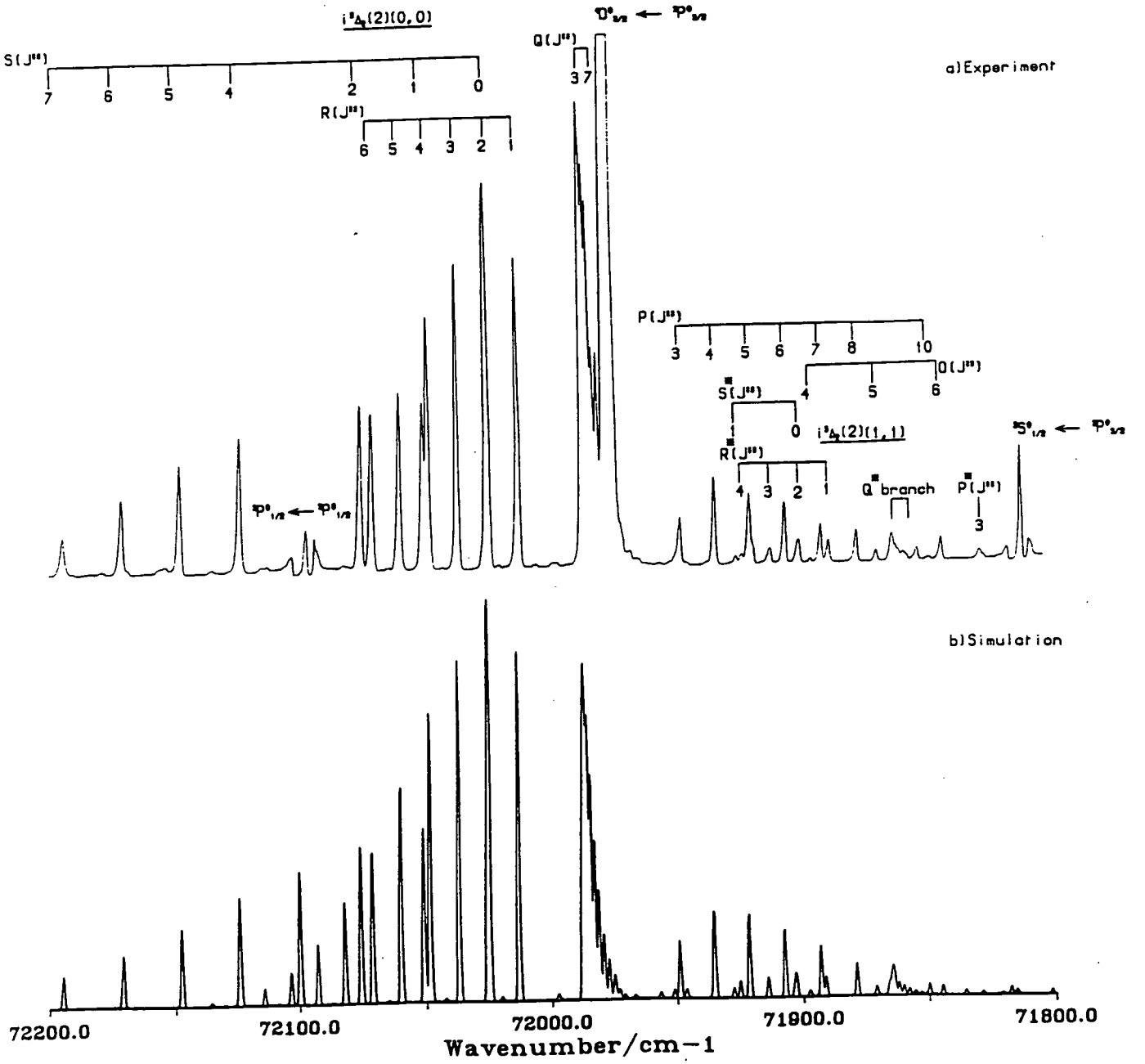

While the rotational constants derived in section 4.6 reproduced the observed line spacings very well, the two band origins which best reproduced the overlap of the separate Ω components of the $i^3\Delta(2)$ state were not those derived from the best squares fitting routine, but were: 71988.6 and 71988.7 cm^{-1} and nevertheless fell within the statistical uncertainties derived from the data. Therefore for the (0,0) band these values may be regarded as being comparable to those in Table 4.4.

4.8 Conclusions

In this Chapter [2+1] REMPI has been used to investigate the excited state spectroscopy of HI at selected regions between 67500 and 73500 cm^{-1}. The HI was generated via the reaction: $H + I_2 \longrightarrow HI + I$, hence investigation of excited ground state population distributions was also possible.

The following conclusions were drawn from this work.

1) The estimated rotational constants and band heads compare favourably with the results obtained from the single photon vuv absorption studies. In general the Ω = 2 states appear to be well behaved spectroscopically while the Ω = 0 states show extensive perturbations and diffuse structure. These observations confirm the extensive mixing between the states of 0^+ symmetry.

2) The single and two photon absorption techniques form valuable complementary tools in the study of the excited states of molecules since additional states may appear in the two photon spectra. In particular transitions to two previously unobserved systems were observed in this work, these were the (0,0)(1,1) and (2,2) bands of the $i^3\Delta(2) - X^1\Sigma^+(0^+)$ sequence bands and the transition to v′ = 1 of the $d^3\Pi_0(0^\pm)$ state.

3) The REMPI technique is capable of probing nascent product state distributions. However, in this work it was not possible to determine whether an efficient energy transfer mechanism and or a predissociative loss process precluded the observation of the expected highly vibrationally excited HI formed from the generating reaction.

4) Application of the two photon linestrength theory was found not to accurately predict the observed rotational contours, with all the excited states appearing to suffer to a greater or lesser extent from predissociation effects.

Therefore in closing it may be concluded that monitoring of ground state population distributions may not be safely performed without a detailed knowledge of the excited state dynamics.

REFERENCES

1. M.R. Levy, Prog. Rn. Kins., 10 1 (1979).
2. I.W.M. Smith in 'Physical Chemistry of Fast Reactions, vol2. Reaction Dynamics' ed. I.W.M. Smith (Plenum Press, London 1980).
3. B.E. Holmes and D.W. Setser in 'Physical Chemistry of Fast Reactions. vol2. Reaction Dynamics' ed. I.W.M. Smith (Plenum Press, London 1980).
4. R.P. Wayne in 'Chemistry of Atmospheres', (Clarendon Press, Oxford 1985).
5. K.G. Anlauf, P.J. Kuntz, D.H. Maylotte, P.D. Pacey and J.C. Polanyi, Diss. Far. Soc. 44 183 (1967).
6. J.D. McDonald, P.R. Le Breton, Y.T. Lee and D.R. Herschbach, J. Chem. Phys., 54 769 (1972).
7. D. Brandt, L.W. Dickson, L.N.Y. Kwan and J.C. Polanyi, Chem. Phys., 39 189 (1979).
8. P.M. Aker, D.J. Donaldson and J.J. Sloan, J. Phys. Chem., 90 3110 (1986).
9. J.C. Polanyi, Proc. R. Soc., Can 54 (c) 25 (1960).
10. J.V.V. Kasper and G.C. Pimental, Phys. Rev. Lett., 14 352 (1965).
11. M.C. Lin, M.E. Unstead and N. Djeu, Ann. Rev. Phys. Chem., 34 557 (1983).
12. R. Zhang, D.J. Rakestraw, K.G. McKendrick and R.N. Zare, J. Chem. Phys., 89 6283 (1988).
13. K.D. Rinnen, D.A.V. Kliner, M.A. Buntine and R.N. Zare, Chem. Phys. Lett., 169 365 (1990).
14. G.D. Kubiak, G.O. Sitz and R.N. Zare, J. Chem. Phys., 83 2538 (1985).
15. D.W. Chandler and R.L. Farrow, J. Chem. Phys., 85 810 (1986).
16. R. Callaghan, Y.L. Huang, S. Arepalli and R.J. Gordon, Chem. Phys. Lett., 158 531 (1989).
17. R. Callaghan, S. Arepalli and R.J. Gordon, J. Chem. Phys., 86 5273 (1987).

REFERENCES (Cont/d)

18. T.A. Spiglanin, D.W. Chandler and D.H. Parker, Chem. Phys. Lett., 137 414 (1987).
19. M.A. Brown 'Multiphoton Laser Spectroscopy and Photochemistry of Electronically Excited HCl' Edinburgh University thesis 1987.
20. S.G. Tilford, M.L. Ginter and A.M. Bass, J. Mol. Spec., 34 327 (1970).
21. M.L. Ginter, S.G. Tilford and A.M. Bass, J. Mol. Spec., 57 271 (1975).
22. D.S. Ginter, M.L. Ginter and S.G. Tilford, J. Mol. Spec., 92 40 (1982).
23. D.S. Ginter, M.L. Ginter, S.G. Tilford and A.M. Bass, J. Mol. Spec., 92 55 (1982).
24. C.E. Moore, 'Atomic Energy Levels' Vol I-III National Bureau of Standards (1971).
25. S.G. Tilford, M.L. Ginter and J.T. Vanderslice, J. Mol. Spec., 33 505 (1970).
26. S.G. Tilford and M.L. Ginter, J. Mol. Spec., 40 568 (1971).
27. D.S. Ginter and M.L. Ginter, J. Mol. Spec., 90 177 (1981).
28. M.L. Ginter and S.G. Tilford, J. Mol. Spec., 34 206 (1970).
29. M.L. Ginter and S.G. Tilford, J. Mol. Spec., 37 159 (1971).
30. D.S. Ginter, M.L. Ginter and S.G. Tilford, J. Mol. Spec., 90 152 (1981).
31. R.S. Mulliken, Phys. Rev., 50 1017 (1936).
32. R.S. Mulliken, Phys. Rev., 57 500 (1940).
33. D.A. Chapman, K. Balasubramanian and S.H. Lin, Chem. Phys. Lett., 118 192 (1985).
34. M. Bettendorf, S.D. Peyerimhoff and R.J. Buenker, Chem. Phys., 66 261 (1982).
35. H. Lefebvre-Brion and R.W. Field in 'Perturbations in the Spectra of Diatomic Molecules', (Academic Press, New York 1986).
36. P.J. Bruna and S.D. Peyerimhoff in 'Ab-initio Quantum Chemistry, vol 1', ed. K.P. Lawley (Wiley, New York 1986).
37. J. Romand, Ann. Rev. Phys (Paris) 4 527 (1949).
38. S. Datta and D.N. Kundu, Proc. Nat. Ins. Sci. India, 7 311 (1941).

REFERENCES (Cont/d)

39. W.C. Price, Proc. Roy. Soc. Ser A167 216 (1938).
40. R.S. Mulliken, Phys. Rev., 51 310 (1937).
41. R.D. Clear, S.J. Riley and K.R. Wilson, J. Chem. Phys., 63 1340 (1975).
42. R. Schmiedl, H. Dugan, W. Meier and K.H. Welge, Z. Phys. A 304 137 (1982).
43. R.S. Mulliken, Phys. Rev., 61 277 (1942).
44. J.H.D. Eland and J. Berkowitz, J. Chem. Phys., 67 5034 (1977).
45. L.D. Spicer and B.S. Rabinovitch, Ann. Rev. Phys. Chem., 21 349 (1970).
46. J.H. Sullivan, J. Chem. Phys., 46 73 (1967).
47. K. Lorenz, H. Gg. Wagner and R. Zellner, Ber. Buns. Phys. Chem., 83 556 (1979).
48. H. Umemoto, S. Nakagawa, S. Tsunashima and S. Sato, Chem. Phys., 124 259 (1988).
49. M.D. Pattengill, J.C. Polanyi and J.L. Schreiber, J. Chem. Soc. Far. Trans. II 72 897 (1976).
50. J.B. Anderson and R.T.V. Kung, J. Chem. Phys., 58 2477 (1973). erratum ibid 60 2202 (1974).
51. J. Grosser and H. Haberland, Chem. Phys. 2 342 (1973).
52. S.H.P. Bly, D. Brandt and J.C. Polanyi, Chem. Phys. Lett., 65 399 (1979).
53. J.C. Polanyi and W.J. Skrlac, Chem. Phys., 23 167 (1977).
54. M.R. Levy and J.P. Simons, J. Chem. Soc. Far. Trans. II 71 561 (1975).
55. W.M. McClain and R.A. Harris in 'Excited States', Vol3 ed. E.C. Lim (Academic Press, New York 1977).
56. I. Kovacs in 'Rotational Structure in the Spectra of Diatomic Molecules', (Institute of Physics, Bristol 1969).
57. R.G. Bray and R.M. Hochstrasser, Mol. Phys., 31 412 (1976).
58. A.C. Kummel, G.O. Sitz and R.N. Zare, J. Chem. Phys., 85 6874 (1986).

REFERENCES (Cont/d)

59. J.H. Kolts and D.W. Setser in 'Reactive Intermediates in the Gas Phase Generation and Monitoring' ed. D.W. Setser (Academic Press, New York 1979).
60. C.R.C. 'Handbook of Chemistry and Physics', 70th edn. ed. R.C. Weast (CRC Press Inc).
61. M.A.A. Clyne and W.S. Nip, J. Chem. Soc. Far. Trans. II 73 161 (1977).
62. A.H. Taylor Jr and R.H. Crist, J. Am. Chem. Soc., 63 1377 (1941).
63. W.E. Hollingsworth, J. Sabbiah, G.W. Flynn and R.E. Weston Jr, J. Chem. Phys., 82 2295 (1985).
64. R.D. Clear and K.R. Wilson, J. Mol. Spec., 47 39 (1973).
65. J.P. Sung and D.W. Setser, J. Phys. Chem., 80 437 (1976).
66. G. Guelachvili, P. Niay and P. Bernage, J. Mol. Spec., 85 253 (1981).
67. P.R. Bevington in 'Data reduction and error analysis for the physical sciences', (McGraw Hill, New York 1969).
68. E.D. Palik, J. Chem. Phys., 23 217 (1955).
69. G. Herzberg in 'Molecular Spectra and Molecular Structure. I. Spectra of Diatomic Molecules', (D. Van Nostrand, New York 1950).
70. J.T. Yardley in 'Introduction to Molecular Energy Transfer', (Academic Press, New York 1980).
71. R.G. MacDonald and C.B. Moore, J. Chem. Phys., 65 5198 (1976).
72. G.P. Quigley and G.J. Wolga, J. Chem. Phys., 62 4560 (1975).
73. F.E. Bartoszek, D.M. Manos and J.C. Polanyi, J. Chem. Phys., 69 933 (1978).
74. D.C. Jacobs and R.N. Zare, J. Chem. Phys., 85 5457 (1986).
75. D.S. Zakheim and P.M. Johnson, Chem. Phys., 46 263 (1980).
76. J. Tellinghuisen, J. Chem. Phys., 57 2397 (1972).
77. M.N.R. Ashfold, R.N. Dixon and R.J. Stickland, Chem. Phys., 88 463 (1984).
78. M.N.R. Ashfold, J.M. Bayley and R.N. Dixon, Can. J. Phys., 62 1806 (1984).
79. M.N.R. Ashfold, R.N. Dixon, K.N. Rosser, R.J. Stickland and C.M. Western, Chem. Phys., 101 467 (1986).

APPENDIX I

Simulation of LIF excitation and REMPI Spectra

To simulate any transition for which resolution is high enough to resolve or partly resolve rotational (fine) structure, it is necessary to have some understanding of the coupling of angular momenta. Angular momentum affects spectral appearance in two ways:

1) Control of the energy level structure in the combining states.

2) Control of allowed transitions via selection rules and intensities of the various branches.

The total wavefunctions of the states of interest are described via differing approximations of the way angular momenta couple in the molecule, (Hunds cases). The various angular momenta are defined as follows:

S is the electronic spin angular momentum
L is the electronic orbital angular momentum
J is the total angular momentum
N is the total angular momentum excluding electronic spin (N=J-S)
R is the nuclear rotational angular momentum (R=N-L)

In a Hunds case (a) basis, L and S are coupled to the internuclear axis and thus have the projection quantum numbers on this axis of Λ and Σ respectively. The resultant $|\Lambda + \Sigma|$ forms the projection quantum number Ω. The total angular momentum J is therefore the sum of $|R + \Omega|$ and this makes the projection M on the space fixed Z axis.

APPENDIX I (Cont/d.)

Hunds case (b) differs primarily from case (a) in that the spin vector S is not coupled to the internuclear axis. In this case the projection quantum number Λ and R couple to form a resultant N. N then couples with S to form the total angular momentum J, which again has the projection M on the space fixed Z axis. When the spin-orbit interaction is strong Λ and Σ are not defined and only the total electronic angular momentum Ω can be used. The nuclear rotation R then adds vectorially to Ω to make the total angular momentum J.

The energy levels for any state follow from the eigenvalues of:

$$\langle \Psi (p^{\pm}) | H^{v}_{rot} | \Psi (p^{\pm}) \rangle \qquad (1)$$

$\Psi (p^{\pm})$ is the wavefunction describing the electronic state and whose nature depends on the type of coupling outlined above. H_{rot} is the rotational part of the Hamiltonian that is capable of reproducing the energy level structure of the particular vibronic level v of the state [2].

i) $^2\Sigma^+ - {}^2\Pi$ single photon transition (SiCl)

The approach adopted here follows the procedure outlined by Meijer et.al. [3]. For the $^2\Pi$ state a Hamiltonian H, capable of reproducing the experimental data is:

$$H=B''(R^2) - D''(R^2)^2 + \gamma'' \, N.S + A'' \, L.S + \tfrac{1}{2} A''_D \, [(R^2)(L.S) + (L.S)(R^2)] \qquad (2)$$

The precise mathematical meaning of the rotational (B), centrifugal distortion (D), spin orbit (A), spin orbit rotation distortion (A_D) and the spin rotation (γ) constants may be found in reference [4], while the constants dealing with lambda doubling effects (p,q,p*,q* and o) are defined in reference [5]. Lambda doubling arises through the interaction of nuclear rotation with the orbital angular momentum [1].

APPENDIX I (Cont/d.)

To extract spectroscopic constants from a spectrum requires that the Hamiltonian be redefined in terms of effective constants. This is necessary because the constants γ'' and A''_D are nearly totally correlated [6]. When expressed in terms of the effective constants and under the assumption $A''/B'' >> 1$ (Hunds case(a) limit), the Hamiltonian matrix becomes:

$$[H] = B''_{eff}\begin{bmatrix} Z+1 & -Z^{1/2} \\ -Z^{1/2} & Z-1 \end{bmatrix} + A''_{eff}\begin{bmatrix} -\frac{1}{2} & 0 \\ 0 & \frac{1}{2} \end{bmatrix} - D''\begin{bmatrix} (Z+1)^2+Z & -2Z^{3/2} \\ -2Z^{3/2} & (Z-1)^2+Z \end{bmatrix}$$

$$+ \gamma''_{eff}\begin{bmatrix} -1 & \frac{1}{2}Z^{1/2} \\ \frac{1}{2}Z^{1/2} & 0 \end{bmatrix} \mp (J+\tfrac{1}{2})\begin{bmatrix} \frac{1}{2}p+q & -\frac{1}{2}qZ^{1/2} \\ \frac{1}{2}qZ^{1/2} & 0 \end{bmatrix} + k\begin{bmatrix} 1 & 0 \\ 0 & 1 \end{bmatrix} \qquad (3)$$

Where $Z = (J-\frac{1}{2})(J+3/2)$

and $k = \frac{1}{2}(q^* + o) - \frac{1}{2}(A''/B'')A''_D$, which is incorporated into the band origin.

The (2x2) submatrices can be recombined to a single (2x2) matrix. The eigenvalues of the Hamiltonian (eq.2) have therefore been reduced to finding the roots of a (2x2) secular determinant. In the general case,

$$\begin{bmatrix} Haa-E & Hab \\ Hab & Hbb-E \end{bmatrix} = 0 \qquad (4)$$

from which application of the formula for the roots of a quadratic yields the eigenenergies:

$$E = \tfrac{1}{2}\left[(Haa + Hbb) \pm \left\{ (Haa - Hbb)^2 + 4Hab^2 \right\}^{2}\right] \qquad (5)$$

The eigenenergies (four in all for each J) from equation (3) were obtained from two applications of equation (5) by simply gathering the appropriate terms into the matrix elements; for example:

APPENDIX I (Cont/d.)

$$Haa1 = B(z+1) - \tfrac{1}{2}A - D[(z+1)^2 + z] - \gamma - (J+\tfrac{1}{2})(\tfrac{1}{2}p+q) \quad (6)$$

$$Hbb = B(z-1) + \tfrac{1}{2}A - D[(z-1)^2 + z] \quad (7)$$

$$Hab = -BZ^{\frac{1}{2}} + 2Dz^{3/2} + \tfrac{1}{2}\gamma z^{\frac{1}{2}} + \tfrac{1}{2}qz^{\frac{1}{2}}(J+\tfrac{1}{2}) \quad (8)$$

While the two other roots are formed by using:

$$Haa2 = B(Z+1) - \tfrac{1}{2}A - D[(z+1)^2 + z] - \gamma + (J+\tfrac{1}{2})(\tfrac{1}{2}p+q) \quad (9)$$

For the $^2\Sigma^+$ state the Hamiltonian used to derive the energy levels is given by:

$$H = B'(N^2) - D'(N^2)^2 + \gamma' N.S \quad (10)$$

This Hamiltonian more easily yields explicit energy level expressions for a $^2\Sigma^+$ state [1], these are:

$$F_1(N) = BN(N+1) - DN^2(N+1)^2 + \tfrac{1}{2}\gamma N \quad (11)$$

$$F_2(N) = BN(N+1) - DN^2(N+1)^2 - \tfrac{1}{2}\gamma (N+1) \quad (12)$$

The labels, F_1 and F_2 are given such that levels with $J = N + \tfrac{1}{2}$ are called F_1, and those with $J = N - \tfrac{1}{2}$ are called F_2.

Under the electric dipole assumption, rotational selection rules for the transition $^2\Sigma^+(b) - {}^2\Pi(a)$, (the subscripts a and b refer to the Hunds case describing the state) for free molecules with unlike nuclei are [7]:

$$\Delta J = 0, \pm 1$$

$$+ \longleftrightarrow - \,, \quad - \longleftrightarrow +$$

APPENDIX I (Cont/d.)

By applying the selection rules to the energy level structure in both the states various rotational branches are predicted. This information is summarised in Figure AI.i. Labelling of branches is performed in accordance with a Hunds case(a) basis [7]. Briefly, the branch is labelled according to ΔJ. However, a preceding superscript represents ΔN, while subscript indices label the F_1 or F_2 spin rotation and spin-orbit components in the Σ and Π states respectively. If the indices are the same then only one is used, the first index conventionally referring to the excited state.

The relative intensities of each branch are described by line strength formulae. The line strength S(J':J") of a single photon transition between an upper state with total angular momentum J' and a lower state with J" is given by:

$$S(J':J") = \sum_{M'M"} |< J'M'|\mu|J"M" >|^2 \qquad (13)$$

Where the summation is over all magnetic sublevel of both J levels. The line strength factor therefore represents the evaluation of the magnitude of the matrix elements of the electric dipole operator between the wavefunctions $\Psi_{J'M'}$ and $\Psi_{J"M"}$. For a $^2\Sigma - {}^2\Pi$ transition these have been explicitly presented in terms of J and the ratio A/B by Earls [8].

ii) $^2\Delta - {}^2\Pi$ single photon transition (SiCl)

The procedure outlined above could be applied to the $^2\Delta - {}^2\Pi$ transition. Such an approach would yield the energy level diagram presented in Figure AI.ii. Line strength factors for this transition

FIGURE AI.i: Energy level diagram for $^2\Sigma^+(b) - {}^2\Pi(a)$ transition. Branches are labelled according to Hunds case (a) basis. In the Π state each J level is split owing to Λ doubling and the excited state J levels are split due to the spin-rotation interaction. The satallite and main branches occur with approximately the same intensity.

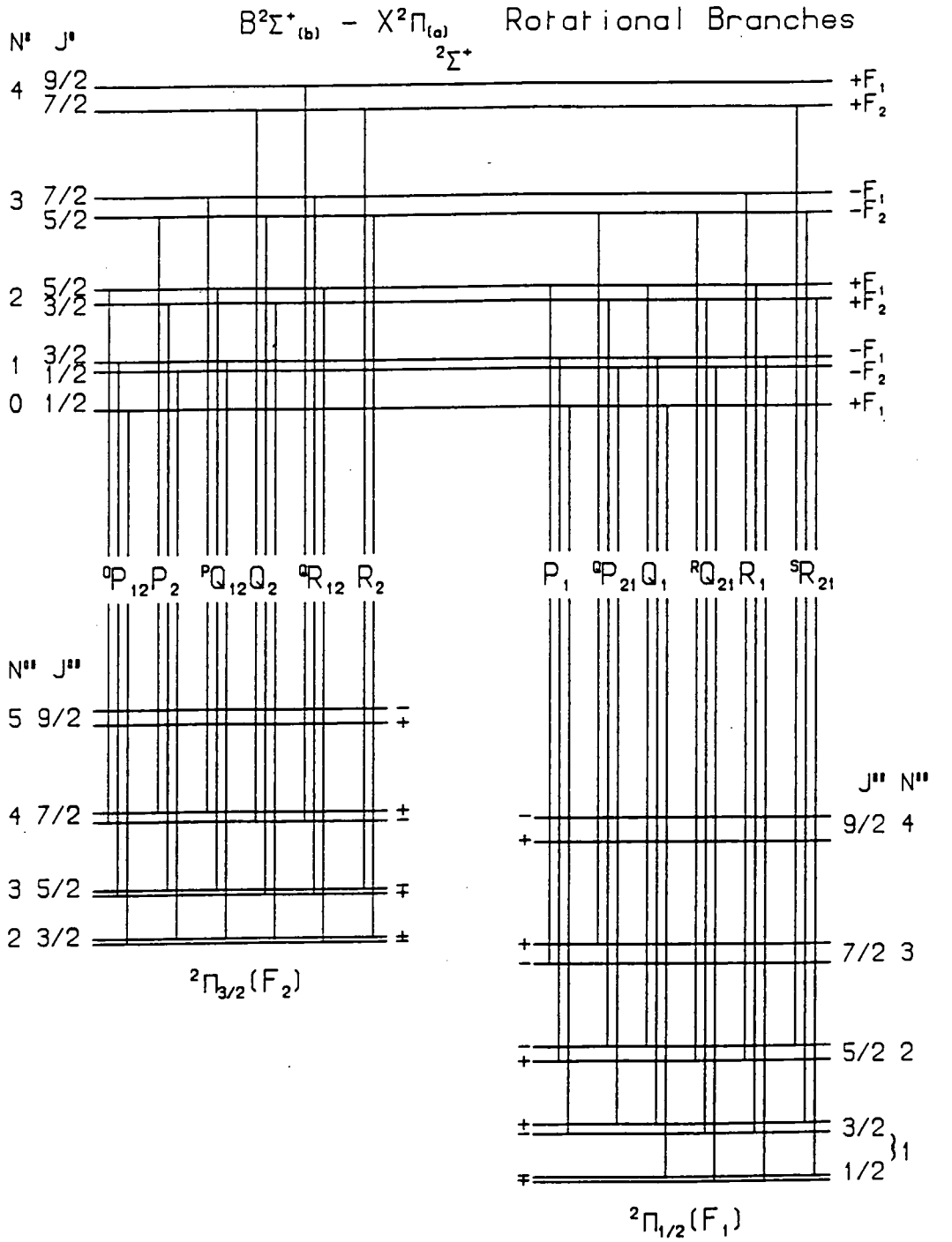

FIGURE AI.ii: Energy level diagram for a $^2\Delta(b) - {}^2\Pi(a)$ transition. Branches are labelled according to a Hunds case (a) basis. In the Π and Δ states each J level is split owing to Λ doubling.

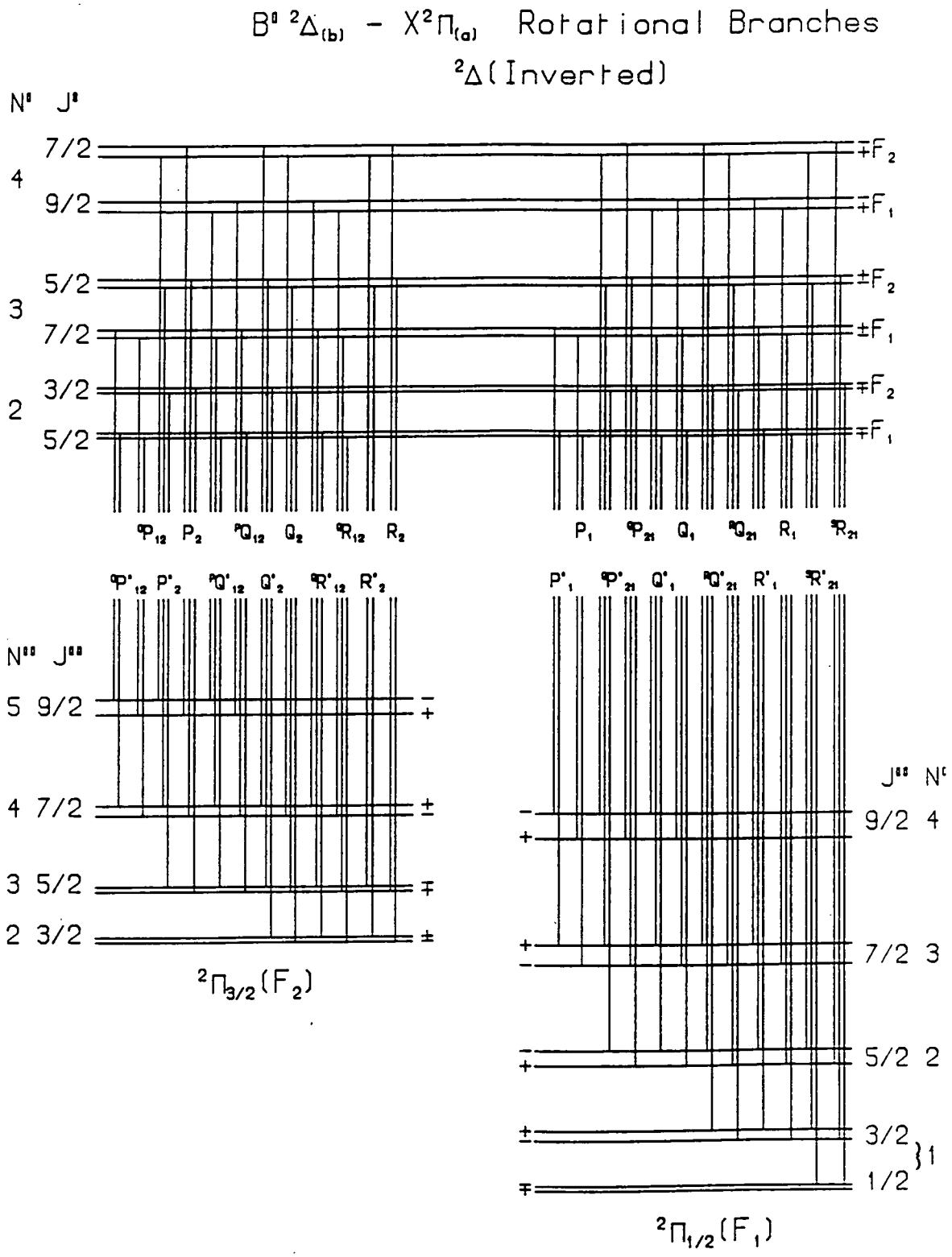

APPENDIX I (Cont/d.)

have been presented by Bennett [9]. However, subsequent to the successful implementation of the $^2\Sigma - {}^2\Pi$ program a general simulation program was acquired from Zare [10]. The program used as input the combining state symmetries, spectroscopic constants and the temperature of the sample. From the symmetry information the program was able to construct a matrix whose eigenvalues yielded the allowed transitions between the states. The line strength factors for the transition was obtained by modifying the generalised Honl-London factors for a symmetric top molecule [4].

The output of the program contained individual line intensities, suitably modified by Boltzmann factors, which reflected the rotational temperature of the sample. The individual lines were infinitely sharp on the transition energy. Hence, the output from the program had to be read into another program where convolution for experimental resolution would occur, (see below).

APPENDIX I (Cont/d)

iii) $^1\Sigma^+(0^+) - {}^1\Sigma^+(0^+)$ two-photon transition (HI)

Generally it may be regarded that Hunds case(c) (and hence $\Omega\omega$ coupling) is like case(a) but with very large multiplet splitting [1]. Since, s and Σ are no longer good quantum numbers the structure of a band with given Ω' and Ω'' is then of exactly the same type as that of the well-known singlet bands. This generalisation is relied upon extensively in this and the next section.

For a $^1\Sigma^+(0^+)$ state the Hamiltonium used to derive the energy levels was given by:

$$H = B(R^2) - D(R^2)^2 \qquad (14)$$

Which yields the well-known expression for the rotational energy levels:

$$E(J) = BJ(J+1) - DJ^2\ (J+1)^2 \qquad (15)$$

In $^1\Sigma$ states L=S=0 and hence J=N=R, then either J,N or R may be used interchangably in equation (15). Similarly for $^1\Sigma$ states the distinction between Hunds coupling cases (a) and (b) is lost.

The rotational selection rules for a $^1\Sigma^+(0^+) - {}^1\Sigma^+(0^+)$ two-photon transition (with unlike nuclei) are [11]:

$$\Delta J = 0, \pm 2$$

$$+ \longleftrightarrow +, \quad - \longleftrightarrow -$$

Application of the selection rules to the energy levels for two $^1\Sigma^+(0^+)$ states leads to three rotational branches. This information is summarised in Figure AI.iii.

FIGURE AI.iii: Energy level diagram for a $^1\Sigma^+ - {}^1\Sigma^+$ two photon transition. Branches and states are labelled according to a Hunds case (a) basis. The alternative labelling of the states (0^+) is for a Hunds case (c) basis, this does not affect the energy level or rotational branch structure.

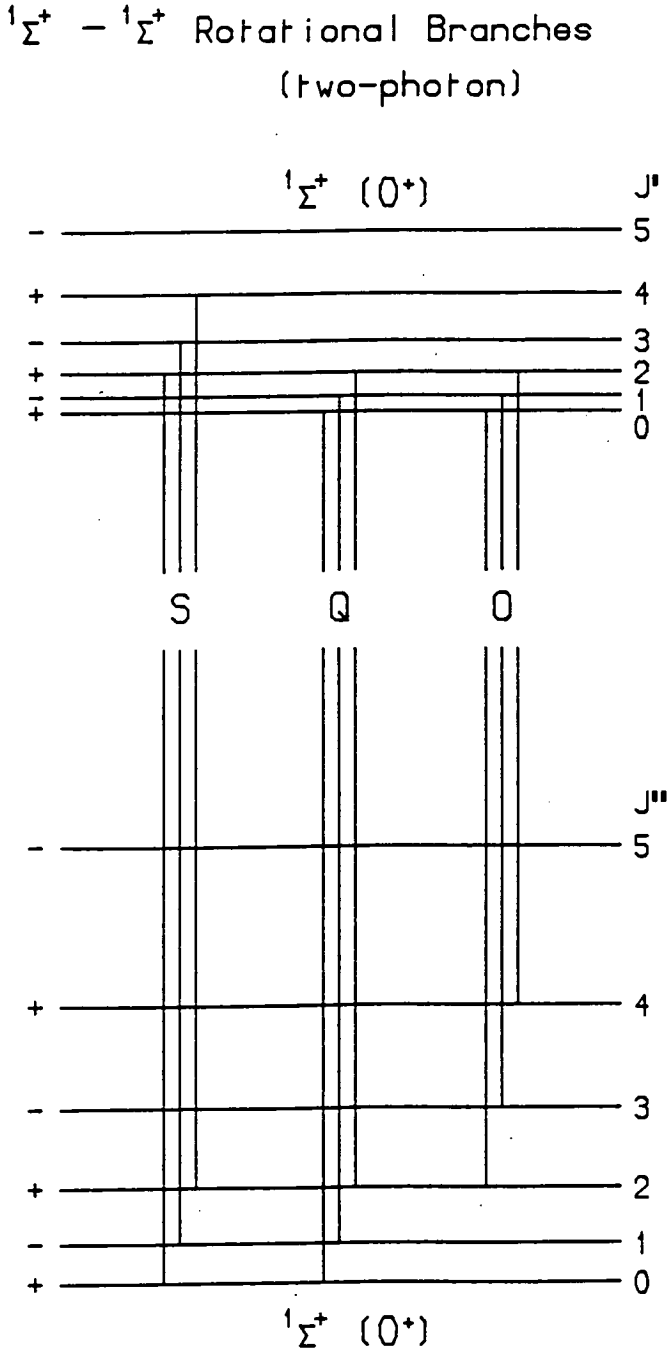

APPENDIX I (Cont/d)

Two-photon linestrength formula have been derived in several places in the literature [11][12][13]. The derivation of these formula is analogous to, but more complex than, that of the single photon case.

In terms of this work, the electronic behaviour of the ground state of HI appears to be well described with Ω being a good quantum number and thus the formulae given by Bray and Hochstrasser [11] were used. For molecules described by case (b) behaviour the treatment of Mainos and Le Duff [12] or of Halpern et.al. [14] may be more appropriate.

iv) $^1\Delta$ (2) - $^1\Sigma^+$(0+) two-photon transition (HI)

Consideration of a $^1\Delta$ (2) electronic states again leads to the familiar term value expression:

$$E(J) = BJ(J+1) - DJ^2(J+1)^2 \qquad (15)$$

However, in this case there are various non-zero non-J dependent terms: arising from the electronic orbital angular momentum, which produce additional contributions to the band origin.

Similarly, it has been shown that, in general, if the interaction of rotation and electronic motion is taken into account in the wavefunction of a molecule, a general formula for the rotational levels of a singlet state with non-zero orbital angular momentum results as [1]:

$$F_i(J) = BJ(J+1) - DJ^2(J+1)^2 + ... + \Phi_i(J) \qquad (16)$$

Where the subscript i stands for c or d (c and d are symmetry labels of differing parity states of a rotational level and are defined in reference [1]) where Φ_i (J) may be represented:

APPENDIX I (Cont/d)

$$\Phi_i (J) = k_i + \delta_i J(J+1) + \mu_i J^2(J+1)^2 + \ldots \quad (17)$$

k_i is a constant, hence it is possible to rewrite equation (16) as [1]:

$$F_i (J) = B_i J(J+1) - D_i J^2(J+1)^2 \quad (18)$$

Where, $B_i = B + \delta_i$ (19)

$$D_i = D + \mu_i \quad (20)$$

and are therefore effective molecular constants.

Hence the lambda (omega) doubling constant q will be given by:

$$q = B^c - B^d = \delta_c - \delta_d \quad (21)$$

Equation (18) indicates that the analysis of a spectrum composed of several rotational branches, may occur as for $^1\Sigma$ states but that only branches connecting the levels of the same symmetry may be analysed together. Also, the constants derived from equation (18) no longer have their true physical meaning.

Additionally, the treatment of Van Vleck [15], showed that for a $^1\Delta$ state the terms δ_i tend to cancel and that the splitting is therefore proportional to $J^2(J+1)^2$.

It appears therefore that $\Lambda(\Omega)$ doubling in $\Delta(2)$ states will be relatively small and hence that the term value expression given in equation (18) will reproduce to a high degree the energy level structure of the 'real' term equation.

APPENDIX I (Cont/d)

The rotational selection rules for a $^1\Delta(2) - {}^1\Sigma^+(0^+)$ two-photon transition (with unlike nuclei) are [11]:

$$\Delta J = 0, \pm 1, \pm 2$$

$$+ \longleftrightarrow +, \quad - \longleftrightarrow -$$

Application of the selection rules to the energy level structures of the $^1\Delta(2)$ and $^1\Sigma^+(0^+)$ states leads to five rotational branches. This information is summarised in Figure AI.iv.

The two-photon linestrength formulae of Bray et.al. [11] were used.

FIGURE AI.iv: Energy level diagram for a $^1\Delta_2$ - $^1\Sigma^+$ two photon transition. Branches and states are labelled according to a Hunds case (a) basis. The states are also labelled according to the alternative Hunds case (c) basis. In the Δ state rotational levels are split due to Λ (Ω) doubling.

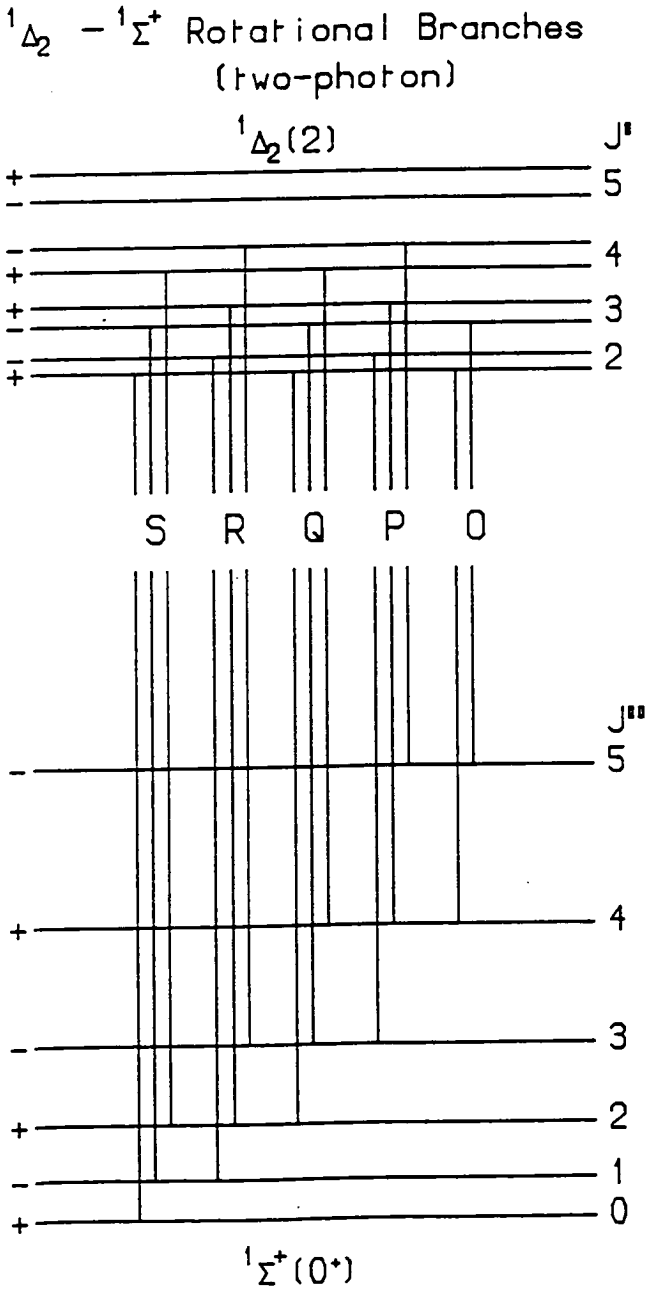

APPENDIX I (Cont/d)

v) Simulation Procedure

It was assumed that, for the simulation procedures I-IV, that the total energy of a molecule undergoing the transition could be written as the sum of the three component parts, that is: electronic, vibrational and rotational contributions. The total expressed as term values, for each electronic state is T, i.e.

$$T = T_e + G + F \tag{22}$$

T_e is the electronic excitation energy

$$G = \omega_e(v + \tfrac{1}{2}) - \omega_e X_e (v + \tfrac{1}{2})^2 + \ldots \tag{23}$$

and is the vibrational term. The constants ω_e and $\omega_e X_e$ are the vibrational and anharmonicity constants. Terms higher than $\omega_e X_e$ were seldom used. The rotational term has been fully discussed for cases I-IV.

Thus the frequency ν (cm^{-1}) of an absorption line is given by:

$$\nu = T' - T'' = (T_e' - T_e'') + (G' - G'') + (F' - F'') \tag{24}$$

A slight simplification is made since T_e'' was normally zero i.e. excitation occurred from the ground electronic state.

The relative line intensities of individual ro-vibronic lines were obtained from:

$$I = CS(J':J'') \exp(-E_{rot}/kT) \tag{25}$$

APPENDIX I (Cont/d)

C represents an arbitrary scaling constant independent of J. S(J':J") is the one or two-photon absorption linestrength. All gaseous samples probed were assumed to exhibit Boltzmann statistics. Hence, the rotational intensities could therefore be weighted by a Boltzmann factor exp $(-E_{rot}/kT)$ where E_{rot} is the rotational energy associated with any rotational level, k is the Boltzmann constant (JK^{-1}) and T is the sample temperature (K).

The line intensities which had been assumed to be infinitely sharp were then convoluted with a laser (experimental) linewidth function which was assumed to be Gaussian in form. The linewidth function was assumed to have a FWHM normally of approximately 0.5 cm^{-1}.

APPENDIX I (Cont/d)

REFERENCES

1. G. Herzberg in 'Molecular Spectra and Molecular Structure I. Spectra of Diatomic Molecules'. (Van Nostrand, New York 1950).
2. R.N. Zare in 'Angular Momentum. Understanding Spatial Aspects in Chemistry and Physics'. (John Wiley and Sons, New York 1988).
3. G. Meijer, B. Jansen, J.J. Ter. Mullen and A. Dynamus, Chem. Phys. Lett., 136 519 (1987).
4. R.N. Zare, A.L. Schmeltekopf, W.J. Harrop and D.L. Albritton, J. Mol. Spec., 46 37 (1973).
5. R.S. Mulliken and A. Christy, Phys. Rev., 38 87 (1931).
6. J.M. Brown and J.K.G. Watson, J. Mol. Spec., 65 65 (1977).
7. G.H. Dieke and H.M. Crosswhite, J. Quant. Spect. Rad. Trans., 2 97 (1961).
8. L.T. Earls, Phys. Rev., 48 423 (1935).
9. R.J.M. Bennett, Mon. Not. R. Astr. Soc., 147 35 (1970).
10. We gratefully acknowledge Prof. R.N. Zare, Dept. of Chemistry, Stanford University, CA 94305, USA. (for the supply of his rotational simulation program).
11. R.G. Bray and R.M. Hochstraser, Mol. Phys., 31 1199 (1976).
12. C. Mainos and Y. Le Duff, Mol. Phys., 60 383 (1987).
13. A.C. Kummel, G.O. Sitz and R.N. Zare, J. Chem. Phys., 85 6874 (1986).
14. J.B. Halpern, H. Zacharias and R. Wallenstein, J. Mol. Spec., 79 1 (1980).
15. J.H. Van Vleck, Phys. Rev., 33 467 (1929).

APPENDIX II

Calculation of Collision Frequencies

Throughout this thesis estimation of the rate of gas phase collisional encounters was made by assuming the hard sphere collision rate. Invariably the studies of interest involved mixtures of at least two gases, one in very great excess over the other. Hence for two gases, A and B the gas kinetic collision rate, or the number of collisions per second made by one molecule of species A with molecules of species B, Z_{AB} is [1]:

$$Z_{AB} = 2\sqrt{2}\, n_B \sigma_{AB}^{\,2} \,(\pi kT/\mu_{AB})^{\frac{1}{2}} \qquad (1)$$

n_B is the number of molecules of species B per unit volume.

$\sigma_{AB}^{\,2} = \left\{ \frac{\sigma_A + \sigma_B}{2} \right\}^2$ and is the mean of the individual collision diameters

$\mu_{AB} = \left(\frac{M_A M_B}{M_A + M_B} \right)$ where M_A and M_B are the respective masses of the colliding molecules. μ_{AB} is therefore the collision reduced mass.

APPENDIX II (Cont/d.)

Values for σ were obtained from references [2][3] and are listed in Table aII.1 below.

TABLE AII.I: Collision diameters for the gaseous species used in this thesis

Gas	σ/Å
He	2.58
Ar	3.47
H_2	2.93
N_2	3.74
CO_2	3.94
CH_4	3.79
CF_4	4.49
HI	4.63
I_2	4.08

REFERENCES

1. J.D. Lambert in 'Vibrational and Rotational Relaxation in Gases', (Clarendon Press, Oxford 1977).
2. J.O. Hirschfelder, C.F. Curtiss and R.B. Bird in "Molecular Theory of Gases and Liquids", (John Wiley and Sons, New York 1954).
3. F.M. Mourits and F.H.A. Rummens, Can. J. Chem., 55 3007 (1977).

APPENDIX III

Kinetic Analysis

Measurement of the rate constants for quenching of the B′ state was achieved with the model explained below.

Implicit in the model are two assumptions:

1) Instantaneous B′ state population, which is reasonable since the laser pulsewidth (~ 10ns) is approximately one hundredth the radiative lifetime of the B′ state (1.0μs for v′ = 0 and 0.8μs for v′ = 1).

2) No recrossing from the B state back to the B′ state, which is reasonable since the radiative lifetime of the B state (~ 10ns) is short compared to that of B′.

Initial excitation to the B′ state can lead to quenching to the B state, transfer into another unspecified loss channel (i.e. one which maintains mass balance) and fluorescence emission. Diagramatically these three decay routes may be shown as:

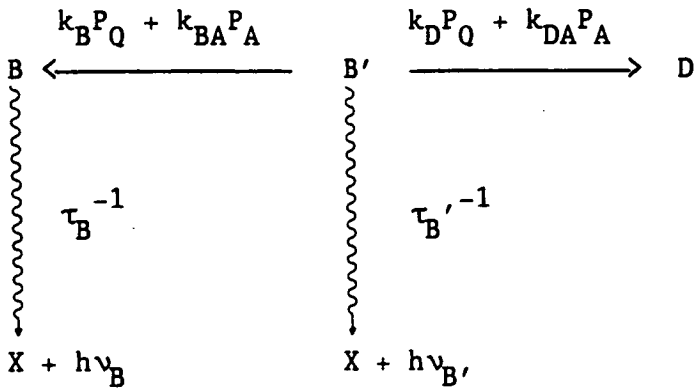

APPENDIX III (Cont/d)

Defining terms:

B'	represents the population of the B′ state (assumed to be instantaneously produced).
B	represents the B state population (in all vibrational levels).
D	represents the additional loss channel which maintains total mass balance.
X	represents the ground state.
τ_B^{-1} $\tau_{B'}^{-1}$	represent the rates of radiative emission for the B and B′ states, respectively, and are the inverse of the natural lifetimes of the states.
$h\nu_B, h\nu_{B'}$	represent the energies of the fluorescence photons emitted by the excited B and B′ states, respectively.
P_A	is the number density of argon (see note 1).
P_Q	is the number density of quenching gas.
k_{DA}	is the rate constant for removal by argon from the B′ state to the D 'state'.
k_{BA}	is the rate constant for quenching by argon from the B′ state to the B state.
k_D	is the rate constant for removal by the quencher from the B′ state to the D 'state'.
k_B	is the rate constant for quenching by the quencher from the B′ state to the B state.

APPENDIX III (Cont/d)

The rate equations are:

$$\frac{dB'}{dt} = -k_B P_Q B' - k_{BA} P_A B' - k_D P_Q B' - k_{DA} P_A B' - \tau_{B'}^{-1} B' \quad (1)$$

$$\frac{dB}{dt} = k_B P_Q B' + k_{BA} P_A B' - \tau_B^{-1} B \quad (2)$$

$$\frac{dD}{dt} = k_D P_Q B' + k_{DA} P_A B' \quad (3)$$

Because of assumption (2), terms in B′ arise only from equation (1)

i) **Time profile of the B′ state population**

$$\frac{dB'}{dt} = B' \left\{ - [k_B + k_D] P_Q - [k_{BA} + k_{DA}] PA - \tau_{B'}^{-1} \right\} \quad (4)$$

which on rearranging may be integrated directly

$$\int_o^t \frac{dB'}{B'} = \int_o^t \left\{ - [k_B + k_D] P_Q - [k_{BA} + k_{DA}] PA - \tau_{B'}^{-1} \right\} dt \quad (5)$$

and hence,

$$B'(t) = B_o' \exp \left[\left\{ - [k_B + k_D] P_Q - [k_{BA} + k_{DA}] P_A - \tau_{B'}^{-1} \right\} t \right] \quad (6)$$

ii) **Time profile of the B state population**

On rearranging eqn (2)

$$\frac{dB}{dt} + \tau_B^{-1} B = B' [k_B P_Q + k_{BA} P_A] \quad (2a)$$

To integrate equation (2a), use an integrating factor:

$$e^{\int \tau_B^{-1} dt} = e^{\tau_B^{-1} t} \quad (7)$$

APPENDIX III (Cont/d)

Hence,

$$\frac{d}{dt}\left(Be^{\tau_B^{-1}t}\right) = e^{\tau_B^{-1}t} \cdot B'\,[k_B P_Q + k_{BA} P_A] \qquad (8)$$

Then by using equation (6) for the temporal profile of the B′ state population, the integral is:

$$\int_{t=o,B=0}^{t=t,B=B(t)} d\left(Be^{\tau_B^{-1}t}\right) = B_o'\,(k_B P_Q + k_{BA} P_A) \cdot$$

$$\int_{t=o}^{t=t} \exp\left[\left\{\tau_B^{-1} - [k_B + k_D]P_Q - [k_{BA} - k_{DA}]P_A - \tau_{B'}^{-1}\right\} t\right] dt \qquad (9)$$

whence,

$$B(t) = \frac{B_o'(k_B P_Q + k_{BA} P_A)}{(\tau_B^{-1} - [k_B + k_D]P_Q - [k_{BA} + k_{DA}]P_A - \tau_{B'}^{-1})} \cdot$$

$$\left[\exp\left[\left\{-[k_B + k_D]P_Q - [k_{BA} + k_{DA}]P_Q - \tau_{B'}^{-1}\right\} t\right] - \exp\left(-\tau_B^{-1} t\right)\right] \qquad (10)$$

iii) The rates of emission

For the B′ state:

$$\frac{d(h\nu_{B'})}{dt} = \tau_{B'}^{-1} B' \qquad (11)$$

$$= B_o' \tau_{B'}^{-1} \exp\left[\left\{-[k_B + k_D] P_Q - [k_{BA} + k_{DA}]P_A - \tau_{B'}^{-1}\right\} t\right] \qquad (12)$$

and for the B state:

$$\frac{d(h\nu_B)}{dt} = \tau_B^{-1} B \qquad (13)$$

APPENDIX III (Cont/d)

$$= \frac{B_o' \, \tau_B^{-1} \, (k_B P_Q + k_{BA} P_A)}{(\tau_B^{-1} - [k_B + k_D]P_Q - [k_{BA} + k_{DA}]P_A - \tau_{B'}^{-1})} \cdot$$

(14)

$$\left[\exp \left[\left\{ - [k_B + k_D]P_Q - [k_{BA} + k_{DA}]P_Q - \tau_{B'}^{-1} \right\} t \right] - \exp (- \tau_B^{-1} t) \right]$$

equation (14) can be simplified if the reasonable assumption that τ_B^{-1} is very much greater than the other rates is made. Then,

$$\frac{d(h\nu_B)}{dt} = B_o' \, (k_B P_Q + k_{BA} P_A) . \exp \left[\left\{ - [k_B + k_D]P_Q - [k_{BA} + k_{DA}]P_A - \tau_{B'}^{-1} \right\} t \right]$$

(15)

equation (15) implies that the B state emission follows the B′ state and that emission from the B state is essentially instantaneous.

However, experimentally the total integrated emission was measured (as a function of quenching pressure P_Q).

iv) Integrated emission intensities

For the B′state

$$\int_{t=o}^{t=\infty} \frac{d(h\nu_{B'})}{dt} \, dt = B_o' \, \tau_{B'}^{-1} \int_o^{\infty} \exp \left[\left\{ - [k_B + k_D]P_Q - [k_{BA} + k_{DA}]P_A - \tau_{B'}^{-1} \right\} t \right] dt$$

(16)

Defining $\int_{t=o}^{t=\infty} \frac{d(h\nu_{B'})}{dt} \, dt = I \, (B')$, then:

APPENDIX III Cont/d

$$I(B') = \frac{B'_o \tau_{B'}^{-1}}{\left\{ [k_B+k_D]P_Q + [k_{BA}+ k_{DA}]P_A + \tau_{B'}^{-1} \right\}} \tag{17}$$

Inverting equation (17) yields

$$\frac{1}{I(B')} = \frac{[k_B + k_D]\ P_Q}{B'_o\ \tau_{B'}^{-1}} + \frac{[k_{BA} + k_{DA}]\ P_A}{B'_o\ \tau_{B'}^{-1}} + \frac{1}{B'_o} \tag{18}$$

Hence, a plot of $\frac{1}{I(B')}$ against P_Q yields a straight line of slope

$$\frac{k_B + k_D}{B'_o\ \tau_{B'}^{-1}}$$ and an intercept of $$\frac{[k_{BA} + k_{DA}]\ P_A}{B'_o\ \tau_{B'}^{-1}} + \frac{1}{B'_o}$$

For the B state:

$$\int_{t=o}^{t=\infty} \frac{d(h\nu_B)}{dt}\, dt = \int_{o}^{\infty} B'_o(k_B P_Q + k_{BA} P_A) \cdot \exp\left[\left\{- [k_B+ k_D]P_Q - [k_{BA} + k_{DA}]P_A - \tau_{B'}^{-1} \right\} t \right] dt \tag{19}$$

Defining $\int_{t=o}^{t=\infty} \frac{d(h\nu_B)}{dt}\, dt = I(B)$, then:

$$I(B) = \frac{B'_o\ (k_B P_Q + k_{BA} P_A)}{\left\{[k_B+k_D]P_Q + [k_{BA}+k_{DA}]P_A + \tau_{B'}^{-1}\right\}} \tag{20}$$

To determine the B′ to B partial quenching rate constant, define the ratio:

$$\frac{I(B)}{I(B')} = \frac{B'_o\ (k_B P_Q + k_{BA} P_A) / \left\{[k_B+ k_D]P_Q + [k_{BA}+ k_{DA}]P_A + \tau_{B'}^{-1}\right\}}{B'_o\ \tau_{B'}^{-1} / \left\{[k_B+ k_D]P_Q + [k_{BA}+ k_{DA}]P_A + \tau_{B'}^{-1} \right\}} \tag{21}$$

$$= \frac{k_B P_Q}{\tau_{B'}^{-1}} + \frac{k_{BA} P_A}{\tau_{B'}^{-1}} \tag{22}$$

APPENDIX III (Cont/d)

Hence, a plot $\frac{I(B)}{I(B')}$ against P_Q will yield a straight line with

slope $\frac{k_B}{\tau_{B'}^{-1}}$ and an intercept $\frac{k_{BA}P_A}{\tau_{B'}^{-1}}$

Consideration of the limiting cases shows the expected asymptotic bbehaviour:

1) $P_Q \rightarrow 0 : I(B') \rightarrow \frac{B'_o \tau_{B'}}{[k_{BA} + k_{DA}]P_A + \tau_{B'}^{-1}}$

which if the argon pressure is also negligble is: $I(B') \rightarrow B'_o$

$I(B) \rightarrow 0$ (if the argon contribution is negligible)

2) $P_Q \rightarrow \infty$ $I(B') \rightarrow 0$

$I(B) \rightarrow \frac{B'_o k_B}{k_B + k_D}$

v) **When only argon carrier gas is present**

In this situation the contribution from the constant term P_A vanishes. Hence determination of the quenching rate constant for argon follows from:

For the B′ state:

For the plot of $\frac{1}{I(B')}$ against P_Q the slope remains $\frac{k_B + k_D}{B'_o \tau_{B'}^{-1}}$

but the intercept becomes $\frac{1}{B'_o}$. Hence, the ratio of the slope to the to the intercept removes the unknown term $\frac{1}{B'_o}$ and thus the total B′ state removal rate (k_B+k_D) may be determined.

and for the B state:

The plot of $^{I(B)}/I(B')$ against P_Q reduces to,

$$\frac{I(B)}{I(B')} = \frac{k_B P_Q}{\tau_{B'}^{-1}} \qquad (23)$$

Thus a plot of $^{I(B)}/I(B')$ against P_Q will yield the argon quenching rate constant. It is worthwhile pointing out that since the values of I(B) and I(B') are obtained from the same experiment, systematic errors due to, for example, gas dynamical effects on the absolute signals cancel out.

NOTES

1. When a collider gas is added to a carrier gas (argon in this case) at a significant mixing fraction, the collider partial pressure is not simply the pressure rise but must be calculated from measured flow rates.

APPENDIX IV

Detection of the products and reactants from the reaction $H + X_2 \longrightarrow HX + X$ by Multiphoton Ionisation

In Chapter 4 it was noted that all the reactants and products of the reaction above (for X = I) could be detected by multiphoton ionisation. The rotational structure due to HI was discussed in detail in Chapter 4, together with the observation that I_2 produced an essentially continuum ionisation. The additional atomic and molecular features due to the other species present in the reactor will now be briefly discussed.

i) Atomic Iodine

The three photon ionisation (two to resonance) spectrum of atomic iodine was used to provide the primary wavelength standards for subsequent molecular line measurements in Chapter 4. A complete list of the lines observed in this work is presented in Table AIV.i together with the transition energies obtained from reference [1]. The atomic line positions measured directly from the laser grating were found to differ with those from reference [1] by less than 1.5 cm^{-1} in all cases. Figure AIV.i shows a 'fast acquistion' spectrum for the multiphoton ionisation of atomic iodine. The spectrum was obtained by passing the laser beam through a uv attenuating filter. The atomic iodine was (in this case) produced via the interaction of molecular iodine with the products of a microwave discharge of argon containing a small amount of oxygen (~ 1%), such that no features attributable to HI were observed.

It was possible to estimate the absolute sensitivity of the apparatus to the detection of iodine atoms by two complementary methods, which related the molecular flow of iodine to the observed intensity of the atomic transition.

APPENDIX IV (Cont/d)

TABLE AIV.i: Atomic iodine lines observed in the [2+1] REMPI spectrum of HI. The atomic transition energies were all obtained from reference [1].

Transition	Energy/cm^{-1}
$^2D^o_{5/2} \leftarrow {}^2P^o_{1/2}$	67588.22
$^4P^o_{3/2} \leftarrow {}^2P^o_{1/2}$	68018.26
$2^o_{3/2} \leftarrow {}^2P^o_{1/2}$	70989.60
$^2P^o_{1/2} \leftarrow {}^2P^o_{1/2}$	71176.89
$^2D^o_{5/2} \leftarrow {}^2P^o_{1/2}$	71251.71
$^2P^o_{1/2} \leftarrow {}^2P^o_{3/2}$	71501.52
$^2S^o_{1/2} \leftarrow {}^2P^o_{3/2}$	71813.97
$^4D^o_{3/2} \leftarrow {}^2P^o_{3/2}$	71976.74
$^2P^o_{1/2} \leftarrow {}^2P^o_{1/2}$	72098.58
np $3^o_{3/2} \leftarrow {}^2P^o_{1/2}$	72436.79
np $4^o_{5/2} \leftarrow {}^2P^o_{1/2}$	72522.42
$^4D^o_{5/2} \leftarrow {}^2P^o_{3/2}$	72529.17
$^2D^o_{3/2} \leftarrow {}^2P^o_{3/2}$	72807.21
$^2P^o_{3/2} \leftarrow {}^2P^o_{3/2}$	73054.56
$^4S^o_{3/2} \leftarrow {}^2P^o_{1/2}$	73117.70
$^4D^o_{1/2} \leftarrow {}^2P^o_{3/2}$	73387.18

APPENDIX IV (Cont/d)

FIGURE AIV.i: Three photon ionisation (two to resonance) of iodine atoms generated via the interaction of molecular iodine with the microwave discharge products of argon and oxygen (present at ~ 1% level).

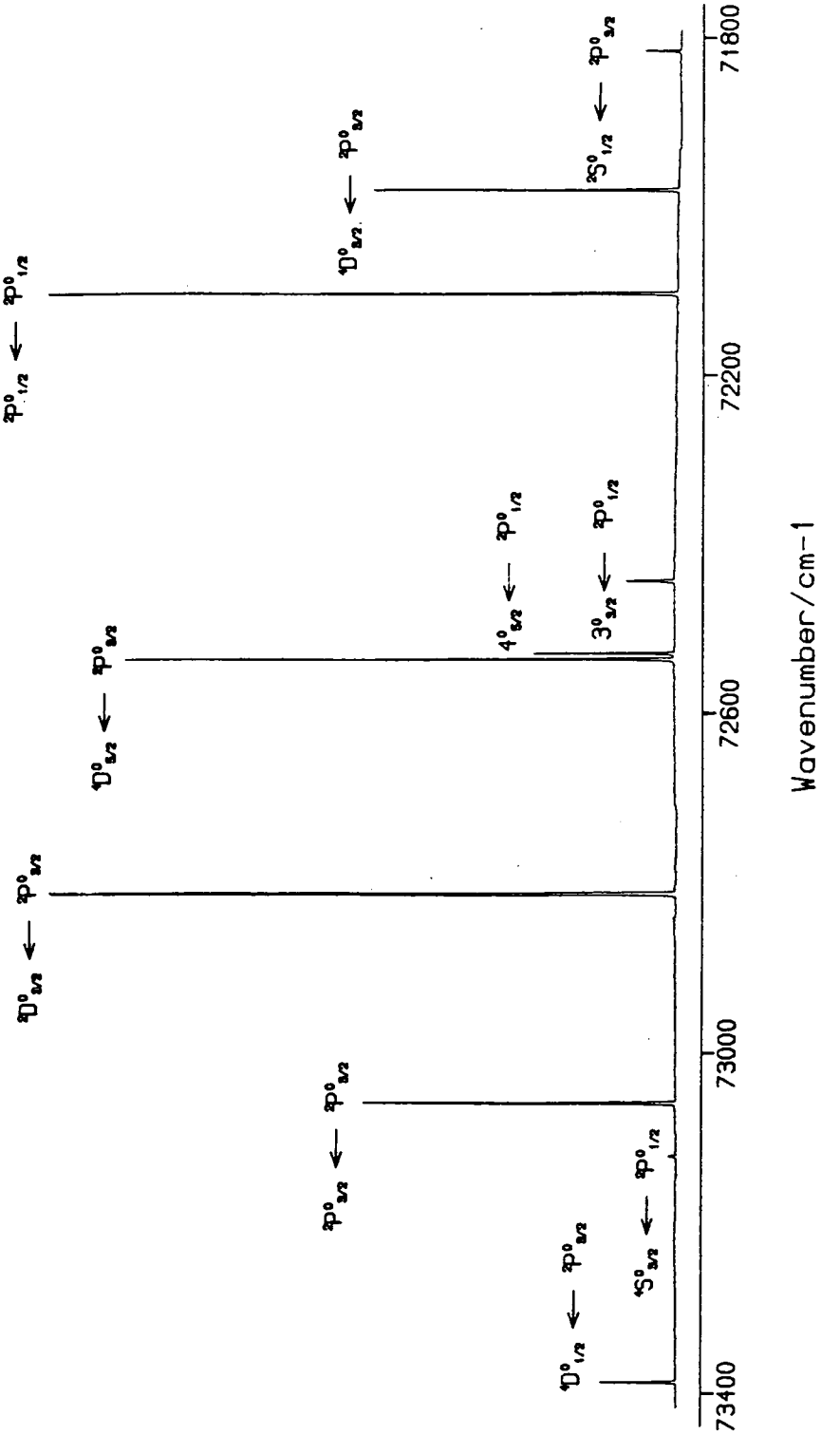

APPENDIX IV (Cont/d)

1) Measurement of the weight loss of I_2 from a known sample weight.
2) Capture of the molecular iodine flow in a liquid nitrogen cold trap, followed by dissolving the captured I_2 in an aqueous KI solution and titrating against $Na_2S_2O_3$, using as an indicator a freshly made starch solution [2].

In both cases the estimated sensitivity to detection of iodine atoms, for a signal to noise ratio of two, was ~ $(8 \pm 5) \times 10^7$ molecules cm^{-3}.

Additionally, brief investigations of the reactions H + Cl_2 and H + Br_2 were made. For the reaction involving molecular chlorine a four photon ionisation (3 to resonance) spectrum was obtained for chlorine atoms. In this case the strongly focussing 6 cm lens was required and hence the spectrum also contained features attributable to molecular hydrogen. The spectrum spanned the wavelength range 300-308.5 nm and did not show any features obviously attributable to HCl. Table AIV.ii presents the observed transitions attributed to atomic chlorine in this wavelength region, together with appropriate comparisons to reference [1].

TABLE AIV.ii: Atomic chlorine transitions observed via [3+1] multiphoton ionisation in the wavelength range 300-308.5 nm.

Assignment	Observed transition energy/cm^{-1}	Transition energy from ref [1]/cm^{-1}	Residual (obs-ref)/cm^{-1}
$^4P_{5/2} \leftarrow {}^2P^o_{3/2}$	97331.9	97334.60	-2.70
$^4P_{3/2} \leftarrow {}^2P^o_{3/2}$	97473.9	97476.20	-2.30
$^4D_{5/2} \leftarrow {}^2P^o_{1/2}$	98466.8	98469.22	-2.42
Unassigned	98510.9	-	-
$^4F_{7/2} \leftarrow {}^2P^o_{1/2}$	98782.0	98783.15	-1.15

APPENDIX IV (Cont/d)

The products of the reaction between a hydrogen atom and a bromine molecule were investigated in the wavelength region bounded by 271.5-280.5 nm. In this case transitions from only the spin-orbit excited state of the ground state term were observed. The observed transitions, together with the appropriate comparisons from reference [3] may be found in Table AIV.iii.

TABLE AIV.iii: Atomic bromine transitions observed via [2+1] multiphoton ionisation in the wavelength region 271.5-280.5 nm.

Assignment	Observed transition Energy/cm^{-1}	Transition energy from ref [3]/cm^{-1}	Residual (obs-ref)/cm^{-1}
$^4D^o_{5/2} \leftarrow\!\!- \ ^2P^o_{1/2}$	72013.4	72011.85	1.55
$^4P^o_{1/2} \leftarrow\!\!- \ ^2P^o_{1/2}$	72129.9	72128.80	1.10
$^4D^o_{3/2} \leftarrow\!\!- \ ^2P^o_{1/2}$	73059.9	73057.88	2.02

ii) Atomic and Molecular Hydrogen

By using the strongly focussing 6 cm lens ionisation signals attributable to atomic and diatomic hydrogen were readily observed between ~ 270-300 nm. A typical survey spectrum of these ionisation features is shown in Figure AIV.ii for the wavelength region 271.5-281.5 nm. The spectrum was obtained by discharging a mixture of H_2 (150 SCCM) and Ar (350 SCCM) in the microwave cavity operating at 35 W.

It was noted that even by stepping the dye laser grating very slowly that assymetric line shapes were observed for all the spectral features throughout the wavelength range investigated. However, the assymetric line shapes were especially obvious for the atomic transitions. The observed atomic linewidths were noted to vary considerably, but often exceeded 10 cm^{-1} (FWHM), and hence were considerably greater than the ~ 0.5 cm^{-1} linewidth of the laser beam.

APPENDIX IV (Cont/d)

FIGURE AIV.ii: Four photon ionisation (three to resonance) of atomic and molecular hydrogen between 271.5-281.5 nm. Transitions to differing principal quantum number, n in atomic hydrogen marked on the spectrum together with transitions attributable to diatomic hydrogen.

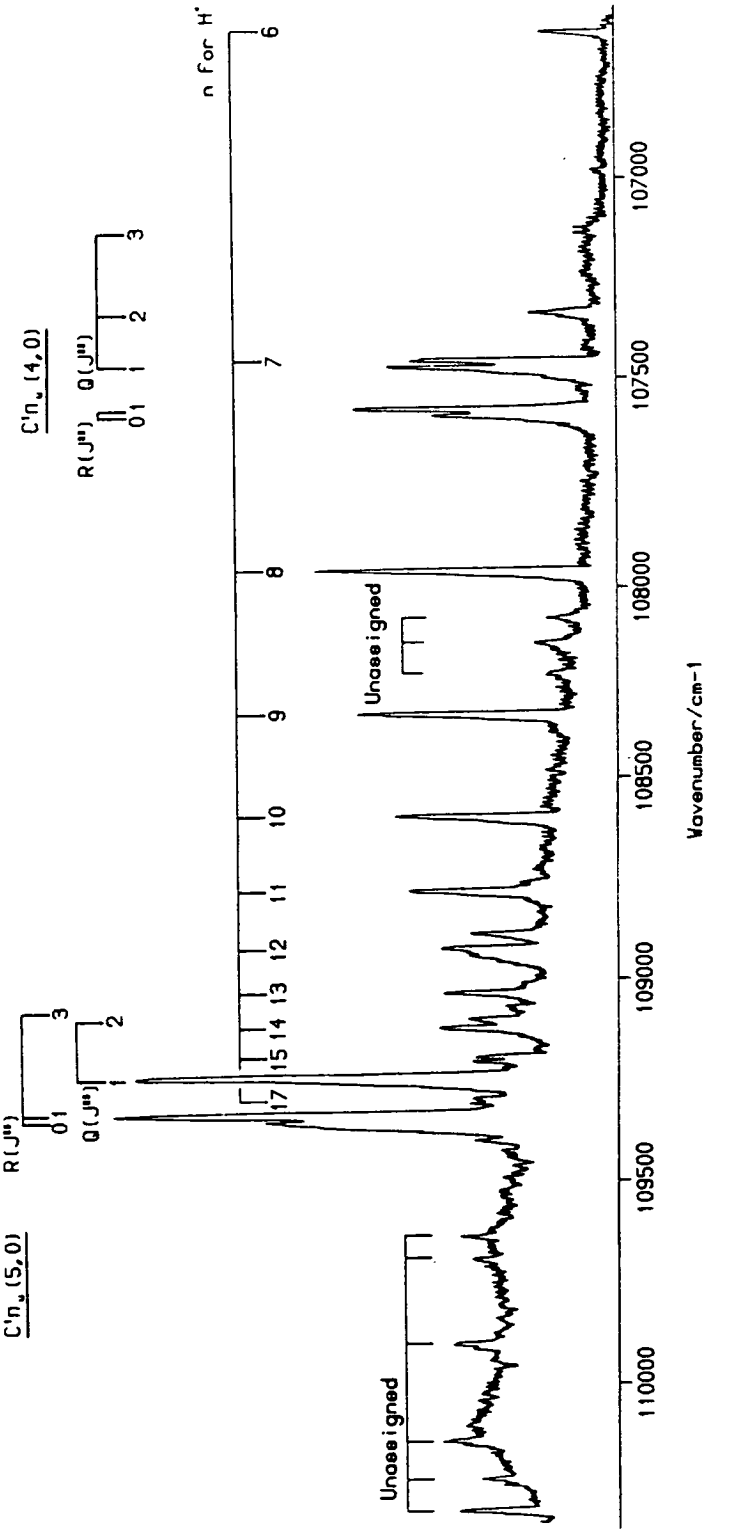

APPENDIX IV (Cont/d)

For the atomic transitions, the asymmetric broadening was noted always to occur to the blue. Additionally it was found that the observed spectral peaks (attributed to atomic hydrogen) matched very poorly those predicted in reference [1]. In fact the difference in the observed and expected positions was noted to vary from < 3 cm^{-1} for n = 6 to > 10 cm^{-1} for n = 10 (near the dye gain maximum), see Figure AIV.ii. These observations were explained in terms of the a.c Stark effect, with the assymetric line shifting to the blue being readily explained in terms of the upper state being more polarisable than the ground state [4]. An approximate method for calculating the energy level shift 'susceptability' for low ($n < 10$) principal quantum number has been presented by Dubreuil and Chapelle [5]. Hence, assuming that the 6 cm lens produces a beam waist, at focus, of $\sim$ 20 μm. Then for a 0.5 mJ pulse delivered in 10 ns an energy level shift for n = 10 is predicted to be $\sim$ 12 cm^{-1}.

The intensities of the transitions associated with the principal quantum number were observed to decrease with increasing n, this was attributed to the decreasing orbital overlap between the ground and excited states as n increases.

Assignment to features due to ionisation of diatomic hydrogen was also made, in this case the observed line positions are presented in Table AIV.ii together with appropriate comparisons from references [6][7].

APPENDIX IV (Cont/d)

TABLE AIV.ii: Observed transitions in the [3+1] REMPI spectrum of H_2 in the wavelength region bounded by 271.5-281.5 nm.

State	Assignment	Observed position/cm^{-1}	Position measured by refs [6,7]/cm^{-1}
$c^1\Pi_u(4,0)$	Q(1)	107463.6	107460.56
	Q(2)	107325.7	107321.54
	Q(3)	107115.2	107114.39
	R(0)	107583.6	107580.83
	R(1)	107567.4	107563.09
$c^1\Pi_u(5,0)$	Q(1)	109252.4	109241.27
	Q(2)	109108.0	109096.82
	R(0)	109368.9	109361.57
	R(1)	109344.2	109336.58
	R(3)	109072.4	109065.88

REFERENCES

1. C.E. Moore 'Atomic Energy Levels' Vol I-III National Bureau of Standards U.S.A. (1971).
2. K. Lorenz, H. Gg. Wagner and R. Zellner, Ber. Buns. Phys. Chem., 83 556 (1979).
3. J.L. Tech, Journal of Research of the National Bureau of Standards, Phys. Chem., 67A 505 (1963).
4. L. Li, B. Yang, P.M. Johnson, J. Opt. Soc. Am. B 2 748 (1985).
5. B. Dubreuil and J. Chapelle, Phys. Lett., 46A 451 (1974).
6. T. Namioka, J. Chem. Phys., 40 3154 1964.
7. I. Dabrowski and G. Herzberg, Can. J. Phys., 52 1110 (1974).

APPENDIX V

Additional Results

During the course of this work, additional multiphoton ionisation results not directly related to Chapters 3 and 4 were obtained on several atomic species. In this appendix the more interesting or novel of these results are reported.

It should be noted that there has been a great deal of experimental work on multiphoton based methods for detection of atomic species. Reviews of the scope of these methods may be found in, for example, references [1] and [2] for the fluorescence and ionisation methods respectively. In particular, for the multiphoton ionisation methods, a completely general approach has been proposed by Hurst and co workers, see [3][4][5][6]; where they have proposed that any one of five possible ionisation schemes can be utilised to selectively and sensitively detect all the atoms in the periodic table. Hurst et.al. have also proposed that the terminology Resonance Ionisation Spectroscopy (RIS) be used to describe these multiphoton ionisation processes, in complete analogy with the molecular equivalent REMPI.

Atomic species have been monitored in 'complex gaseous mixtures', by RIS, as for example: products in a photolysis experiment [7][8], or more recently to follow the progress of a reaction [9][10] or in quenching events [11].

All work presented in this appendix was obtained by using a [2+1] RIS process. The selection rules for such a process may be found in several places in the literature, see for example, references [12][13]. For the case of absorption of two identical photons when Russell-Saunders coupling is a good description of the coupling of the angular momenta in the atom, the rules may be summarised as:

$$\Delta J = 0, \pm 1, \pm 2 \text{ with } J = 0 \not\leftrightarrow 1$$
$$\Delta L = 0, \pm 1, \pm 2 \text{ with } \Delta L \not\leftrightarrow L = 1$$

APPENDIX V (Cont/d)

$\Delta S = 0$

even $\longleftrightarrow$ even, odd $\longleftrightarrow$ odd, even $\longleftrightarrow$ odd

Methods of estimating the relative intensities of particular transitions between J' and J" within individual atomic terms has been outlined by Pindzola [14] and subsequently extensively utilised by Brewer et.al. [12][15][16] on studies of S, Si and Te atoms respectively.

Within this appendix all spectra were taken without normalising the observed signal to the variations in laser power, hence no effort was made to interpret the observed intensities theoretically. All studies utilised the flow reactor, whose walls had additionally been coated in halocarbon wax. However, it was found sufficient to operate the microwave discharge with an uncoated discharge side arm. Most experiments were characterised by a reactor pressure near 1 Torr with argon acting as the carrier gas. The atomic line positions were measured relative only to the reasonably accurately calibrated laser grating. An average typical laser power was estimated to be in the 300 - 500 μJ per pulse range.

i) **[2+1] RIS of Phosphorous Atoms**

By passing a low flow (~1 SCCM) of helium over a sample of PBr_3, the nascent PBr_3 vapour could be entrained into a gas flow. This flow was then added to the main argon carrier gas flow before entering the flow reactor via the discharge cavity. The discharge cavity was operated at 50 W. Figure AV.i presents a typical spectrum obtained from such an experimental methodology. Phosphorous atoms were found to appear at the detector plane almost immediately, similarly problems of 'conditioning' the reactor walls were essentially non-existent. No deposits within the discharge side-arm, were noticed to build up over the course of these experiments.

FIGURE AV.i: [2+1] RIS spectrum of phosphorous atoms. The spectrum is not normalised for the variation of laser power with wavelength.

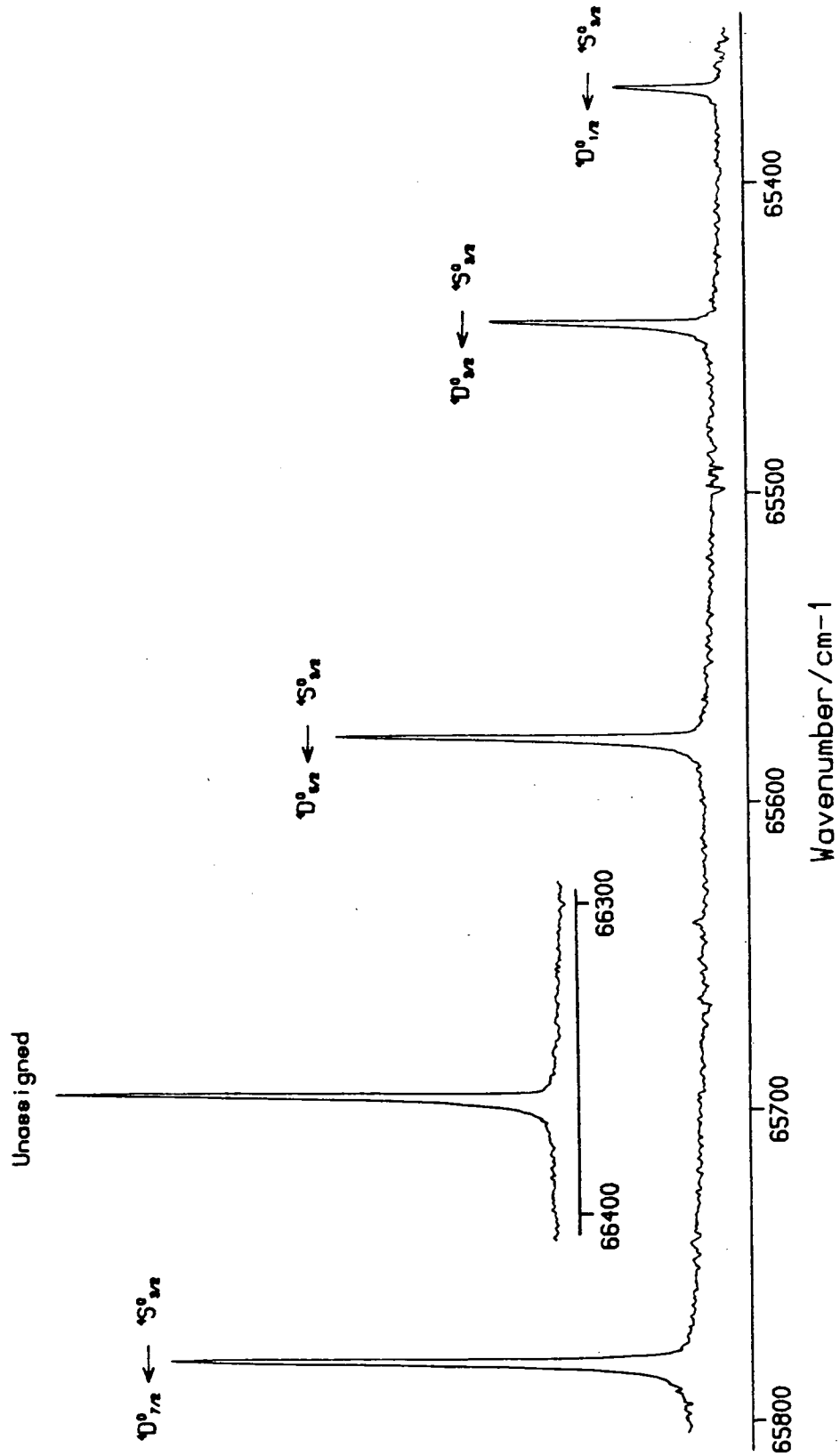

APPENDIX V (Cont/d)

By switching the discharge of additional molecular peaks appeared 'immediately' in the spectrum. Hence, the observed phosphorous atom spectrum must be due to the discharge.

Table AV.i lists the observed line positions and their assignments.

TABLE AV.i Atomic transition energies and assignments of phosphorous atoms following the [2+1] RIS process

Transition	Observed Transition Energy/cm^{-1}	Transition Energy from ref [17]/cm^{-1}	Residual (obs - ref)/cm^{-1}
$^4D^o_{1/2} \leftarrow {}^4S^o_{3/2}$	66373.0	65373.6	-0.6
$^4D^o_{3/2} \leftarrow {}^4S^o_{3/2}$	65450.2	65450.2	0.0
$^4D^o_{5/2} \leftarrow {}^4S^o_{3/2}$	65585.9	65585.1	0.8
$^4D^o_{7/2} \leftarrow {}^4S^o_{3/2}$	65788.2	65787.3	0.9
Unassigned	66361.7		

Since the residence time in the reactor, between the generation and probing zones, was near 100 ms the phosphorous atom population distribution would be expected to be thermal except possibly that some very long lived metastable species are known to be generated in microwave discharges [18]. The unassigned transition at 66361.7 cm^{-1} lies acceptably close to the transition $^4P^o_{3/2} \leftarrow {}^4S^o_{3/2}$ (66360.2 cm^{-1}). However, such a transition is forbidden by the atomic selection rules, as evidenced by the fact that transitions to the $^4P^o_{1/2}$ or $^4P^o_{5/2}$ terms were not observed.

Similarly the line could not be attributed to a transition in atomic bromine. Hence it was concluded that this line must belong to a transition from the excited $^2D^o_J$ ($^2P^o_J$) phosphorous atom term.

APPENDIX V (Cont/d)

ii) [2+1] RIS of Sulfur Atoms

RIS studies on sulfur atoms have previously been reported, as the products of a photodissociation experiment on CS_2 [12][19] and for the quenching of $S(^1D)$ [9] following photodissociation of OCS.

It was found that microwave discharges of various species containing sulfur led to a rapid sulfur deposition on the discharge side arm, with essentially no atomic sulphur being detected by the laser probe. However relatively high concentrations of sulfur atoms could be generated via two bimolecular stripping reactions [20].

$$F + H_2S \xrightarrow{k_1} HF + HS \qquad (1)$$

$$F + HS \xrightarrow{k_2} HF + S \qquad (2)$$

Where under pseudo first order reaction conditions, $[H_2S] \ll [F]$ the rate constants are: $k_1 = 1.28 \times 10^{-10}$ cm^3 s^{-1} and $k_2 = 2.0 \times 10^{-10}$ cm^3 S^{-1}. Assuming then that heterogeneous losses could be overcome in the reactor, reactions 1 and 2 and the RIS technique could be used to follow the subsequent reactions of the sulfur atoms.

By adjusting the flow of CF_4 to 30 SCCM out of a total flow of 800 SCCM (mostly of argon) with a microwave discharge power of 20 W and then adding down the sliding injector a low flow (no more than 5 SCCM) of 10% H_2S in argon and allowing of the order of a 10 ms reaction time, no strong molecular features were observed. Figure AV.ii presents a typical spectrum obtained under these conditions, while Table AV.ii presents the observed line positions and assignments.

FIGURE AV.ii: [2+1] RIS spectrum of sulphur atoms. The spectrum is not normalised for variations of the laser power with wavelength.

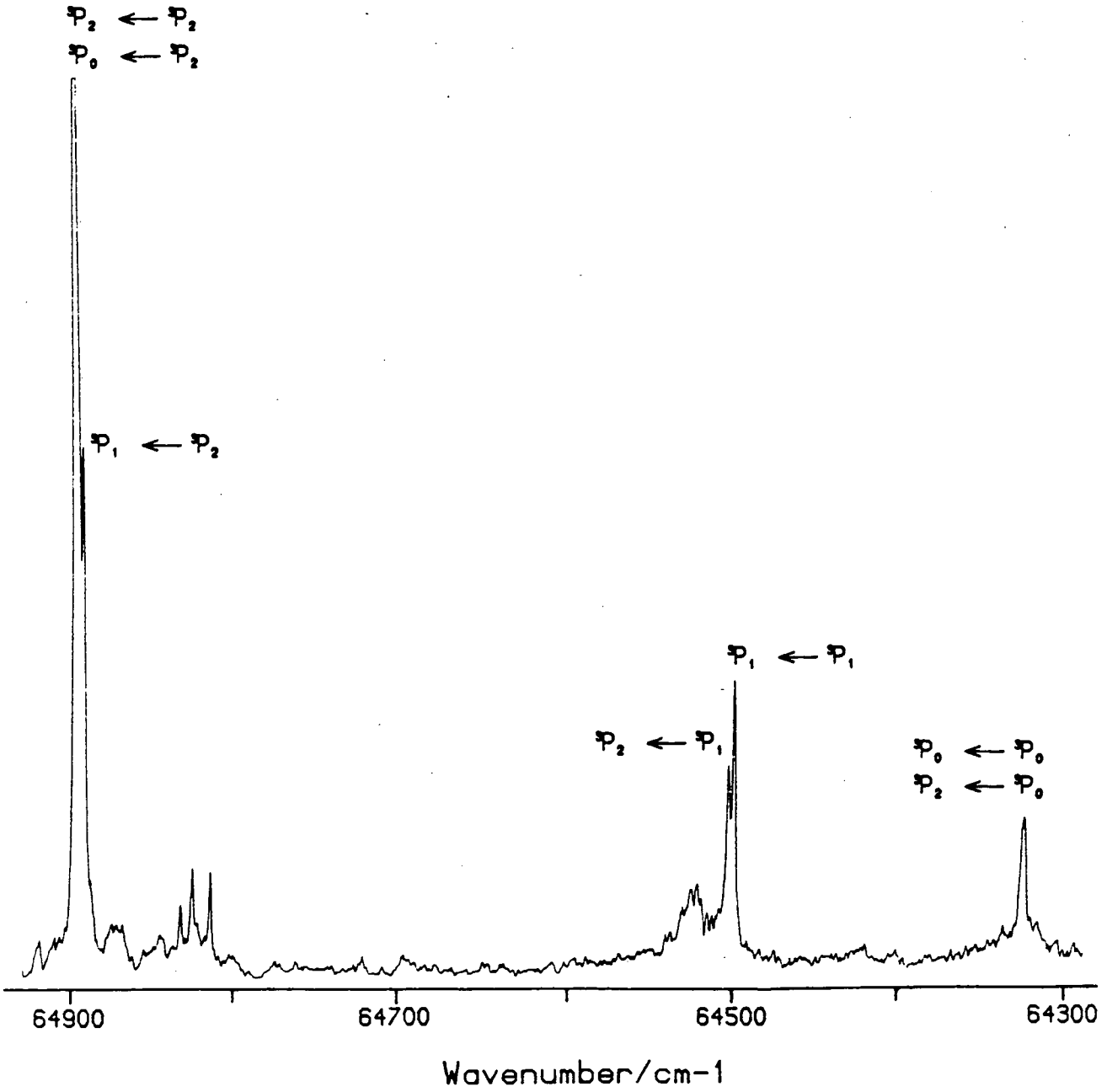

APPENDIX V (Cont/d)

TABLE AV.ii Atomic transition energies and assignments of sulfur atoms following the [2+1] RIS process

Transition	Observed Transition Energy/cm^{-1}	Transition Energy from ref [17]/cm^{-1}	Residual (obs - ref)/cm^{-1}
$^3P_1 \leftarrow {}^3P_2$	64889.8	64889.27	0.53
$^3P_2, {}^3P_0 \leftarrow {}^3P_2$	64892.3	64892.89 64891.71	
$^3P_1 \leftarrow {}^3P_1$	64492.9	64492.43	0.47
$^3P_2 \leftarrow {}^3P_1$	64497.2	64496.09	1.01
$^3P_2, {}^3P_0 \leftarrow {}^3P_0$	64320.3	64319.29 64318.71	

iii) [2+1] RIS of Carbon Atoms

Like sulfur, carbon atoms have been monitored by multiphoton processes following, normally, the photodissociation of stable precursor molecules such as C_2O_3 or CCl_4, [21][22][23].

It was found that by discharging a mixture of ~ 0.5% CH_4 in argon that transitions attributable to carbon atoms were observed. While this experimental configuration did lead relatively rapidly to a noticebale carbon deposit on the discharge side arm, relatively stable discharges could be obtained over at least 2 hours. Also the experimental s/n ratio was relatively poor, because it appeared that the ion collection plates acted as extremely efficient energy dumps for the metastable species present in the gas flow. Figure AV.iii shows a typical spectrum obtained under such conditions, all of the expected transitions between the $^3P_J \leftarrow {}^3P_J$ terms were observed in the spectrum except the $^3P_o \leftarrow {}^3P_o$ transition. This observation was explained in terms of this transition having the least oscillator strength of any of the $^3P_J \leftarrow {}^3P_J$ components. Table AV.iii presents the observed line positions.

FIGURE AV.iii: [2+1] RIS spectrum of carbon atoms. The spectrum is not normalised for variation of the laser power with wavelength.

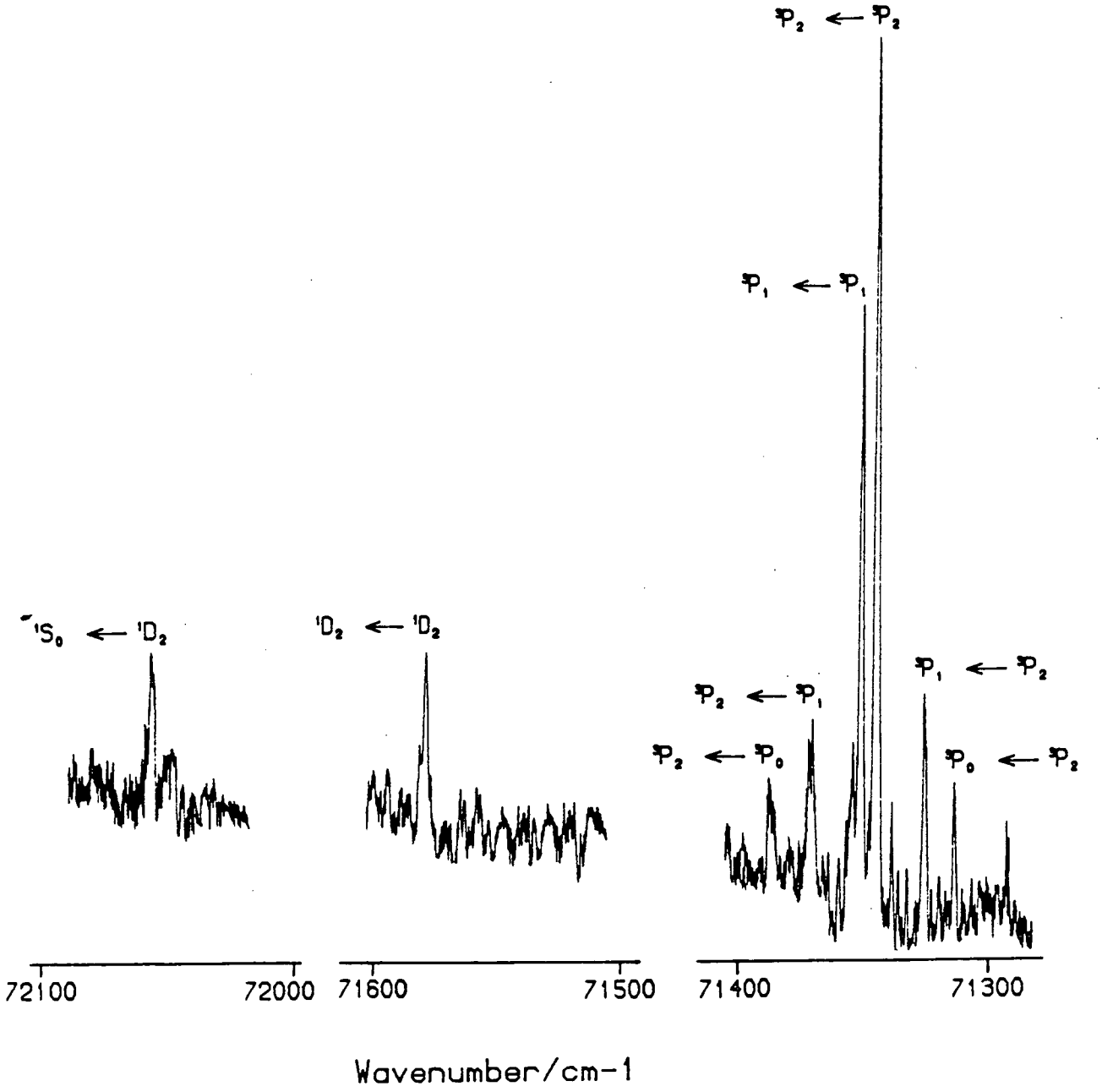

APPENDIX V (Cont/)

TABLE AV.iii Atomic transition energies and assignments of carbon atoms following the [2+1] RIS process

Transition	Observed Transition Energy/cm^{-1}	Transition Energy from ref [17]/cm^{-1}	Residual (obs-ref)/cm^{-1}
$^3P_0 \leftarrow\!\!- {}^3P_2$	71310.0	71309.31	0.69
$^3P_1 \leftarrow\!\!- {}^3P_2$	71322.2	71321.73	0.47
$^3P_2 \leftarrow\!\!- {}^3P_2$	71342.4	71342.20	0.20
$^3P_1 \leftarrow\!\!- {}^3P_1$	71348.2	71348.83	-0.63
$^3P_2 \leftarrow\!\!- {}^3P_1$	71368.6	71369.30	-0.70
$^3P_2 \leftarrow\!\!- {}^3P_0$	71385.1	71385.70	-0.60
$^1D_2 \leftarrow\!\!- {}^1D_2$	71577.6	71576.66	0.94
$^1S_0 \leftarrow\!\!- {}^1D_2$	72060.5	72058.61	1.89

APPENDIX V (Cont/d)

REFERENCES

1. M.A. Bol'shov in 'Laser Analytical Spectrochemistry' ed. V.S. Letokov (Adam Hilger, Bristol 1986).
2. G.I. Bekov and V.S. Letokov in 'Laser Analytical Spectrochemistry' ed. V.S. Letokov (Adam Hilger, Bristol 1986).
3. J.P. Young, G.S. Hurst, S.D. Kramer and M.G. Payne, Anal. Chem., 51 1050A (1979).
4. G.S. Hurst, M.G. Payne, S.D. Kramer and C.H. Chen, Phys. Today, 33 24 (1980).
5. M.G. Payne, C.H. Chen, G.S. Hurst and G.W. Foltz, Adv. At. Mol. Phys., 17 229 (1981).
6. G.S. Hurst, Phil. Trans. R. Soc. London Ser.A, 323 155 (1987).
7. P.C. Engelking, Chem. Phys. Lett., 74 207 1980.
8. A. Gedankin, M.B. Robin and N.A. Kueber, J. Phys. Chem., 86 4096 (1982).
9. G. Black and L.E. Jusinski, J. Chem. Phys., 82 789 (1985).
10. C.M. Phillips, J.I. Steinfeld and S.M. Miller, J. Phys. Chem., 91 5001 (1987).
11. L.E. Jusinski, G. Black and T.G. Slanger, J. Phys. Chem., 92 5977 (1988).
12. P. Brewer, N.Van Veen and R. Bersohn, Chem. Phys. Lett., 91 126 (1982).
13. K.D. Bonin and T.J. McIlrath, J. Opt. Soc. Am. B, 1 52 (1984).
14. M.S. Pindzola, Phys. Rev. A. 17 1021 (1978).
15. P.D. Brewer, Chem. Phys. Lett., 136 557 (1987).
16. P.D. Brewer, Chem. Phys. Lett., 141 301 (1987).
17. C.E. Moore 'Atomic Energy Level' Vol.I National Bureau of Standards (1971).
18. J.H. Kolts and D.W. Setser in 'Reactive Intermediates in the Gas Phase: Generation and Monitoring' ed. D.W. Setser (Academic Press, New York 1979).
19. J.L. Hardwick, Y. Ono and J.T. Moseley, J. Phys. Chem., 91 4506 (1987).

APPENDIX V (Cont/d)

REFERENCES

20. G. Schonle, M.M. Rahman and R.N. Schindler, Ber. Buns. Phys. Chem., 91 66 (1987).
21. M. Umemeto, H. Shinohara and N. Nishi, J. Photochem., 20 277 (1982).
22. P. Das, G. Ondray, N. Van Veen and R. Bersohn, J. Chem. Phys., 79 724 (1983).
23. S.T. Pratt, J.L. Dehmer and P.M. Dehmer, J. Chem. Phys., 82 676 (1985).

APPENDIX VI

Courses Attended

Recent Developments in Physical Chemistry (Various Speakers, University of Edinburgh).

Signal Processing (Dr M A D Fluendy, University of Edinburgh).

Mass Spectrometry (Prof K R Jennings, University of Warwick).

Theoretical Chemistry (Dr K P Lawley, University of Edinburgh).

Lasers (Dr A G Rae, University of Edinburgh).

Reaction Dynamics (Various Speakers, University of Edinburgh).

Atmospheric Chemistry (Prof R J Donovan and Dr J P T Wilkinson, University of Edinburgh).

Fortran (Edinburgh University Computing Service)
Graphics (Edinburgh University Computing Service)

In addition all the regular laser group meetings and physical chemistry seminars were attended, as were regular interdepartmental meetings with the Heriot Watt laser group.

Conferences Attended

9th International Symposium in Gas Kinetics, Bordeaux, July 1986.

11th International Symposium on Molecular Beams, Edinburgh, July 1987.

10th International Symposium in Gas Kinetics, Swansea, July 1988.